POLITECNICO DI MILANO
DEPARTMENT OF AEROSPACE SCIENCE & TECHNOLOGY
DOCTORAL PROGRAMME IN AEROSPACE ENGINEERING

SIMULATION AND DETECTION OF ICE FORMATION AND SHEDDING ON ROTORCRAFT

Doctoral Dissertation of:
Myles Morelli

Under the Supervision of:
Prof. Alberto Guardone

October 2017/2020 – Cycle XXXIII

Supervisor:
Prof. Alberto Guardone

Tutor:
Prof. Luigi Vigevano

The Chair of the Doctoral Program:
Prof. Pierangelo Masarati

External Examiners:
Dr. Boris Disken
National Institute of Aerospace

Prof. Manuel Keßler
Universität Stuttgart

Dr. Nicola Ceresola
Leonardo Aircraft Division

Prof. Enrico Nobile
Università degli Studi di Trieste

This work is part of the Network for Innovative Training on ROtorcraft Safety. The NITROS project has received funding from the European Union's Horizon 2020 research and innovation program under the Marie Skłodowska-Curie grant agreement No. 721920.

Acknowledgements

THIS thesis is the outcome of an opportunity afforded to me by Politecnico di Milano. For this, I am truly grateful to my supervisor, Prof. Alberto Guardone. In particular, the experience and knowledge passed down from Prof. Alberto Guardone has helped me develop both as an early-stage-researcher as well as a person. Your constant enthusiasm and positivity, even during the toughest of times, has made this Ph.D. an enlightening experience. During your supervision, you gave me a licence and freedom to be exploratory in my research, in which I rejoiced. It gives me great pride to say I am a student of yours. I would also like to collectively thank the individuals who have been part of Prof. Alberto Guardone's icing research group, including Barbara and Tommaso, amongst others.

Special acknowledgements should be paid to Prof. Giuseppe Quaranta for coordinating the *Network for Innovative Training on ROtorcraft Safety* (NITROS). The tuition provided by NITROS has given me a broad perspective on all essential aspects of rotorcraft safety by going above and beyond the norm of Ph.D. training. Furthermore, NITROS would not have been the same if it were not for my fellow colleagues: Daniel, Federico, Neda, Noor, Paolo, Sara, Sergio, Simone, and Ying.

The narrative of my Ph.D. would have been very different if it were not for Dr. Beckett Y. Zhou. Our collaboration has been a pleasure, highlighting the benefits of open-source communities like SU2, who also need thanking for their welcoming nature.

Importantly I now move towards the more personal acknowledgements, regarding my family and friends. My parents, where to begin ... you are the most intelligent and selfless people I know, and for this, I dedicate my thesis to your life's hard work since it has enabled me to be where I am today. The thing I have been looking forward to most is seeing the smile on your faces when I finally arrive home alongside my degree.

I would also like to thank my girlfriend, Julia. I treasure every second of joy and happiness you have brought into my life. You have been with me from the very beginning until the very end. Travelling around Italy together, while creating beautiful memories, has been a dream, and it is true that Italy is indeed, the country of love.

Last, but not least, I would like to acknowledge my friends: Karthik, Stefan, Ioannis, Mirko, and Matteo, partially for your helpful words of advice, but mainly for my many terrible headaches on a Tuesday morning.

Abstract

IN-FLIGHT icing is a peculiar phenomenon. Clouds of supercooled liquid water droplets exist within the atmosphere that are in an unstable state while undisturbed. However, when brought into contact with aircraft at sub-zero temperatures, these supercooled water droplets freeze on impact leading to the formation of ice. Ice induced geometric modifications on aerodynamically sensitive surfaces such as wings or rotors presents a serious issue to flight safety. Operating in the presence of icing clouds is therefore inherently dangerous and ill-advised without prior assessment of the effects of ice accretion. Accordingly, this influences the decision to provide icing clearance by the regulatory authorities. Moreover, the altitude in which rotorcraft operate coincides with the icing envelope where the likelihood of encountering supercooled water droplets is highest. Subsequently, rotorcraft are particularly vulnerable to the icing environment which makes understanding the phenomenon critical. Understanding this safety-critical issue for rotorcraft however is non-trivial, as this thesis will go on to present. The scarce knowledge of both rotorcraft ice shapes and of their detection is disconcerting. Numerical modelling techniques represent a powerful tool to investigate the physics of rotorcraft icing and to assist in the design of new ice detection and protection technologies.

Progress in the multidisciplinary field of computational rotorcraft icing requires knowledge of research disciplines such as computational fluid dynamics, particle in cell techniques, phase change modelling, and mesh deformation strategies. This thesis presents original research in each of these aforementioned disciplines associated to computational rotorcraft icing. The core of the thesis is divided into three main technical parts and aims to; (i) introduce a conceptual framework for ice modelling and detection in a non-inertial, rotating framework; (ii) develop and validate novel three-dimensional numerical tools suitable for simulating rotorcraft aerodynamics and icing; (iii) analyse high-fidelity rotorcraft icing simulations while addressing the limitations identified within the literature.

The first part of the thesis is devoted to the conceptual design phase of an acoustic ice detection system. An acoustic characterization of glaze and rime ice structures is intro-

duced to quantify different ice shape noise signatures which directly transcend from the iced performance characteristics. The feasibility of the detection technique is assessed on a two-dimensional oscillating Sikorsky 2110 airfoil based on the experimental model from *Phase-I* of the *High Fidelity Icing Analysis for Rotors* consortium.

The second part of the thesis is committed to the development and validation of three-dimensional rotorcraft icing tools, namely; (i) efficient and robust mesh deformation strategies for aircraft icing, (ii) open-source rotorcraft computational fluid dynamics software, (iii) influence of rotor-wing interactions on predictions, and (iv) novel particle tracking techniques. Firstly, radial basis function mesh deformation techniques and data reduction schemes are introduced to address the issues intrinsic to the moving ice boundary. Radial basis functions provide a suitable cost-effective approach to ensure high-quality mesh deformation for challenging iced geometries and multi-step ice accretion. While the data reduction schemes presented, facilitate the use of radial basis functions even on large datasets. Secondly, this thesis provides the first open-source and validated rotorcraft Computational Fluid Dynamics code by developing the well established SU2 solver. The incorporation of a new core feature to accommodate the blade kinematics of rotorcraft has been introduced. Thirdly, the flow physics associated to complex interactional behaviour of rotors and wings can be unlike that of isolated components and thus requires additional investigation. To this purpose, the turbulent flow field around a wing-tip mounted propeller configuration was simulated and validated using the model and test conditions released by the *Workshop for Integrated Propeller Prediction*. Fourthly, new techniques are introduced concerning Lagrangian particle tracking in mesh with arbitrary motion as well as across non-conformal boundary interfaces to enable the simulation of clouds containing individual supercooled water droplets in complex rotorcraft flow fields.

The third part of the thesis is dedicated to establishing state-of-the-art rotorcraft icing codes to help understand complex icing physics which can be difficult to comprehend using already existing icing analysis approaches. An original high-fidelity approach for the modelling of rotorcraft icing using new and entirely three-dimensional techniques is introduced, harnessing the previously developed numerical tools. The new approach is demonstrated on the experimental SRB-II model rotor in forward-flight developed at the Anti-icing Material International Laboratory in the Université du Québec à Chicoutimi, Canada. Overall, the numerical predictions are in good agreement with the experimental data. Subtleties in the modelling techniques, which subsequently have a significant impact on the final ice shapes, are highlighted. Additionally, the instantaneous pressure fluctuations of the iced rotors are analysed to provide an early insight into the potential use of computational aeroacoustic codes further down the line.

Contents

List of Figures

List of Tables

Nomenclature

Latin Symbols

A	Area
a	Speed of Sound
b	Semi-Span
C	Transformation Matrix
C_d	Drag Coefficient
C_l	Lift Coefficient
C_m	Moment Coefficient
C_n	Normal Force Coefficient
C_p	Pressure Coefficient
C_T	Thrust Coefficient
c	Chord
c_p	Specific Heat at Constant Pressure
D	Support Distance of the Wall Distance Function
d	Diameter
$\mathcal{D}_t$	Time Operator
E	Total Energy per Unit Mass
$\mathcal{E}_{AB}$	Intersection Area of Elements A and B
$\mathbf{E}$	Error Vector of Surface Displacements
F	Force
F_S	Safety Factor
$\boldsymbol{F}$	Combined Vector of Fluxes
$\boldsymbol{F}^c$	Convective Flux
$\boldsymbol{F}^v$	Viscous Flux

$f(\mathbf{r})$	Function to Be Evaluated at Position $\mathbf{r}$
h	Ice Thickness
$\boldsymbol{H}$	Spectral Operator Matrix
k	Reduced Frequency
M	Mach Number
m	Ice Mass
N	Number of Points
$\mathcal{N}(i)$	Neighbouring Nodes to Node i
$\mathcal{O}$	Order of Convergence
Pr_l	Laminar Prandtl Number
Pr_t	Turbulent Prandtl Number
$\mathcal{P}$	Particle
p	Static Pressure
p'	Instanteous Pressure Fluctuation
$\boldsymbol{Q}$	Vector of Source Terms
Q_∞	Freestream Dynamic Pressure
$\boldsymbol{q}_{\rho\upsilon}$	Generic Momentum Source Term
q_ρ	Generic Density Source Term
$q_{\rho E}$	Generic Density Source Term
R	Radius
Re	Reynolds Number
$\mathcal{R}(\boldsymbol{U})$	System of Governing Equations
$\mathfrak{R}$	Refinement Ratio
$\boldsymbol{r}$	Radial Position
r	Radial Distance
S	Solid Wall Flow Domain Boundary
ΔS	Surface Displacement
ΔS_{ij}	Area of Face Belonging to edge ij
T	Temperature
t	Time variable
U	Velocity
$\boldsymbol{U}$	Vector of Conservative Variables
$\boldsymbol{u}_{\Omega_i}$	Grid Velocity over Control Volume i
v	Volume Reduction Factor
ΔV	Volume Displacement
W_{swirl}	Swirl Velocity

W_+	Vector of Characteristic Variables
W_∞	Far-Field Characteristic Variables
w_i	Weight of Intersection Area i
$\boldsymbol{x}$	Position Vector
$\Delta\mathbf{X}$	X-Displacement Vector of Mesh Coordinates
$\Delta\mathbf{Y}$	Y-Displacement Vector of Mesh Coordinates
$\Delta\mathbf{Z}$	Z-Displacement Vector of Mesh Coordinates

Greek Symbols

$\boldsymbol{\alpha}$	Weight Coefficients of the Basis Points
α	Angle-of-Attack
β	Blade Flapping Angle
β_0	Blade Coning Angle
β_c	Lateral Cyclic Flap
β_s	Longitudinal Cyclic Flap
Γ	Flow Domain Boundary
Γ_p	Permeable Surface Boundary
Γ_∞	Far-Field Boundary Domain
δ	Blade Lead-Lag Angle
ε	Tolerance
η	$(\mathbf{r} - \mathbf{r}_i)/R$
θ	Blade Pitch Angle
θ_0	Blade Collective Pitch
θ_c	Lateral Cyclic Pitch
θ_s	Longitudinal Cyclic Pitch
$\theta_{0.75}$	Blade Pitch at 75% Radius
μ_{dyn}	Laminar Dynamic Viscosity
μ_{tur}	Turbulent Eddy Viscosity
ξ	$d(\mathbf{r})/D$
ρ	Fluid Density
$\bar{\tau}$	Strain Rate Tensor
τ	Pseudotime
τ_{shear}	Adehsive Shear Stress
$\boldsymbol{\Phi}$	Universal Basis Matrix
ϕ	Radial Basis Function
$\boldsymbol{v}$	Flow Velocity Vector
χ	Wall Distance Function

ψ	Azimuth Angle
Ω	Flow Domain
Ω_i	Control Volume Surrounding Node i
$\boldsymbol{\omega}$	Rotational Velocity Vector
ω	Angular Velocity

Subscripts and Superscripts

c	Control Points
f	Fluid
l	Multi-Level
p	Particle
s	Surface Points
v	Volume Points
∞	Free-Stream

Abbreviations

2D	Two-Dimensional
3D	Three-Dimensional
AoA	Angle of Attack
CAA	Computational Aero-Acoustics
CFD	Computational Fluid Dynamics
CPU	Central Processing Unit
EDDES	Enhanced Delayed Detached Eddy Simulation
FWH	Ffowcs-Williams and Hawkings
GCI	Grid Convergence Index
IRT	Icing Research Tunnel
LWC	Liquid Water Content
MVD	Mean Volume Diameter
NASA	National Aeronautics and Space Administration
OAT	Outside Air Temperature
RANS	Reynolds Averaged Navier-Stokes
RBF	Radial Basis Function
RPM	Revolutions Per Minute
SA	Spalart-Allmaras
SRB	Spinning Rotor Blade
SST	Shear Stress Transport
URANS	Unsteady Reynolds Averaged Navier-Stokes
WIPP	Workshop for Integrated Propeller Prediction

CHAPTER 1

Introduction

Make safety a religion.

Franklin D. Harris, “No Accidents – That’s the Objective”
The 26th Alexander A. Nikolsky Lecture, 2006

1.1 Background and Motivation

ROTORCRAFT possess the capability to vertically take-off and land, allowing them to operate in challenging flight conditions where more conventional fixed-wing aircraft cannot. Their operational environment lends itself to low-level altitudes, and many missions are often towards the boundary of the flight envelope. Throughout the course of aviation, the requirement for flight in poor weather conditions and at night has always been a driver for innovation and rotorcraft are no exception. In the past, rotorcraft were fair weather vehicles with marginal performance, however, now they regularly operate in conditions from hot and dry to cold, wet and windy [1]. Cold climates can potentially leave aircraft susceptible to dangerous icing conditions. In-flight icing encounters can jeopardise the performance and handling qualities of aircraft and hence pose a serious threat to flight safety [2, 3]. This threat to flight safety is brought forth as ice accretion can rapidly alter aerodynamic lifting surfaces such as wings and rotors during flight which are highly sensitive to geometric modifications. Naturally, establishing a comprehensive understanding of the fundamental physics of aircraft icing is paramount to ensure the reduction of ice related accidents and the progression of safety critical technology.

1.1.1 Physics of Ice Accretion

Icing events occur when an aircraft flies through clouds of supercooled droplets which contain drops of liquid water with a temperature below the freezing point. While undisturbed within the atmosphere, these supercooled water droplets remain in the liquid phase. However, external perturbations, such as upon impact with aircraft, cause these droplets to freeze forming ice. Hereinafter, both the rate and type of ice accretion are highly dependent upon environmental and operational parameters.

Environmental parameters which influence the rate and type of ice accretion include the outside-air-temperature, liquid water content of the supercooled water droplets, and supercooled water droplet size. The primary parameter influencing the accretion of ice from supercooled clouds is the outside-air-temperature. It influences the convective heat transfer and the surface temperature. Lower values of outside-air-temperature increase the likelihood of droplets freezing on impact. In addition to the temperature, the liquid water content is a critical parameter and measures the mass of liquid water that can be present within a volume of cloud. The mass of freezing water depends on the liquid water content. Consequently, high rates of ice accretion are associated with supercooled water droplets with high liquid water content. Furthermore, the size of the supercooled water droplets may influence the location of ice accretion. Droplets with a smaller diameter and mass tend to follow the airflow streamlines. While droplets with a larger diameter and mass can cross airflow streamlines. Resultantly, the ratio of inertial to aerodynamic forces acting on a droplet determines the impingement location.

Operational parameters which indirectly influence the rate and type of ice accretion include the altitude and airspeed. Firstly, the outside-air-temperature has a direct correlation with the altitude. High altitudes increase the potential for condensation of water droplets and their supercooling. Secondly, the airspeed influences the rate of ice accre-

tion and surface temperature. High airspeeds increase the volume of intercepted air per unit time and increase the kinetic heating on the aircraft surface.

Ice can be characterised into three distinct categories; *rime*, *glaze*, and *mixed* ice. The freezing process of the supercooled water droplets determines the type of ice which accretes. *Rime* ice is characterised by an opaque appearance and low density. This is due to air bubbles becoming trapped during the phase change process. Furthermore, this behaviour can be explained as supercooled water droplets instantaneously phase change forming ice upon impact. In the event of prolonged exposure to icing clouds, the *rime* ice profile may take the form of a pointed *spearhead*. *Rime* ice largely dominates at low outside-air-temperatures and flight speeds. On the contrary, *glaze* ice forms closer to the melting point and is characterised by a transparent appearance and high density. *Glaze* ice accretes as supercooled water droplets impact and flow over the aircraft surface before freezing. Momentarily, a portion of water remains in a liquid state forming a thin liquid film. This allows air bubbles to separate from the water before freezing giving rise to a homogeneous ice structure. Moreover, the water which remains in a liquid state has the potential to flow which may produce localised ice thickening. Extended exposure to icing clouds during *glaze* conditions may lead to the formation of ice *horns*. Finally, due to variations in local velocities, it is possible that both *rime* and *glaze* ice accretion is present simultaneously. An exemplary case is a rotor blade where, *rime* ice accumulates at radially inward locations, while *glaze* ice forms at radially outward locations.

1.1.2 Ice Detection and Protection

Ice detection and protection systems can be installed on rotorcraft to mitigate against icing. Nevertheless, these require extensive certification tests before being granted permission for use. Ice detection systems can be used for warning pilots of ice formation during flight [4]. However, the simplest method of visual detection is flawed for blades rotating at such high speeds and a correlation between icing on stationary and moving components is yet to be established. Ice protection systems can be used as a mitigation method against icing [5]. However moving components become a hindrance for the implementation of ice protection systems, as heating moving components consumes high quantities of available power and is inefficient. A limited number of rotorcraft therefore have ice detection and protection systems installed, and problems arise when rotorcraft inadvertently encounter icing conditions.

1.1.3 Safety Concerns

The concerns for the safety of aviation in icing conditions are widely recognised by the governing authorities. The European Parliament and the Council of the European Union introduced regulation $376/2014$ to ensure a high general level of aviation safety and to commit to reducing the number of accidents and incidents [6]. In correspondence, the European Aviation Safety Agency has begun applying a European Risk Classification Scheme to generate a safety risk portfolio. In the European Aviation Safety Agency's 2019 annual report, in-flight icing was identified as a priority-1 issue for large aeroplanes with the aggregated European Risk Classification Scheme score being amongst

the highest of all safety issues [7]. However, the lack of rotorcraft data prevented the European Aviation Safety Agency from providing a risk assessment for onshore category, offshore category, specialised operation, and non-commercial operation rotorcraft, which is deeply concerning. To address this high priority, the European Aviation Safety Agency has released the European Plan for Aviation Safety which will run from 2020 to 2024 and has identified a number of actions motivated to improve aviation safety in icing conditions [8]. Actions include the development of numerical tools for the three-dimensional modelling of ice to aid design and certification [9] as well as the development of approaches for detecting the presence of ice on critical components [10].

1.2 Rotorcraft Icing Certification

Entering into icing conditions is strictly prohibited by the regulatory authorities if the rotorcraft in question does not have icing clearance. The following section will discuss the certification specifications and acceptable means of compliance to gain icing clearance in the European Union and the United States.

1.2.1 European Aviation Safety Agency

Clearance for entering into known icing conditions in the European Union is obtained by appeasing the regulations from the European Aviation Safety Agency. Small and large rotorcraft must respectively satisfy certification specifications CS-27 [11] and CS-29 [12]. The European Aviation Safety Agency has introduced special conditions for limited icing clearance which applies only to large rotorcraft. Acceptable compliance for limited icing clearance requires a means of safely vacating icing conditions throughout the entire flight path and subsequent demonstration of natural de-icing of the main rotor. Rotorcraft with clearance by the European Aviation Safety Agency for both limited as well as full icing conditions include the AgustaWestland 139 and 189 [13, 14]. Compliance with the subsequent statement from the European Aviation Safety Agency is a requirement for certification:

> *It must be demonstrated that the rotorcraft can be safely operated in the continuous maximum and intermittent maximum icing conditions determined under Appendix C within the rotorcraft altitude envelope. An analysis must be performed to establish, on the basis of the rotorcraft's operational needs, the adequacy of the ice protection system for the various components of the rotorcraft.* [15, 16]

Accordingly, means of analysis for the safe operation of rotorcraft in icing conditions involves approaches such as icing experiments, and, flight tests. The analysis may be of isolated components, models, or full rotorcraft configurations. Compliance with the European Aviation Safety Agency also requires suitable means of ice detection for certification:

> *A means must be identified or provided for determining the formation of ice on critical parts of the rotorcraft. Unless otherwise restricted, the means*

must be available for night-time as well as day-time operation. The rotorcraft flight manual must describe the means of determining ice formation and must contain information necessary for safe operation of the rotorcraft in icing conditions. [17, 18]

1.2.2 Federal Aviation Administration

Eligibility for flight into known icing conditions in the United States is achieved by satisfying the airworthiness standards supplied by the Federal Aviation Administration. Certification of normal category rotorcraft is achieved by adhering to Advisory Circular 27-1B [19] and certification of transport category rotorcraft is achieved by adhering to Advisory Circular 29-2C [20]. In March 1984, a Sikorsky UH-60 Black Hawk became the first rotorcraft to be certified for flight into known icing conditions [21, 22]. The Federal Aviation Administration are explicit as to the purpose of icing certification:

The objective of icing certification is to verify that throughout the approved envelope, the rotorcraft can operate safely in icing conditions expected to be encountered in service (i.e., Appendix C of Part 29 or the altitude-limited icing envelope). This will entail determining that no icing limitations exist or defining what the limitations are, as well as establishing the adequacy of the ice warning means (or system) and the ice protection system. A limiting condition may manifest itself in one of several areas such as handling qualities, performance, autorotation, asymmetric shedding from the rotors, visibility through the windshield, etc. Prior to flight tests in icing conditions, sufficient analyses should have been conducted to determine the design points for the particular item of the rotorcraft being analyzed (wind shield, engine inlet, rotor blades, etc.). After the analyses are reviewed and found adequate, tests should be conducted to confirm that the analyses are valid and that the rotorcraft can operate safely in any supercooled cloud icing condition defined by Part 29, Appendix C, or the altitude-limited icing envelope. [23, 24]

Suitable methods for the analyses of components such as the rotor blades are therefore required to demonstrate compliance of the ice detection and ice protection systems prior to full flight test programs. However, demonstrating the compliance of these systems can itself be difficult as this thesis will go onto discuss. The Federal Aviation Administration also recognise the high level of uncertainty associated with ice accretion on rotorcraft. It is even acknowledged that the formation of ice on different rotorcraft under the same icing conditions could potentially be contrasting. An extract from the airworthiness certification standard reads:

The effects of ice can vary considerably from rotorcraft to rotorcraft. Experience gained for a rotor system with an identical blade profile could provide valuable information but should be used cautiously when applied to another rotorcraft. Assumptions cannot necessarily be made based on icing test results from another rotorcraft. Particular care should be exercised when drawing from fixed-wing icing experience as the widely different

> *and varying conditions seen by the rotor blades make many comparisons with fixed-wing results invalid. Likewise, icing effects on rotor blades vary significantly from those on other parts of the rotorcraft. This is due to changing blade velocity as compared with the constant velocity of the remaining parts.* [25, 26]

Compliance with the certification standards from the Federal Aviation Administration can be established once there is assurance that while operating in icing conditions there is no deterioration of the handling qualities, performance, visibility, and system operations. Compliance must also ensure that an in-flight ice detection sensing systems is installed to warn the pilot of potential icing conditions of vital components and for the activation of the anti-icing and de-icing systems:

> *There should be a means identified or provided for determining the formation of ice on critical parts of the rotorcraft which can be met by a reliable and safe natural warning or an ice detection system.* [27, 28]

1.3 Literature Review

This Chapter will now look towards the current literature for assuring acceptable means of compliance with the certification specifications laid out by the European Aviation Safety Agency and Federal Aviation Administration for flight in known icing conditions. Performing planned in-flight icing certification tests on rotorcraft in natural icing conditions can be challenging due to the unpredictability of natural icing events. Factors such as the geographic location can help to improve the likelihood of suitable meteorological conditions for scheduling natural in-flight icing tests. However, this can lead to icing trails in hostile and potentially unsafe locations. More controlled alternative approaches are therefore required to learn about the hazardous nature of in-flight icing on rotorcraft. Approaches which have been adopted by manufacturers and operators include artificial in-flight icing spray systems, experimental icing wind tunnels, and numerical icing codes. While all of these artificial icing approaches have shown considerable promise both individually and collectively, none are able to satisfy the full requirements for certification without natural icing flight tests. However, these approaches can and are encouraged to be used to aid the certification process to analyse critical design points which are difficult to find in natural icing conditions.

1.3.1 Artificial In-Flight Icing Systems

Artificial in-flight icing systems were introduced to achieve conditions as close to natural icing events as possible. Many different approaches have been utilized to simulate artificial icing clouds due to promising early findings. In the 1970's and 80's, this led to extensive government-backed research programs with multiple phases of development. In general, artificial in-flight icing systems can be characterised into three types: 1) Large icing test chamber spray systems capable of accommodating full-scale aircraft. 2) Fixed base icing spray systems which rely on the outside wind to convect the spray

into the path of the aircraft. 3) Leader-Chaser aircraft icing spray system which are deployed during flight. A schematic displaying the three different types of artificial icing spray systems is shown in Fig. 1.1.

The United States Air Force McKinley Climatic Laboratory was first designed in 1947 and is a climatic laboratory used for temperature-controlled operation in icing environments [29]. It was originally designed for artificial ground fog icing capabilities and was not intended to be used for artificial in-flight icing conditions. The main chamber is large at approximately $75\,\mathrm{m}$ wide, $80\,\mathrm{m}$ in length, and has a height of approximately $20\,\mathrm{m}$. This allows it to accommodate even the largest of rotorcraft. Artificial icing conditions are created by two nozzle systems which spray atomized water. The icing cloud is then blown towards the aircraft by three large wind machines. Between 1975 and 1976 the McKinley Climatic Laboratory was first used for an airworthiness and flight characteristics evaluation on a U.S Army, Bell 214A model helicopter in icing conditions, although it was reported as having limited success [30]. In 2001, the McKinley Climatic Laboratory began a four-year project to redesign the chamber for improved in-flight icing capabilities such as to increase the size of the artificial cloud as well as to increase cloud stability, uniformity and duration [29]. In 2004, these improvements to the McKinley Climatic Laboratory cloud generating capabilities allowed for artificial icing tests on the Sikorsky S-92A helicopter and in particular the operation of the fuel system during icing [31]. A schematic illustrating the McKinley Climatic Laboratory configuration is shown by Fig. 1.1a.

In 1960, the National Research Council of Canada designed a spray rig which could be used to study icing on helicopters in flight [32]. The National Research Council spray rig is located in Ottawa, Canada where winter conditions are favourable for artificial icing tests. The Canadian National Research Council spray rig is approximately $18\,\mathrm{m}$ tall while, the nozzle array is $5\,\mathrm{m}$ in height and $22\,\mathrm{m}$ in width. The array contains 156 nozzles which spray atomized water with a mean volume diameter of $30\,\mu\mathrm{m}$ to produce the artificial cloud. The spray rig system operates by using the wind to convect the cloud into the rotor streamtube. This means that it can only be used for hover and very low speed forward flight. Between January and March of 1983, a two-phase helicopter icing flight test program of a Bell UH-1H helicopter was established by the United States Army [33–35]. During the first phase of this program, they were able to document the ice shapes present on the main rotor [33]. During the second phase of the program, it allowed for the evaluation of the UH-1H Helicopter hover performance degradation caused by rotor icing [34]. An overview of the two-phase program concluded that the performance degradation caused by rotor icing in hover could not be correlated with the quantity of accreted ice using a single free hover point and that additional research needed to be conducted to validate the artificial ice shapes [35]. A schematic illustrating the Canadian National Research Council spray rig configuration is shown by Fig. 1.1b.

Since 1973, the United States Army has utilized a highly modified and heavily instrumented Boeing CH-47 Chinook as an airborne spray tanker to generate artificial icing clouds for in-flight icing tests [36]. The modifications to the Boeing CH-47D Chinook include a Helicopter Icing Spray System which consists of an internal water tank and an external nozzle system. When the Helicopter Icing Spray System is deployed during flight, a chaser aircraft can follow the leader CH-47D Chinook helicopter

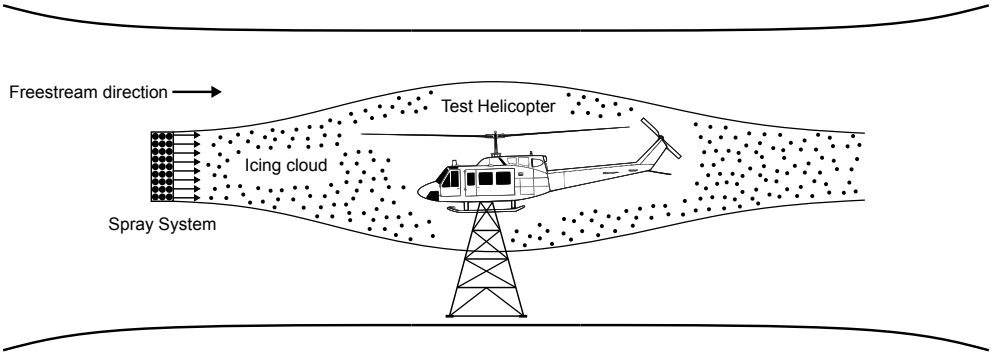

(a) *Test chamber spray system.*

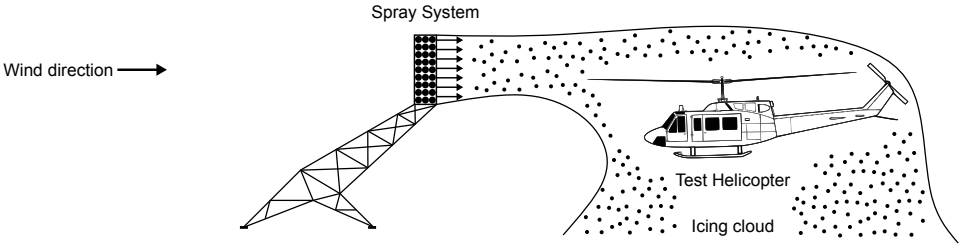

(b) *Fixed base icing spray system.*

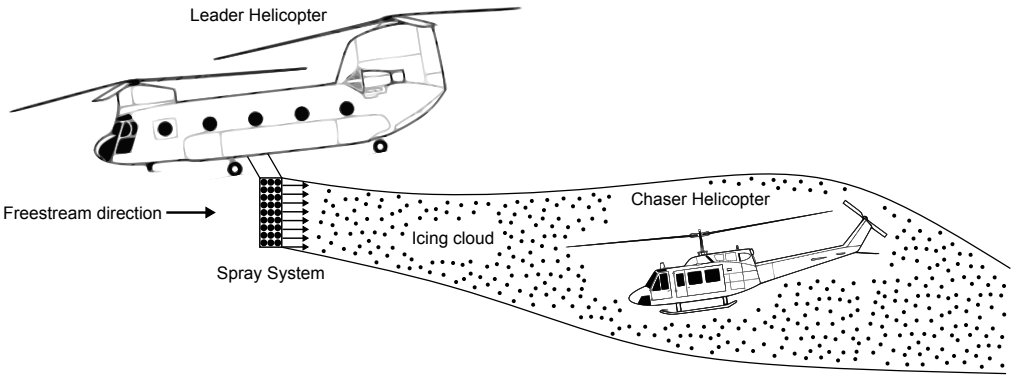

(c) *Leader-Chaser aircraft icing spray system.*

Figure 1.1: *Schematic of icing spray systems for producing artificial icing clouds.*

and be exposed to a spray of water representative of an icing cloud. A two-phase program then set out to improve the instrumentation and modification of the Helicopter Icing Spray System. During the first phase in 1979, a program was conducted to evaluate nozzle improvements to the Helicopter Icing Spray System for its acceptance as a means of replicating natural icing clouds [37]. During the second phase in 1986, a program aimed to evaluate the operational performance and spray cloud characteristics of the Helicopter Icing Spray System from a set of in-flight icing tests [38]. After the two-phase program, the following conclusions about the Helicopter Icing Spray System were reached: (i) the artificial cloud produces droplets of the desired size ranging between $15\,\mu\mathrm{m}$ to $25\,\mu\mathrm{m}$ which are characteristic of natural icing clouds; (ii) the test aircraft ice formations produced with the artificial compared favourably with those seen in the natural icing environment [37, 38]. Since then, the Boeing CH-47D Chinook configuration instrumented with the Helicopter Icing Spray System has been used extensively over the past 40 years for artificial icing tests. It has helped provided limited and full icing clearance on an AgustaWestland EH101, AW139, and AW189 [39, 40] as well as for the Sikorsky S-92A [31]. A schematic illustrating the Helicopter Icing Spray System configuration is shown by Fig. 1.1c.

Nevertheless, each of the aforementioned artificial in-flight icing spray systems has its own set of constraints. A major limitation of both the McKinley Climatic Laboratory and the National Research Council spray rig is that they can only be used for hover and very low flight speeds. The Helicopter Icing Spray System also has limitations. The size of the artificial cloud generated by the Helicopter Icing Spray System was primarily designed to ice components of rotorcraft, not the complete rotorcraft. Moreover, flight speeds are limited by the Chinook helicopter, which makes flight tests for high-speed rotorcraft such as the AW609 challenging. In general, all outdoor icing tests are also reliant on subzero outside air temperatures, restricting the number of months in a year which the tests can take place.

1.3.2 Experimental Tests

Apprehension towards the limitations of artificial in-flight icing spray systems led to the establishment of experimental icing research test facilities. In the early 1940's, NASA designed and build the Icing Research Tunnel. The Icing Research Tunnel is a closed-loop wind tunnel which is maintained at sub-freezing temperatures and is capable of reproducing icing conditions [41]. The test section of the tunnel is $1.8\,\mathrm{m}$ in height and $2.7\,\mathrm{m}$ in width. Originally it could be used for airspeeds up to $134\,\mathrm{m\,s^{-1}}$ and the heat exchanger allowed for the total temperature to range from $-1.1\,^{\circ}\mathrm{C}$ to $-42\,^{\circ}\mathrm{C}$. The spray nozzle can provide droplet mean volume diameters from approximately $10\,\mu\mathrm{m}$ to $40\,\mu\mathrm{m}$ and droplet liquid water contents varying from $0.2\,\mathrm{g/m^3}$ to $3.0\,\mathrm{g/m^3}$. However, it was not until 1985 when a program to establish the first set of model rotor tests in the Icing Research Tunnel was designed. The NASA program enlisted help from the United States helicopter manufacturing community to build a *Helicopter Icing Consortium* consisting of members from NASA Lewis, Bell Helicopter, Boeing Helicopters, McDonnell Douglas Helicopters, Sikorsky Aircraft, and Texas A&M University.

In the early months of 1989, Miller and Bond designed the first phase of the program and decided to use a simple Bell OH-58 Tail Rotor Rig to begin the icing research

program [42]. The experiment successfully demonstrated the viability of the Icing Research Tunnel to model rotor icing. The data gathered was suggested to be comparable to full-scale flight test data. The techniques learnt from the first phase of the program were then used by the *Helicopter Icing Consortium* for the second phase of the program. Towards the end of 1989, Flemming, Bond, and Britton designed the second phase of the program in the Icing Research Tunnel and used a more advanced Sikorsky Power Force Model [43, 44]. The Power Force Model has a Sikorsky UH-60 Black Hawk fuselage, uses a four-bladed main rotor and was fully articulated. A load measurement system recorded the forces and moments of the iced rotor. The blades had a radius of $0.915\,\mathrm{m}$ and used a NACA0012 airfoil profile. Examination of the data recorded from the tests showed the influence of ice on the lift and torque on the rotor. The effect of the temperature, rotor speed, liquid water content and droplet size were also shown. In 1995, Britton, Bond, and Flemming reviewed the previous Helicopter Icing Consortium program and decided that there was certain test conditions missing from the data-base [45]. Additional test were therefore performed to improve the icing database. Tests conditions identified as needing addressed included several high power rotor performance points, warm temperature operating conditions, and operation of the model during constant lift mode. The experimental test models used throughout phase one and two of the *Helicopter Icing Consortium* are displayed in Fig.1.2.

Over a decade and a half then past where there was limited rotorcraft related icing research performed in the Icing Research Tunnel. A collaborative project between industry, academia, and the United States government as part of the Vertical Lift Consortium called the "*High Fidelity Icing Analysis for Rotors*" was then established [46, 47]. Partners involved in the consortium included Bell Helicopter, The Boeing Company, Sikorsky Aircraft Corporation, Georgia Institute of Technology, NASA, and the United States Army. The goal of the project was to provide a high-fidelity suite of validated rotorcraft icing tools which could be utilized for design and certification. In May 2010, the objective of the first phase of the *High Fidelity Icing Analysis for Rotors* project was to perform a series of oscillating Sikorsky SC2110 airfoil icing tests to address the issue that all previous icing tests were performed on stationary airfoils [46]. Between August and September of 2013, the goal of the second phase of the *High Fidelity Icing Analysis for Rotors* project was to perform icing tests on a Bell 206 heated tail rotor model to obtain high-quality data on rotor ice accretion, ice shedding and impact, as well as rotor performance [47].

Evidentially the NASA Icing Research Tunnel has played an important role in providing a large database of rotorcraft icing information. However, a significant limitation of the NASA Icing Research tunnel for rotor icing studies is that it is restricted to maximum rotor diameters of approximately $1.8\,\mathrm{m}$ [48]. Moreover, NASA themselves have identified that there is no single scaling method that has been systematically developed and evaluated for rotorcraft icing applications [49]. Due to the continuous interest in rotorcraft icing, separate institutions have started designing their own icing wind tunnels for further research. In 2012, a new Adverse Environmental Rotor Icing Test Stand was constructed at the Pennsylvania State University to help reduce the limitations of current rotor icing test facilities [50]. The Adverse Environmental Rotor Icing Test Stand facility is capable of reproducing icing condition for rotors with a maximum diame-

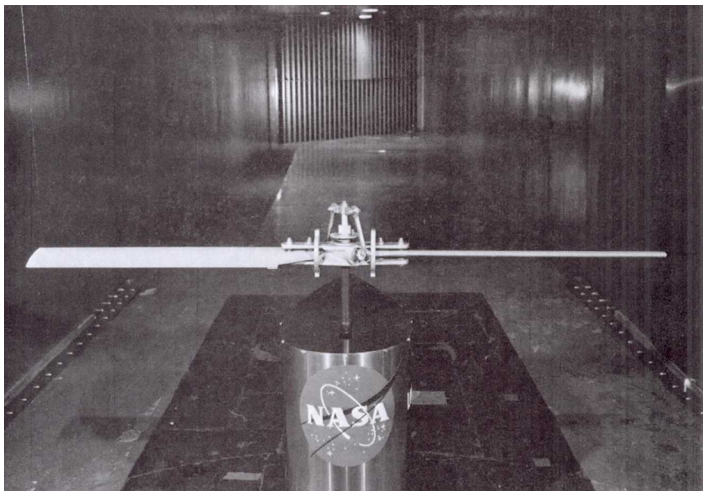

(a) *Phase-I: OH-58 tail rotor.*

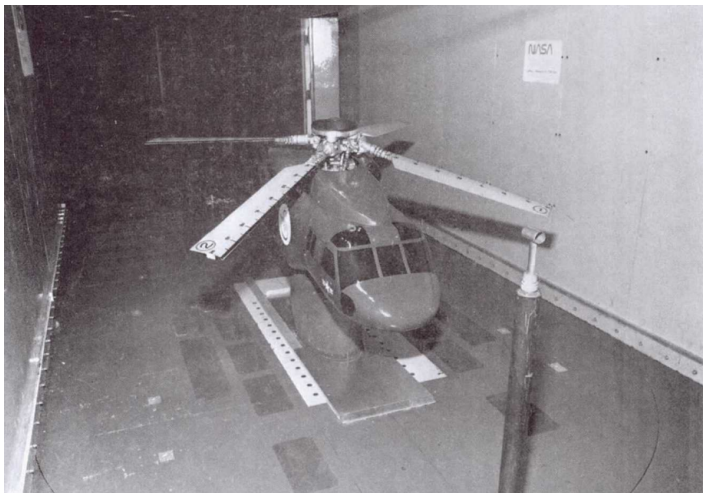

(b) *Phase-II: Power Force Model attached to a Sikorsky UH-60 Black Hawk fuselage.*

Figure 1.2: *Experimental models in the NASA IRT during the Helicopter Icing Consortium. Photographs sourced from Ref. [43].*

ter of up to approximately $2.75\,\mathrm{m}$. An experimental correlation between the Adverse Environmental Rotor Test Stand and NASA's Icing Research Tunnel was performed to validate the test facility [51]. The Adverse Environmental Rotor Icing Test Stand experiments were shown to recreate icing results in good agreement with NASA's Icing Research Tunnel. Furthermore, it was concluded that the Adverse Environmental Rotor Icing Test Stand facilitates the study of unique features of rotorcraft icing that cannot be accomplished through the use of an icing wind tunnel. Additionally, the Adverse Environmental Rotor Icing Test has been used to investigate ice shedding characteristics [52]. The work focused on the location and time of ice shedding events caused by centrifugal forces.

The natural phenomena of ice shedding on rotor blades represents a logical method for de-icing on rotorcraft. Fortin and Perron understood this, and together with Bell Helicopter, they used to the Anti-icing Material Laboratory at the Université du Québec à Chicoutimi, to design the Spinning Rotor Blade model to study low-energy de-icing systems based on hydro-phobic blade coatings [53]. The Spinning Rotor Blade configuration uses a $1/18$ sub-scale model helicopter rotor. The experimental tests investigated different hydro-phobic blade surface coatings and their influence on the time required to produce shedding events and the length of ice shed. The increased power consumption of the Spinning Rotor Blade motor was also recorded during the icing experiments.

Despite the best efforts of the helicopter icing research community, even the largest icing research wind tunnels are unable to conduct icing experiments on full-scale rotor blades. Subsequently, ice scaling methods have been introduced. However, there remains no consensus on the best-practise for ice scaling laws on rotor blades. This issue is compounded by the size of the sub-scale experimental rotors. The experiments conducted in the NASA Icing Research Tunnel on the Power Force Model used 0.175 scale UH-60 main rotor blades [43,44]. More recently NASA has moved towards using a full-scale Bell 206 tail rotor with a $65\,\mathrm{in}$ diameter to address this issue [47]. However, correlations made between main and tail rotor ice shapes should be carefully considered. While at the Université du Québec à Chicoutimi a $1/18$ sub-scale model rotor was used for testing ice protection systems [53]. However, since ice protection systems do not scale with the size of the rotor, using a $1/18$ sub-scale model is a significant assumption. The largest rotor icing experimental tests are from the Adverse Environmental Rotor Icing Test Stand where rotor diameters up to $9\,\mathrm{ft}$. have been demonstrated [50]. Within these test facilities, rotors with chord lengths representative of full-scale helicopter blades have been used. However, sub-scale rotor diameters remain a requirement.

1.3.3 Numerical Modelling

The simulation of in-flight ice accretion on rotorcraft is a challenging multidisciplinary problem which requires high-level numerical modelling. The development of numerical tools to simulate rotorcraft icing is not a trivial task. A defined structure is yet to be established for full three-dimensional modelling of main rotor icing. Moreover, the lack of high-quality and repeatable experimental data makes code validation difficult. For this reason, regulation authorities are yet to accept certification via means of simulation for rotorcraft flight in icing conditions despite this now being an acceptable means of

certification for their fixed-wing counterparts [54]. Resultantly, very few rotorcraft are certified with limited or full icing clearance due to the significant expense of the certification process. The considerable cost is associated to the time involved with the overall process. In-flight icing trails can frequently take several years to complete due to the reliance on natural icing environmental events providing suitable conditions across the entire flight envelope to satisfy EASA Certification Standard 29 Appendix C [12]. Establishing the best practices for the simulation of full three-dimensional rotorcraft icing is therefore imperative to improve understanding of this complex phenomena and to potentially provide certification by means of simulation for rotorcraft as well as fixed-wing aircraft.

Fixed-Wing Icing Code Development

Prior to discussing rotorcraft icing simulation techniques, it is first beneficial to understand the simulation structure used for predicting fixed-wing aircraft icing. Conventional fixed-wing aircraft icing tools are well established and in the mature stages of development such as LEWICE3D from NASA [55], FENSAP-ICE from Ansys [56], and POLIMICE from Politecnico di Milano [57]. Three-dimensional ice accretion capabilities are now commonplace in many codes although they remain a key area of research as outlined by the EASA and their commitment to three-dimensional numerical tool development with the ICE GENESIS project [58]. The simulation structure routinely involves a three-stage process which iteratively updates to account for unsteady ice accretion. This simulation process is commonly known as multi-step ice accretion and is shown through the use of a diagram in Fig. 1.3. The first stage involves the use of a flow solver to determine the aerodynamic flow-field around regions exposed to icing such as the wing, fuselage or even pitot tube. The second stage entails the use of a droplet solver to compute the trajectories of supercooled water droplets in the fluid flow to determine their impingement locations and collection efficiency. The third stage concerns the use of an icing solver to calculate the ice shape based on icing models which are dependent on the surface temperature and collection efficiency as well as other influential parameters. Multi-step ice accretion then introduces a fourth stage to update the iced mesh usually through means of mesh deformation techniques.

Rotorcraft Icing Code Development

In order to address the weaknesses of both artificial in-flight icing systems and experimental icing test facilities for rotorcraft, numerical modelling techniques have been developed. A brief history of recent techniques developed to simulated rotorcraft icing will now be discussed. A summary of the different numerical modelling techniques introduced in the literature for simulating rotorcraft icing is displayed in Table 1.1. It highlights the key authors, the period of research development, and the assumptions made when analysing the flow-field, droplet trajectories, and ice accretion.

Between 1991 and 1994, Britton, Bond, and Flemming developed and reviewed the LEWICE icing code for rotorcraft. Together their work played a significant role in the early progress of rotorcraft icing tools [48, 59, 60]. They were part of the Helicopter Icing Consortium which conducted icing experiments on the Power Force Model in the

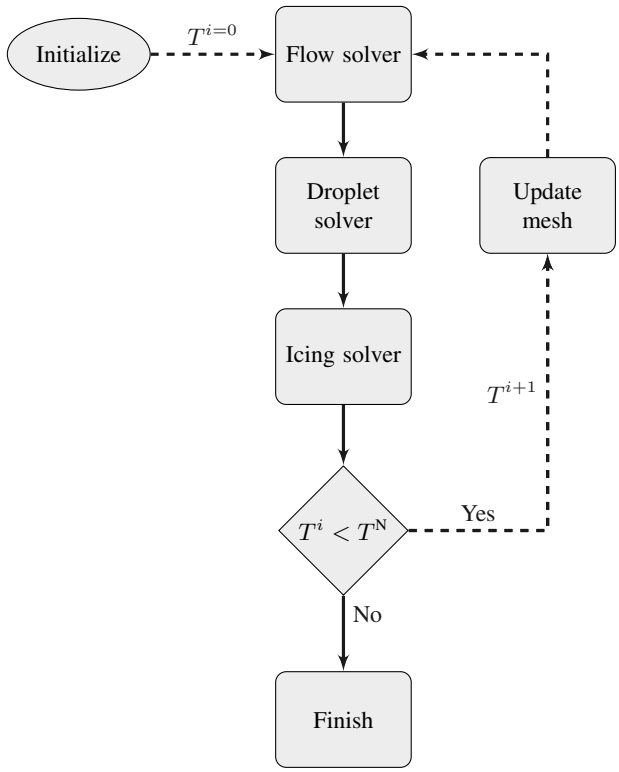

Figure 1.3: *Schematic of a standard multi-step icing simulation.*

NASA Lewis Icing Research Tunnel [45]. The experimental data was used for code validation with theoretical models. Britton is recognised with the development of an analytical method to predict helicopter main rotor performance in icing conditions [60]. The analytical method was based on the LEWICE code [61] and utilized potential flow theory [62] to describe the flow-field. The local angle-of-attack and velocity at different radial positions was then averaged azimuthally and given as the input to LEWICE due to it being a steady-state code. The thermodynamic process and freezing fraction was described by Messinger's model [63]. The ice shape computations were therefore two-dimensional in nature at selected radial locations. Flemming is credited with recognising the role of wind tunnel tests and computer codes in the certification and qualification of rotorcraft for flight in forecast icing [48]. In 1994 NASA put rotorcraft icing research on hold to focus on fixed-wing icing research due to a number of high profile accidents such as flight 4184 where an American Eagle passenger aircraft crashed causing 64 fatalities [64].

Over a decade later, the numerical modelling of rotorcraft icing garnered new interest which coincided with the development of Computational Fluid Dynamic (CFD) codes which were now able to accurately model three-dimensional flows around rotors. Between 2009 and 2011 a group of established researchers including Sankar, Flemming, Kreeger, Bain, Rajmohan, and Nucci developed a methodology for modelling the effects of ice accretion on rotorcraft performance in hover and forward flight [65–68]. Their

Table 1.1: *Summary of Numerical Modelling Approaches for Rotorcraft Icing*

Authors *(Organisation)*	**Period**	**Approach**	**Flow Analysis**	**Droplet Analysis**	**Icing Analysis**
Britton, Bond, & Flemming [45,48,59, 60] *(NASA, Sikorsky Aircaft)*	1991 – 1994	Full 2D	2D	2D	2D
Sankar, Flemming, Kreeger, Bain, Rajmohan, & Nucci [65–68] *(Georgia Tech, NASA, Sikorsky Aircaft)*	2009 – 2011	Hybrid 2D/3D	3D	2D	2D
Narducci & Kreeger [69, 70] *(The Boeing Company, NASA)*	2010 – 2011	Hybrid 2D/3D	3D	2D	2D
Kelly, Habashi, Quaranta, Masarati, & Fossati [71, 72] *(McGill Uni., Polimi, Uni. Strathclyde)*	2014 – 2018	Hybrid 2D/3D	2D	2D	3D
Chen, Zhao, & Barakos [73–75] *(Nanjing Uni. of Aeronautics & Astronautics, Uni. of Glasgow)*	2016 – 2019	Full 3D	3D	3D	3D

approach was to use a loosely-coupled suite of tools automated in a python framework. A hybrid CFD solver was used to solve the flow-field. The hybrid CFD solver computes the Navier-Stokes equations near a single blade and uses a Lagrangian wake mode in the far-field. The CFD solver was then loosely coupled with a Computational Structural Dynamics (CSD) code to determine the rotor trim. The LEWICE3D code [55] was used at two-dimensional sections along the rotor to compute ice accretion. A three-dimensional grid was generated consisting of the two-dimensional ice shapes and the iced rotor performance was obtained. In this approach hybrid three-dimensional icing analysis was achieved.

Between 2010 and 2011 a similar hybrid three-dimensional icing approach was published by Narducci and Kreeger [69, 70]. The icing analysis approach developed first established rotor trim, clean rotor performances, and the initial flow-field using a full Navier-Stoked CFD solver coupled with a CSD code. Two-dimensional conditions were extracted at various radial locations along the blade. LEWICE3D [55] was then used to predict a series of two-dimensional ice shapes. A three-dimensional iced rotor was then constructed and the rotor trim and performance was established. Their work highlighted the challenge of directly extracting two-dimensional conditions from a three-dimensional solution. It was assumed that the ice shape is not a strong function of the azimuthal velocity variation and angle-of-attack and can be characterized by a slow-moving blade. The blade motion was then considered as a series of quasi-static events and only the mean and extreme azimuthal velocity variation and angle-of-attack were used.

Between 2014 and 2018, Kelly et al. devised a numerical approach for assessing the degraded aerodynamics and flight characteristics of iced rotors [71, 72]. A trimmed flight condition was initially found through the use of a multibody approach for rotor dynamics to determine the angle-of-attack and incident velocity. The aero-icing module FENSAP-ICE [56] simulated the ice accretion and determined performance degradation. To simulate the ice accretion, a hybrid three-dimensional approach was developed in which the blade was discretized into two-dimensional sections along the blade span and the aerodynamics and droplet impingement are computed. Three-dimensional fields of the aerodynamic quantities and droplet dynamics were then interpolated over the blade surface to enable three-dimensional ice accretion. The blade surface mesh was then rotated during the icing process allowing for spanwise motion of the liquid film generated by centrifugal forces.

Hybrid two/three-dimensional approaches have provided an encouraging insight into the potential of numerical techniques for rotorcraft icing. However, reservations should be had of results using this approach given that rotorcraft are primarily dominated by three-dimensional flow features and any two-dimensional assumption is severely limiting. Fully three-dimensional rotorcraft icing codes are therefore taking precedence over hybrid approaches, with numerical limitations being the major constraint in technological advancements.

Between 2016 and 2019 the first attempt to model rotor icing in a fully three-dimensional process was made by Chen and Zhao from Nanjing University of Aeronautics and Astronautics [73–75] and Barakos from the University of Glasgow. A new method for predicting three-dimensional ice accretion on rotors was proposed. The

CLORNS code was used to determine the aerodynamic characteristics of an unsteady iced rotor flow-field [76]. A three-dimensional Eulerian method with a shadow zone dispersion model was developed for computing the droplet trajectories and collection efficiency [77]. An icing model based on the classical Messinger model [63] and a new model to account for the movement of the liquid film in the centrifugal direction [74] was used. In this approach, there were no two-dimensional assumptions introduced. The numerical method was demonstrated on a rotor blade in hover and forward flight.

However, even this latest three-dimensional approach is not without its own limitations. Eulerian particle tracking approaches are appealing for three-dimensional problems due to their high efficiency, however, they possibly fail to account for the fundamental physics of the individual supercooled water droplets, especially Supercooled Large Droplet with peculiar aerodynamics. Behaviour which cannot currently be captured using an Eulerian approach includes particle splashing during impact and particle breakup. The splashing of particles has been demonstrated as of first-order importance while simulating supercooled large water droplets [78]. Moreover, icing models based on the classical Messinger model have been shown to under-predict the rate of ice accretion [79].

1.3.4 Ice Detection Techniques

In 2002, Bragg et al. [80] critically assessed aircraft safety during icing conditions and suggested the introduction of smart icing systems to reduce aircraft accident rates. Their work introduced the concept that a smart icing system is potentially a better way to manage the ice protection system. They recognised that warning the pilot of ice conditions through the use of ice detection systems could significantly increase the safety of aircraft to either optimize the use of ice protection systems or to avoid icing conditions altogether. Over the past two decades, this has led to sustained technological advancements in ice detection systems. A timeline of recent and significant published ice detection technological innovations is shown in Table 1.2. It indicates that there is no single technology which dominates and that competition is promoting the development from many different research disciplines.

The methods used for the detection of ice on aircraft can be characterised into either direct or indirect approaches. Methods that use different kinds of sensors to detect ice accretion on the airframe or atmospheric conditions symptomatic of icing environments can be characterised by the direct approach. Methods that rely on a change in response to the aircraft state due to icing can be characterised by the indirect approach. A summary of the different ice detection techniques introduced in the literature is shown in Table 1.3. The approaches are grouped by indirect and direct techniques and their own subcategories. It exhibits the capabilities of each method for measuring the type of ice, ice thickness, and ice location. As well as highlighting the advantages and disadvantages of each method.

Direct methods of sensing ice have received the most scientific interest and promising methods involve measuring changes in surface properties due to ice accretion. Sensing techniques may involve the reaction of a signal or electric field to ice. Promising methods will now go on to be discussed.

Direct detection methods which involve the reaction to a signal include surface gen-

Table 1.2: *Timeline of Recent Ice Detection Technological Innovations.*

1997	**Capacitive/Love Waves – Varadan et al.** [81]: Discussed using smart sensors which include; micro-interdigital transducers, micro-surface acoustic wave devices, and micro-electromechanical systems for measuring ice detection. The onset of ice formation can be detected with surface generated Love waves.
1998	**Impedance – Roy et al.** [82]: A piezoelectric sensing element and microprocessor controller was developed to automatically sense ice and water films up to 0.5 mm thick. The accreted ice on the sensor modifies the effective stiffness of the vibrating transducer and these variations are sensed by measuring the changes in the transducer resonant frequency.
2000	**Aircraft Dynamics – Melody et al.** [83]: Proposed parameter identification of the flight dynamics for in-flight ice detection and characterization of aircraft icing. Different parameter identification algorithms were investigated.
2002	**Ultrasonics – Hongerholt and Rose** [84]: Demonstrated ultrasonic guided waves provide a method for ice detection. Suggesting ultrasonics are a convenient and reliable method to detect contaminants on the surface of a structure which the wave travels.
2007	**Impedance/Thermal – Jarvinen** [85]: Introduced an ice detection method which utilized a combination of impedance, thermal conductivity, and temperature measurements to detect the presence of glaze ice and to determine its thickness.
2007	**Optical – Bassey & Simpson** [86]: Identified the limited success of conventional time domain reflectometry due to sensors not being suitable for such accurate measurements and explored the use of coplannar transmission lines for time domain reflectometry ice detection to improve ice thickness measurements.
2008	**Aircraft Dynamics – Caliskan et al.** [87]: Proposed an ice detection and identification approach based on the statistical properties of aircraft dynamics and reconfigurable control. A Kalman filtering sequence method was used to detect ice and a neural network was trained to predict the aircraft flight dynamics affected by ice.
2009	**Ultrasonics – Gao and Rose** [4]: Presented an ice detection technique based on ultrasonic shear horizontal guided waves. The guided wave signals can be used to quantitatively determine the ice thickness and type by considering the substrate of the wing and ice layer as a two-layer structure.
2012	**Thermal – Zhuge et al.** [88]: Discussed a method based on near infrared image processing for the visual detection of ice on aircraft wings. Their work utilize the theory that the near infrared reflectance characteristics of ice and water are different.
2013	**Optical – Zou et al.** [89]: Reported a novel ice type detection technique using an oblique end-face fibre-optic ice sensor. Ice growth curves are shown to identify the ice type and with this the thickness can be determined.

2013 · · · · · ·
Optical – Ikiades et al. [90]:
Discussed the development of ice detection using an optical sensing technique relying on Mie scattered and reflected light from the ice surface and volume to determine the ice accretion rate and type. Measuring the optical intensity of the backscattered and reflected light gives information of the accreted ice on the leading edge of a wing.

2014 · · · · · ·
Ultrasonics – Liu et al. [91]:
Measured the attenuation coefficient of ultrasonic waves in different types of ice for aircraft ice detection. The attenuation coefficient of ultrasonic waves for rime ice was shown to be much higher than that of glaze at all frequencies. Their work suggested that the attenuation properties are closely related to the ice acoustic properties and micro-structure.

2015 · · · · · ·
Capacitive – Schlegl et al. [92]:
Presented a solar-energy powered wireless ice detection and temperature measurement system based on the different electrical properties of air, water, and ice. The properties of the ice accretion are measure by means of capacitive sensing.

2016 · · · · · ·
Ultrasonics – Xiang and Rose [93]:
Exhibited experimental validation of ultrasonic guided wave tomography for ice detection. A probability-based reconstruction algorithm was used to reconstruct the ice images. The tomographic image reconstruction method utilized Lamb waves to visualize and monitor the ice as it developed.

2017 · · · · · ·
Aircraft Dynamics – Bagherzadeh and Asadi [94]:
Discuss the detection of ice on aircraft using empirical mode decomposition enhanced by multi-objective optimization. Providing system identification of the flight dynamics during icing.

2017 · · · · · ·
Ultrasonics – Liu et al. [95]:
Presented a new method for ultrasonic attenuation based ice detection capable of distinguishing ice types. It was developed to leverage the discrepancies in attenuation of ultrasonic waves travelling in different types of ice.

2018 · · · · · ·
Aircraft Acoustics – Cheng et al. [96]:
Recognised the correlation between the ice-induced surface roughness and the broadband noise level during experimental work. Due to the strong correlation it was then thought that the broadband noise signals of the rotor blades could be used as an ice detection tool for helicopters.

2019 · · · · · ·
Aircraft Acoustics – Chen et al. [97]:
Investigated the potential of acoustic-based ice detection for helicopters by the numerical analysis of artificial ice notches at various positions along the blade. It was shown that the artificial ice notches do have an affect on the aero-acoustics of the rotor.

2020 · · · · · ·
Aircraft Performance – Deiler and Fezans [98]:
Introduced a performance based ice detection methodology. The developed system relies on the change in flight performance during steady flight states contrary to many unsuccessful attempts based on the estimation of disturbances in the aircraft's dynamic behaviour.

Table 1.3: *Summary of Ice Detection Techniques for Aircaft*

Detection Technique	Ice Measurements			(+) Advantages	(–) Disadvantages
	Type	Thickness	Location		
Aircraft Acoustic Ref. [96, 97]	**No**	No	No	• Low-cost and simple • In-flight and real-time	• Development stage • Spurious external noise
Aircraft dynamics Ref. [83, 87, 94]	No	No	No	• No additional sensors • Mature dynamic models	• Dynamics does not account for iced induced drag
Aircraft performance Ref. [98]	No	No	No	• Detection prior to stall • No dynamic excitation	• Cannot distinguish the different types of ice
Capacitive techniques Ref. [81, 92]	Yes	Yes	Yes	• Commercially available • Low power consumption	• Inaccurate measurements • High-frequency efficiency
Impedance techniques Ref. [82, 85]	No	Yes	No	• Retrofit to original blades • Low power consumption	• Cannot be used with IPS • Not commercialized
Infrared techniques Ref. [85, 88]	No	No	Yes	• Non-invasive sensing • High resolution/accuracy	• Moving surface sensitivity • Contaminated emissivity
Optical techniques Ref. [86, 89, 90]	Yes	Yes	Yes	• High resolution/accuracy • Modern technology	• Moving surface sensitivity • High-cost / not commercial
Surface Love waves Ref. [81]	No	No	Yes	• Highly sensitive to ice • Detection of ice and water	• Complicated operation • Difficult maintenance
Ultrasonic waves Ref. [4, 84, 91, 93, 95]	Yes	Yes	No	• Extensively researched • Mature technology	• High frequencies vanish • Sensor mounting

erated wave, infrared thermography, optical reflectometry and ultrasonics wave techniques. Varadan et al. [81] discussed using surface generated Love waves as a mechanism for ice detection. The method involves using piezoelectric devices for producing Love waves. The waves are then propagated through the surface, and as ice accretes, the amplitude and velocity of the waves are altered, which can then be measured. Hongerholt and Rose [84] demonstrated the use of ultrasonic guided waves for ice detection on the surface of a wing. In principle, ultrasonic guided waves can be propagated and reflected on the surface of a wing and the attenuated amplitude of the reflected waves in different mediums can be measured. Zhuge et al. [88] discussed a method of infrared thermography technique for ice detection. Infrared thermography techniques emit electromagnetic signals which are reflected by the surface and once received back the signals are analysed for temperature variations. Bassey and Simpson [86] introduced an advanced method of optical time domain reflectometry for ice detection. Optical time-domain reflectometry is used to measure the dielectric permittivity and volumetric water content on the aircraft surface.

Direct detection methods which involve the reaction of an electric field include capacitive and impedance techniques. Schlegl et al. [92] discussed using capacitive techniques for sensing ice. Capacitive techniques monitor the presence of dielectric substances on the surface which change the capacitance. The working principle relies on the different electrical properties of air, water, and ice. Roy et al. [82] introduced impedance techniques for ice detection. In principle, the impedance technique generates an excitation signal which is delivered to electrodes embedded in the surface. When ice accretes on the electrodes the impedance of the electrodes is affected and by measuring the changes in voltage ice can be detected.

In the main, ice detection techniques which can be characterised into the direct subcategory allow for precise information regarding the ice location, thickness, and location. However, a major drawback of these methods is that most are either commercially unproven due to preliminary testing not exceeding the laboratory environment, or are unpractical for moving components, making their implementation on rotorcraft challenging.

Indirect ice detection systems have received renewed interest of late. Irrespective of the indirect method, all utilize previously established aircraft states to compare against that of the iced state. The difference between the clean and iced aircraft states then acts as an indicator for icing. Melody et al. [83] discussed using aircraft dynamics as an indicator for in-flight icing. In principle, using the aircraft dynamics as an indicator for icing requires identification algorithms to identify aircraft performance, stability, and control parameters over time, based on measurements of the aircraft state variables and control input. Deiler and Fezans [98] introduced a performance-based ice detection methodology. Performance-based identification uses the change in the steady flight state meaning it can be used prior to reaching dynamic stall conditions and during steady flight conditions contrary to the aircraft dynamics approach. A major limitation of using either the dynamics or performance of aircraft for ice detection is that the type, location, and thickness of ice cannot be determined. Additionally, the detection of ice prior to dynamic stall is fundamental to aircraft safety.

Indirect ice detection methods which involve the use of acoustic noise as an indica-

tor for ice accretion are particularly relevant for rotorcraft. For this reason ice detection techniques based on aircraft acoustic within Table 1.2 and underlined. A characteristic and largely undesirable feature of rotorcraft is their rotor noise. Rotor noise sources are complex and are a combination of loading noise, thickness noise, shock noise, blade-vortex interaction noise, and broadband noise. However, Cheng et al. [96] recognised the strong correlation between the ice-induced surface roughness and the broadband noise level suggesting rotor acoustics could be a viable technology for rotorcraft ice detection. Chen et al. [97] further investigated using numerical techniques and an artificial iced notch and concurred that the acoustics could be potentially used to indicate the formation of ice on a rotor. Ice detection via means of aircraft acoustics however remains in the early stages of research. In the main, a major critique of the literature so far is that the detection of natural ice shapes is yet to be investigated. The experimental work from Cheng et al. [96] used sandpaper to represent ice roughness, while the numerical work from Chen et al. [97] used an artificial ice notch based on the experimental iced surface roughness results of a straight wing from the University of Illinois, presented by Broeren and Bragg [99]. A summary of the current capabilities of aircraft acoustics for ice detection is shown in Table 1.3. The ice type has been highlighted in bold due to its potential for being identified through the use of aircraft acoustics.

Hybrid direct-indirect ice detection systems have become of interest as delineated by the SENSors and certifiable hybrid architectures FOR safer aviation in ICing Environment (SENS4ICE) EU funded research project [100]. The project is coordinated by the German Aerospace Center (DLR) and consists of 19 different partners from 10 different countries. The project intends to develop novel hybrid approaches for ice detection although, any new findings are yet to be published. Furthermore, there is no indication that there is any interest in developing hybrid ice detection systems specifically with rotorcraft in mind.

1.4 Research Questions and Hypotheses

Research Question 1: Are the acoustic signals generated by glaze and rime ice types distinguishable on rotor blades?

Hypothesis 1: Currently, it is understood that the ice induced surface roughness increases the broadband noise of the rotor. The noise generated from artificial ice notches on a rotor has been shown to influence the loading noise and was shown to have a limited effect on the thickness noise. However, the effect of the location and type of ice on the rotor noise remains unknown from genuine ice shapes. The noise of a rotor is strongly related to the flow physics and with different types of ice producing contrasting flow features, it is expected that different noise signals would be generated and could potentially be distinguishable.

Research Question 2: What are the most effective mesh deformation strategies to account for moving ice boundaries?

Hypothesis 2: Traditional mesh deformation techniques including the spring analogy and linear elasticity analogy are computationally expensive for large problems and cannot guarantee high mesh quality during large deformations. Despite this, the

spring analogy, in particular, has been widely used to account for the moving ice boundary on practical three-dimensional engineering problems. Moreover, mesh deformation techniques have primarily been developed with large, smooth deformations in mind, such as present during shape optimization or Fluid-Structure-Interaction problems opposed to local, non-smooth shapes such as ice accretion. Consequently, there is currently no singular standout mesh deformation technique which can be recommended.

Research Question 3: What is the status of open-source Computational Fluid Dynamics software for rotorcraft flows?

Hypothesis 3: Rotor aerodynamics are rich in complex flow physics consisting of highly three-dimensional behaviour and the presence of complex phenomena such as blade-vortex interactions. Additionally, rotor blades are required to move independently from one another to provide control and stability of the aircraft. Resultantly, specialist Computational Fluid Dynamics codes have been designed specifically to deal with these challenges over the past two decades. New advanced capabilities have to be implemented in the present open-source Computational Fluid Dynamic codes to allow modelling such demanding behaviour.

Research Question 4: Are particle tracking techniques able to capture the fundamental physics of clouds containing supercooled water droplets entrained in rotor flows?

Hypothesis 4: The idiosyncrasies of supercooled water droplets can only truly be understood when modelled at an individual particle level. Subsequently, tracking clouds of individual supercooled water droplets in rotor flows needs focused research. While Eulerain particle tracking methods are appealing computationally, they fail to capture some fundamental physics such as particle breakup and splashing which are typical of Certification Standard 25 Appendix O conditions [101]. Lagrangian particle tracking techniques, on the other hand, enable modelling this physics, however, remain unproven for rotorcraft configurations. Developing Lagrangian particle tracking techniques for rotorcraft configurations is therefore crucial to the progression of rotorcraft icing codes.

Research Question 5: Are numerical tools at a stage where they can be used to aid the certification process for rotorcraft flight in icing conditions?

Hypothesis 5: Given that the certification process is used to provide rotorcraft with the authority to fly in a range of icing conditions the reliance on numerical tools needs careful consideration. The current fidelity of numerical tools for rotorcraft icing is not high enough. Hybrid two and three-dimensional approaches introduce an oversimplification of the complex multi-physics icing problem. Meanwhile fully three-dimensional rotorcraft icing codes have only recently been established. To that end, there is a need for code-to-code model verification of three-dimensional rotorcraft icing codes due to there being limited high-quality full-scale flight test data and uncertainty in ice scaling laws introduced by model experimental data.

1.5 Thesis Organization

In order to guide the reader through the remainder of the thesis, the organisation of the subsequent chapters and the associated areas of research are hereinafter briefly outlined:

Part-I: Begins by discussing the conceptual design phase of the thesis. Its purpose is to identify the potential for the recognised technology based on fundamental principles at an early phase of the design process.

- **Chapter 2:** Introduces an acoustic characterization of glaze and rime ice structures to quantify different ice shape noise signatures in order to develop acoustic ice detection technologies for rotorcraft. The feasibility of the detection technique is assessed numerically on an oscillating, two-dimensional airfoil.

Part-II: Moves towards establishing and alleviating the challenges at the forefront of modelling three-dimensional ice accretion on rotorcraft. The development and validation of different numerical tools used throughout the modelling process are presented.

- **Chapter 3:** Presents a new method to account for the issue of the moving ice boundary. The method is based on radial basis function mesh deformation and is desirable owing to its high-quality three-dimensional mesh features. Data reduction schemes utilized to improve the efficiency of the mesh deformation are assessed in detail.
- **Chapter 4:** Develops the first open-source CFD code for rotor performance prediction. Computational aerodynamic analyses of rotorcraft main rotor blades are conducted in both hover and forward flight. The prediction capabilities of the solver are validated with the measured experimental data.
- **Chapter 5:** Presents particle tracking techniques for simulating the development of clouds containing supercooled water droplets entrained in complex rotorcraft flow systems. Original techniques for tracking clouds in mesh with arbitrary motion and across non-conformal boundaries are introduced.

Part-III: Demonstrates the progression towards fully three-dimensional modelling of ice accretion on rotorcraft. Permitting a high-fidelity numerical analysis of acoustic ice detection technologies to mature the design phase.

- **Chapter 6:** Exhibits a new high-fidelity approach for the three-dimensional modelling of ice accretion on rotorcraft. The simulations setup is based on the experimental Spinning Rotor Blade model and test conditions. Furthermore, this allows for the acoustic signatures of clean and various iced rotors to be assessed.

Part-IV: Introduces an Appendix to discuss important aspects of work that were not per se directly related to rotorcraft icing, however, remain integral to advancements in numerical methodologies.

- **Appendix A:** Further investigates the turbulent flow field around a wing-tip mounted propeller configuration using the model and test conditions released by the Workshop for Integrated Propeller Prediction. An assessment of the sliding mesh technique is conducted by comparing the numerical predictions to the measured experimental data.

Part I

Conceptual Framework

CHAPTER 2

Acoustic Characterization of Glaze and Rime Ice Structures on an Oscillating Airfoil

The contents of this chapter appeared in:

Morelli, M., Zhou, B.Y. & Guardone, A., *Journal of the American Helicopter Society*, Volume 65, Number 4, pp. 1-12(12), October 2020.
DOI: 10.4050/JAHS.65.032000.

Abstract

The development of low-cost and simple technologies to improve pilot awareness in icing environments is crucial to improve the safety of rotorcraft. To that end, an acoustic characterization of glaze and rime ice structures is hereby introduced to quantify different ice shape noise signatures. This work harnesses the relationship between the unsteady flow physics and characteristic noise of rotorcraft. The conceptual feasibility of the detection technique for identifying the type of ice is assessed on an oscillating, two-dimensional airfoil. The experimental database of a Sikorsky SC2110 rotor airfoil undergoing pitching motion during icing conditions in the NASA Glenn Icing Research Wind Tunnel has been selected for simulation. Moreover, a test matrix describing a range of icing conditions has been established. An unsteady collection efficiency approach is introduced within this work to compute the mass of supercooled water droplets which impact on the oscillating airfoil. The numerically predicted ice shapes are in good agreement with both the experimental measurements and an external proprietary icing code. Furthermore, the results show a distinct division in the lift and moment coefficient hysteresis loops for glaze and rime ice shapes. This is primarily caused by the glaze ice shapes inducing flow separation at high angles-of-attack. Resultantly, iced airfoils which operate within the glaze ice regime can be characterized by much higher frequency noise content than those which operate within the rime ice regime.

2.1 Introduction

THE use of computational modeling to simulate ice shapes on rotor blades helps further understand the rotorcraft icing problem [102, 103]. However, as with so many other aerospace technologies, rotorcraft icing codes lag behind fixed-wing aircraft icing codes which have been well established for many years now. This is partly due to the additional complexities that the rotor blade introduces which results in a highly unsteady flow field. Subsequently, icing on the main rotor blade of a helicopter should be considered inherently as an unsteady problem which makes simulating the process challenging. Hence, rotorcraft icing simulations are required to include both the effect of the centrifugal force and the effect of the blade oscillations on the final ice shape. This however requires the use of high-fidelity icing codes which is computationally challenging.

A joint venture in 2010 between Bell Helicopter, The Boeing Company, Sikorsky Aircraft, Georgia Institute of Technology, and NASA set out to enhance understanding of rotorcraft icing with the development and validation of high-fidelity icing analysis tools. With the consensus that current data was insufficient for validation two main experimental initiatives were outlined: 1). A high-quality oscillating airfoil test to enhance the scarce dataset for validating the rotorcraft icing problem during pitching motion [46] and 2). A spinning rotor test to assess the feasibility of ice scaling parameters and evaluate hydrophobic and icephobic materials [47]. These experimental tests were then the basis for the validation of high-fidelity computational rotorcraft icing tools [104, 105]. This work focuses on the validation of the oscillating airfoil test and uses the experimental test data from Reinert et al. [46] and calculated ice shapes from Narducci and Reinert [105] for ice shape comparisons.

As part of this collaboration between the US Government and industry, The Boeing Company calculated ice shapes on an oscillating airfoil [105] and used the experimental work conducted in the NASA Glenn Icing Research Tunnel (IRT) [46] to validate the code. The main goal of the work was to accurately calculate oscillating airfoil ice shapes and resultant performance characteristics. The analysis approach used was built on the premise that the ice shape is not a strong function of the frequency of oscillation which was supported by the similarity in ice shapes with different oscillatory frequencies. A further assumption was then made that the time history of a helicopter rotor blade pitching at 1/rev can be represented by a very slow-moving blade. Accordingly, it was then assumed that only the mean angle of attack and extreme amplitudes of angle of attack are considered in a series of quasi-static icing events.

One of the main drawbacks of this method, however, is that it does not consider the effect of the unsteady flow field as the ice accretes. To help theoretically understand if a flow field can be considered as steady the reduced frequency is regularly used. The degree of unsteadiness of the oscillation can be expressed by the reduced frequency and defined in terms of the semi-chord, $b = c/2$. Where the factor of $c/2$ is inserted so that the reduced frequency becomes dimensionally correct [106]. The reduced frequency, k can then be given as,

$$\text{Reduced Frequency, } k = \frac{\omega c}{2U_\infty} \tag{2.1}$$

for $0 \leq k \leq 0.05$ flow can be considered quasi-steady and for $k \geq 0.05$ flow is considered unsteady [107], where ω is the oscillatory frequency and U_∞ is the free stream velocity. For a rotor blade pitching 1/rev, the quasi-steady assumption may be applicable. However, this may not be an appropriate assumption for rotors with higher pitching frequencies.

Alternative approaches to predict ice shapes were also suggested in Ref. [105] which merit discussion. The first alternative approach suggested was an average angle of attack, however, then the airfoil does not oscillate and the simulation is considered entirely steady. The second alternative approach proposed was an averaging of ice shapes, where, a clean airfoil is iced at various static angles of attack and using weighted averages the final ice shape is computed. This also considers the unsteady oscillating airfoil to be steady and again neglects all aerodynamic characteristics and hysteresis behaviour associated with the oscillating motion of the airfoil outlined in Ref. [105].

Five years later in 2015 another collaboration arose between The Boeing Company, Georgia Institute of Technology, Penn State University, and NASA, which involved much of the same personnel, and aimed to further develop and progress rotorcraft icing computational tools [108]. This study focused on coupled CFD/CSD analysis for rotorcraft in forward flight to assess the trim state of an iced rotor. Once again however this used the method to assume that the time history of an oscillating airfoil can be represented by a slow-moving blade so that eventually the icing analysis can be thought of as a series of quasi-static events.

Since as recently as 2016, experimental work from Cheng et al. begun to help develop technologies to detect ice formation through the quantification of rotor surface roughness due to ice via broadband noise measurements [96, 109]. Several tests were conducted at different roughness levels to measure the broadband noise during the early stages of ice accretion. Two parameters, the arithmetic average roughness height, and, the average roughness height based on the integrated ice thickness at the blade tip were used to describe the ice-induced roughness. The study found that the high-frequency spectra of the rotor broadband noise was particularly sensitive to the blade surface roughness.

An alternative approach later proposed by Chen et al. [97, 110] in 2018 involved numerical simulations of ice accretion and computing the far-field noise signature of the iced rotor blade shape using computational aeroacoustics. This work used a very small prescribed ice notch at various ice lengths along the rotor and measured its influence on the acoustics of different rotor blade sets in hover and forward flight. It found that for limited lengths of ice accretion, the location of the sound monitor is important to successfully capture any difference in the acoustic characteristics of iced rotors.

The goal of this work is to establish the first acoustic characterization of glaze and rime ice structures to aid in further developing acoustic ice detection warning systems for improving rotorcraft flight safety. The NASA Glenn IRT database of a pitching rotor airfoil during icing conditions has been identified as it produces a vast array of ice structures. The test cases chosen from this experimental database are first described within the chapter. The unsteady computational methods used for simulating the ice shapes are then introduced alongside a spatial convergence study. The computational results of the different test cases are then discussed. Each of the test cases then ana-

lyzes the ice structure, the performance degradation due to the ice formation, the iced airfoil flow field, and the iced airfoil acoustics. The objective is thus to categorize the sound spectra of the glaze and rime ice structures and link the acoustics signals to the known performance characteristics of glaze and rime ice structures to further improve rotorcraft safety. With this concept being in the early stages of development, there are many limitations of this work through the simplification of only considering a pitching rotor airfoil, however despite this, much of this work serves as a proof-of-concept for further developments in the near future. These limitations mainly revolve around the simulations being considered as two-dimensional, meaning no centrifugal forces are considered during in the ice formation, and, the computational aeroacoustics does not account for important three-dimensional noise sources such as impulsive blade vortex interactions. The turbulent flow separating from the leading edge of an iced rotor blade is typically also three-dimensional in nature, and whilst only considering a two-dimensional airfoil, this remains another limitation to the study.

2.2 Experimental Test Cases

The computations of the oscillating airfoil ice shapes are compared against both experimental work and other computational in-flight icing codes. Thanks to the experimental icing tests which took place in the NASA Glenn IRT to help improve the scarce data-set of oscillating airfoils numerous different test cases have been identified. The experimental work from Rienert et al. [46] has been used for verification of the icing computations within this work. The icing computations from Narducci and Rienert are then shown for code comparisons using their IceMaker software [105]. At the time of the experiment, acoustic noise signals were not being considered within the consortium for the use as ice detection systems. For this reason, there was no acoustic data recorded of the oscillating airfoil ice shapes.

These test cases assess the effect of the flow field on the ice shapes, the meteorological conditions which are inherently the driver causing icing, and the length of time when exposed to icing conditions. The operating conditions from these test cases used for examination can be found in Table 2.1.

Table 2.1: *Test cases chosen for examination taken from Rienert et al.*[α]*. Conditions selected to produce a range of ice shapes and assess multiple influential parameters in both glaze and rime ice regimes.*

Test Case [-]	Air Speed [m/s]	Oscillation Freq. [Hz]	Oscillating Motion [°]	LWC [g/m^3]	Time [s]	Ice Type [-]
R-T600	77	2.8	5 ± 6	0.5	600	Rime
G-LWC	77	2.8	5 ± 6	1.0	600	Glaze
R-T900	77	2.8	5 ± 6	0.5	900	Rime
G-AoA5	135	2.8	5 ± 6	0.5	600	Glaze
G-AoA10	135	2.8	10 ± 6	0.5	600	Glaze

[α]Test cases based on the experimental work from Rienert et al. in the NASA IRT facilities [46]

The different operating conditions represent an airfoil at both low and high flight speeds and at both low and high mean angles of attack with significant amplitudes of oscillations. The length of time exposed to icing conditions is long enough to expect significant ice accretion such that it could have severely damaging effects on the performance of the airfoil. The Mean Volume Diameter (MVD) of the supercooled water droplets within these cases is constant at $22\,\mu\mathrm{m}$ and is of a typical value for many icing experiments. The liquid water content (LWC) of the supercooled water droplets ranges from moderate to high. Two different oscillating frequencies were discussed at which a conventional helicopter rotor blade would pitch per revolution, one a high-frequency oscillation at $5.6\,\mathrm{Hz}$ and the other a low-frequency oscillation at $2.8\,\mathrm{Hz}$. Results showed that the effect of the rate of oscillation was minimal on the final ice shape and as there was more experimental data openly available for the icing tests with the lower frequency of oscillation, simulations were conducted with an oscillation rate of $2.8\,\mathrm{Hz}$. The effect of the rate of oscillation on the ice shapes is, however, a parameter that will be considered at a later date. One of the most intriguing conditions from the experimental tests is the outside air temperature (OAT) which is at $-14\,^{\circ}\mathrm{C}$. The OAT is representative classically of mixed rime-glaze ice accretion which can during extensive ice formation lead to the formation of symmetrical double-horn structures. These ice structures are renowned for being demanding to simulate and require an accurate ice accretion model to account for the heat diffusion within the ice layer and mass transfer from glaze to rime ice cells.

The experimental tests consisted of an untwisted Sikorsky SC2110 wing designed by Sikorsky/Lednicer and Owen as a rotorcraft airfoil and is undergoing pitch oscillation. The wing dimension has a $0.381\,\mathrm{m}$ chord and stretches from the floor to the ceiling of the wind tunnel. The airfoil has a maximum thickness of $9.9\,\%$ at $37.7\,\%$ chord and has a maximum chamber of $1.9\,\%$ at $15.7\,\%$ chord. Work from Zocca et.al has shown that the interference of wind tunnel walls in the NASA Glenn IRT does not greatly influence the final ice shape at the central station of the airfoil and so icing simulations can essentially be considered two-dimensional [111]. This, however, was tested based on a steady icing wind tunnel experiment and did not look further into three-dimensional effects introduced from unsteady flow fields. For simplicity and to ensure this analysis is within the scope of the timeline of the project the impending icing simulations are considered to be two-dimensional. This is also in agreement with the results obtained from the oscillating airfoil ice shapes which report little change along the spanwise direction although this is something that will require further investigation.

2.3 Computational Method

The open-source SU2 software suite was used to determine the unsteady flow field over the oscillating airfoil [112]. The SU2 software suite solves partial differential equations on general unstructured grids. The core of the suite is a Reynolds-averaged Navier-Stokes (RANS) solver which was used in this simulation in tandem with the Menter shear-stress transport turbulence model. Spatial discretization was achieved using an edge-based finite volume method. The convective and viscous fluxes are then evaluated at the midpoint of an edge. The Jameson-Schmidt-Turkel numerical scheme was used to

solve the convective fluxes with a 2^{nd} order limiter for the up-wind convective scheme. Whilst to evaluate the viscous fluxes using a finite volume method the Green-Guass numerical scheme was used. To account for the unsteady nature of the problem a 2^{nd} order accurate dual-time-stepping approach was used to transform the unsteady problem into a series of steady problems. Each physical time-step was then solved consecutively for a fictitious time until converged to a steady-state problem. A volumetric rigid motion was used to account for the sinusoidal movement of the oscillating airfoil where the whole grid rotates about a centred origin at each physical time-step. Convergence acceleration was achieved using an agglomeration multi-grid implementation to generate 4-levels of grid coarsening from the fine grid at run-time.

In-house codes PoliDrop and PoliMIce were used to respectively to determine the collection efficiency and final ice shapes [57]. The PoliDrop code is a Lagrangian based particle tracking code which uses previously computed flow field data to determine the particle trajectories and impingement locations. The code has been developed to account for moving boundaries present in unsteady problems. After computing the particle trajectories it calculates the value of the collection efficiency, which can be thought of as the collected mass of particles on the impacted area divided by the mass of the total number of particles in the entire cloud.

The PoliMIce software library provides state-of-the-art ice formation models. The model used in this work to capture the complex experimental ice shapes is the local exact solution of the unsteady Stefan problem for the temperature profiles within the ice layer in glaze conditions [113]. This model moves from Myers' formulation and includes an unsteady description of the heat diffusion problem within the ice layer and uses local values of the air temperature outside the boundary layer to compute the convective heat fluxes. Furthermore, it is able to account for the mass transfer between rime and glaze regions. The ice shapes are then computed using an unsteady multi-step approach, whereby, non-linear ice accretion is accounted for by iteratively updating the surface solution on which the ice accretes. To account for this, the grid is re-meshed at each multi-step iteration to update the iced surface.

Within this research ice accretion on an oscillating airfoil is considered inherently as a fully unsteady problem to aid in further developing rotorcraft icing tools. It thus accounts for the iced airfoil geometry, reduced frequency, and amplitude of oscillations which are the primary factors causing dynamic stall [114]. This is achieved using the process shown in Fig. 2.1 where the collection efficiency on the airfoil over a full period of oscillation is calculated. In doing so the impingement limits and distribution of super-cooled water droplets fully take into account any possible unsteady aerodynamic flow field effects. This is ensured so that at every unsteady aerodynamic pseudo-time at which the airfoil oscillates, there is a cloud front of super-cooled water droplets impacting on the airfoil. The collection efficiency is then calculated after a full oscillation of the airfoil once it passes through the cloud. This information is then passed onto the icing solver PoliMIce which, using ice accretion laws governed by the meteorological conditions during flight, computes the newly formed ice shape. This process is then iteratively solved in a multi-step process for a given length of ice accretion. In this approach there is no assumption of steady or quasi-steady flow even whilst $0 \leq k \leq 0.05$.

The clean and iced airfoil shapes are then subject to a computational aeroacoustic

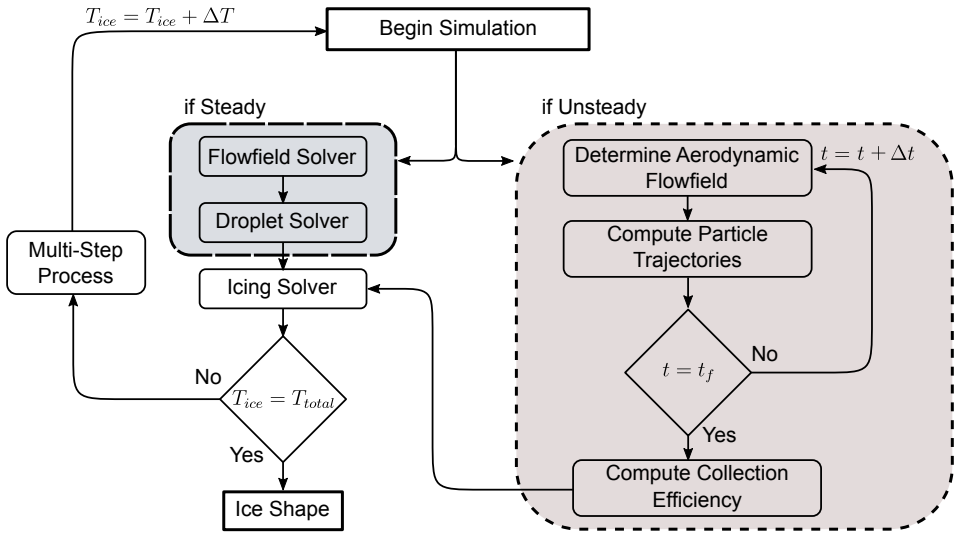

Figure 2.1: *Flowchart of the implementation of an ice accretion simulation. Displaying the different approaches for steady and unsteady flow field ice accretion simulations used in this work. Where, T_{ice} represents the duration of the icing simulation, and, t represents the physical time of the unsteady flow field.*

(CAA) analysis using the permeable-surface Ffowcs-Williams-Hawkings (FWH) formulation in SU2 [115], in order to help predict the early stages on ice accretion during flight to aid in warning the pilot of ice formation. The permeable FWH formulation allows fluid to flow through the fictitious surface Γ_p. Details of the flow field are then extracted and the noise source is then propagated to the far-field. This implementation is shown in the schematic from Figure 2.2. The computational domain is thus divided into two separate regions; the near-field CFD region, Ω_1 and the far-field CAA region, Ω_2. The permeable surface Γ_p can be described by the shape function, $\mathrm{f} = 0$ where if $\mathrm{f} < 0$ it is inside the surface and if $\mathrm{f} > 0$ it is outside the surface. The position of the FWH lies $\frac{3}{4}$ chords length from the airfoil trailing edge. The position of the observer locations was chosen based on where noise would likely be perceived on a conventional main rotor/tail rotor helicopter, either under the main rotor directly or slightly forward or aft of it. Hence three different observer locations are used to assess the noise in the far-field at 10 chords length from the centre of the airfoil at $45°,\ 90°\ \&\ 135°$ from the inflow direction.

In accordance with the icing simulation, the acoustic analysis is likewise considered as a two-dimensional model, although it is understood the rotor blade noise is most definitely not two-dimensional in nature. Furthermore, the current unsteady Reynolds-averaged Navier-Stokes (URANS)-FWH approach does not account for non-uniform flow around the airfoil. If acoustic waveforms are subject to significant distortion, for instance during more representative test cases such as blade vortex interactions, this approach has its limitations. It is for this reason, that this analysis is just for a proof-of-concept for the detection of different ice structure characterizations.

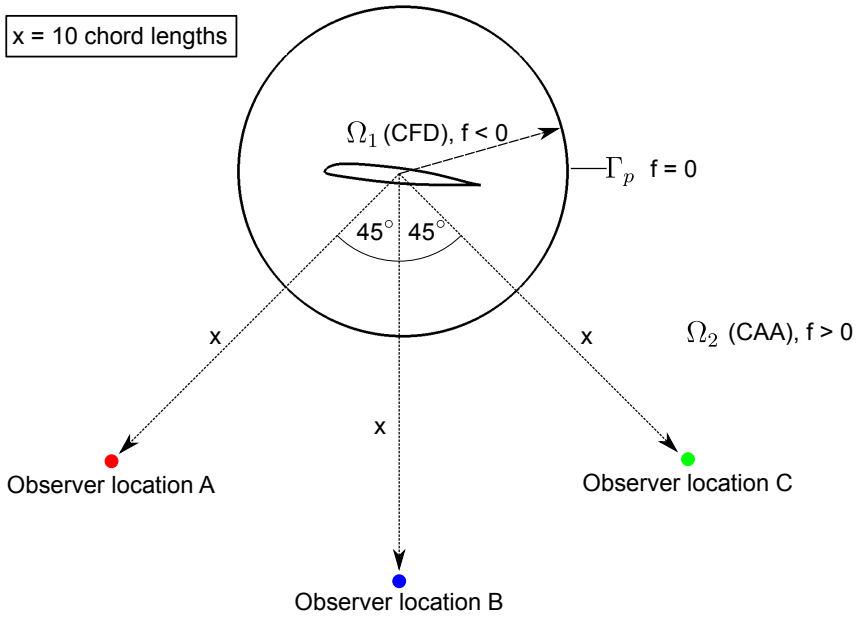

Figure 2.2: *Schematic of the permeable control surface Γ_p separating the CFD and CAA domains and the relative observer locations.*

2.4 Spatial Grid Convergence

The surface node spacing of the mesh was determined through examining the spatial convergence of the coefficient of lift, C_l and the coefficient of drag, C_d. With the shape of the ice formation and thus the mesh structure unknown before the computation, the study was conducted on an un-iced airfoil. A constant angle of attack of $\alpha = 5°$ was used opposed to a sinusoidal oscillating motion so direct comparisons of C_l and C_d could be examined that would be time-independent. Three levels of mesh refinement were assessed at a ratio of $\mathfrak{R} = 2$. Whilst the surface node spacing was being reduced at each mesh refinement level, the wall distance remained constant to ensure a near-wall $y^+ \leq= 1$. The results of the mesh refinement on the C_l and C_d are shown in Table 2.2.

Table 2.2: *Mesh refinement levels*

Refinement Level [-]	Surface Node Spacing [m]	Refinement Ratio [-]	y^+ [-]	C_l [-]	C_d [-]
1	0.00100	2	0.77	0.728955	0.011112
2	0.00050	2	0.77	0.725284	0.011036
3	0.00025	2	0.77	0.724400	0.011018

The Richardson extrapolation method [116] was used for obtaining higher-order estimates of the continuum value at zero grid spacing, f_{exact} from a series of lower-order discrete values $(f_1,\ f_2,\ ..,\ f_n)$. The objective values used here were the C_l and C_d and as the grid spacing reduces they approach an asymptotic zero-grid spacing value which is assumed to be close to the true numerical solution.

The order of convergence, $\mathcal{O}$ can be obtained from three solutions using a constant grid refinement ratio, $\mathfrak{R}$ and can be given as,

$$\mathcal{O} = \ln\left(\frac{f_3 - f_2}{f_2 - f_1}\right) / \ \ln(r) \tag{2.2}$$

where the theoretical order of convergence is $\mathcal{O} = 2$, however, this is not usually achievable due to the grid quality. The Richardson extrapolation can then be generalized by introducing the $\mathcal{O}^{th}$-order methods to solve for f_{exact} and to estimate the continuum value,

$$f_{exact} \cong f_1 + \frac{f_1 - f_2}{\mathfrak{R}^{\mathcal{O}} - 1} \tag{2.3}$$

whilst the relative error, ε can be described as,

$$\varepsilon_{i+1,i} = \frac{f_{i+1} - f_i}{f_i} \tag{2.4}$$

The grid refinement error estimator derived from the theory of the generalized form of the Richardson extrapolation was then used to determine the Grid Convergence Index, GCI [117]. The GCI provides a measure of the percentage the computed value is away from the value of the asymptotic numerical value. The GCI and can be written as,

$$GCI_{i+1,i} = F_S \frac{|\varepsilon_{i+1,i}|}{\mathfrak{R}^{\mathcal{O}} - 1} \tag{2.5}$$

where a factor of safety, $F_S = 1.25$ was used. The results of the spatial convergence analysis are shown in Table 2.3. There is a reduction in the GCI value for successive grid refinements for both the C_l and the C_d. It shows that during the first mesh refinement, from level $1 \rightarrow 2$, there is a significant difference compared to the asymptotic numerical solution, f_{exact}. During the second mesh refinement however, from level $2 \rightarrow 3$, the difference from the asymptotic numerical solution, f_{exact} is less.

Table 2.3: *Grid Convergence Index results*

f	ε_{32}	ε_{21}	$\mathcal{O}$	f_{exact}	GCI_{32}	GCI_{21}
C_l	1.22	5.04	1.94	0.724090	0.53%	2.21%
C_d	1.63	6.84	1.92	0.011011	0.73%	3.07%

With there being minimal difference between the $2 \rightarrow 3$ mesh refinements, and with the extra computational cost undesirable, the 2$^{\text{nd}}$ mesh refinement level was considered suitable and used for the subsequent computations. Thus, the mesh contained a node spacing at the surface of the airfoil of $0.0005\,\mathrm{m}$. The mesh then contained a cluster of finer cells close to the leading and trailing edges. The far-field was placed 14 chord lengths from the airfoil with a spacing of $0.05\,\mathrm{m}$. The overall size of the mesh was $42\,614$ elements. A schematic of a close-up of the mesh around the clean airfoil is shown in Figure 2.3.

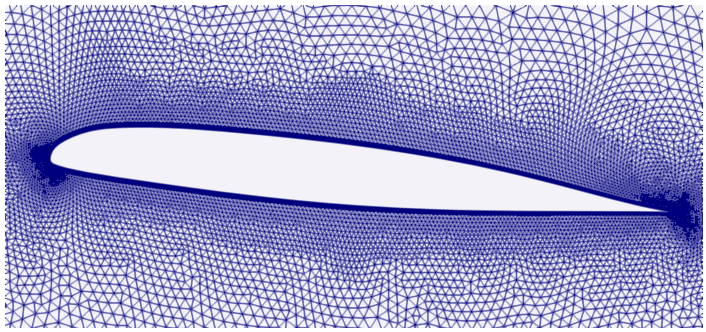

Figure 2.3: *Close-up of the mesh around the clean airfoil with 2-levels of surface mesh refinement.*

2.5 Numerical Results and Discussion

The results of the unsteady icing simulations from each of the different test cases are shown in Fig.2.4. Each of which displays the results from the NASA Glenn IRT experimental tests, the Boeing Company's "IceMaker" computational icing analysis tool-set, and the computations using the "PoliMIce" ice accretion software suite. All the performance characteristics and acoustic signals of these test cases have been simulated, nevertheless, for readability this chapter only focuses on the effect of the glaze and rime ice shapes produced from conditions R-T600 and G-LWC shown in Table 2.1. These two exemplary test cases were chosen due to the LWC being the only influencing parameter on the ice structure allowing for a direct comparison of the performance characteristics and acoustic signals. The prediction of the lift and moment performance degradation caused from these two ice shapes is compared against the performance characteristics of a clean airfoil operating in the same flow conditions and is shown in Fig. 2.5. In each performance analysis, there is initially an assessment of the lift coefficient hysteresis loops. This is then proceeded by an assessment of the moment coefficient hysteresis loops. The performance characteristics can be further explained when examining the flow fields of the iced airfoils as depicted in Fig. 2.6. This is visualized through displaying the normalized velocity with spatially uniform streamlines at the minimum, mean and maximum angles of attack. The velocity magnitude is normalized by the incoming freestream velocity. The acoustic signals of clean and iced airfoils are then shown in Fig. 2.7. The acoustic pressure, $p' = p_{\text{observer}} - p_{\text{mean}}$ which can be defined as the fluctuating part of the far-field pressure around its mean, is normalized by the freestream pressure for each of the test cases. The normalized acoustic pressure is then shown at different observer locations from the centre of the oscillating airfoil. The noise signals are shown over a time window long enough to display the noise sources periodicity. At all observer locations, the rate of oscillation drives the harmonic frequency of the pressure perturbations. The magnitude of the acoustic pressure in all cases is significant to be detectable. The continuous noise signals are then described in terms of how the power of the signal is distributed over frequency using a power spectral density diagram to characterize the noise signals produced from the glaze and rime ice structures and is shown in Fig. 2.8.

2.5.1 Icing Analysis

The first test case considered is condition R-T600 from the experimental work shown in Table 2.1. This is considered to be the baseline test condition which all other flow fields and meteorological conditions are based on for the comparison of ice shapes. R-T600 is a low flight speed case with a moderate value of LWC present during icing conditions. The results of the icing simulation of R-T600 are shown in Fig. 2.4a. The simulated ice shapes produced from PoliMIce display a characteristic "spearhead" generated typically during rime ice conditions. The ice thickness appears moderate with slight asymmetry caused by the mean angle of attack. The experimental results show a rougher shape than the results computed from PoliMIce. The rough feather shapes were found to be very difficult to capture due to their large irregularities over the surface. The overall shape however appears to be in very good agreement with the experimental data. In particular agreement is the impingement limits of ice on the upper and lower surface of the airfoil. The IceMaker code from Boeing is used for code comparison with their quasi-static icing approach [105]. The results from PoliMIce using the fully unsteady collection efficiency approach share many similarities with the results from IceMaker. Both codes, however are unable to replicate the uneven ice profile and approximate smoothed curves opposed to the much rougher experimental ice shape. This however is not of the greatest concern as the reproducibility of these experimental uneven shapes would likely change from one experimental test to another.

The second test case considered is condition G-LWC from the experimental database displayed in Table 2.1. This test case is identical to R-T600 except for a single environmental condition, the LWC. In this case, there is a higher value of LWC at the upper scope of which would be expected in the meteorological environment. This means that the initial clean airfoil experiences the same flow conditions in both test cases and differences only arise after the first step of the multi-step ice accretion. Therefore, every droplet of super-cooled water impacting on the airfoil contains a greater quantity of liquid water per cubic meter, resulting in, greater rates of ice accretion. The results of the icing simulation from condition G-LWC are shown in Fig. 2.4b and produce distinct "double-horn" ice structures paradigmatic of mixed glaze-rime ice regimes. This is by far the most challenging of shapes simulated as it demands an ice accretion model which has an accurate account of the local air temperature and the mass flux of liquid water from neighbouring cells. At the stagnation point, the static air temperature is higher producing a large amount of liquid water and as it runs back it reaches areas of lower air temperature giving rise to the double-horn ice structure. The reason behind the double-horn ice structure being present here and not in R-T600 is due to there being less LWC per super-cooled water droplet meaning there is less mass flux of liquid water between neighbouring cells and a lower rate of ice accretion. The ice shape results themselves are in good correlation with the experimental data especially the upper horn which is very closely reassembled. The lower horn is offset slightly, however, despite this, the general shape is within good proximity to the experimental data. Similarly to the previous test case the computed ice shapes fail to capture the roughness of the ice.

The third test case considered is condition R-T900 from the experimental work shown in Table 2.1. This test case is identical to condition R-T600 except for the period of which the airfoil is exposed to the icing environment. This test case extends the

duration of time exposed to the icing environment from 600 seconds to 900 seconds. This test case also reverts to more moderate values of liquid water content contained within the super-cooled water droplets. The results of the icing simulation associated to condition R-T900 are shown in Fig. 2.4c. The simulated ice shape displays an extension of the characteristic "spearhead" displayed previously from condition R-T600 in Fig.2.4a. The analogy can thus be confirmed that the ice thickness is indeed a function of icing time as one would expect. Unsurprisingly then, since the flight conditions and the meteorological environment remain the same and with only the duration of icing time influencing the ice shape, the thickness of ice is the only parameter affected.

The penultimate test case considered is condition G-AoA5 outlined in Table 2.1. This is regarded as the high-speed test case where the incoming flow is at Mach 0.4. All other test conditions remain the same as in the baseline test. The increase in freestream velocity has the effect that it increases the kinetic energy of the airfoil and subsequently reverberates in an increase in the airfoil surface temperature. Fundamentally, the outcome of this means the ice regime moves away from the dominantly rime conditions and towards mixed glaze-rime conditions, thus different ice structures are present. The formation of double-horn ice structures can hence be observed in Fig. 2.4d. This double-horn ice feature appears to be well represented again by the PoliMIce icing software when compared against the experimental results.

The final test case considered is condition G-AoA10 based on the experimental research and its details are shown in Table 2.1. This is another high-speed test case where the incoming flow is at Mach 0.4. The influential parameter assessed here is the mean angle of attack. This airfoil is operating at higher angles of attack with a mean amplitude of $10 \pm 6^{\circ}$. As this is a high-speed case double-horn ice structures are present once more as observed in Fig. 2.4e. The increase in the mean angle of attack, however, exacerbates the asymmetry of the ice structure. This intensifies the upper-horn ice structure making it more prolific than the lower-horn ice structure which is subsequently weakened. The upper-horn ice structure was predicted markedly close to the experimental work, however, the lower-horn ice structure was found to be difficult to predict.

2.5.2 Performance Analysis - Glaze vs Rime

The lift coefficient produced from the rime ice structure of condition R-T600 is shown in Fig. 2.5a. Immediately it is noticed how close the two lift hysteresis loop results correlate and in fact, the iced airfoil increases the lift coefficient. This result can be explained by the fact that as the ice thickness increases the characteristic length used to compute the lift coefficient remains unchanged giving rise to an increase in lift. Furthermore, the smooth ice shape does not greatly disturb the airfoils flow characteristics. It also effectively increases the airfoil chamber which may slightly help at high angles of attack during low flight speeds.

The moment coefficient produced from the rime ice structure of condition R-T600 is shown in Fig. 2.5b. It is clear here that despite the lift coefficient remaining largely unaffected by the ice structure, the moment coefficient is affected quite severely by icing even with such aerodynamically acceptable ice shapes. At low angles of attack, there is a stronger nose-up pitching moment and at high angles of attack, there is a stronger nose-down pitching moment when in comparison with the clean airfoil moment

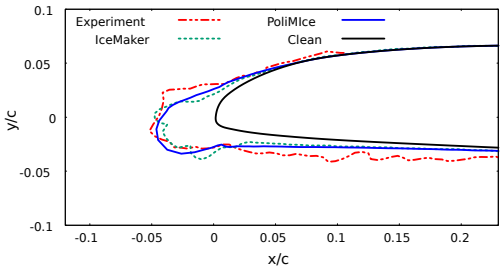

(a) *Ice shapes associated to condition R-T600.*

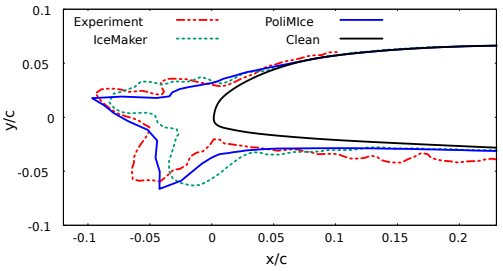

(b) *Ice shapes associated to condition G-LWC.*

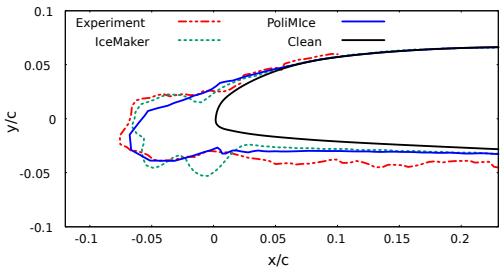

(c) *Ice shapes associated to condition R-T900.*

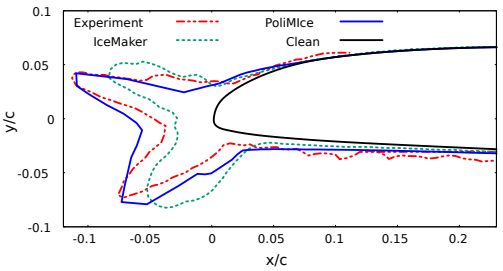

(d) *Ice shapes associated to condition G-AoA5.*

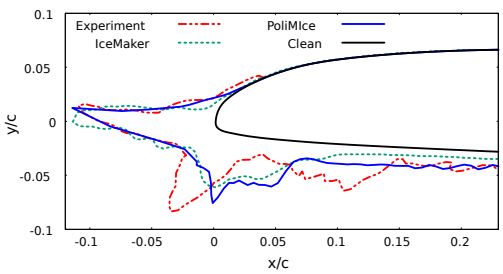

(e) *Ice shapes associated to condition G-AoA10.*

Figure 2.4: *Comparison of the experimental ice shapes and simulated ice shapes from the PoliMIce and IceMaker computational icing codes. Displaying spearhead ice structures characteristic of rime ice as well as double-horn ice structures characteristic of glaze and mixed ice structures.*

characteristics. The thickness of the hysteresis loop also broadens compared to the thickens of the clean airfoil. Despite this, the moment coefficient hysteresis loops share the same profiles. These differences may be attributed to the ice increasing the chord and changing the location of the $\frac{1}{4}$chord at which the moment is computed. Although the increase in chord due to ice is slight it is clear that is has a significant effect on the moment coefficient computations.

The lift coefficient produced from the glaze ice structure of condition G-LWC is shown in Fig. 2.5c. Unlike the previous test case, the difference between the results is clear-cut and the lift coefficient hysteresis loops show little similarity. The iced airfoil depicts an airfoil experiencing dynamic stall as it approaches high angles of attack. On the upstroke of the oscillation, the lift coefficient is consistently less and as the airfoil reaches around 9° it experiences stall leading to a large reduction in lift. On the down-stroke, after the period of stall, the lift coefficient settles as the flow reattaches and the lift coefficient reduces with the angle of attack. Here the increase in chord length appears insignificant compared the shape of the ice structure to increase the lift coefficient.

The moment coefficient produced from the glaze ice shape of condition G-LWC is shown in Fig. 2.5d. Immediately it is apparent the detrimental effect the ice shape has on the moment coefficient and in particular dynamic stall. On the upstroke of the oscillation, the moment coefficient fluctuates at a slight order of magnitude lower than the clean airfoil. As the airfoil reaches around 9° stall occurs and there is a severe peak in the moment coefficient causing a strong nose-up moment. On the down-stroke of the oscillation, as the flow becomes reattached to the surface, the moment coefficient settles and again begins to fluctuate at a lower order of magnitude.

2.5.3 Flow-field Analysis - Glaze vs Rime

The results from Fig. 2.6a show that the rime ice shape from Fig. 2.4a has very minimal effect on the flow field. As the flow passes over the leading edge of the iced airfoil it remains attached to the upper surface at all angles of attack. The stagnation location is not affected and there is no flow separation from this ice shape. It is for this reason why the two observed performance characteristics of the clean and iced airfoils remain largely recognizable as shown in Fig. 2.5a & 2.5b.

The results from Fig. 2.6b show the severity the glaze double-horn ice structure displayed in Fig. 2.4b has on the flow field as it induces large amounts of flow separation causing dynamic stall. A stagnation point is present at the centre location of the two horns and as the flow moves downstream it is shown to accelerate around the horns. At the minimum angle of attack, its shows that aft of the lower horn there is a strong vortex produced generating an area of chaotic flow. As the airfoils angle of attack increases the strength of the vortex aft of the lower horn decreases and the strength of the vortex aft of the upper horn increases. When the airfoil reaches the maximum angle of attack it shows complete flow separation from the airfoils upper surface causing the dynamic stall shown in the lift coefficient in Fig. 2.5c. The fluctuations in the moment coefficient in Fig. 2.5d may be explained by the strengthening and weakening of the two vortices just aft of the upper and lower horns until high angles of attack when the large scale vortex on the upper surface dominates causing dynamic stall.

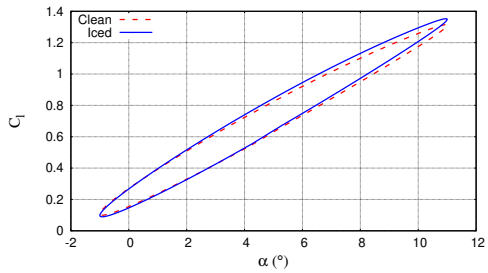

(a) *Lift coefficient hysteresis loop produced from the rime ice structure of R-T600.*

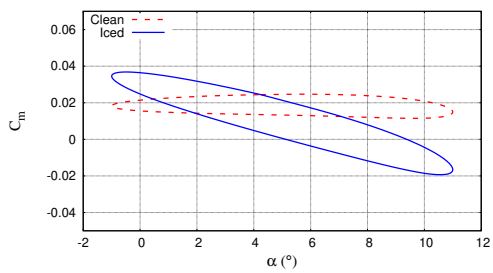

(b) *Moment coefficient hysteresis loop produced from the rime ice structure of R-T600.*

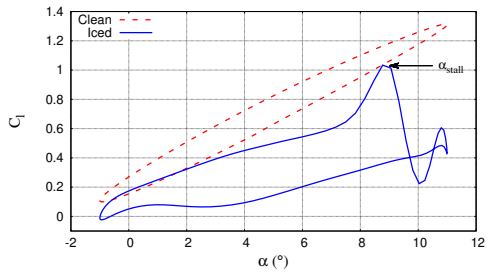

(c) *Lift coefficient hysteresis loop produced from the glaze ice structure of G-LWC.*

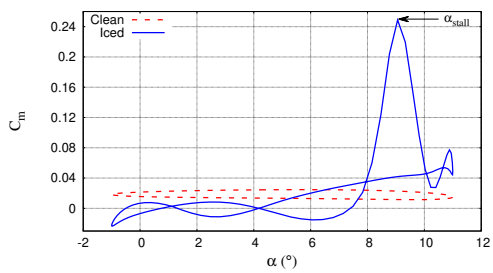

(d) *Moment coefficient hysteresis loop produced from the glaze ice structure of G-LWC.*

Figure 2.5: *Comparison of the predicted clean and iced airfoil lift and moment coefficients hysteresis loops generated from conditions R-T600 and G-LWC based on the test matrix from Table 2.1. Displaying the detrimental influence the double-horn ice structure generated during glaze conditions has on the airfoils dynamic performance.*

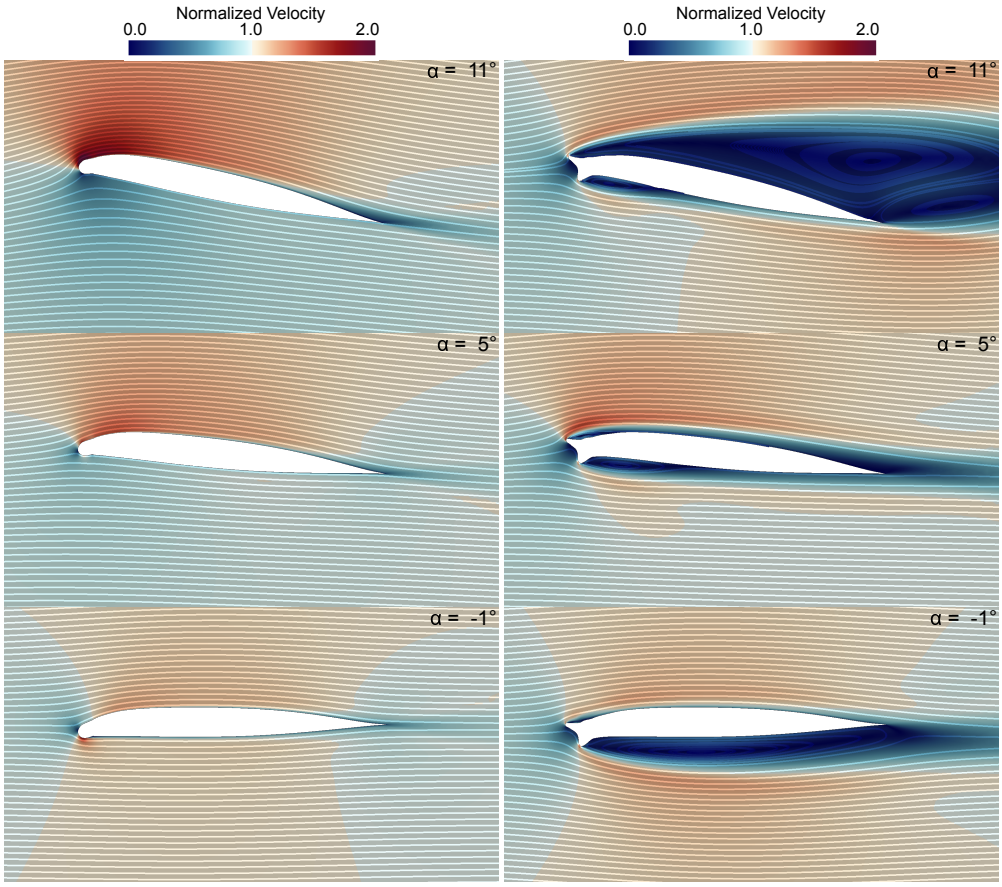

(a) *Flow field produced from the rime ice structure during condition R-T600.*

(b) *Flow field produced from the glaze ice structure during condition G-LWC.*

Figure 2.6: *Flow field comparison of glaze and rime iced airfoils from Table 2.1. Diagram shows the normalized velocity flow field and uniformly spaced streamlines across the flow fields. Where the velocity is normalized by the incoming free-steam velocity.*

2.5.4 Acoustic Analysis - Glaze vs Rime

The time history of the pressure perturbations producing the noise signals of the clean and rime iced airfoils from R-T600 are shown in Figure 2.7a. At all observer locations there is a very slight increase in fluctuations in normalized acoustic pressure of the rime iced airfoil at the peaks of the waves and as the strength of the signal increases the difference in normalized acoustic pressure increases with it as shown at observer location B. Due to there being such similar flow characteristics between the clean and iced airfoils as shown in Figure 2.6a the noise signals are almost identical.

The time history of the pressure perturbations producing the noise signals of the clean and glaze iced airfoils from G-LWC are shown in Figure 2.7b. The fluctuations in normalized acoustic pressure of the glaze iced airfoil, in this case, show vastly different noise signals than to the clean airfoil. Once again the frequency of the oscillating airfoil drives the pressure fluctuations so there is clear periodicity present. The visibly different noise signals are attributed to be caused by the significant differences in the flow field as shown in Fig. 2.6b. On the upstroke of the iced airfoil, the perturbations of normalized acoustic pressure show similar values to the clean airfoil. That is until the occurrence of the dynamic stall behaviour at which point large scale vortices are produced developing peaks of broadband noise at a magnitude far greater than the peaks of the clean airfoil noise signal. These peaks then begin to oscillate at a far higher frequency. Furthermore, what is noteworthy is the similarity between the high-frequency oscillations over each main oscillation.

2.5.5 Acoustic Characterization of Glaze and Rime Ice Structures

The noise signals of all test cases are then described in terms of how the power of the signal is distributed over frequency through a power spectral density diagram shown in Fig. 2.8. The power spectral density estimate of the input signal was found using Welch's overlapped segment averaging estimator. The length of the analysed signals used for the spectra is approximately $1.071\,\mathrm{s}$ corresponding to 3 periods with a sampling frequency of $280\,\mathrm{Hz}$. Through analysing these signals it is clear that there is a distinct division between the high-frequency noise of the glaze and rime ice structures. The rime ice structures from conditions R-T600 and R-T900 display a tonal peak at $2.8\,\mathrm{Hz}$ corresponding to the oscillating frequency of the airfoil. The glaze ice structure from condition G-LWC displays identical noise level at this frequency. The glaze ice structures from conditions G-AoA5 and G-AoA10 exhibit an increase in the tonal noise at $2.8\,\mathrm{Hz}$ due to the increase in free-stream velocity. All glaze ice structures from conditions G-LWC, G-AoA5 and G-AoA10 then contribute to significant levels of noise at the higher frequency range of the sound spectra whilst there is minimal contribution from the rime ice structures.

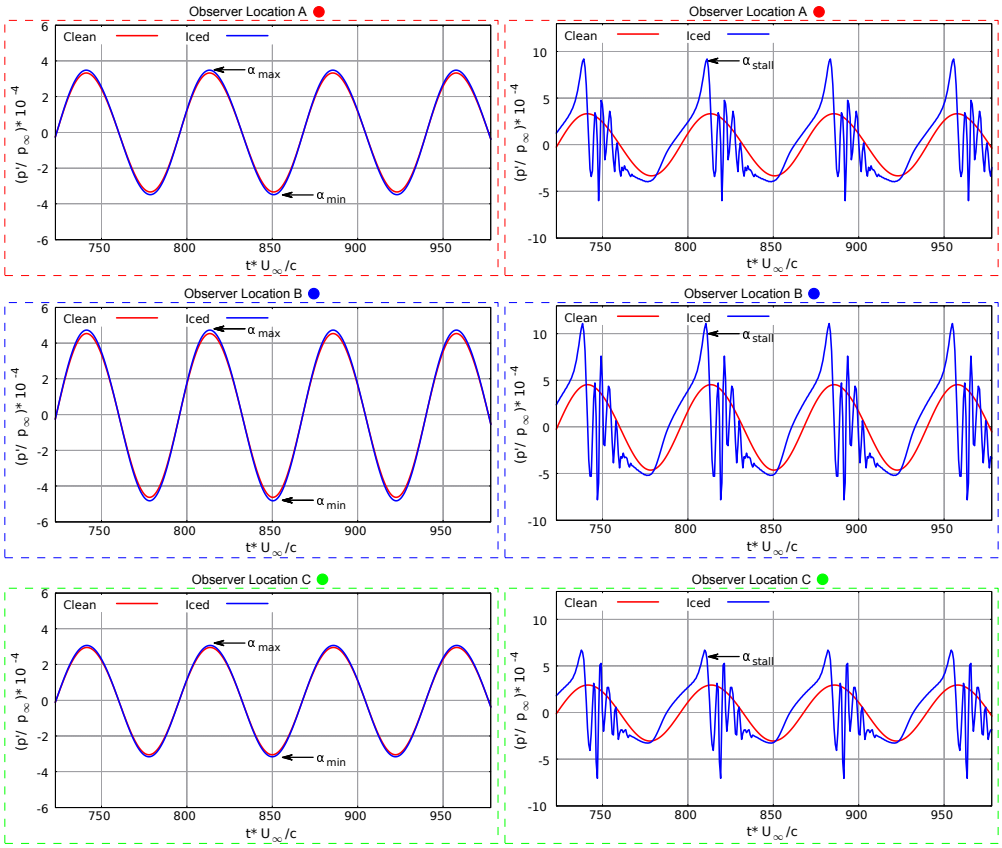

(a) *Acoustic signal produced from the rime ice structure during condition R-T600.*

(b) *Acoustic signal produced from the glaze ice structure during condition G-LWC.*

Figure 2.7: *Comparison of the predicted clean and iced airfoil acoustic signals from Table 2.1. Displays the acoustic signals over a time window long enough to display their periodicity related to the oscillation of the airfoil. Where the acoustic pressure is normalized by freestream pressure and the time is non-dimensionalized to the convective time unit based on the freestream velocity and the chord length.*

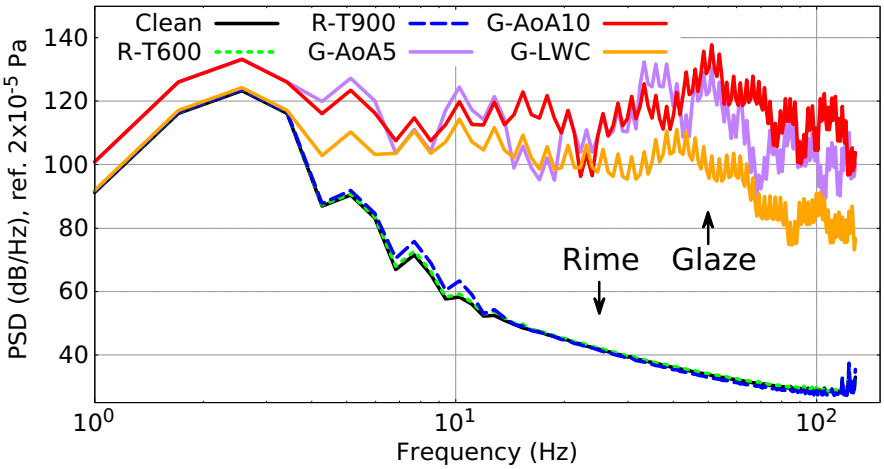

Figure 2.8: *Far-field sound spectra of the iced airfoils. Displaying how the sound spectra can be characterized into two distinct noise signals produced from glaze and rime ice structures. R-T600 and R-T900 represent the test conditions where rime ice was formed and G-LWC, G-AoA5 and G-AoA10 represent the test conditions where glaze ice was formed.*

2.6 Conclusion

An unsteady multi-step ice accretion method coupled with a fully unsteady collection efficiency approach is used here oversee the feasibility of predicting ice shapes over an airfoil oscillating in an unsteady flow field. Experiments from the NASA Glenn IRT were used for comparisons of ice shapes. The aerodynamics of the airfoil is modelled using an unsteady time accurate approach. The super-cooled water droplets are transported within the unsteady flow field and the airfoils moving boundaries are supported within the Lagrangian based particle tracking. The local solution of the unsteady Stefan problem was used to capture the complex experimental ice shapes. Ice shapes are then subject to a computational aeroacoustic analysis using the permeable-surface Ffowcs-Williams-Hawkings formulation. The acoustic signals produced from the varying ice structures can then be characterized into two distinct categories; glaze ice noise signals and rime ice noise signals. Overall some conclusions from this work can be drawn as follows:

1. The fully unsteady collection efficiency approach used to ensure unsteady aerodynamic effects are imposed on the super-cooled water droplet trajectories helps predict ice shapes very close to the experimental data and especially for mixed rime-glaze ice double-horn ice structures.

2. The contrast in the effect the ice structure has on the performance characteristics is observed, and mixed rime-glaze ice double-horn ice structure displays severe degradation in performance and the occurrence of premature on-set stall.

3. The acoustic analysis shows definite scope for the use of computational aeroacoustics to help detect and characterize different types of ice formation in real-time for ice detection warning systems as the different glaze and rime ice structures produce recognizably different noise signatures.

It is apparent from this work that if a relatively simple and low-cost noise ice detection system was in place it would be possible to detect which type of ice accretion was present on the surface in real-time and the pilot would be able to react accordingly. This could be done by detecting large differences in the peak magnitude of the noise source or by detecting high-frequency noise sources associated to flow separation from double-horn ice structures.

With the inherent nature of rotor blades being largely dominated by three-dimensional flows the limitations of this work are understood, however, the fundamental principals behind this study will remain intact for the future when this work is to be extended to three-dimensional simulations of the full rotor. One area of particular interest, is the possibility of the use of scale resolving methods like the Delayed Detached Eddy Simulations (DDES) in SU2 [118, 119], to improve the resolution of the smaller scales and thus higher frequency noise signals caused from the double horn ice structures at the leading edge of the airfoil. A natural transition from the current work would be the acoustic characterization of glaze and rime ice structures on a pitching wing where three-dimensional effects are present at the wing tips. Another intriguing phenomena which would be present, is the formation of omega-type vortical structures, which are

a generic feature of three-dimensional finite high aspect-ratio wings experiencing dynamic stall, and thus, as shown in the two-dimensional simulations within this work could have a significant impact on the acoustic signals during in-flight icing.

Part II

Numerical Tool Development and Validation

CHAPTER 3

Efficient Radial Basis Function Mesh Deformation Methods for Aircraft Icing

The contents of this chapter is to appear in:

Journal of Computational Applied Mathematics
(status: accepted for publication).

Abstract

This chapter presents an approach to update the moving ice boundary present during aircraft icing simulations using radial basis function mesh deformation techniques. State-of-the-art surface and volume point reduction schemes are used to reduce the computational cost of the mesh deformation. The data reduction schemes which are utilized include multi-level greedy surface point selection and volume point reduction. The multi-level greedy surface point selection reduces the control point list to increase the efficiency of the interpolation operation. While the volume point reduction improves the computational cost of the volume mesh update operation which is important for large data sets. The chapter assesses the capabilities of radial basis function mesh deformation for both two and three-dimensional problems. Furthermore, the effectiveness of the deformation technique is assessed for both local, non-smooth deformations and global, smooth deformations. The convergence history of the multi-level greedy point selection is assessed in terms of number of control points and computational cost. The location of the selected control points near the ice accretion illustrates the efficacy of the method for localised deformations. The results show that the radial basis function mesh deformation performs well for both the two and three-dimensional problems. The three-dimensional problems require a larger number of control points resulting in a higher computational cost. Nevertheless, the data-reduction schemes utilized in this work represent a significant improvement to standard radial basis function mesh deformation for aircraft icing problems comprising of large data-sets.

3.1 Introduction

THE ability to use computational techniques to simulate in-flight ice accretion has introduced an alternative approach to costly in-flight icing trails and experimental wind tunnel tests. As a consequence, it is helping to further understand this safety-critical issue. However, the simulation of in-flight icing using computational techniques is not without its own set of challenges. With the desire to move towards fully three-dimensional in-flight icing simulations comes the issue of accounting for the moving ice boundary in the computational domain. Ice accretion can produce geometrically complex shapes and with numerical simulations being highly sensitive to the mesh quality, suitable mesh deformation schemes are required to maintain mesh orthogonality.

Well established techniques for mesh deformation such as the spring analogy [120, 121], the linear elasticity analogy [122, 123] and the interpolation method based on radial basis functions [124–127] have been principally developed for moving boundary problem present in simulations such as fluid-structure interaction problems and aerodynamic shape optimization. The spring analogy, first developed by Batina [120], is one of the most widely used methods and models each edge of the mesh as a linear spring connected together at corresponding nodes. Significantly, Farhat et al. [121] further developed the spring analogy and introduced torsional stiffness to alleviate the mesh crossover problem. A concern with the spring analogy is that it is expensive to solve and cannot guarantee high mesh quality during large deformations. The linear elasticity analogy extends from the spring analogy and models each mesh element as an elastic solid. The linear elasticity analogy has very high mesh quality during large mesh deformations however this comes at the expense of an increase in the CPU cost.

Boer et al. first applied radial basis function interpolation to mesh deformation [124]. Radial basis functions mesh deformations techniques have the unique property that they do not require the grid connectivity meaning that even for three-dimensional problems they are relatively simple to implement. Their work observed the superior mesh quality of radial basis function interpolation when compared to the spring analogy [124]. Rendall and Allen [126] then went on to show that radial basis function methods are robust and preserve high-quality mesh even during large deformations. One of the biggest deterrents to the radial basis function method, however, is that it is expensive for large scale problems when the number of surface points to be displaced becomes high. To address this issue and Rendall and Allen introduced data reduction schemes based upon greedy point selection algorithms to improve the efficiency of the interpolation operation [125, 128]. To further enhance this Wang et al. [129] introduced the concept of a multi-level subspace radial basis function interpolation method. To improve the volume update procedure Xie et al. [130] developed a volume reduction scheme for large data sets. It is clear from the expedited literature that radial basis function mesh deformation is becoming increasingly appealing as the CPU expense reduces with the latest data reduction schemes.

While deformations present during shape optimisation or due to the effects of wing or airframe elasticity can be characterised by large, smooth deformations. Deformations present during aircraft icing are usually local in nature and can be characterised by non-

smooth deformations. Consequently, accounting for the moving iced boundary using conventional mesh deformation techniques is challenging and is highlighted within the literature as being an issue [131].

This work seeks to explore how radial basis functions can be used with their robust mesh deformation properties for computational aircraft icing simulations during the mesh update procedure. Groth et al. [132] first demonstrated the use of standard radial basis function mesh deformation techniques for icing simulations. Their work highlights the promise and potential of radial basis functions. However, significantly what it did not highlight was the critical issue of the costly nature of radial basis functions. The computational cost of radial basis function mesh deformation is one of the main disadvantages of the method and needs addressing if it is to be used in future aircraft icing simulations. Within this work the most concurrent data reduction schemes are utilized to efficiently update the moving iced boundary. These methods are implemented within the open-source SU2 code [133]. The ice accretion simulations are performed using the in-flight icing software suite developed by Politecnico di Milano called PoliMIce [57].

An outline of the remaining chapter follows: An introduction to radial basis functions and their use for mesh deformation is discussed in Section 3.2; The multi-level subspace data reduction schemes used in this work are described in Section 3.3; The volume reduction method for large data sets is discussed in Section 3.4; The results applied to both two- and three-dimensional problems are presented in Section 3.5; The main talking points from this study are discussed in Section 3.6;

3.2 Radial Basis Function Mesh Deformation

The term radial basis function refers to a series of functions whose values depends on their distance to a supporting position. In the most general of forms, radial basis functions can be written as, $\phi(\mathbf{r}, \mathbf{r}_i) = \phi\left(\|\mathbf{r} - \mathbf{r}_i\|\right)$, where the distance corresponds to the radial basis centre, $\mathbf{r}_i$. This distance is frequently taken as the Euclidean distance, meaning it becomes the spatial distance between two nodes. An interpolation function, $f(\mathbf{r})$ can then be introduced as a method for describing the displacement of a set of nodes in space and can be approximated by a weighted sum of basis functions. However, the interpolation relies on the weight coefficients of the basis points, α. The interpolation introduced by Ref. [126] will now be discussed and takes the form

$$f(\mathbf{r}) = \sum_{i=1}^{N} \alpha_i \phi\left(\|\mathbf{r} - \mathbf{r}_i\|\right). \tag{3.1}$$

The weight coefficients of the basis points described in equation 3.1 can be obtained through the exact recovery of the known function values at the surface nodes. A prerequisite to this is knowing the surface node displacements a priori, however, this is typically the case for aircraft icing simulations so is not an issue. The displacement of the surface points are contained within the vector, $\Delta\mathbf{X}$ as described by

$$\Delta\mathbf{X}_s = \left[\Delta x_{s_1}, \Delta x_{s_2}, \ldots, \Delta x_{N_s}\right]^T, \tag{3.2}$$

where the subscript "s" denotes the surface points. This expression is reduced for the total number of surface points, N_s. The displacement in all x, y and z directions can be simplified to

$$\Delta S = \Delta \mathbf{X}_s \hat{\mathbf{x}} + \Delta \mathbf{Y}_s \hat{\mathbf{y}} + \Delta \mathbf{Z}_s \hat{\mathbf{z}} \,. \tag{3.3}$$

Similarly to the surface node displacements, the weight coefficients, $\boldsymbol{\alpha}$, can be contained within a vector

$$\boldsymbol{\alpha}_x = \left[\alpha_{x,s_1},\, \alpha_{x,s_2},\, \ldots,\, \alpha_{x,N_s}\right]^T \,. \tag{3.4}$$

For conciseness only the x components of the coefficients are shown, however, the y and z components are analogous. The universal basis matrix, $\boldsymbol{\Phi}$ can be constructed from the radial basis functions at each of the surface nodes and is consequently of the size of N_s^2. The universal basis matrix can then be shown in its compact form as

$$\boldsymbol{\Phi}_{s_j,\, s_i} = \phi \left\| r_{s_i} - r_{s_j} \right\| . \tag{3.5}$$

The coefficients can then be found by solving the following linear system:

$$\boldsymbol{\Phi}_{s,s} \boldsymbol{\alpha} = \Delta S \,, \tag{3.6}$$

the volume displacements, ΔV, can finally be interpolated through the multiplication of the weight coefficients from equation 3.6 and the newly formed volume node basis matrix, $\boldsymbol{\Phi}_{v,s}$, now of the size $N_v \times N_s$, as described by

$$\Delta V = \boldsymbol{\Phi}_{v,s} \boldsymbol{\alpha} \,, \tag{3.7}$$

where the subscript "v" represents the of volume points.

Multiple forms of radial basis functions exist within the literature which can be used for interpolating data sets and can be characterised into functions with global, local and, compact support. Functions with global support are always non-zero and grow with increasing distance from the radial basis function centre. Likewise, functions with local support are also always non-zero however decay with increasing distance from the radial basis function centre. Compact functions differ from global and local functions in that they decay to zero with increasing distance from the radial basis function centre. The choice of basis function is significant; global and local functions cover the entire interpolation space, leading to dense matrix systems which requires solving the linear system of a fully populated and ill-conditioned matrix. Compact functions are limited to a given support radius, R, resulting in sparse matrix systems which can be solved more easily however this sacrifices interpolation accuracy.

With practical application in mind, functions with compact support were considered within this work such that, $\phi\left(\left\|\mathbf{r} - \mathbf{r}_i\right\| / R\right)$. The Wendland compact radial basis functions [134] are shown in Table 3.1, where, $\eta = \left(\left\|\mathbf{r} - \mathbf{r}_i\right\| / R\right)$. The lower-order basis functions reduce the interpolation accuracy while the higher-order basis functions require a greater CPU cost. Considering this, the Wendland C2 basis function was chosen due to it providing improved smoothness in comparison to the C0 function and due to it

being more efficient than the C4 and C6 functions and takes the form of

$$\phi(\eta) = \begin{cases} (1-\eta)^4 (4\eta+1) & 0 \leq \eta < 1 \\ 0 & \eta \geq 1 \end{cases} . \tag{3.8}$$

Table 3.1: *Wendland radial basis functions with compact support where,* $\eta = (\|\boldsymbol{r} - \boldsymbol{r}_i\| / R)$.

Name	Basis Function
Wendland C0	$\phi(\eta) = (1-\eta)^2$
Wendland C2	$\phi(\eta) = (1-\eta)^4 (4\eta+1)$
Wendland C4	$\phi(\eta) = (1-\eta)^6 (\frac{35}{3}\eta^2 + 6\eta + 1)$
Wendland C6	$\phi(\eta) = (1-\eta)^8 (32\eta^3 + 25\eta^2 + 8\eta + 1)$

Additionally, radial basis functions with global support are also shown in Table 3.2 and were implemented within the solver for completeness.

Table 3.2: *Radial basis functions with global support where,* $\eta = (\|\boldsymbol{r} - \boldsymbol{r}_i\|)$.

Name	Basis Function
Gaussian	$e^{-\eta^2}$
Thin Plate Spline	$\eta^2 \log(\eta)$
Multi Quadratic Bi-Harmonics	$\sqrt{(1+\eta^2)}$
Inverse Multi Quadratic Bi-Harmonics	$\sqrt{(1+\eta^2)^{\frac{1}{2}}}$

3.3 Multi-Level Greedy Surface Point Selection

The high-quality mesh deformation properties of radial basis functions make them appealing, however, their relatively high CPU cost may prevent their use on larger-scale problems where the number of surface points can frequently exceed 10^5. As introduced in equations 3.6 & 3.7, the size of the surface and volume basis matrices are N_s^2 and $N_s \times N_v$ respectively. The relative CPU cost associated with solving the linear algebra in equation 3.6 thus scales with N_s^3 while the CPU cost of interpolating equation 3.7 scales with $N_s \times N_v$. Methods throughout the literature have identified the size of N_s as being an issue for the solving of equation 3.6 and the interpolation of equation 3.7. Notably, Rendall and Allen published a method for reducing the number of surface points based on a greedy algorithm [128]. Their method starts with an initial control point and sequentially uses radial basis function interpolation to find the subsequent control point with the largest error signal. The process repeats itself until the surface interpolation meets a desired tolerance. The implementation of this greedy point selection will now be introduced.

An initial control point is first selected and added to the control points vector, $\mathbf{X}_c$. The choice of the first control point is arbitrary thus, the first point on the list of surface nodes is used, $\mathbf{X}_s^{(0)}$. Such that

$$\mathbf{X}_c = \mathbf{X}_s^{(0)} , \tag{3.9}$$

where the subscript "c" denotes the control points and the subscript "s" represents the surface points. The size of the control points vector is of the size N_c, and since this is the first iteration of the greedy selection process $\mathbf{X}_c$ contains only a singular element.

An error signal is then used to guide the greedy algorithm when selecting control points. Within this work an error vector, $\mathbf{E}$, based on the difference between actual surface displacements and computed surface displacements is used

$$\mathbf{E} = \Delta S - \mathbf{\Phi}_{s,c}\boldsymbol{\alpha}\,, \tag{3.10}$$

with the basis matrix, $\mathbf{\Phi}_{s,\,c}$, now being of the size of $N_s \times N_c$ and where $\mathbf{E}$ is of the size of N_s. The element of the error vector with the largest error signal, $\mathbf{E}^{(\max)}$, is then used to identify the subsequent control point to be added to $\mathbf{X}_c$. This greedy selection process continues until the largest error signal normalized by ΔS meets a desired tolerance, ε, as described by

$$\frac{\mathbf{E}^{(\max)}}{\Delta S} < \varepsilon\,. \tag{3.11}$$

The size of $\mathbf{X}_c$ therefore depends on the number of iterations of the greedy selection process.

The greedy point selection thus allows for the reduction in the number of points being used for solving the linear algebra in equation 3.6 and for the interpolation in equation 3.7, however, the greedy system itself requires significant outlay as every time a control point is added to the system the coefficients need to be solved once more. This therefore means that the CPU cost associated with solving the greedy selection process becomes of the order of N_c^4. Wang et al. addressed this issue by introducing a multi-level subspace radial basis function interpolation where, at the end of each level, the error of that interpolation step is used as the object for the subsequent interpolation step [129] and can be expressed as

$$\Delta S_{l+1} = \mathbf{E}\,, \tag{3.12}$$

where the subscript "$l+1$" denotes the next level of the multi-level greedy selection process. The new error is then computed based on the residual from the previous step and with $\Delta S_{l+1} \ll \Delta S_l$ the size of the displacements is reduced significantly. The error signal described by equation 3.10 is consequently updated and becomes

$$\Delta S_{l+1} = \Delta S_l - \mathbf{\Phi}_{s,c}\boldsymbol{\alpha}\,. \tag{3.13}$$

The number of subspace levels, N_l, is used to continuously reduce the error which allows the multi-level greedy method to be more efficient than the single-level greedy method. The multi-level greedy selection process can be summarised as follows

$$\Delta S \;=\; \textstyle\sum_{i=0}^{i=N_l-1} \Delta S^{(i)} \;=\; \sum_{i=0}^{i=N_l-1} \mathbf{\Phi}_{s,c}^{(i)}\boldsymbol{\alpha}^{(i)}\;, \tag{3.14}$$

$$\Delta V \;=\; \textstyle\sum_{i=0}^{i=N_l-1} \Delta V^{(i)} \;=\; \sum_{i=0}^{i=N_l-1} \mathbf{\Phi}_{v,c}^{(i)}\boldsymbol{\alpha}^{(i)}\;. \tag{3.15}$$

3.4 Volume Point Reduction

The reduced control point list after the multi-level greedy point selection now means that the CPU cost of interpolating equation 3.7 scales with $N_l \times N_c \times N_v$. To efficiently obtain the volume point displacements, it is thus of interest to reduce N_v for large-scale problems since it can often be in the order of magnitude of $N_s \times \sqrt{N_s}$. A wall distance-based function, ψ, is therefore introduced to restrict the N_v based on the work from Xie and Liu [130], namely

$$\psi = \psi\left(\frac{d(\mathbf{r})}{D}\right) , \tag{3.16}$$

where $d(\mathbf{r})$ signifies the wall distance and D is the support distance of the wall function. The wall distance function is of compact support, which means it decays and is zero outwith the support distance as shown,

$$\psi(\xi) = \begin{cases} (1-\xi) & 0 \leq \xi < 1 \\ 0 & \xi \geq 1 \end{cases} , \tag{3.17}$$

where $\xi = d(\mathbf{r})/D$ is the wall distance normalised by the support distance. The distance D is computed as a function of the maximum surface displacement and by using a volume reduction factor, k. Accordingly, distance D, can be expressed as

$$D = k(\Delta S_l)^{max} . \tag{3.18}$$

The wall distance function is then included in the interpolation function, $f(\mathbf{r})$, in equation 3.1 and the updated function has the form:

$$f(\mathbf{r}) = \psi\left(\frac{d(\mathbf{r})}{D}\right) \sum_{i=1}^{N} \alpha_i \phi\left(\|\mathbf{r} - \mathbf{r}_i\|\right) . \tag{3.19}$$

Updating the support distance after each level is possible since $\Delta S_{l+1} \ll \Delta S_l$, meaning the number of volume points in the sphere of influence of the basis function is less. Therefore $D_{l+1} \ll D_l$ and so the number of updated volume points $N_{v,l+1} \ll N_{v,l}$ helping to reduce the cost of the interpolation step.

3.5 Results

In order to assess radial basis function mesh deformation techniques for aircraft icing two test cases are evaluated. The first test case is conducted on a two-dimensional airfoil and the second test case is conducted on a three-dimensional swept-wing. The performance of the data-reduction schemes and robustness of the deformation in terms of the mesh quality are evaluated. Additionally, the non-smooth ice deformations are compared to well-known benchmark test cases for radial basis function mesh deformation with smooth deformations. Finally there is a comparison of the radial basis function mesh deformation technique with the standard linear-elasticity approach. All simulations are run on a single processor to focus on the efficiency of the mesh deformation

techniques opposed to the scalability and parallelism of the code. The processor used was an Intel(R) Xeon(R) X5660 CPU with a clockspeed of $2.80\,\mathrm{GHz}$.

3.5.1 2D – NACA0012 Airfoil

The aim of the first test case is to assess the efficiency and robustness of radial basis function mesh deformation data-reduction schemes on a two-dimensional icing problem. Experimental icing tests on a NACA0012 airfoil performed in the NASA Lewis Icing Research Tunnel (IRT) [135] are used as a reference for the numerical icing predictions. One subset of these conditions is chosen and is outlined in Table 3.3.

Table 3.3: *NACA0012 airfoil icing conditions.*

Airfoil [-]	Time [s]	AoA [°]	Chord [m]	Pressure [Pa]	Airspeed [$\mathrm{m\,s^{-1}}$]	OAT [K]	LWC [$\mathrm{g/m^3}$]	MVD [µm]
NACA0012	120	0	0.3	90 700	129	260.55	0.5	20

The spatial discretization of the two-dimensional airfoil mesh is achieved using a structured multi-block grid and is shown in Fig. 3.1. The total number of elements in the domain is $44\,055$ and the total number of nodes is $44\,500$. The NACA0012 airfoil has 247 nodes distributed around its surface with nodes congregated around the leading and trailing edges. The far-field is placed 25 chord lengths from the airfoil. The grid resolution is sufficient at the wall to ensure $\mathrm{y}+ < 1$.

The SU2 solver [133] is used to determine the flow field by solving the RANS equations. The standard one-equation SA turbulence model is used for closure of the RANS equations. The convective fluxes are computed using the Roe scheme and second-order accuracy is achieved using the MUSCL scheme. The viscous fluxes are approximated using the weighted-least-squares numerical method.

The PoliMIce software library provides state-of-the-art ice formation models [57]. The model used in this work to capture the complex experimental ice shapes is the local exact solution of the unsteady Stefan problem for the temperature profiles within the ice layer in glaze conditions [136]. Multi-step ice accretion simulations are performed at $5\,\mathrm{s}$ intervals to iteratively update the solution and account for unsteady ice accretion. The final predicted ice shape after $120\,\mathrm{s}$ of ice accretion is compared against the measured data from Ref. [135] and is shown in Fig. 3.2. The ice shape exhibits distinct horns paradigmatic of the glaze ice regime and the overall mass of ice is in agreement with the experimental measurements.

The compactly supported Wendland C2 function is used to deform the iced mesh. Points within the support radius of $R = 2c$ are deformed. Altogether five levels of multi-level greedy surface point reduction are used. Each level is updated when there is a reduction of $\varepsilon = 10^{-1}$ in the normalized error. A volume reduction factor of $k = 5$ is chosen.

The non-smooth, local deformations caused by ice accretion are compared to a benchmark test case taken from Ref. [130] with global, smooth deformations. The benchmark test case imposes a sinusoidal perturbation to the airfoil which can be described by:

$$\Delta y = 0.01 \sin(15\pi x) \ , \tag{3.20}$$

where Δy describes the displacement of the airfoil as a function of its position in the x-direction along its chord, c. The sinusoidal perturbation thus represents a more globalised deformation of the airfoil. Identical radial basis function parameters are used to ensure maximum similarity between local and global deformations.

The results of the radial basis function deformation due to ice accretion and sinusoidal perturbation are summarised in Table 3.4. The main findings will now be discussed.

Table 3.4: *Influence of the kind of deformation on the performance of the multi-level greedy surface point selection scheme: local vs. global*

Kind of Deformation	N_c	N_v	CPU (s)	Min. Ortho.
Ice Accretion:				
Level-1	23	16 406	0.018	0.305
Level-2	48	10 502	0.078	0.308
Level-3	107	6199	0.383	0.353
Level-4	132	2727	0.591	0.355
Level-5	179	743	1.137	0.355
Sinusoidal:				
Level-1	11	18 347	0.032	0.370
Level-2	24	11 853	0.084	0.372
Level-3	49	6943	0.187	0.372
Level-4	110	3223	0.509	0.372
Level-5	182	743	1.158	0.372

The convergence history of the normalized displacement error for both the iced and sinusoidal deformation are respectively illustrated in Figs. 3.3 & 3.4. The efficiency of the multi-level greedy point selection performs well in terms of maintaining a low number of control points and in terms of CPU time for both test cases. Both kinds of deformation achieve 5 levels of greedy surface point selection. The sinusoidal deformation shows marginally improved performance during the initial levels. However, at the highest level both kinds of deformation show similar performance. The iced deformation shown in Fig. 3.3 requires 179 control points at the 5^{th} level and has an associated CPU time of approximately $1.14\,\text{s}$. While the sinusoidal deformation shown in Fig. 3.4 requires 182 control points at the 5^{th} level and thus exhibits a similar CPU time of approximately $1.16\,\text{s}$.

The control points selected from the $1^{\text{st}} \rightarrow 4^{\text{th}}$ levels of the greedy process for both the iced and sinusoidal deformation are respectively shown in Figs. 3.5 & 3.6. The local ice deformation has control points which are predominately distributed around the leading edge of the airfoil as shown in Fig. 3.5. This leads to a highly anisotropic control point distribution. It is evident that for ice shapes with any kind of level of roughness or horns, a large number of control points are required otherwise the radial interpolation may potentially smooth over these local features. Contrarily, the global sinusoidal deformation has control points which are relatively evenly distributed as shown in Fig. 3.6. At the lower levels, the control points are selected at the peaks of the sinusoidal waves.

As the greedy algorithm progresses, the control point list becomes more populated and control points are relatively evenly distributed along the airfoil.

The influence of the kind of deformation on the mesh quality is shown in Fig. 3.7. The mesh quality is evaluated by the orthogonality angle. The results show that a relatively high orthogonality angle is preserved throughout the simulations when compared to the clean mesh as shown in Fig. 3.7a. The localised ice deformation shown in Fig. 3.7b causes an isolated reduction in the mesh quality at the leading edge. While the global sinusoidal deformation shown in Fig. 3.7c causes a more universal reduction in the mesh quality with the greatest degradation located at the peaks of the sinusoidal waves.

To further assess the effectiveness of this technique for aircraft icing, it is compared to the more traditional linear elasticity analogy. For this two-dimensional test case, the elastic stiffness of each element is inversely proportional to the cell volume to help preserve the mesh quality within the boundary-layer. For completeness, the standard radial basis function technique is also compared. A summary of the results is described in Table 3.5 while the resultant mesh quality is shown in Fig. 3.8. The results show that both radial basis function mesh deformation techniques provide identical mesh orthogonality irrespective of the number of control points. Meanwhile, the linear-elasticity approach provides similar mesh orthogonality near the ice horns. The CPU time for each technique is comparable for this two-dimensional problem.

Table 3.5: *Influence of the deformation technique on the performance.*

Deformation Technique	N_c	N_v	CPU (s)	Min. Ortho.
RBF Standard	247	44 500	2.731	0.355
RBF Multi-Level	179	743	2.207	0.355
Linear-Elasticity	247	44 500	2.558	0.334

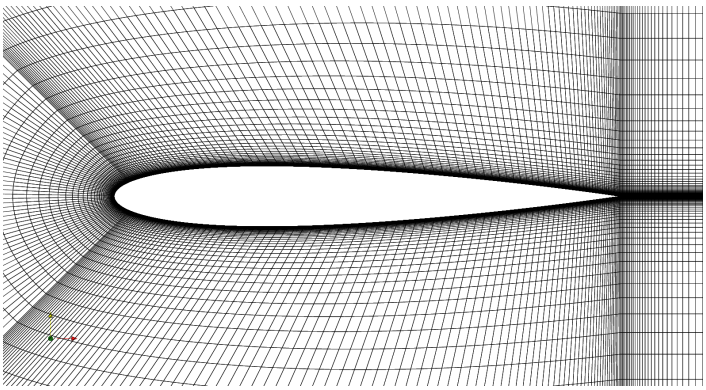

Figure 3.1: *Structured NACA0012 airfoil mesh. Constructed using the multi-block grid strategy.*

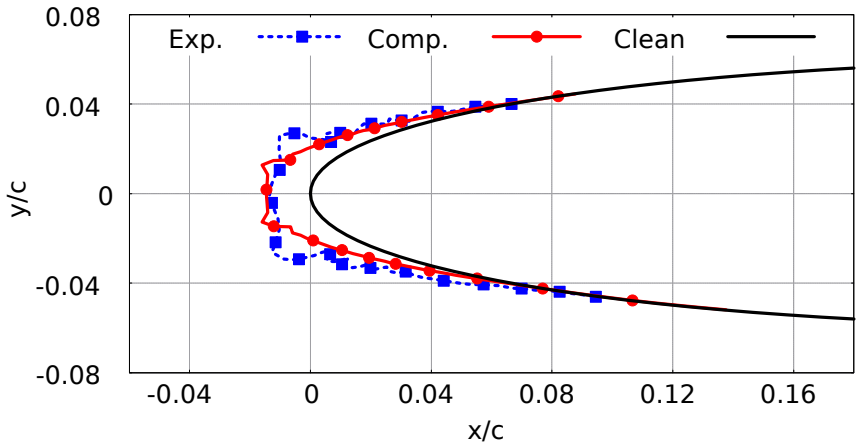

Figure 3.2: *Comparison of computed and experimental ice shapes on a NACA0012 airfoil under conditions identified in Table 3.3.*

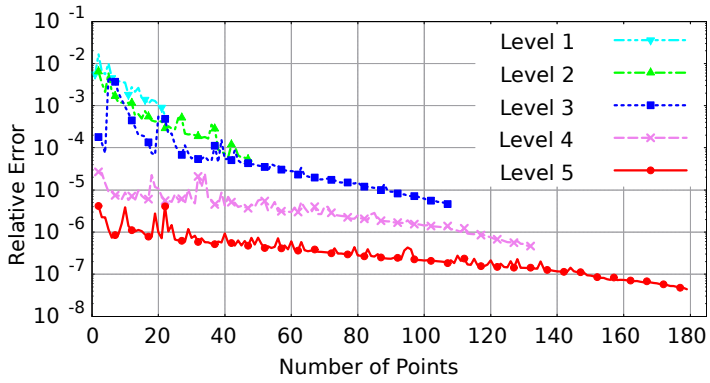

(a) *Convergence history in terms of selected points.*

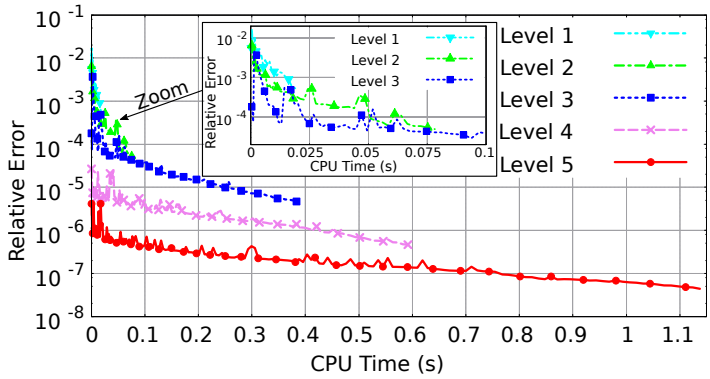

(b) *Convergence history in terms of CPU time.*

Figure 3.3: *Comparison of error reduction rates in terms of selected points and CPU time for the NACA0012 airfoil under icing conditions.*

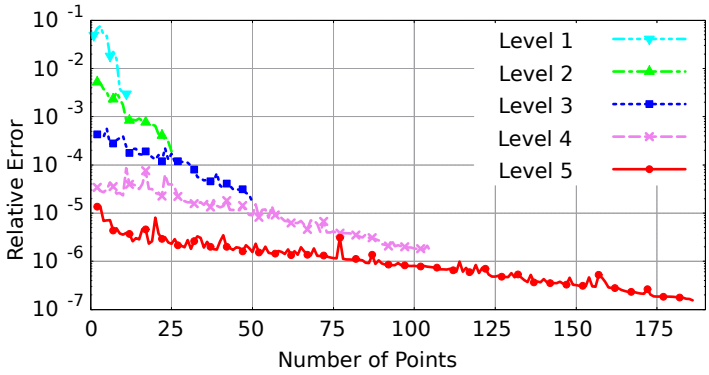

(a) *Convergence history in terms of selected points.*

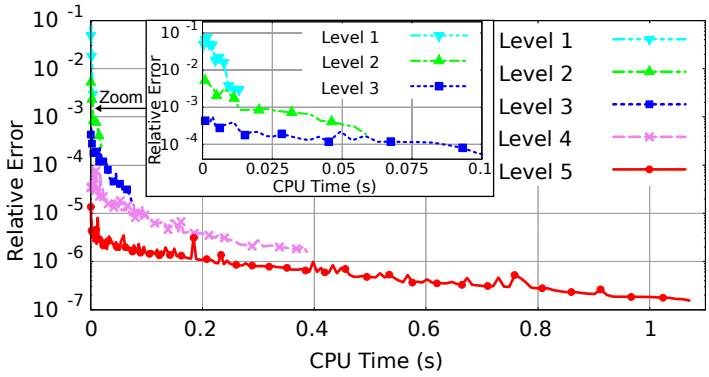

(b) *Convergence history in terms of CPU time.*

Figure 3.4: *Comparison of error reduction rates in terms of selected points and CPU time for the NACA0012 airfoil with sinusoidal perturbation.*

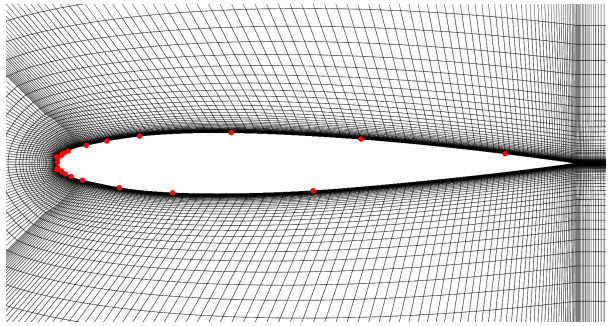

(a) *Level 1: 23 Control Points.*

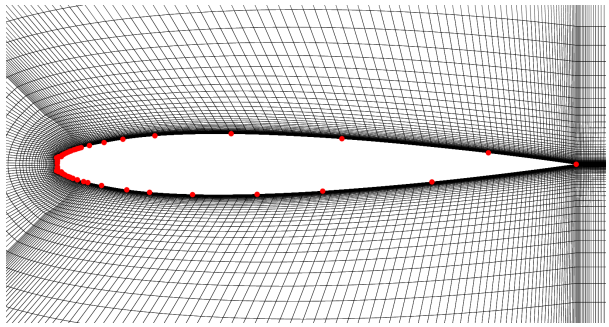

(b) *Level 2: 48 Control Points.*

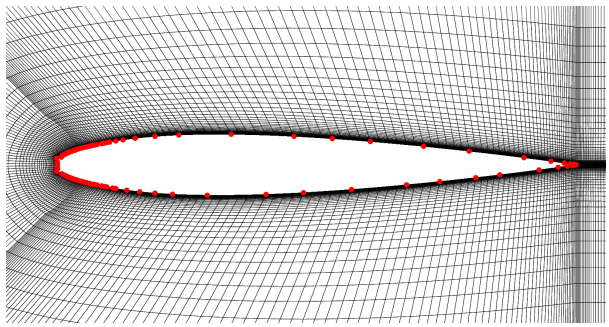

(c) *Level 3: 107 Control Points.*

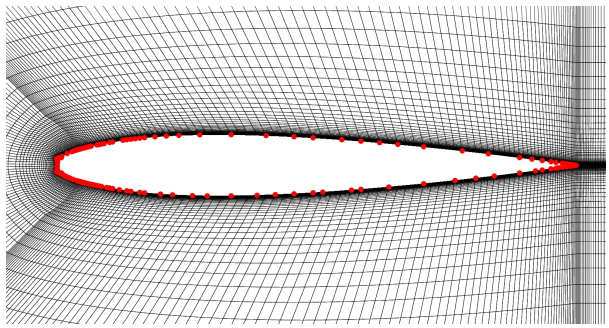

(d) *Level 4: 132 Control Points.*

Figure 3.5: *Control points selected during the multi-level greedy point selection for the NACA0012 airfoil under icing conditions; where the red points indicate the control points.*

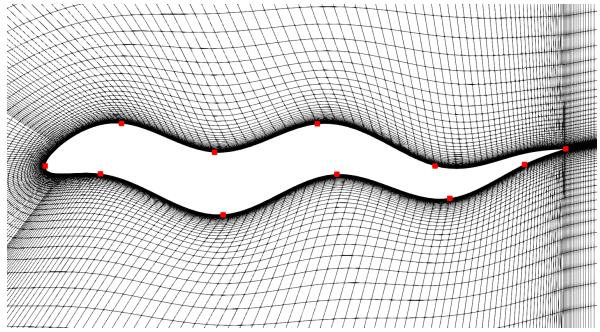

(a) *Level 1: 11 Control Points.*

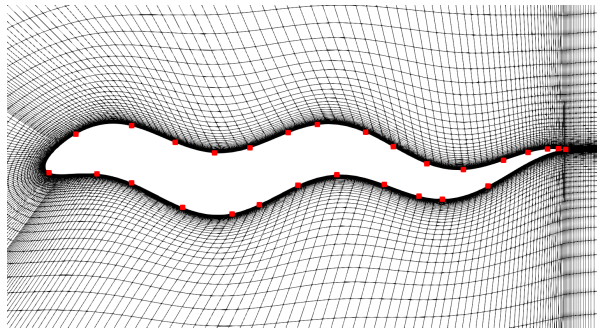

(b) *Level 2: 27 Control Points.*

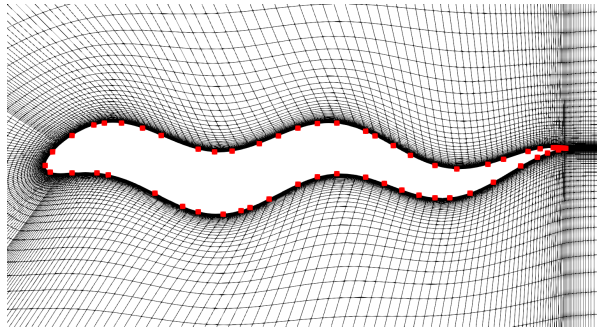

(c) *Level 3: 53 Control Points.*

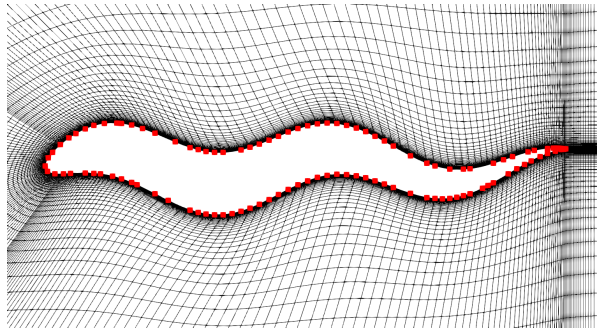

(d) *Level 4: 108 Control Points.*

Figure 3.6: *Control points selected during the multi-level greedy point selection for the NACA0012 airfoil with a sinusoidal perturbation; where the red points indicate the control points.*

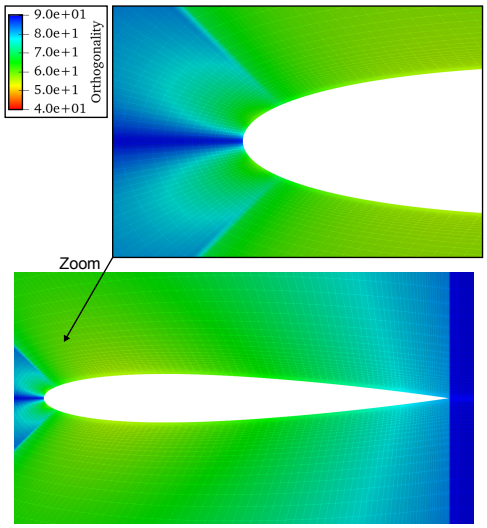

(a) *Orthogonality of the clean airfoil mesh prior to deformation.*

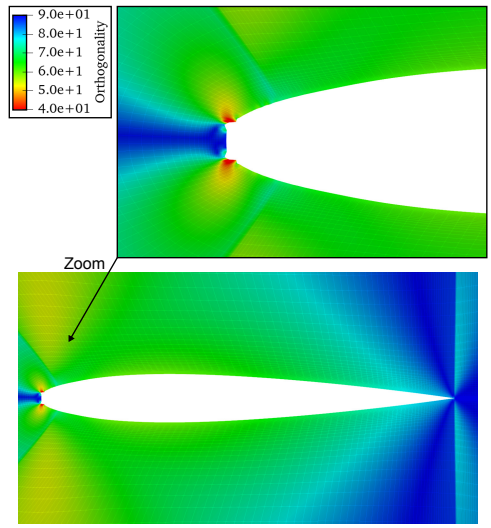

(b) *Orthogonality of the iced airfoil mesh post deformation.*

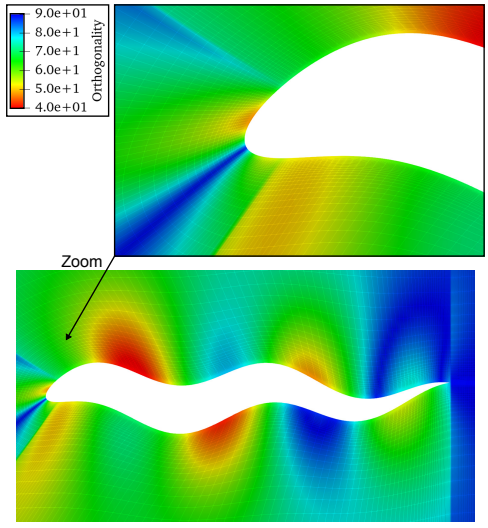

(c) *Orthogonality of the sinusoidal airfoil mesh post deformation.*

Figure 3.7: *Influence of the kind of deformation on the mesh quality. Comparing localised deformation to global deformation.*

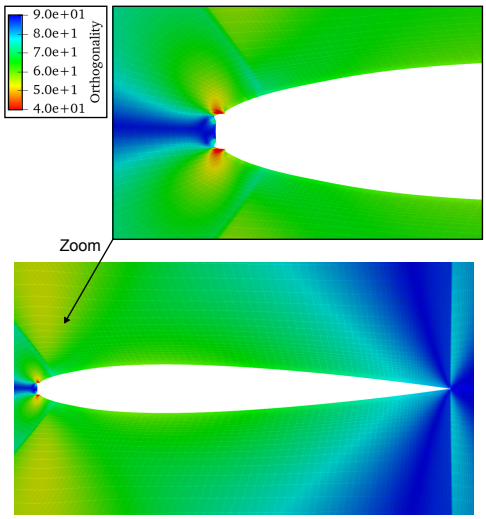

(a) *Standard RBF approach.*

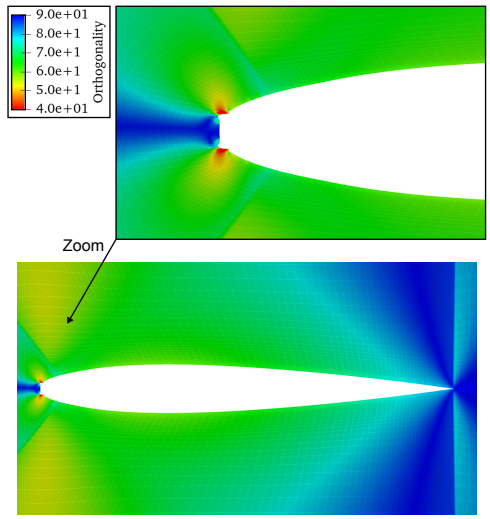

(b) *Multi-level RBF approach.*

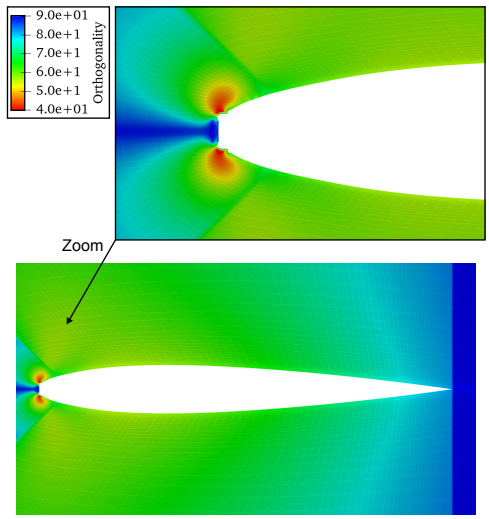

(c) *Linear-elasticity approach.*

Figure 3.8: *Influence of the deformation technique on the mesh quality. Comparing the standard RBF, multi-level RBF, and linear-elasticity approaches.*

3.5.2 3D – Swept Wing

The aim of the second test case is to assess the efficiency and robustness of radial basis function mesh deformation data-reduction schemes on a three-dimensional icing problem. Experimental icing tests on a swept-wing with a NACA0012 profile performed in the NASA Glenn Icing Research Tunnel (IRT) [137] are used. One subset of these conditions is chosen and is outlined in Table 3.6.

Table 3.6: *Swept-wing icing conditions.*

Wing Profile	Sweep [°]	Time [min]	AoA [°]	Chord [m]	Airspeed [$\mathrm{m\,s^{-1}}$]	OAT [K]	LWC [$\mathrm{g/m^3}$]	MVD [µm]
NACA0012	45	19.8	0	0.914	51.44	260.55	0.57	44

The spatial discretization is achieved using an unstructured mesh which is shown in Fig. 3.9. The total number of elements in the domain is $2\,030\,599$ and the total number of nodes is $591\,225$. The swept wing has $21\,650$ nodes distributed around its surface with there being an even distribution around the wing. The far-field is placed 20 chord lengths from the wing. The grid resolution is sufficient at the wall to ensure $\mathrm{y+} < 1$.

The SU2 solver configuration settings used to determine the aerodynamic flow field of the two-dimensional case are also used for the three-dimensional swept-wing case. The same applies to the ice accretion simulation settings of PoliMIce. The final predicted ice shape after $19.8\,\mathrm{min}$ of ice accretion is shown in Fig. 3.10a. The ice shape exhibits a spearhead like shape paradigmatic of the rime regime along the leading edge of the wing.

The compactly supported Wendland C2 function is used to deform the iced mesh. Points within the support radius of $R = 3c$ are deformed. Three levels of multi-level greedy surface point reduction are used. Each level is updated when there is a reduction of $\varepsilon = 10^{-1}$ in the normalized error. A volume reduction factor of $k = 5$ is chosen.

The sinusoidal perturbation benchmark test case is extended to the three-dimensional swept-wing test case. A sinusoidal perturbation is applied to the swept-wing in the spanwise direction and can be described by:

$$\Delta y = 0.03 \sin\left(4\pi z\right) \,, \tag{3.21}$$

where Δy describes the displacement of the swept-wing as a function of its position in the z-direction along its span, b. The deformation applied to the swept-wing is shown in Fig. 3.10b. Identical radial basis function parameters are again used to ensure maximum similarity between the localised iced deformation and the global sinusoidal deformation.

The three-dimensional results of the radial basis function deformation due to ice accretion and sinusoidal perturbation are summarised in Table 3.7. The main findings will now be outlined.

The convergence history of the normalized displacement error for both the iced and sinusoidal deformation of the swept-wing are respectively illustrated in Figs. 3.11 & 3.12. Given the increase in size of the data-set, the efficiency of the multi-level greedy point selection performs well in terms of maintaining a low number of control points and in terms of CPU time. When comparing these two test cases it is clear that the global

Table 3.7: *Influence of the kind of deformation on the performance: local vs. global*

Kind of Deformation	N_c	N_v	CPU (s)	Min. Ortho.
Ice Accretion:				
Level-1	492	498 261	8.411	0.386
Level-2	2767	360 000	1072.064	0.398
Level-3	5214	260 321	10 087.194	0.399
Sinusoidal:				
Level-1	102	646 725	1.286	0.366
Level-2	395	579 973	16.762	0.367
Level-3	1297	205 057	256.408	0.372
Level-4	3437	90 457	4148.168	0.375

sinusoidal deformation performs better. While the localised iced deformation shown in Fig. 3.11 can obtain three-levels of greedy surface point selection, the global sinusoidal deformation shown in Fig. 3.12 can obtain four-levels of greedy surface point selection. In essence, while global sinusoidal deformations can be characterised by a small number of control points, localised iced deformations simply cannot. Despite this, satisfactory reduction in the normalised surface error is achieved by both test cases. Most significantly of all, the data-reduction techniques do indeed help to reduce the high CPU cost associated to radial basis function mesh deformation on large data-sets. Notably within the first $60\,\mathrm{s}$ of the iced and sinusoidal deformations, normalized surface errors of 10^{-3} and 10^{-4} are respectively achieved as revealed in Figs. 3.11b & 3.12b.

The control points selected throughout the multi-level greedy selection process for both the iced and sinusoidal deformation are respectively shown in Figs. 3.13 & 3.14. The test cases exhibit significantly different distributions of control points. The local iced deformation illustrated in Fig. 3.13 depicts the intelligence of the selection process to use control points primarily congregated around the leading edge of the swept-wing where ice is accreted. Resultantly an anisotropic control point distribution is present. The global sinusoidal deformation visible in Fig. 3.14 displays a more expansive distribution of selected control points around the swept-wing which reflects the deformation described by Eq. 3.21.

The influence of the kind deformation on the mesh quality is shown in Figs. 3.15 & 3.16. The orthogonality angle of iced and sinusoidal deformed mesh is compared to that of the undeformed mesh. The first location of interest is in the $x - z$ plane at $y = 0$ and is shown in Fig. 3.15. This cut-plane provides a convenient view of the iced mesh. It shows there is a slight decrease in the mesh quality along the leading edge of the iced mesh. Despite this, the overall impact of the ice accretion on the mesh quality appears low. In this plane of view it is difficult to asses the impact of the sinusoidal deformation on the mesh quality. The second location of interest is in the $y - z$ plane at $x = c$ and is shown in Fig. 3.16. Likewise to the previous view, this exposes the marginal reduction in the mesh quality at the leading edge of the iced mesh. This cut-plane however provides a more favourable view of the sinusoidal deformation. Resultantly, it can be adjudged that the mesh quality of the sinusoidal deformation is also satisfactory.

To further evaluate the performance of this technique for three-dimensional aircraft icing problems, it is compared to the more standard linear elasticity analogy. The linear

elasticity equations contain material properties which are related to the mesh characteristics and may be solved using different approaches. This three-dimensional test case considers three different approaches with the elastic stiffness being inversely proportional to the cell volume, the elastic stiffness being inversely proportional to the wall distance, and a constant elastic stiffness with Poisson's ratio being equal to the aspect ratio of the element. Alongside this, the standard radial basis function mesh deformation technique is compared to the multi-level implementation. A summary of the results is described in Table 3.8 while the resultant mesh quality is shown in Fig. 3.17. The results show that all variants of the radial basis function techniques produce viable mesh. On the contrary, only the linear elasticity approach based on the inverse of the wall distance produces a viable mesh. The approach based on the inverse volume has negative volume elements towards the wing-tip while the approach based on the constant stiffness has negative volume elements within the boundary-layer. Additionally, it can be concluded that two levels of greedy surface point selection are sufficient to obtain a high-quality mesh at a fraction of the CPU cost of standard radial basis function techniques and the linear elasticity approach.

Table 3.8: *Influence of the deformation technique on the performance.*

Deformation Technique	N_c	N_v	CPU (s)	Min. Ortho.
RBF:				
Standard	21 650	2 030 599	275 684	0.399
Multi-Level (2)	2767	360 000	1072	0.398
Multi-Level (3)	5214	260 321	10 087	0.399
Linear-Elasticity:				
Inverse Volume	21 650	2 030 599	4080	-0.350
Wall Distance	21 650	2 030 599	4104	0.356
Constant Stiffness	21 650	2 030 599	4158	-0.898

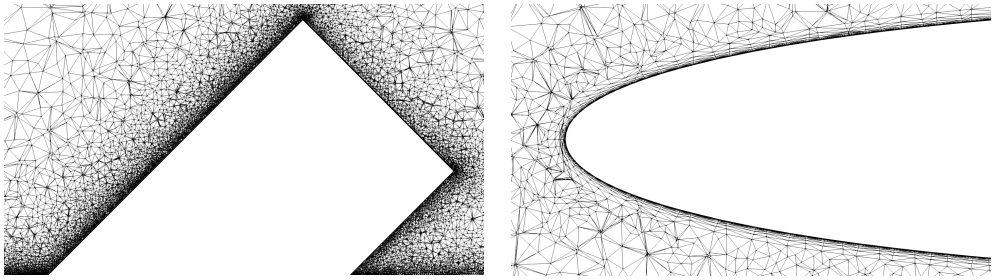

(a) *Unstructured volume mesh in the $x - z$ cut-plane at $y = 0$.*

(b) *Close-up view of the leading edge volume mesh in the $x - y$ cut-plane at $z = 0.5b$.*

Figure 3.9: *Unstructured swept wing mesh. Constructed using a NACA0012 airfoil and based on a 45° sweep angle.*

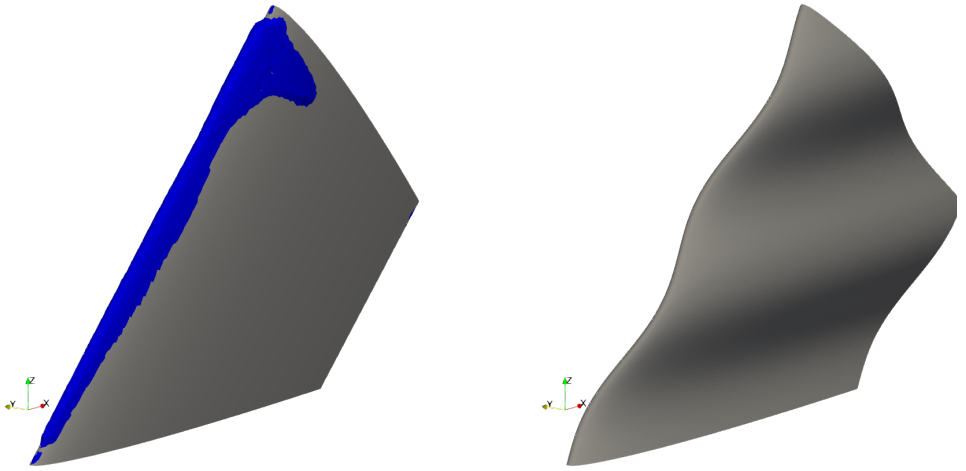

(a) *Predicted ice shape under the conditions identified in Table 3.6.*

(b) *Sinusoidal perturbation of the wing described by Eq. 3.21.*

Figure 3.10: *Different kinds of deformation applied to the swept wing. Firstly, the ice shape which is displayed in blue and depicts a non-smooth, local deformation. Secondly, the sinusoidal perturbation which represents a smooth, global deformation.*

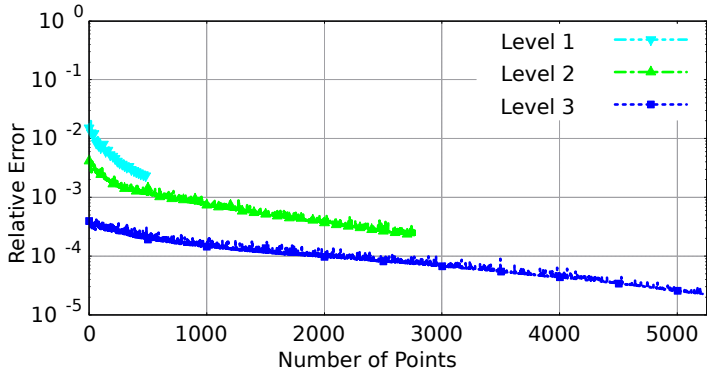

(a) *Convergence history in terms of selected points.*

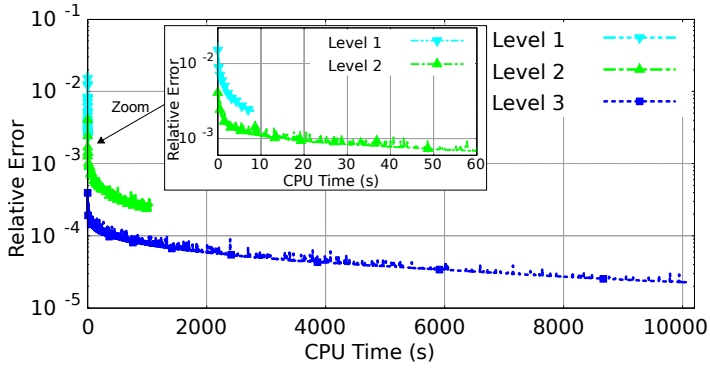

(b) *Convergence history in terms of CPU time.*

Figure 3.11: *Comparison of error reduction rates in terms of selected points and CPU time for the NACA0012 swept wing post deformation due to icing.*

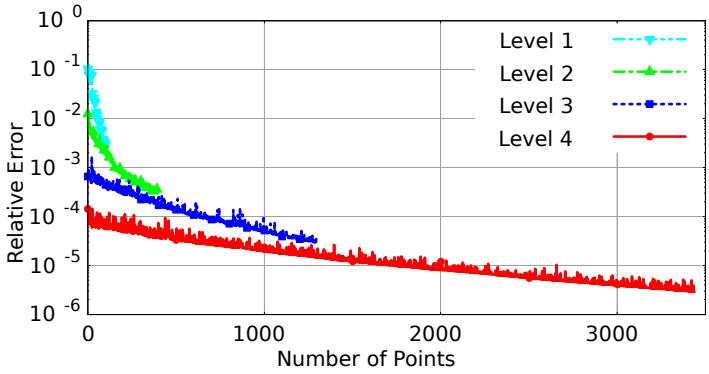

(a) *Convergence history in terms of selected points.*

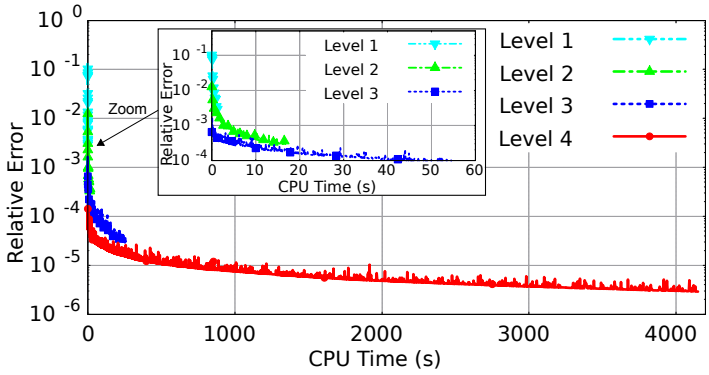

(b) *Convergence history in terms of CPU time.*

Figure 3.12: *Comparison of error reduction rates in terms of selected points and CPU time for the NACA0012 swept wing post deformation due to sinusoidal perturbation.*

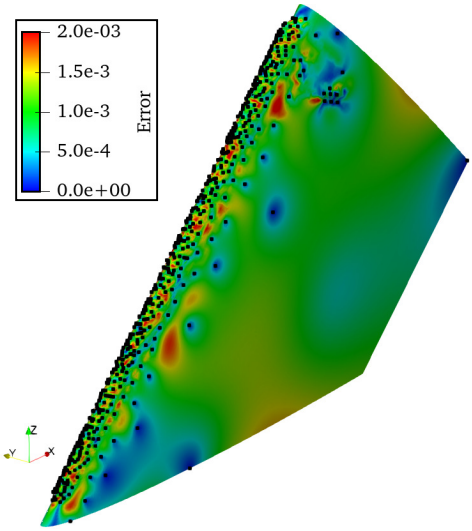

(a) *Level 1: 492 Control Points.*

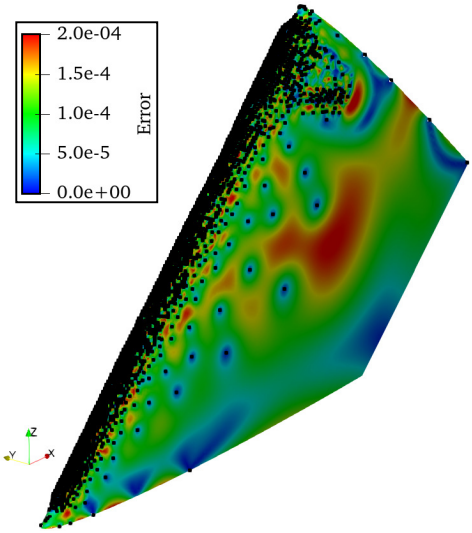

(b) *Level 2: 2767 Control Points.*

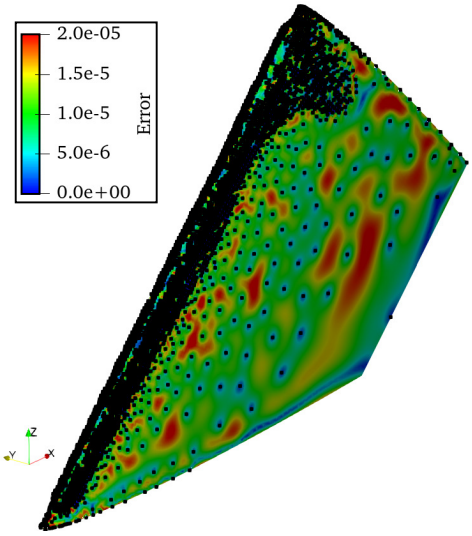

(c) *Level 3: 5214 Control Points.*

Figure 3.13: *Contour map of the normalized surface error during the multi-level greedy point selection on the iced wing. The black points indicate the control points.*

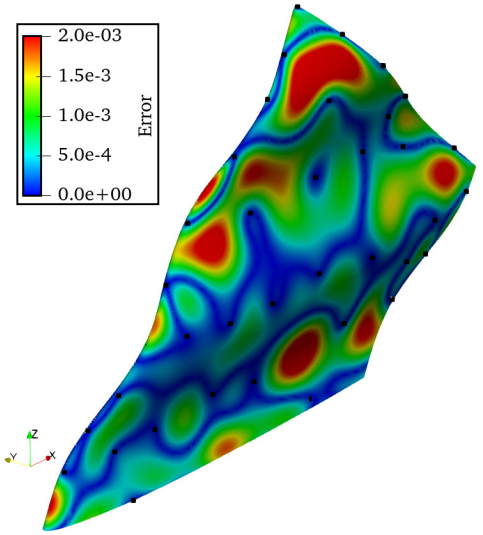

(a) *Level 1: 102 Control Points.*

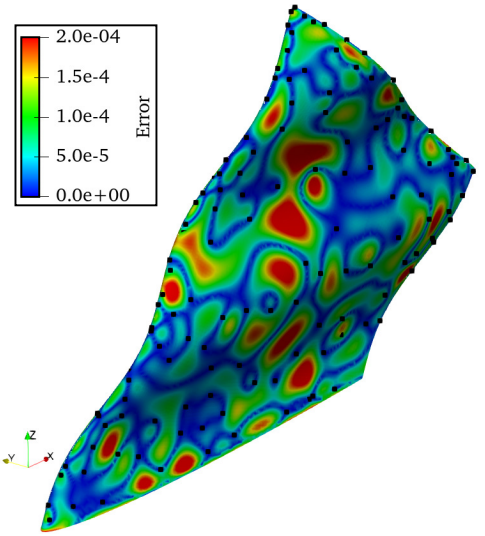

(b) *Level 2: 395 Control Points.*

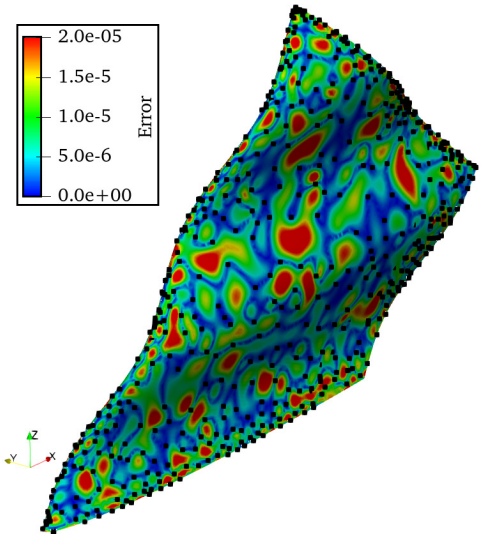

(c) *Level 3: 1297 Control Points.*

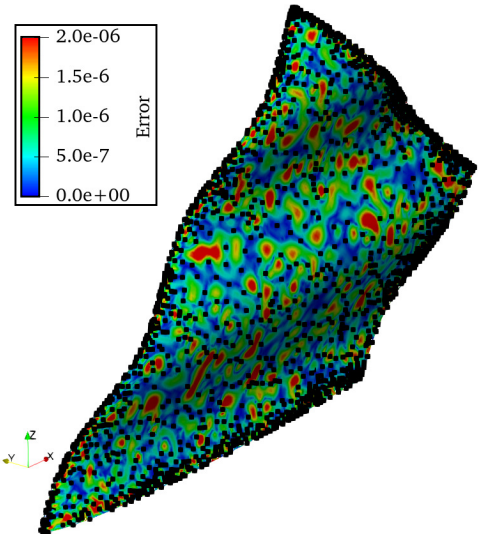

(d) *Level 4: 3437 Control Points.*

Figure 3.14: *Contour map of the normalized surface error during the multi-level greedy point selection on the sinusoidal. The black points indicate the control points.*

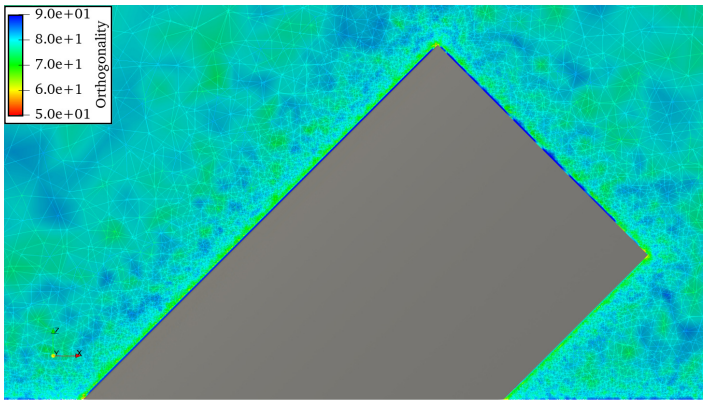

(a) *Orthogonality of the clean wing mesh prior to deformation.*

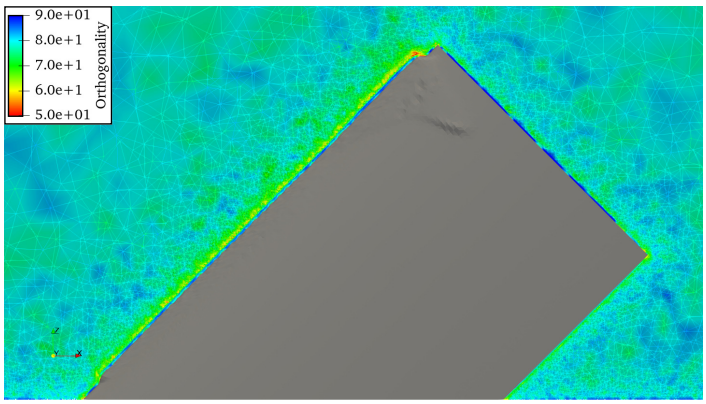

(b) *Orthogonality of the iced wing mesh post deformation.*

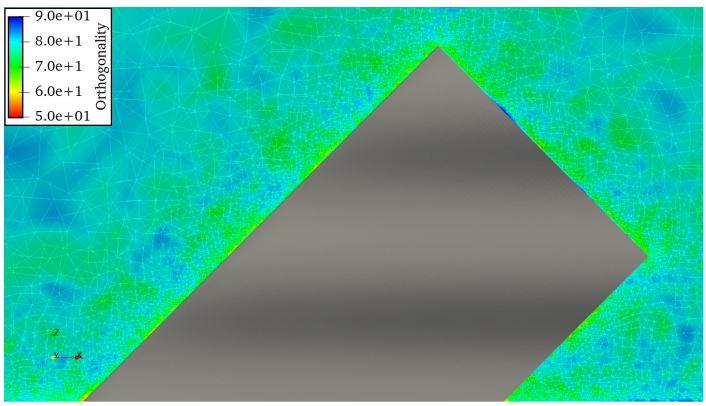

(c) *Orthogonality of the wing mesh post sinusoidal deformation.*

Figure 3.15: *Influence of the kind of mesh deformation on the quality of the swept wing mesh in the $x-z$ plane at $y=0$.*

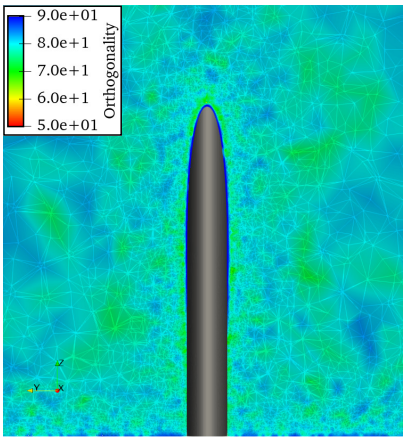

(a) *Orthogonality of the clean wing mesh prior to deformation.*

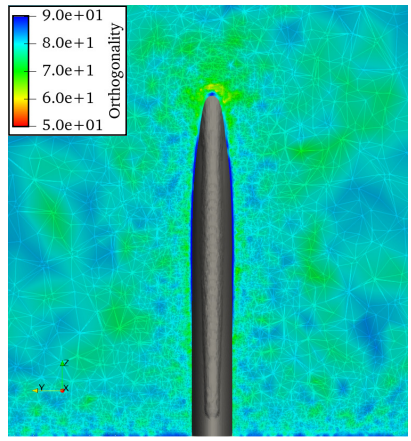

(b) *Orthogonality of the iced wing mesh post deformation.*

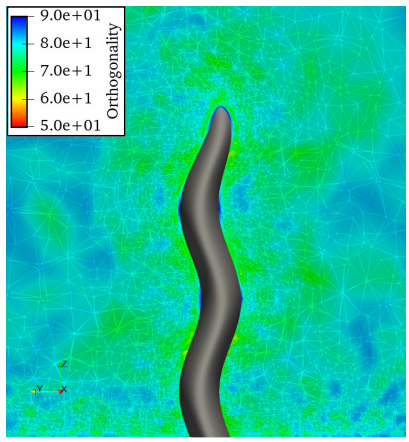

(c) *Orthogonality of the wing mesh post sinusoidal deformation.*

Figure 3.16: *Influence of the kind of mesh deformation on the quality of the swept wing mesh in the $y-z$ plane at $x = c$.*

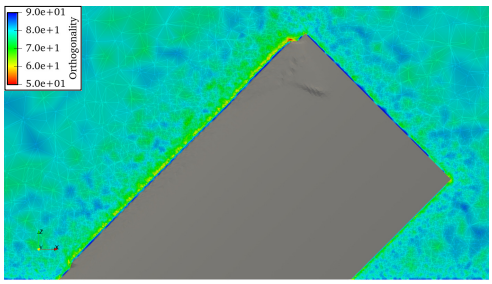

(a) *RBF: 2 levels of greedy selection.*

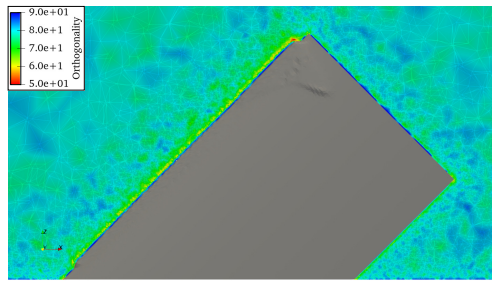

(b) *RBF: 3 levels of greedy selection.*

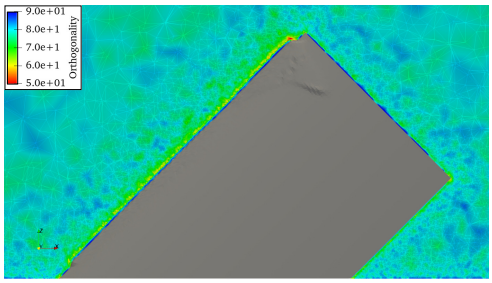

(c) *Standard RBF.*

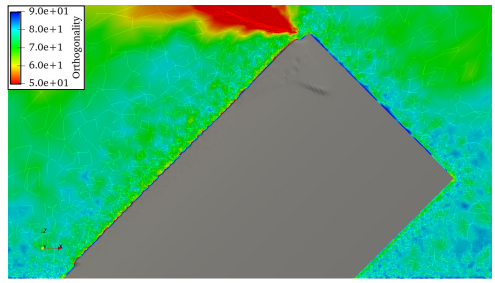

(d) *Linear-elasticity: inverse volume.*

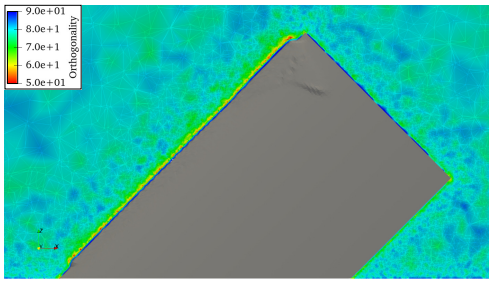

(e) *Linear-elasticity: wall distance.*

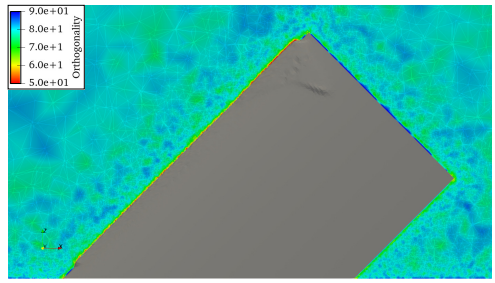

(f) *Linear-elasticity: constant stiffness.*

Figure 3.17: *Influence of the kind of deformation technique on the mesh quality of the swept wing mesh in the $x - z$ plane at $y = 0$.*

3.6 Conclusion

This work evaluates radial basis function mesh deformation techniques for their use within aircraft icing simulations. In this work state-of-the-art multi-level greedy surface point reduction and volume point reduction algorithms are used. The efficiency and robustness of the approach is illustrated using a two-dimensional iced airfoil and three-dimensional swept-wing exposed to icing conditions. The data-reduction methods help to reduce the computational cost of the deformation process while maintaining a high mesh quality. The method allows for the isolation of control points where the ice is present. The convergence history of the airfoil test case performs well with limited control points required at each level and subsequently ensures high performance. The convergence history of the much larger swept-wing test case also performs well and is able to achieve three levels of greedy surface point selection. The introduction of these techniques to aircraft icing simulations provides a significant improvement to the efficiency of standard radial basis function mesh deformation and to the robustness of traditional mesh deformation techniques. Simultaneously, this work highlights the promise of radial basis function mesh deformation techniques and hopes to help provide a reasonable solution to the challenge that is accounting for the moving ice boundary.

CHAPTER 4

Development and Preliminary Assessment of the Open-Source CFD toolkit SU2 for Rotorcraft Flows

The contents of this chapter appeared in:

Morelli, M., Bellosta, T. & Guardone, A., *Journal of Computational Applied Mathematics*, Volume 389, No. 113340, June 2021. https://doi.org/10.1016/j.cam.2020.113340

Abstract

Computational aerodynamic analyses of rotorcraft main rotor blades are performed in both hover and forward flight. The open-source SU2 code is used for rotor performance prediction. The core of the code is the set of RANS equations, which are solved for determining the flow. In hover, both steady-state and time-accurate modelling techniques of varying complexity are used and assessed. Simulation specific parameters which have a significant influence on the solution are also addressed. In forward flight, the code is developed to include the main rotor blade kinematics which is a prerequisite for modelling a trimmed rotor. Two databases are used for the validation of the rotor performance prediction. The renowned Caradonna-Tung experimental tests of a model rotor are used to evaluate the pressure distribution along the blade during hover. The extensive aerodynamic and aeroacoustic data survey of the AH-1G Cobra helicopter is used to assess the pressure distribution at different advancing and retreating azimuth angles during forward flight. The prediction capabilities of the solver in terms of rotor performance are demonstrated and are overall in good agreement with the measured data.

4.1 Introduction

ROTORCRAFT have the unique ability to be able to vertically take-off and land. This allows for their operation in highly demanding and challenging flight scenarios where conventional fixed-wing aircraft cannot pursue. Their frequent use for demanding operations however can lead to dangerous in-flight situations which can be seen from the relatively high number of accident reports from the National Transportation Safety Board (NTSB) [138]. Tools that allow the analysis of rotorcraft are therefore essential for supporting design and for reducing accident rates. Sustained computational development over the past 30 years [139] means that many codes are now capable of modelling rotorcraft behaviour. Computational advancements have enabled CFD-based methods to simulate and further understand complex rotorcraft aerodynamics which are rich in flow physics.

NASA have a long history of rotorcraft CFD code development with OVERFLOW [140] and FUN3D [141]. Of the two codes, OVERFLOW has been used more extensively for rotorcraft simulations [142–152]. OVERFLOW uses body-fitted structured grids near solid surfaces and automatically generated Cartesian grids in the background and is a finite-difference node-based solver. FUN3D uses unstructured grids throughout the domain and is a finite volume node-based solver. This has enabled FUN3D to be utilized as part of a multidisciplinary rotorcraft optimization framework [151, 152]. Academia also plays a leading role in rotorcraft CFD code development. In-house codes HMB from the University of Glasgow [153] and ROSITA from Politecnico di Milano [154] are both finite-volume solvers and utilize structured Chimera multi-block grids to account for the blade motion. Each of the codes have been part of large-scale collaborations for the assessment of their predictive capabilities such as the GOAHEAD project [155]. Another code developed within academia is the TURNS research code from the University of Maryland [156,157]. The TURNS code has Chimera overset grid capabilities and uses a finite difference numerical algorithm that evaluates the inviscid fluxes using an upwind-biases flux scheme. European research centers also have their own codes which have been heavily developed. French and German research institutes ONERA and DLR have their own multi-block Chimera based rotorcraft codes. ONERA have the elsA solver [158] and DLR have the FLOWer solver [159].

Despite all of the codes showing excellent predictive capabilities, none of the mentioned codes are freely available in the open-source domain which hinders technological development. Furthermore, Validation and Verification (VnV) is shown to be increasingly important so to identify a wide variety of physical modelling, discretization, and solution errors [160]. To that end, an open-source code with an active and growing community of users provides a platform for extensive VnV and innovative new solutions.

This work looks to provide the first open-source and validated rotorcraft CFD code by developing the well established SU2 code [133]. Related work by the SU2 community associated with rotary-wing development and validation includes the simulation of rotors in hover conditions and propeller/tilt-rotor configurations in forward flight with fixed collective and cyclic. Palacios et al. performed validation work on the Caradonna and Tung. rotor in hover conditions using a rotating frame approach [161]. Economon et al. introduced a continuous adjoint framework for the design of rotating engineering

applications, while also utilizing the rotating frame approach [162]. Icke et al. presented work on the aeroacoustic optimization of the XV-15 tilt-rotor blades using a time-accurate CFD approach and the Ffowcs Williams and Hawkings formulation for the computational aeroacoustics [163]. Overall, the SU2 code has comprehensively demonstrated its potential for simulating rotorcraft flows. However, the capability to simulate rotorcraft in forward flight remains problematic. This is primarily due to the rotor blade collective and cyclic motion and the trimming of the rotor. The main contribution of this work is the introduction of the blade motion and an approach for modelling forward flight.

Furthermore, the contemporary nature of the code means that it can benefit from new and effective numerical techniques. The recent implementation by Gori et al. [164] of a method for dealing with non-conformal boundary interfaces using the supermesh technique is one example of this. Another example of this is radial basis function mesh deformation which can now utilize computationally efficient algorithms for dealing with large-scale problems.

The outline of this chapter is as follows; the physical modelling of the RANS equations is discussed in Section 4.2, the numerical implementation is described in Section 4.3, the validation work and results of an isolated rotor in hover and forward flight are discussed in Section 4.4, and finally the main talking points of the work are concluded in Section 4.5.

4.2 Physical Modelling

The following section on the physical modelling of the Reynolds-averaged Navier-Stokes equations inside of the SU2 code is primarily a summary of the work from Economon et al. [133] and is here to give context to the numerical implementation in Section 4.3.

4.2.1 Reynolds-Averaged Navier-Stokes Equations

Within this framework, we are interested in time-accurate turbulent flow around rotor blades with arbitrary motion. Therefore we are concerned with compressible flow governed by the Reynolds-averaged Navier-Stokes (RANS) equations. These mass, momentum, and energy conservation equations can be expressed in arbitrary Lagrangian-Eulerian differential form as,

$$\begin{cases} \mathcal{R}(\boldsymbol{U}) &= \frac{\partial U}{\partial t} + \nabla \cdot \boldsymbol{F}^{c}_{ale} - \nabla \cdot (\mu^{1}_{tot}\boldsymbol{F}^{v1} + \mu^{2}_{tot}\boldsymbol{F}^{v2}) - \boldsymbol{Q} = 0 \quad \text{in} \quad \Omega, \quad t > 0 \\ \boldsymbol{v} &= \boldsymbol{u}_{\Omega} \quad \text{on} \quad S \\ \partial_n T &= 0 \quad \text{on} \quad S \\ (W)_{+} &= W_{\infty} \quad \text{on} \quad \Gamma_{\infty} \end{cases} \tag{4.1}$$

with the vector of conservative variables being represented by, $\boldsymbol{U} = \{\rho, \rho\boldsymbol{v}, \rho E\}^{T}$, inside the flow domain, Ω. The term, $\boldsymbol{v} = \boldsymbol{u}_{\Omega}$, denotes the no-slip condition on the surface, S. The expression, $\partial_n T = 0$, represents the adiabatic condition on the surface, S. The final condition, $(W)_{+} = W_{\infty}$, is the characteristic-based boundary condition at

the far-field, Γ_∞. The convective fluxes, viscous fluxes and source terms within Eq. 4.1 can then be respectively expressed as,

$$\boldsymbol{F}^c_{ale} = \begin{Bmatrix} \rho(\boldsymbol{v} - \boldsymbol{u}_\Omega) \\ \rho \boldsymbol{v} \otimes (\boldsymbol{v} - \boldsymbol{u}_\Omega) + \bar{\bar{I}}_p \\ \rho E(\boldsymbol{v} - \boldsymbol{u}_\Omega) + p\boldsymbol{v} \end{Bmatrix}, \boldsymbol{F}^{v1} = \begin{Bmatrix} \cdot \\ \bar{\bar{\tau}} \\ \bar{\bar{\tau}} \cdot \boldsymbol{v} \end{Bmatrix}, \boldsymbol{F}^{v2} = \begin{Bmatrix} \cdot \\ \cdot \\ c_p \nabla T \end{Bmatrix}, \boldsymbol{Q} = \begin{Bmatrix} q_\rho \\ \boldsymbol{q}_{\rho v} \\ q_{\rho E} \end{Bmatrix} \tag{4.2}$$

where the fluid density, flow velocity vector, static pressure, temperature, and specific heat are respectively given by the orthodox notation ρ, $\boldsymbol{v}$, p, T, c_p. Of the remaining variables; E, is the total energy per unit mass; $\bar{\bar{\tau}}$ is the viscous stress tensor; $\boldsymbol{u}_\Omega$ is the grid velocity.

4.2.2 Turbulence Models

Here we are concerned with rotorcraft which during forward flight, climb, descent, and manoeuvre can be characterised by unsteady turbulent flows. With this in mind, the solution of the unsteady Reynolds average Navier-Stokes equations need to be solved which requires the inclusion of a turbulence model. Using the Boussinesq hypothesis [165], the effect of turbulence is represented as an increase in the viscosity. The total viscosity is then separated into laminar and turbulent viscosity and can be respectively denoted as μ_{dyn} and μ_{tur}. The laminar viscosity is determined based upon Sutherland's law [166]. The total viscosity as part of the momentum and energy equations in Eq. 4.1 is then substituted by

$$\mu^1_{tot} = \mu_{dyn} + \mu_{tur}, \quad \mu^2_{tot} = \frac{\mu_{dyn}}{Pr_l} + \frac{\mu_{tur}}{Pr_t} \tag{4.3}$$

where the laminar and turbulent Prandtl numbers are given by Pr_l and Pr_t.

The turbulent viscosity is computed using a suitable turbulence model which itself is dependent upon the flow state and a new set of variables, $\hat{\nu}$, to represent the turbulence, such that, $\mu_{tur} = \mu_{tur}(\boldsymbol{U}, \hat{\nu})$. One of the most widely used models for aeronautical attached flows is the one-equation Spallart-Allmaras (SA) turbulence model [167].

4.2.3 Rotating Frame of Reference

The unique ability of rotorcraft to be able to hover as well as to climb and descend vertically in axial flight helps to distinguish them from other aircraft. During these specific operational flight conditions, the flow around the main rotor can be considered as a steady rotation. Under this assumption, it is then possible to transform the unsteady problem into a steady problem to improve the efficiency of the simulation. This is possible by transforming the system of governing equations in Eq. 4.1 into a rotating frame of reference which rotates at the constant rotational velocity of the main rotor blades. This modification to the system was implemented by Economon et al. [162] inside the SU2 code and can be written as,

$$\frac{\partial \boldsymbol{U}}{\partial t} = 0, \quad \boldsymbol{u}_\Omega = \boldsymbol{\omega} \times \boldsymbol{r}, \quad \boldsymbol{Q} = \begin{Bmatrix} \cdot \\ -\rho(\boldsymbol{\omega} \times \boldsymbol{v}) \\ \cdot \end{Bmatrix} \tag{4.4}$$

where the rotational velocity vector of the rotating frame of reference is specified by $\boldsymbol{\omega} = \{\omega_x, \omega_y, \omega_z\}^T$ and the radial distance from the center of rotation is specified by $\boldsymbol{r}$.

4.3 Numerical Implementation

Alongside the physical modelling in the work from Economon et al. [133] there is also a full description of the numerical implementation. In detail, it discusses the spatial and temporal integration which are the foundation for more application-specific methods such as the harmonic balance and non-conformal boundary interface treatment. The concurrent implementation for modelling rotor blade kinematics will finally be introduced.

4.3.1 Spatial Integration

The flow equations are solved numerically via a finite volume method [168] which is applied on unstructured grids with an edge-based structure. Integrating the governing equations over a control volume and using the divergence theorem to obtain the semi-discretized form gives,

$$\int_{\Omega_i} \frac{\partial \boldsymbol{U}}{\partial t} d\Omega + \sum_{j \in \mathcal{N}(i)} (\tilde{\boldsymbol{F}^c_{ij}} + \tilde{\boldsymbol{F}^v_{ij}}) \Delta S_{ij} - \boldsymbol{Q} \, |\Omega_i| = \int_{\Omega_i} \frac{\partial \boldsymbol{U}}{\partial t} d\Omega + \mathcal{R}_i(\boldsymbol{U}) = 0 \tag{4.5}$$

where $\mathcal{R}_i(\boldsymbol{U})$ includes the convective and viscous fluxes integrated over the surface area of a control volume and any source terms. The numerical approximations of the convective and viscous fluxes are expressed respectively by, $\tilde{\boldsymbol{F}^c_{ij}}$ and $\tilde{\boldsymbol{F}^v_{ij}}$. The area of the face belonging to the edge ij is represented by ΔS_{ij} and the set of neighbouring nodes to node i is expressed by $\mathcal{N}(i)$. The volume of control volume i in the domain is denoted by $|\Omega_i|$.

The convective and viscous fluxes are evaluated at the mid-point of an edge. Centered or upwind schemes such as the Jameson-Schmidt-Turkel scheme [169] or the approximate Riemann solver of Roe [170] are then used to discretize the convective fluxes. Second-order of accuracy of upwind schemes is achieved by using Monotone UpStream-Centered schemes for conservation Laws (MUSCL) [171] to reconstruct the variables on the cell interfaces. Green-Gauss or weighted least-squares methods are used approximate the spatial gradients of the flow at the cell faces to determine the viscous fluxes.

4.3.2 Time Integration

In conjunction with the spatial discretization, there is also the requirement for temporal discretization of the governing equations and so Equation 4.5 is further discretized over

a control volume, $|\Omega_i|$, in time such that it becomes,

$$\frac{d}{dt}(|\Omega_i|\,\boldsymbol{U}) + \mathcal{R}_i(\boldsymbol{U}) = 0 \tag{4.6}$$

and a backward Euler scheme can be used to evaluate the solution state at the updated time for steady problems.

The temporal discretization for unsteady simulations is achieved using a dual-time stepping approach which allows for second order accuracy in time [172]. Using this approach, an additional fictitious time is introduced so that the unsteady problem becomes a series of pseudo-steady problems. The fictitious time is introduced in front of the governing equations such that,

$$|\Omega_i|\,\frac{\partial \boldsymbol{U}_n}{\partial \tau} + \mathcal{R}^*(\boldsymbol{U}_n) = 0 \tag{4.7}$$

with the subscript n denoting the physical time level and to achieve second-order backward difference in time,

$$\mathcal{R}^*(\boldsymbol{U}_n) = \mathcal{R}(\boldsymbol{U}_n) + \frac{3}{2\Delta t}\,|\Omega_i|_n\,\boldsymbol{U}_n - \frac{2}{\Delta t}\,|\Omega_i|_{n-1}\,\boldsymbol{U}_{n-1} + \frac{1}{2\Delta t}\,|\Omega_i|_{n-2}\,\boldsymbol{U}_{n-2} \tag{4.8}$$

where the physical and fictitious time are expressed by Δt and τ respectively. The convergence of every physical time in pseudo time results in the modified residual equating to $\mathcal{R}^*(\boldsymbol{U}_n) = 0$ and once it is satisfied $\boldsymbol{U}_n = \boldsymbol{U}_{n-1}$.

4.3.3 Harmonic Balance

Rotorcraft flows contain strong periodic content. As a consequence, implicit time-spectral methods can be used to substantially reduce the cost of computing the full time-dependent solution [173]. Time-spectral methods are based on the use of discrete Fourier analysis. Within this framework we are specifically interested in the harmonic balance method which transforms the unsteady equations in the physical domain to a set of steady equations in the frequency domain [174]. The subsequent harmonic balance method was implemented by Ref. [175] in SU2 and will briefly be summarised.

In the harmonic balance method the time operator, $\mathcal{D}_t$, is introduced and is approximated using spectral interpolation. Applying the spectral operator to the vector of conservative variables, $\tilde{\boldsymbol{U}}$, which are now to be evaluated at $\mathcal{N}$ time instances, one obtains,

$$\mathcal{D}_t(\boldsymbol{U}) \approx \mathcal{D}_t(\tilde{\boldsymbol{U}}) \tag{4.9}$$

and the harmonic balance operator $\mathcal{D}_t$ can eventually take the form,

$$\mathcal{D}_t(\tilde{\boldsymbol{U}}) = \boldsymbol{H}\tilde{\boldsymbol{U}} \tag{4.10}$$

where $\boldsymbol{H}$ is the spectral operator matrix. While now considering $\tilde{\boldsymbol{U}}$ as the vector of conservative variables evaluated at $\mathcal{N}$ time instances, Equation 4.7 can be rewritten for a single time instance as,

$$|\Omega_i| \frac{\Delta \boldsymbol{U}_n^{q+1}}{\Delta \tau_n} + \boldsymbol{H}\tilde{\boldsymbol{U}} + \mathcal{R}(\boldsymbol{U}_n^{q+1}) = 0 \tag{4.11}$$

where $q+1$ is the physical time step index and where n is now the time instance. The expression can then be linearised and a semi-implicit approach can be used to solve for each time instance. An unsteady problem can then be characterized by K frequencies.

4.3.4 Non-Conformal Boundary Interface Treatment

The numerical discretization of complex rotorcraft geometries is a non-trivial task. It requires the main and tail rotor blades to move in relative motion to the fuselage. To permit this, the computational domain should be split into separate sub-regions, thus introducing non-conformal boundary interface. Suitable treatment of each artificial boundary interface is achieved through the supermesh technique [176] implemented by developers Gori et al. [164] of SU2. The supermesh acts an additional auxiliary grid between two non-conformal interfaces and is of size $n-1$ dimensional elements where n is the dimension of the computational domain. The algorithm used to construct the supermesh of two generic parent mesh is shown in Fig. 4.1 and subsequently outlined:

1. Identify the nodes of the control volume element $\mathcal{E}_B$ contained within $\mathcal{E}_A$.
2. Determine the points of intersection between the edges of $\mathcal{E}_A$ and $\mathcal{E}_B$.
3. Decompose the overlap region into triangles.
4. Calculate the overlapping area of $\mathcal{E}_B$ inside of $\mathcal{E}_A$ and the weight W_i.

this procedure is repeated for each of the overlapping neighbouring elements and its contribution to the numerical flux is assembled by $\sum_{q=1}^{N_{sf}} W_q$. Where the number of supermesh faces that are mapped to each control volume is denoted by $\mathcal{N}_{sf}$. The flux balance across the supermesh interface is obtained through incorporating the neighbouring cells either side of the boundary into Eq. 4.5, which can then be re-written in the semi-discrete form in the cell center of each control volume, k as,

$$\frac{\partial \boldsymbol{U}_k}{\partial t} = -\frac{1}{|\Omega_k|}\left[\sum_{p=1}^{\mathcal{N}_f} \boldsymbol{F}(\boldsymbol{U}_k, \boldsymbol{U}_p)\Delta S_p + \sum_{p=1}^{\mathcal{N}_{bf}} \Delta S_p \left(\sum_{q=1}^{\mathcal{N}_{sf}} W_q \boldsymbol{F}(\boldsymbol{U}_k, \boldsymbol{U}_q)\right)\right] \tag{4.12}$$

where the number of internal faces and boundary faces of each control volume is represented by $\mathcal{N}_f$ and $\mathcal{N}_{bf}$. The area of the face is represented by ΔS. The vector of fluxes are represented as $\boldsymbol{F}$. The conservative variables are once again represented by $\boldsymbol{U}$ and the subscripts p and q denote the neighbouring and boundary cells.

4.3.5 Main Rotor Blade Kinematics

The method in which conventional main-rotor/tail-rotor helicopters generate their vertical and propulsive forces, as well as moments to control the attitude and position of the helicopter in three-dimensional space, will now be introduced and its implementation

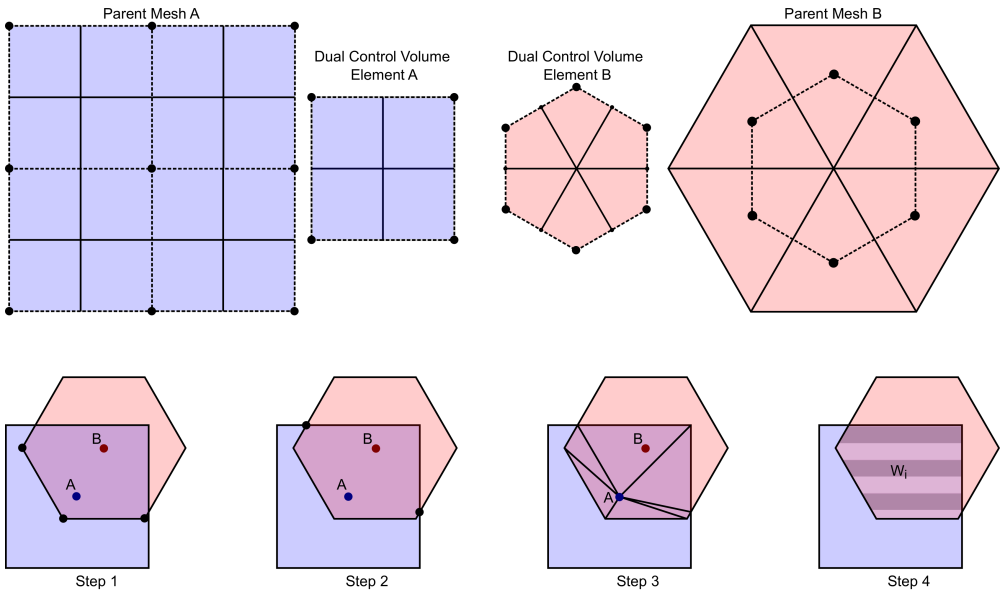

Figure 4.1: *Schematic showing the steps for the construction of the supermesh.*

within SU2 discussed. A schematic depicting the blade motion is shown in Fig. 4.2. Unlike fixed-wing aircraft, the rotor blades alone must provide both the lifting forces and the control meaning the aerodynamics and dynamics of the blades are coupled so that it is hard to understand one without the other. During hover and axial flight, the velocity variation along the blade is azimuthally axisymmetric and depends solely upon the relationship of ωr. In forward flight, however, this is not the case and a component of the free-stream velocity alters the blade velocity such that it now depends upon its azimuthal position, ψ as given by,

$$M_{\mathrm{n}}(\psi) = M_{\mathrm{tip}}\frac{r}{R} + M_{\infty}\sin\psi = M_{\mathrm{tip}}\left(\frac{r}{R} + \mu\sin\psi\right) \tag{4.13}$$

where M_{n} represents the blade normal Mach number and M_{∞} is the freestream Mach number. The advance ratio, μ, can be considered as the relationship of $M_{\infty}/M_{\mathrm{tip}}$. A repercussion of local variations in velocity is that each blade is now required to be individually controlled to eliminate rolling and pitching moments. With this, each blade is typically connected to a rotor head by a set of hinges which allows the blades to move independently. In reality, the rotor blades are also highly elastic in nature, however, for simplification this work considers the blades to be rigid with the ramifications of this being understood. Rigid blades are then able to move with respect to the hinge positions. Each of the hinges will now be introduced: a flap hinge allows the blade to move in the plane containing the blade and the shaft; a pitch hinge allows the blade to move around the quarter chord and spanwise axis; finally a lead-lag hinge allows the blade to move in-plane forward or backwards. The flapping β, lead-lag δ, and pitching θ motion can then be described as a function of the azimuthal position ψ of the blades as they rotate,

$$
\begin{aligned}
\psi &= \omega t \\
\beta(\psi) &= \beta_0 - \beta_{1s}\sin(\psi) - \beta_{1c}\cos(\psi) - \beta_{2s}\sin(2\psi) - \beta_{2c}\cos(2\psi) - ... \\
\delta(\psi) &= \delta_0 - \delta_{1s}\sin(\psi) - \delta_{1c}\cos(\psi) - \delta_{2s}\sin(2\psi) - \delta_{2c}\cos(2\psi) - ... \\
\theta(\psi) &= \theta_0 - \theta_{1s}\sin(\psi) - \theta_{1c}\cos(\psi) - \theta_{2s}\sin(2\psi) - \theta_{2c}\cos(2\psi) - ...
\end{aligned}
\tag{4.14}
$$

where β_0 denotes the coning angle and θ_0 denotes the collective pitch applied equally to all the blades. The lateral and longitudinal components of the motion are represented by subscripts c and s respectively.

A rotation matrix then transforms the blade Cartesian coordinates, $\boldsymbol{x}$, from the fixed frame of reference into the hub frame of reference. The hub reference system is then transformed into each of the blade reference systems and the blade motion laws described in Equation 4.14 are applied. If we now consider the definition of the reference system where; the rotation occurs around the z-axes, the flapping occurs around the y-axes, the lead-lag motion around the z-axes, and the pitching occurs around the x-axes as depicted in Fig. 4.2 the following transformation matrices can be introduced to prescribe the blade motion,

$$
\begin{aligned}
C_{\text{rot}} &= \begin{pmatrix} \cos\psi & -\sin\psi & 0 \\ \sin\psi & \cos\psi & 0 \\ 0 & 0 & 1 \end{pmatrix}, \qquad C_{\text{flap}} = \begin{pmatrix} \cos\beta & 0 & -\sin\beta \\ 0 & 1 & 0 \\ \sin\beta & 0 & \cos\beta \end{pmatrix} \\
C_{\text{lead-lag}} &= \begin{pmatrix} \cos\delta & -\sin\delta & 0 \\ \sin\delta & \cos\delta & 0 \\ 0 & 0 & 1 \end{pmatrix}, \qquad C_{\text{pitch}} = \begin{pmatrix} 1 & 0 & 0 \\ 0 & \cos\theta & -\sin\theta \\ 0 & \sin\theta & \cos\theta \end{pmatrix}
\end{aligned}
\tag{4.15}
$$

The transformation from the fixed $\rightarrow$ hub reference system using C_{rot} is implemented by a rigid rotation of the entire grid as the azimuthal rotation of the blades far exceeds the blade deflections. The rate of rotation is currently constrained and is maintained constant such that,

$$
C_{\text{rot}} = \begin{pmatrix} \cos\psi & -\sin\psi & 0 \\ \sin\psi & \cos\psi & 0 \\ 0 & 0 & 1 \end{pmatrix}
\tag{4.16}
$$

The transformation from the hub $\rightarrow$ blade reference system can then be combined and applied to the blade surface. This is achieved through deforming the mesh at each physical time step and is required as each blade has its own independent motion. The subsequent transformation matrix, $C_{\text{flap-leadlag-pitch}}$ can then be introduced,

$$C_{\text{flap-leadlag-pitch}} = \begin{pmatrix} \cos\beta\cos\delta & \sin\beta\sin\theta - \cos\beta\cos\theta\sin\delta & \cos\theta\sin\beta + \cos\beta\sin\delta\sin\theta \\ \sin\delta & \cos\delta\cos\theta & -\cos\delta\sin\theta \\ -\cos\delta\sin\beta & \cos\beta\sin\theta + \cos\theta\sin\beta\sin\delta & \cos\beta\cos\theta - \sin\beta\sin\delta\sin\theta \end{pmatrix} \tag{4.17}$$

The motion can then be applied to the coordinates, $\boldsymbol{x} = \{x, y, z\}^T$ at an arbitrary point, i on the blade as,

$$\boldsymbol{x}_i = C_{\text{rot}} C_{\text{flap-leadlag-pitch}} (\boldsymbol{x}_i - \boldsymbol{x}_{\text{hinge}}) \tag{4.18}$$

where $\boldsymbol{x}_{\text{hinge}}$ is the position of the hinge about which the flapping, lead-lag and pitching occurs. Furthermore the grid velocity is updated using a second order finite difference scheme,

$$\boldsymbol{u}_{\Omega_i} = \frac{3\boldsymbol{x}_i^{n+1} - 4\boldsymbol{x}_i^{n} + \boldsymbol{x}_i^{n-1}}{2\Delta t} \tag{4.19}$$

Additionally, the Geometrical Conservation Law (GCL) [177] should be satisfied while using a dynamic mesh approach to account for the the movement of the rotor blades in unstructured grids. The numerical implementation of the discrete GCL [178, 179] is thus included and added to the dual-time source terms.

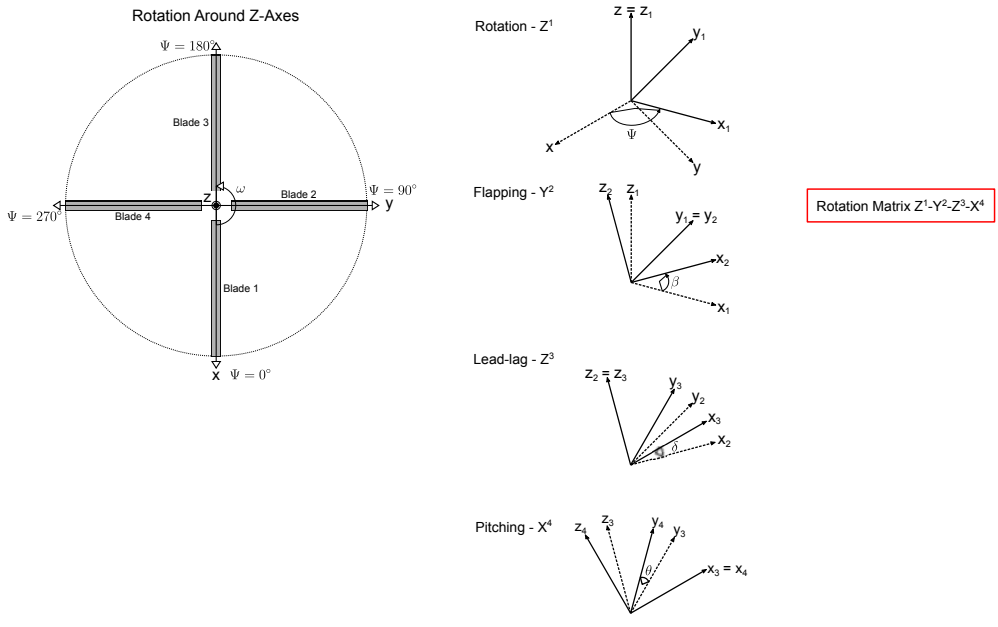

Figure 4.2: *Schematic of the main rotor blade motion and respective rotations.*

4.3.6 Radial Basis Function Mesh Deformation

To allow the rotor blades to move independently requires the mesh to deform at each physical time step. Rendall and Allen, to the authors' knowledge, were the first group to demonstrated how Radial Basis Functions (RBF) could be used to account for the blade motion [180]. The outlook of using RBF mesh deformation for rotor blade motion was promising however one major drawback was the high computational cost for large meshes. To address this issue, work from Schuff et al. [181] introduced an efficient grid coarsening algorithm based on an octree approach and applied it to rotor blades. Despite being computationally prohibitive, RBF mesh deformation methods are robust and preserve high-quality mesh even during large deformations. They also have the unique property that they do not require the grid connectivity meaning that even for three-dimensional problems they are relatively simple to implement.

The term radial basis function refers to a series of functions whose values depends on their distance to a supporting position. In the most general of forms, radial basis functions can be written as, $\phi(\mathbf{r}, \mathbf{r}_i) = \phi\left(\|\mathbf{r} - \mathbf{r}_i\|\right)$, where the distance corresponds to the radial basis centre, $\mathbf{r}_i$. This distance is frequently taken as the Euclidean distance, meaning it becomes the spatial distance between two nodes. An interpolation function, $f(\mathbf{r})$ can be introduced as a method for describing the displacement of a set of nodes in space and can be approximated by a weighted sum of basis functions. The interpolation takes the form

$$f(\mathbf{r}) = \sum_{i=1}^{N} \alpha_i \phi\left(\|\mathbf{r} - \mathbf{r}_i\|\right) \tag{4.20}$$

The primary expense of RBF mesh deformation is associated to the solving the linear system to obtain the weight coefficients. To address these concerns, multi-level greedy surface point selection algorithms [129] and volume point reduction methods [130] for large scale problems are introduced which greatly improve the efficiency. This RBF mesh deformation technique alongside these numerically enhanced methods were implemented by Ref. [182] in SU2 and are now used within this rotorcraft simulation framework.

4.4 Results

4.4.1 Hover

The benchmark Caradonna and Tung experimental tests of a model rotor in hover [183] are used for hover performance validation. The experiment was carried out in the U.S. Army Aeromechanics Laboratory's hover test facility which included special ducting designed to eliminate room recirculation. The rotor employed two manually adjustable cantilever-mounted blades attached to a drive shaft at the top of a column test stand. The blades were untwisted and untapered with an aspect ratio of 6. The profile of the blades used a symmetric NACA0012 airfoil. The rotor radius was $1.143\,\mathrm{m}$ and the blade chord was $0.191\,\mathrm{m}$. The data recorded during the tests consisted of pressure measurements along the chord of the blade at various radial positions. The tests were conducted at a

variety of collective pitch angles and tip Mach numbers. The conditions used for the validation of the blade loading predictions are detailed in Table 4.1.

Table 4.1: *Hover test conditions taken from the Caradonna-Tung experiment [183].*

Collective Pitch (°)	Rotational Speed (RPM)	Tip Mach No. ( )
8	1250	0.439

The problem is transformed into a rotating frame of reference for computational efficiency and the RANS equations are solved to first assess the influence of the radial position on the surface pressure distribution. Computed and experimental surface pressure distributions are compared at select radial positions $r/R = 0.68\%$, $r/R = 0.80\%$, $r/R = 0.89\%$ and $r/R = 0.96\%$ as represented by Fig. 4.3.

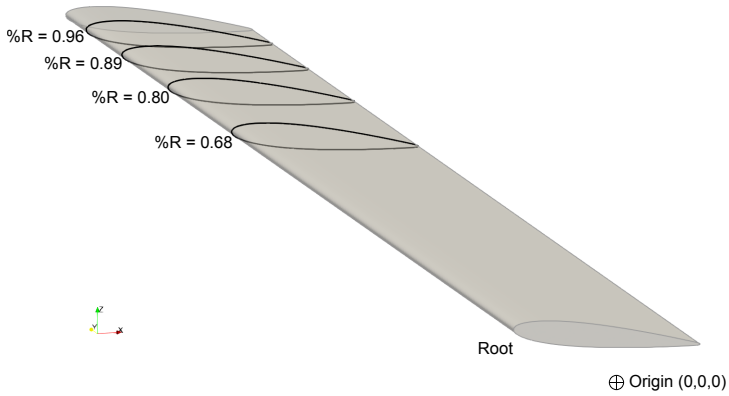

Figure 4.3: *Blade stations where the static pressure measurements were taken during Ref. [183]. Select radial positions $r/R = 0.68\%$, $r/R = 0.80\%$, $r/R = 0.89\%$ and $r/R = 0.96\%$ are used for the assessment of numerical predictions.*

The standard one-equation SA turbulence model is used with the RANS equations. The SA turbulence variable is convected using a first-order scalar upwind method. The convective fluxes are computed using the Roe scheme and second-order accuracy is achieved using the MUSCL scheme. The spatial gradients for the viscous fluxes are approximated using the weighted least-squares method. A Venkatakrishnan slope limiter was used with a coefficient of 0.03. The flow solution was considered converged when there was a reduction of 6 orders of magnitude on the density residual while also monitoring the SA turbulence residual.

The predicted results in Fig. 4.4 are in close agreement with the measured data at all radial positions. Both the upper and lower surface pressure profiles follow the measured data. The suction peak on the upper surface is captured well. There are however discrepancies at the trailing edge and this is expected to be caused by modelling the trailing edge as flat which was done to aid with the mesh generation process and convergence of the solver. The results reaffirm the calculations from Ref. [161].

An assessment of the most influential parameters during hover simulations are displayed in Fig. 4.5. Each of the parameters are compared against the measured data at

$r/R = 0.80\%$. The spatial mesh resolution is assessed in Figs. 4.5a & 4.5b. Four levels of mesh refinement are used ranging from coarse $\rightarrow$ very fine. The 'coarse' mesh has 1.56×10^6 volume elements and 22×10^3 surface elements. The 'medium' mesh has 2.62×10^6 volume elements and 41×10^3 surface elements. The 'fine' mesh has 5.19×10^6 volume elements and 80×10^3 surface elements. The 'very fine' mesh has 11.09×10^6 volume elements and 157×10^3 surface elements. The coarse mesh exhibits oscillations in the pressure profile at the leading-edge. The medium mesh shows a smoother profile however the suction peak remains below the measured data. The fine mesh slightly improves the suction peak compared to the medium mesh. There appear to be no discernible differences between the fine and very fine mesh suggesting the mesh has reached convergence.

It is frequently desirable to model the rotor as a time-accurate problem where the blades are physically moving. As the flow initialises, the influence of the number of rotor revolutions on the solution is investigated and is shown in Figs. 4.5c & 4.5d. The fine grid is hereinafter used to understand the influence of the number rotor revolutions during initialisation and other influential parameters based on the previous mesh sensitivity study. The simulation shows that the time for convergence of the solution is at least 3 full rotor revolutions.

The influence of the choice of steady or time-accurate modelling on the pressure profiles is shown in Figs. 4.5e & 4.5f. The general pressure profile distribution is captured by all methods. The rotating frame method shows the closest agreement to the experimental measurements. The largest difference between the methods are located at the suction peak. There is a very slight difference on the upper surface for the time-accurate sliding mesh, rigid motion and harmonic balance methods. Furthermore, all of the time-accurate methods appear overlapping.

Finally the flow regime is evaluated in Figs. 4.5g & 4.5h. It depicts the influence of inviscid, laminar and turbulent flow on the pressure distribution. The results illustrate the importance of considering fully turbulent flow for rotorcraft flow simulations.

A contour map of the pressure coefficient on both the suction and pressure sides of the blades for time-accurate problems is shown in Fig. 4.6. The approach using unsteady rigid motion is displayed at 10° azimuth increments in Fig. 4.6a. The approach using the harmonic balance is displayed at 3 time instances with the input frequencies of $\boldsymbol{\omega} = (0, \pm\omega_1)$ in Fig. 4.6b. Both sets of results show that the pressure coefficient during hover is axisymmetric about the out-of-plane axis.

The iso-surface of the Q criterion visualizing the near-field wake and blade tip vortices during hover are displayed in Fig. 4.7. The wake exhibits no blade-vortex interaction effects due to the preceding blade tip vortices passing above previous blade tip vortices and due to the isolated blades being modelled without a hub or test stand.

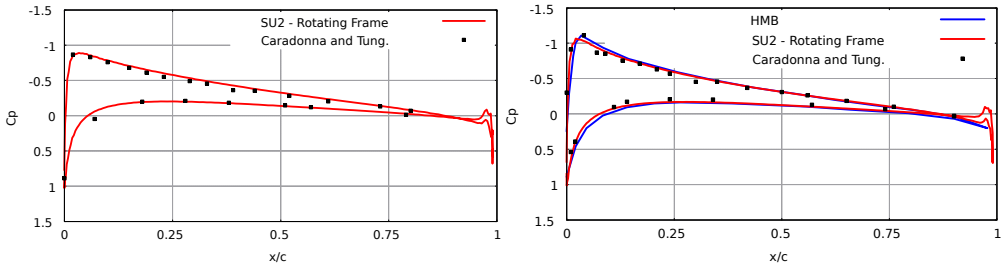

(a) $r/R = 0.68\%$.

(b) $r/R = 0.80\%$.

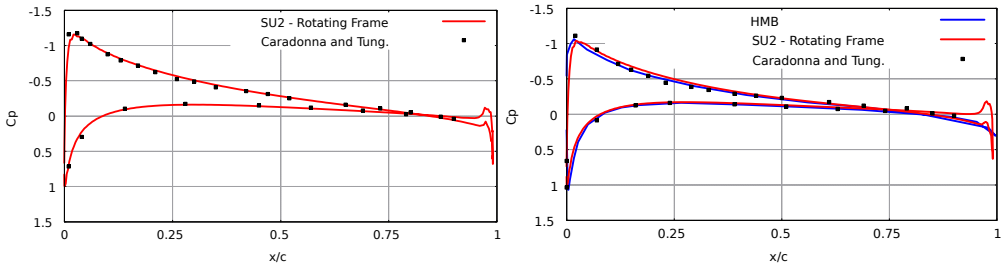

(c) $r/R = 0.89\%$.

(d) $r/R = 0.96\%$.

Figure 4.4: *Pressure distributions at different radial positions computed using the rotating frame method during hover. Predictions compared against measured data taken from Caradonna-Tung [183] and the code from the University of Glasgow named HMB [153].*

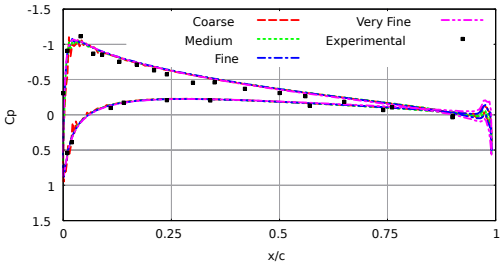

(a) *Grid sensitivity.*

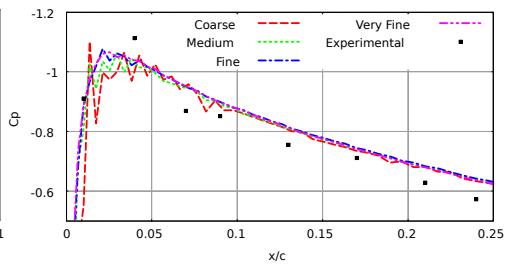

(b) *Region around the leading-edge.*

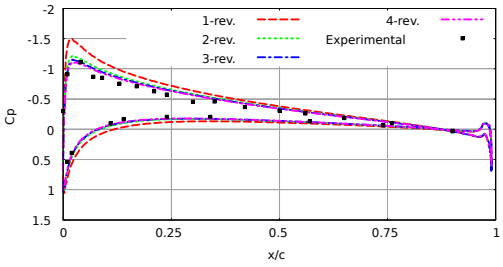

(c) *Rotor revolutions.*

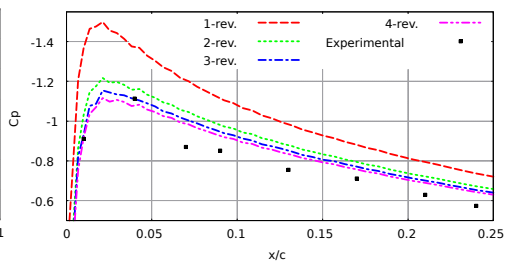

(d) *Region around the leading-edge.*

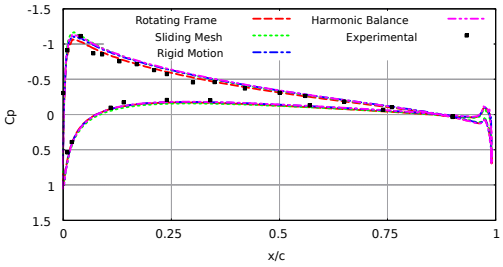

(e) *Steady-state vs. time accurate approaches.*

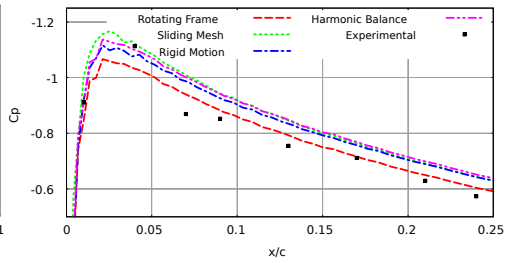

(f) *Region around the leading-edge.*

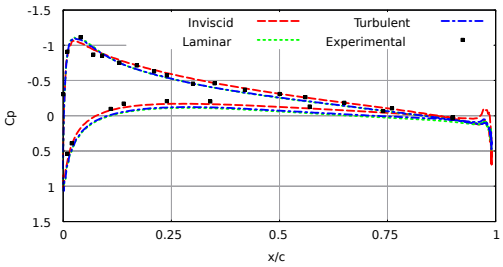

(g) *Inviscid, laminar and turbulent-SA.*

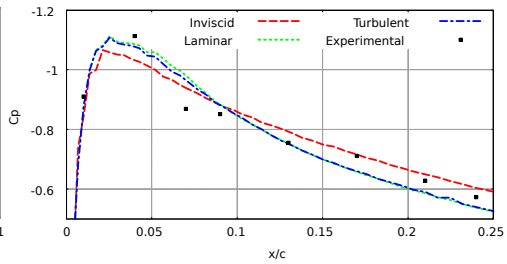

(h) *Region around the leading-edge.*

Figure 4.5: *Comparison of different influential parameters on the performance prediction during hover. Pressure distributions shown at $r/R = 0.80\%$ and compared against measured data taken from Caradonna-Tung [183].*

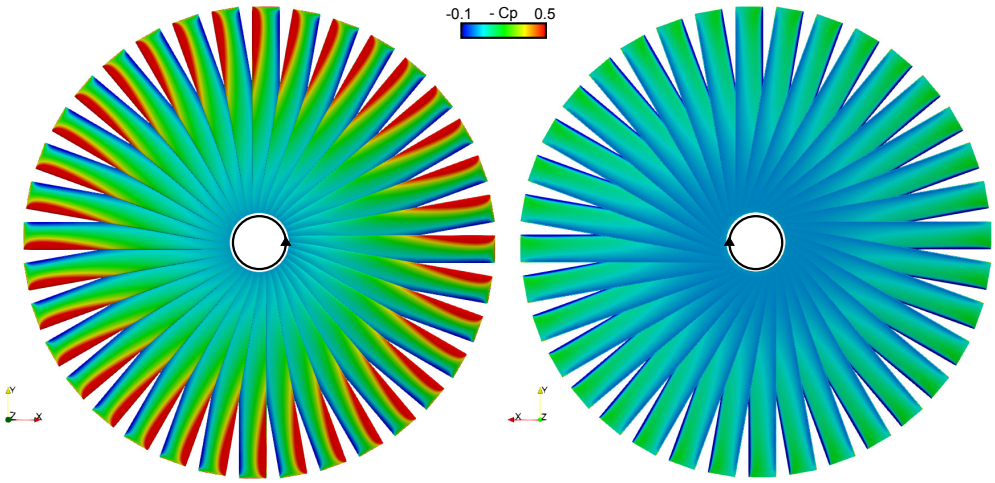

(a) *Unsteady rigid motion at* 10° *azimuth increments.*

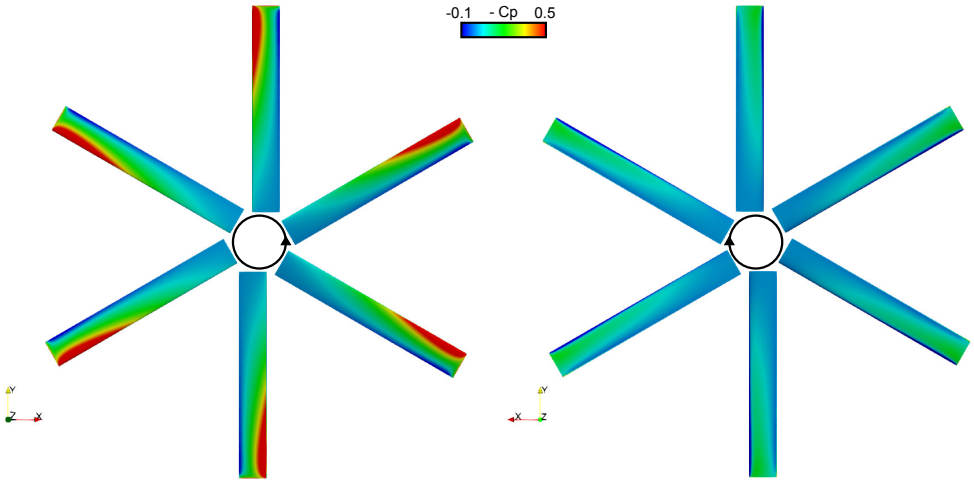

(b) *Harmonic balance at 3 time instances with the input frequencies of* $\boldsymbol{\omega} = (0, \pm\omega_1)$.

Figure 4.6: *Contour maps of the pressure coefficient on the upper and lower blade surface during hover. Comparing the reduced order harmonic balance method against a fully time-accurate method.*

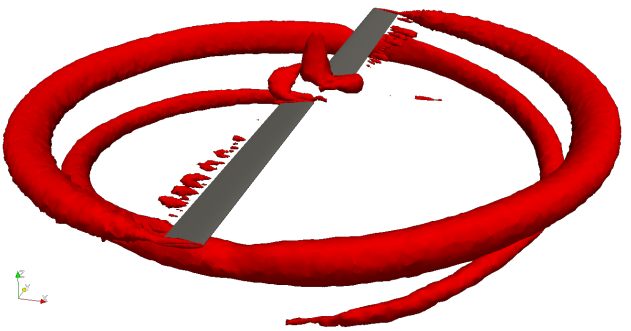

Figure 4.7: *Iso-surface of the Q-criterion visualizing the near-field wake and blade tip vortices as they are convected downstream in the wake of the rotor during hover.*

4.4.2 Forward Flight

The extensive report and data survey from Cross and Watts on tip aerodynamics and acoustics [184] is used for forward flight performance validation. The report describes the Tip Aerodynamic and Acoustics Tests (TAAT) carried out at the NASA Ames Research Center. The TAAT used a highly instrumented AH-1G cobra helicopter and measured the rotor airloads at multiple radial locations. The AH-1G is a two-person single-engine helicopter. It has a two-bladed teetering rotor. The blades are untapered and have a linear twist of $-10°$ from root to tip. The rotor radius is $6.71\,\mathrm{m}$ and the blade chord is $0.686\,\mathrm{m}$ resulting in an aspect ratio of 9.8. The profile of the blades use a symmetric highly modified 540 airfoil section stemming from the NACA0012 family. In the aerodynamics phase of testing several specific thrust coefficients, tip Mach numbers, and advance ratios were flown to study the correlation between these parameters and the pressure distributions.

The flight tests chosen for the present validation work are detailed in Table 4.2. Two subsets of the flight tests are used. The first being a low-speed test which correlates to counter number 2157 from the database and the second being a high-speed test which correlates to counter number 2152 from the database. During the $150\,\mathrm{km\,h^{-1}}$ low-speed test the rotor is operated at a tip Mach number of 0.65 and an advance ratio of 0.19. The collective pitch of $11.7°$ is set to be congenial with the measured rotor thrust of $C_T = 0.00464$ and the cyclic pitch is trimmed to eliminate pitching and rolling moments. The sine and cosine cyclic pitch angles are respectively set to $1.7°$ and $-5.5°$. The sine and cosine cyclic flap angles are respectively set to $-0.15°$ and $2.13°$. During the $290\,\mathrm{km\,h^{-1}}$ high-speed test the rotor is operated at a tip Mach number of 0.64 and an advance ratio of 0.24. The collective pitch of $18.0°$ is set to be congenial with the measured rotor thrust of $C_T = 0.00464$ and the cyclic pitch is trimmed to eliminate pitching and rolling moments. The sine and cosine cyclic pitch angles are respectively set to 3.6 and -11.8. The sine and cosine cyclic flap angles are respectively set to 1.11 and 2.13.

Table 4.2: *Forward flight tests taken from the TAAT data survey [184].*

Variable	Low Speed Counter 2157	High Speed Counter 2152
V_∞	$150\,\mathrm{km\,h^{-1}}$	$290\,\mathrm{km\,h^{-1}}$
M_∞	0.12	0.24
M_T	0.65	0.64
Re_T	9.7×10^6	10.2×10^6
μ	0.19	0.38
θ_0	$11.7°$	$18.0°$
$\theta_{0.75}$	$5.7°$	$12.0°$
θ_s	$1.7°$	$3.6°$
θ_c	$-5.5°$	$-11.8°$
β_0	$2.75°$	$2.75°$
β_c	$2.13°$	$2.13°$
β_s	$-0.15°$	$1.11°$
C_T	0.00464	0.00474

The spatial discretization is achieved using a single-zone mesh of the two main rotor blades. The outer far-field is placed 5 radii away from the blades. A mixed-element grid composed of 30.25×10^6 elements and 760×10^3 nodes is used. Each blade has 105×10^3 surface elements. A density region surrounding the rotor blades is used to sufficiently resolve the near-field wake. Elements within the density region have a maximum element size of $0.0075\,x/c$.

The standard one-equation SA turbulence model is used with the RANS equations. The SA turbulence variable is convected using a first-order scalar upwind method. The convective fluxes are computed using the Roe scheme and second-order accuracy is achieved using the MUSCL scheme. Spatial gradients are approximated using the Green-Guass numerical method. The flow solution was considered converged when there was a reduction of 6 orders of magnitude on the density residual. Per rotor revolution, there are 360 physical time-steps equating to 1° azimuth increments. At each physical time-step, there are a maximum of 30 internal pseudo time-steps. Each simulation was run for a total of 5 rotor revolutions corresponding to 1800 physical time steps.

The blade motion is prescribed using the implementation introduced in Section 4.3.5 with the values outlined in Table 4.2. The mesh is updated at each physical time-step using the RBF mesh deformation strategy. Multi-level surface point reduction and volume point reduction algorithms are used to improve the efficiency. Four levels are employed with the surface point selection error reduction rates and efficiency being shown in Fig. 4.8. It shows that the multi-level method for updating the blade position is highly effective in minimizing the computational cost while simultaneously reducing the surface error. The control points and associated normalized surface error of the computed displacement at each level are shown in Fig. 4.9. The minimum orthogonality angle of the grid prior to deformation was 40.979°. The minimum orthogonality angle of the grid post 1800 deformations is 40.997°. This indicates there is no detrimental effect on the grid quality from the continuous deformation.

The pressure coefficient distributions at selected advancing and retreating azimuth positions as well as radial locations are obtained from the data survey and are used for validation. The low-speed test uses data at $r/R = 0.60$ for the advancing side of the rotor at azimuth angles $\psi = 30^\circ$, $\psi = 90^\circ$, and $\psi = 180^\circ$ with the results being shown in Fig. 4.10. Data at $r/R = 0.91$ on the retreating side of the rotor at azimuth angles $\psi = 270^\circ$, $\psi = 285^\circ$, and $\psi = 300^\circ$ are also used and the results are shown in Fig. 4.11. In general, the trends are relatively well captured when compared against the measured data. On the advancing side of the rotor, the suction peak is marginally over-exaggerated. On the retreating side of the rotor, the prediction of the suction is improved slightly. Additionally, the numerical predictions of SU2 are compared to the code from the Korea Advanced Institute of Science and Technology (KAIST) [185]. The code-to-code comparison shows that the results on the advancing side of the rotor are in good agreement, while on the retreating side slight discrepancies arise.

The high-speed test uses data at $r/R = 0.86$ for the advancing side of the rotor at azimuth angles $\psi = 70^\circ$, $\psi = 90^\circ$, and $\psi = 110^\circ$ with the results being shown in Fig. 4.12. Data at $r/R = 0.96$ on the retreating side of the rotor at azimuth angles $\psi = 250^\circ$, $\psi = 270^\circ$, and $\psi = 290^\circ$ are also used and the results are shown in Fig 4.13.

The higher flight speed initiates the presence of shocks on the advancing side of the blade and dynamic stall on the retreating side of the blade which makes replicating the measured data more challenging than in the low-speed test. Consequently there are significantly different pressure coefficient distributions. The suction peaks on the upper surface of the blade on the advancing side of the rotor are represented well. However, the shock positions show discrepancies when compared to the measured data. The pressure coefficient distributions on the retreating side of the blade close to the blade-tip appear to be better represented.

The normal force coefficient predictions as a function of the azimuth angle at radial locations $r/R = 0.75$ and $r/R = 0.86$ are shown in Figs. 4.14 & 4.15. The low-speed predictions are displayed in Fig. 4.14 and closely resemble the experimental measurements. The high-speed predictions are displayed in Fig. 4.15 and display larger discrepancies to the measured data. The rotor normal force coefficient distribution provides an effective metric for assessing the rotor performance during forward-flight. Furthermore, the predictions are compared to the FLOWer code from DRL with the results being taken from Ref. [186]. The comparison highlights the challenge associated with the prediction of the high-speed test conditions.

A contour map of the pressure coefficient on the upper surface of the blades for both the low- and high-speed tests are shown in Fig. 4.16. Both sets of results show that the pressure coefficient during forward flight is no longer axisymmetric about the out-of-plane axis. To achieve the higher flight speed an increase in the collective pitch is required. However, this results in a low speed stalled region on the retreating side of the rotor near the blade root where there is a high angle-of-attack. This effect can be seen in Fig. 4.16b which is not present in Fig. 4.16a.

The iso-surface of the Q-criterion visualizing the near-field wake and blade tip vortices is shown in Fig. 4.17. It displays the different flow field behaviour in low-speed and high-speed forward flight. In low-speed forward flight, the vortex upstream of the preceding blade passes below the advancing blade close to the tip. Due to the low flight speed, the vortex downstream remains close to the rotor blades. In high-speed forward flight the vortex upstream of the preceding blade passes below the advancing blade closer to the root of the blade. With the flight speed being much higher the vortex downstream is no longer in the vicinity of the rotor blades. Due to both cases being straight and level flight there are no blade-vortex interactions present. It is of note that even with a density region and such a large grid that it is challenging to reduce artificial numerical dissipation of the blade tip vortices.

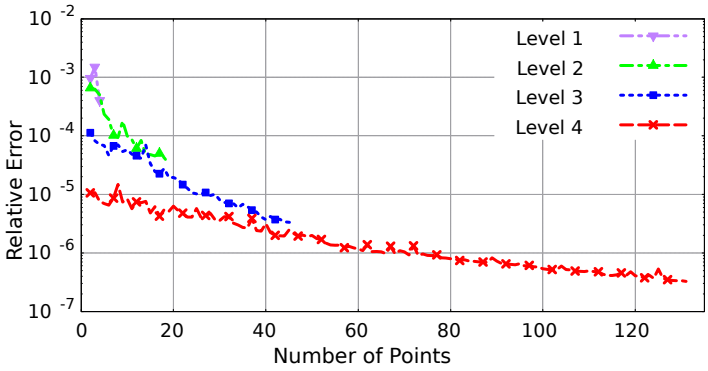

Figure 4.8: *Multi-level greedy surface point selection error reduction rates for a single deformation on the AH-1G rotor during forward flight.*

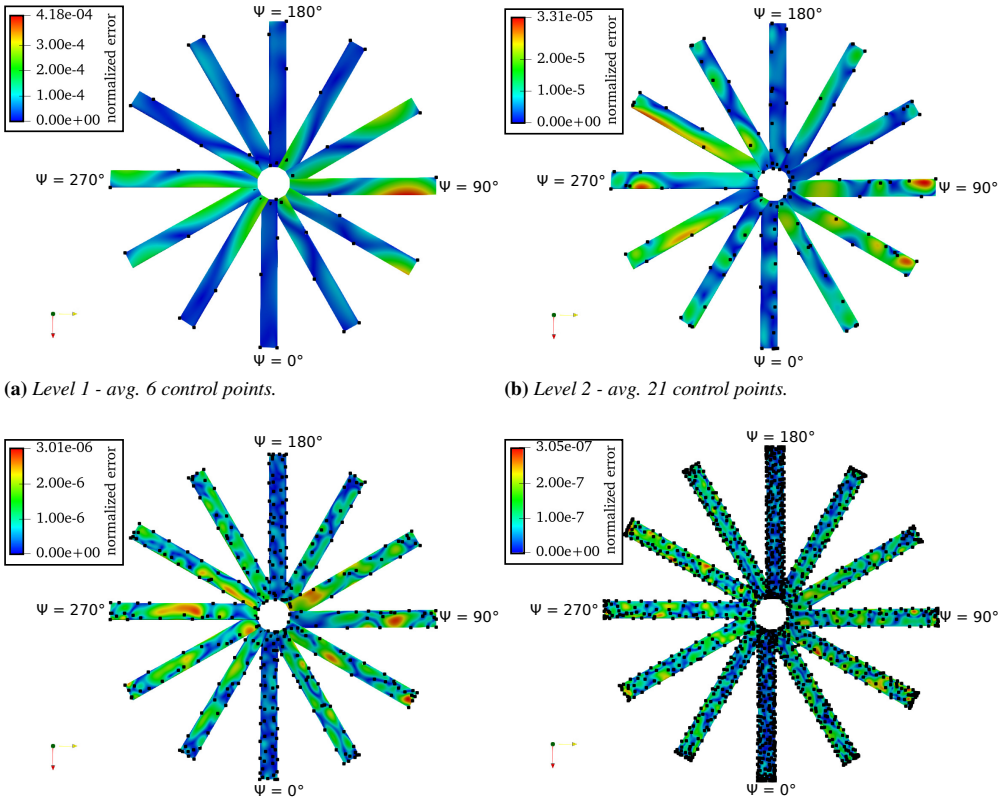

(a) *Level 1 - avg. 6 control points.*

(b) *Level 2 - avg. 21 control points.*

(c) *Level 3 - avg. 42 control points.*

(d) *Level 4 - avg. 136 control points.*

Figure 4.9: *Evolution of the multi-level greedy surface point selection algorithm used for the RBF mesh deformation. Displaying the control points as black dots and the contours of the normalized surface error displacement. Where the normalized error is computed as the difference between the computed displacement and the actual displacement.*

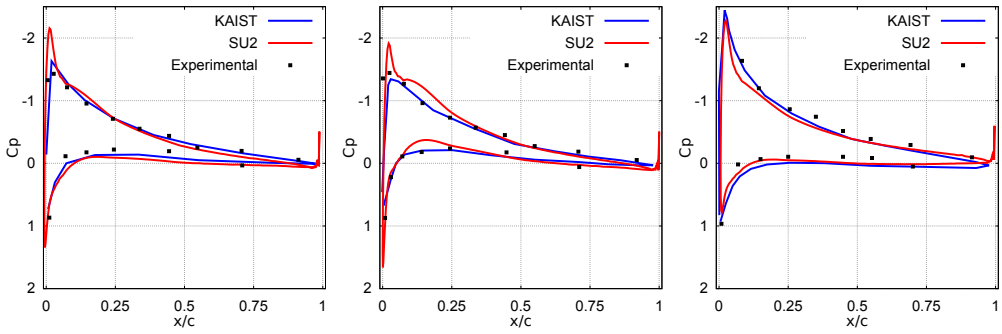

(a) $\psi = 30^{\circ}$. **(b)** $\psi = 90^{\circ}$. **(c)** $\psi = 180^{\circ}$.

Figure 4.10: *Pressure distributions at $r/R = 0.60$ on the advancing side of the rotor during low-speed forward flight. Predictions compared against the measured data taken from the TAAT [184] and the code from the Korea Advanced Institute of Science and Technology (KAIST) [185].*

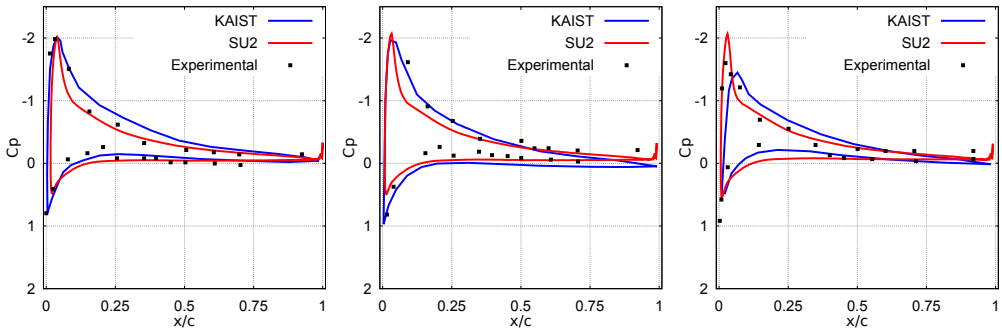

(a) $\psi = 270^{\circ}$. **(b)** $\psi = 285^{\circ}$. **(c)** $\psi = 300^{\circ}$.

Figure 4.11: *Pressure distributions at $r/R = 0.91$ on the retreating side of the rotor during low-speed forward flight. Predictions compared against the measured data taken from the TAAT [184] and the code from the Korea Advanced Institute of Science and Technology (KAIST) [185].*

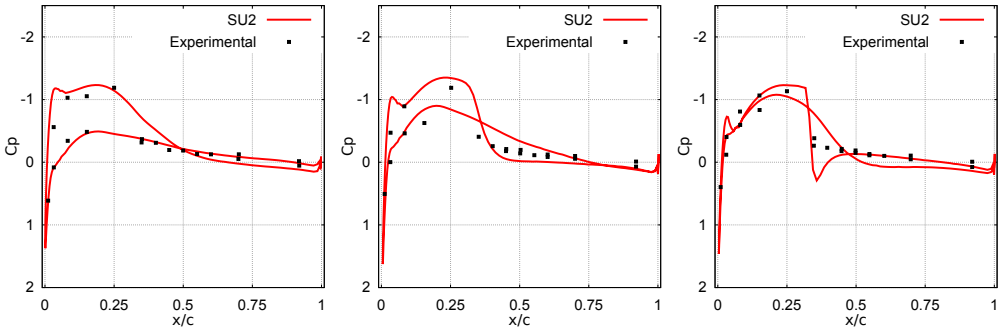

(a) $\psi = 70^{\circ}$. **(b)** $\psi = 90^{\circ}$. **(c)** $\psi = 110^{\circ}$.

Figure 4.12: *Pressure distributions at $r/R = 0.86$ on the advancing side of the rotor during high-speed forward flight. Predictions compared against the measured data taken from the TAAT [184].*

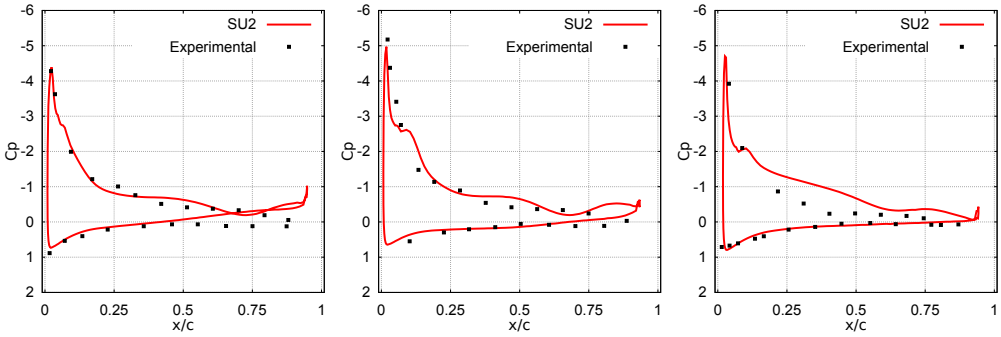

(a) $\psi = 250^{\circ}$. **(b)** $\psi = 270^{\circ}$. **(c)** $\psi = 290^{\circ}$.

Figure 4.13: *Pressure distributions at $r/R = 0.96$ on the advancing side of the rotor during high-speed forward flight. Predictions compared against the measured data taken from the TAAT [184].*

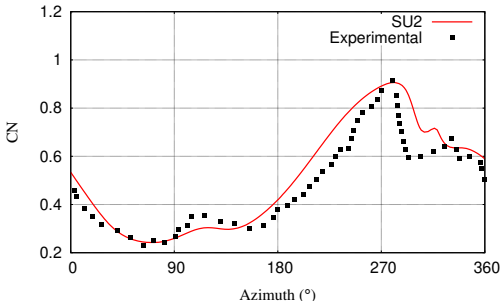

(a) $r/R = 0.75$.

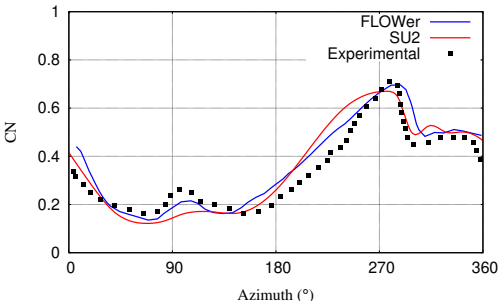

(b) $r/R = 0.86$.

Figure 4.14: *Blade normal force distribution as a function of azimuth angle at* $r/R = 0.75$ *and* $r/R = 0.86$ *during low-speed forward-flight. Predictions compared against the measured data taken from the TAAT [184] and the simulations taken from Ref. [186] based on the FLOWer code.*

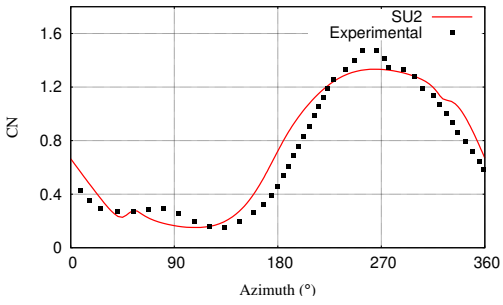

(a) $r/R = 0.75$.

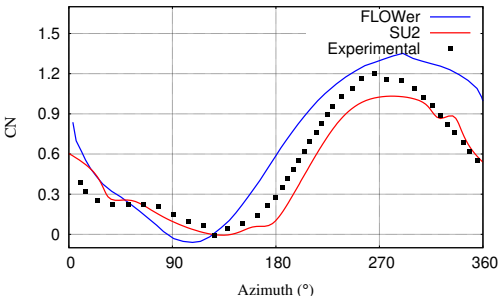

(b) $r/R = 0.86$.

Figure 4.15: *Blade normal force distribution as a function of azimuth angle at* $r/R = 0.75$ *and* $r/R = 0.86$ *during high-speed forward-flight. Predictions compared against the measured data taken from the TAAT [184] and the simulations taken from Ref. [186] based on the FLOWer code.*

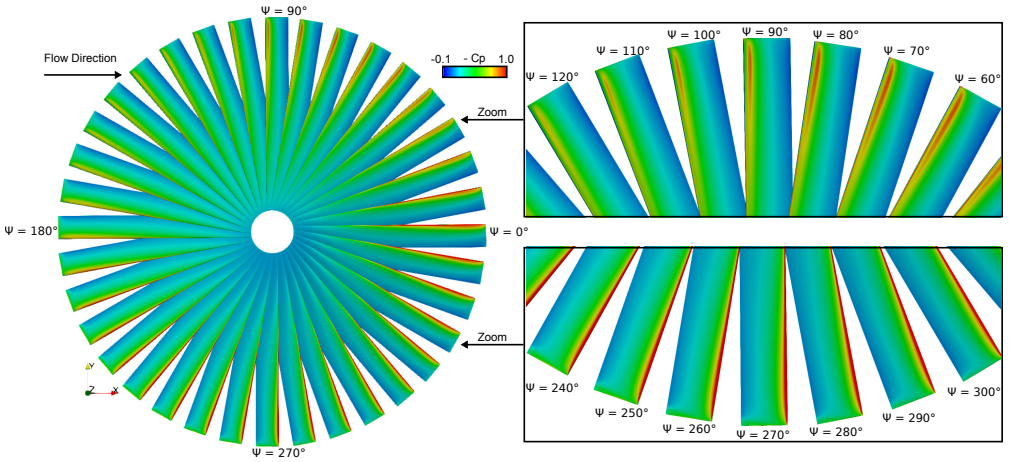

(a) *Low speed forward flight.*

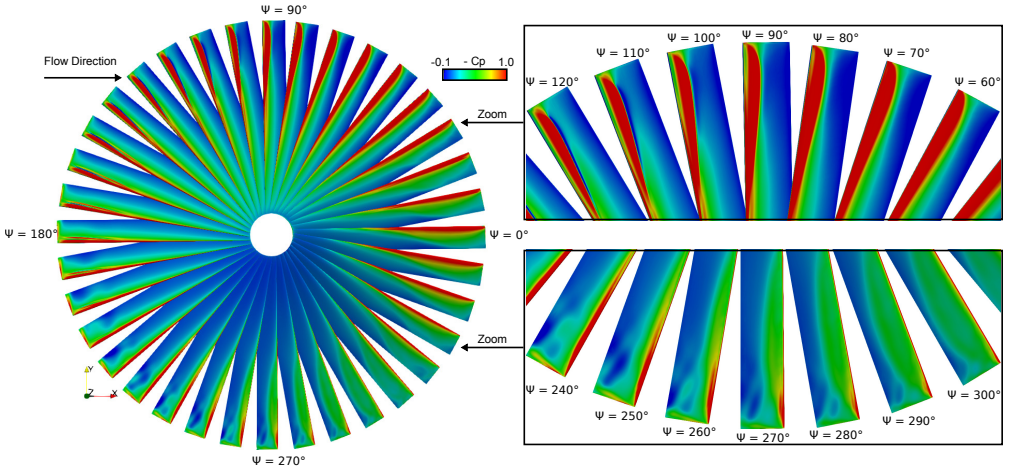

(b) *High speed forward flight.*

Figure 4.16: *Contour maps of the pressure coefficient on the upper blade surface during forward flight. Displaying the both low-speed and high-speed test conditions.*

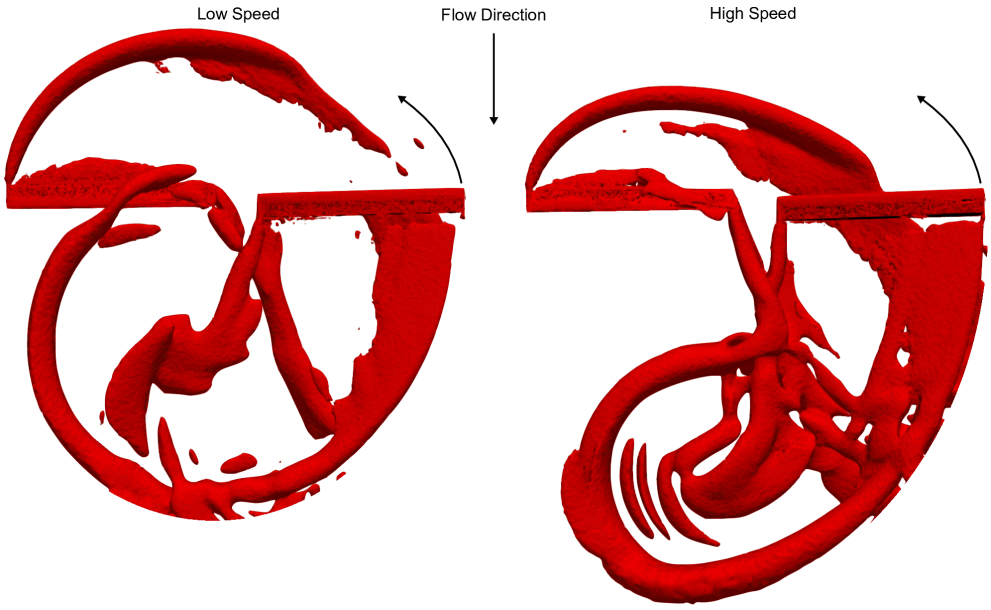

Figure 4.17: *Iso-surface of the Q-criterion visualizing the near-field wake and blade tip vortices. Displaying the different flow field behaviour in low speed and high speed forward flight.*

4.5 Conclusion

This work provides a unique open-source framework for the modelling of rotorcraft aerodynamics in hover and forward flight using the SU2 solver. The performance prediction capabilities are demonstrated on two test cases for preliminary validation. The first test case of the Caradonna-Tung model rotor in hover allowed for the assessment of the pressure coefficient distribution along four different radial positions. Models with varying fidelity ranging from steady-state to fully time-accurate were assessed alongside significant influential parameters. The second test case of the AH-1G rotor in forward flight required the introduction of the blade motion. Low and high speed forward flight tests were modelled. The low-speed test condition was found to be easier to simulate and the performance predictions are in good agreement. The high-speed test condition was more challenging due to the presence of a shock near the blade tip on the advancing side and dynamic stall on the retreating side of the blade near the root.

Accordingly, further validation of SU2 solutions is still needed. Despite the results of this work being mostly favourable compared to the measured data, it is not yet sufficient to suggest this is satisfactory for complete validation of complex rotorcraft flows. It is important that more tests are to be carried out with different configurations and test conditions. Moving forward, likely areas of research will include rotor-fuselage interaction effects, blade design optimization, rotor acoustics, mesh adaptation, and the extension of rigid blades to elastic blades. To that end, to critically assess the supermesh approach for non-conformal boundaries, a wing mounted propeller configuration has been simulated and compared to experimental measurements. The comparison includes wing surface pressure profiles and wake data. This provides further validation of the SU2 code for rotary-wing applications and is shown in Appendix A.

CHAPTER 5

Lagrangian Particle Tracking in Deforming Sliding Mesh For Rotorcraft Icing Applications

The contents of this chapter was presented at:

Morelli, M., Bellosta, T. & Guardone, A., 45^{th} *European Rotorcraft Forum*, paper 146, Warsaw, Poland, September 17–20, 2019.

Abstract

Lagrangian particle tracking in unstructured grids requires the development of efficient and robust point-locating algorithms. In this work, particle in cell techniques are presented to address the issues associated with tracking particles in numerically discretized rotorcraft domains. Two separate issues have been identified. The first issue concerns tracking particles in mesh with arbitrary motion including unsteady deforming mesh. The second issue concerns tracking particles across non-conformal boundary interfaces such as those present in sliding mesh configurations. Subsequently, these techniques are presented with the purpose of simulating the development of clouds containing supercooled water droplets entrained in complex rotorcraft flow systems. These techniques are first described and verified for two-dimensional problems before the results of three-dimensional practical engineering applications are shown. Three main test cases are discussed. The first, an oscillating wing to assess the performance of tracking particles in mesh with arbitrary motion. The second, a two-bladed rotor in hover to assess tracking particles across non-conformal sliding mesh interfaces. The final, a tilt-rotor configuration to assess the point-locating algorithm on a large-scale, industrially relevant problem.

5.1 Introduction

THE numerical discretization of highly complex geometries such as rotorcraft often requires the generation of unstructured multi-zone or structured multi-block grids to ensure a high-quality computational domain. This allows the grid to be split into subregions so moving parts such as helicopter rotor blades can move or deform in relative motion to the fuselage. However, this subsequently results in subregions with non-matching interface boundaries where suitable treatment of the artificially introduced boundaries is pivotal.

One of the most widely used schemes for rotorcraft applications is the Chimera interpolation technique on overlapping grids. In its original formulation, the Chimera scheme is considered non-conservative [187] as it suffers from inaccuracy across interfaces during discontinuities such as shocks waves [188]. To account for this efforts have been made to subsequently improve the Chimera scheme over interface discontinuities [189]. With this recent development on the conservation property of Chimera it can now be considered a conservative scheme by replacing the overlapped zones with patched zones. Different implementations of the Chimera scheme can be found in many rotorcraft CFD codes such as the HMB solver from the University of Glasgow [153], the ROSITA solver from Politecnico di Milano [154], FLOWer from DLR [159], and TURNS from NASA Ames research center [157] as well as many more. Most of the codes are largely based on structured grid topologies.

While Chimera schemes are quite common in rotorcraft codes the contrary is true for schemes such as the sliding mesh technique [190]. A method implemented by Rinaldi et al. [176] presented a scheme for flux-conservation treatment of non-conformal interfaces using the concept of a supermesh which acts as a supplementary interface grid that enables sliding mesh connectivity between mesh interfaces. This sliding mesh technique using the supermesh concept has been implemented into the SU2 solver [164] which is an open-source suite for multi-physics simulation and design based on unstructured meshes [133]. Different sliding mesh techniques have also been implemented in other rotocraft codes such as e.g. HMB [191] and a code from the Korea Advanced Institute of Science and Technology by Nam et al. [192].

The next crucial problem for in-flight icing simulations is the computation of the trajectories of the supercooled water droplets within the computational domain. Two possible frameworks can be adopted: the Eulerian frame of reference and the Lagrangian frame of reference. In the Eulerian approach, the particle phase is considered as a continua whose dynamics is described by a system of partial differential equations. An advantage of this is that it allows the use of standard numerical tools already available for aerodynamics. In the Lagrangian approach, the particle phase is described using a discrete particle method and the balance of forces acting on each discrete particle is resolved. The Lagrangian approach is thus advantageous as it better resembles the particle physics. However, it soon becomes computationally expensive when modelling a large quantity of particles.

In this work, the Lagrangian method is used to compute the particle trajectories. The following system of ordinary differential equations is used to compute the particle positions:

$$\begin{cases} \dfrac{d\mathbf{u}_p}{dt} = \dfrac{3}{4}\dfrac{\mu_f Re_p C_D}{\rho_p d_p^2}(\mathbf{u}_f - \mathbf{u}_p) + \mathbf{g}\left(1 - \dfrac{\rho_f}{\rho_p}\right) \\ \dfrac{d\mathbf{x}_p}{dt} = \mathbf{u}_p \end{cases} \tag{5.1}$$

where the subscripts p and f are representative of the particle and fluid. Additionally, μ, ρ, and $\mathbf{u}$ denote the gas viscosity, density and velocity at the particle position, $\mathbf{x}_p$. The gravity vector is given by $\mathbf{g}$. While the diameter of each particle is represented by d. Finally, the particle drag coefficient and Reynolds number can respectively be described by C_D and Re. An assumption is that only the aerodynamic drag, gravity and particle inertia influence the particle trajectory. Although effects including particle-particle interactions and deformable particles may also influence the final trajectory they are currently not considered.

The particle Reynolds number describes the relative flow around the particle. The drag force acting on any given particle is a combination of the models from Morrison [193] and Clift et al. [194] to best fit experimental data and is given by,

$$C_D = \begin{cases} \dfrac{24}{Re_p} + 2.6\dfrac{\frac{Re_p}{5}}{1+\left(\frac{Re_p}{5}\right)^{1.52}} + 0.411\dfrac{\left(\frac{Re_p}{263000}\right)^{-7.94}}{1+\left(\frac{Re_p}{263000}\right)^{-8}} + 0.25\dfrac{\frac{Re_p}{10^6}}{1+\frac{Re_p}{10^6}} & Re_p \leq 10^6 \\ 0.19 - \dfrac{8\cdot 10^4}{Re_p} + \delta & Re_p > 10^6 \end{cases} \tag{5.2}$$

In order to solve the above equations the position of the particle relative to the mesh is needed. In the case of regular structured grids, the problem can be solved relatively easily, however, for applications where unstructured grids are required the design of efficient point-locating algorithms becomes a challenging task [195]. Many papers in the literature have discussed this matter [196–198]. However, to the authors knowledge what is lacking in all of these algorithms are methods for the treatment of non-conformal boundary interfaces such as those present in sliding mesh and Chimera techniques, as well as, methods to account for deforming mesh. For complex rotorcraft configurations, commonly with multiple non-conformal interface boundaries and deforming mesh, Lagrangian particle tracking soon becomes problematic. With no interface treatment particles, are unable to move across boundary interfaces from one zone to another, and, with no deforming mesh consideration, particles are easily lost.

The purpose of this chapter is to present new Lagrangian based particle tracking methods for 1) arbitrary grid motion, such as, through deforming or rigidly moving grids; and 2) non-conformal interfaces, such as, multi-zone sliding mesh. The method to account for the arbitrary mesh motion will first be discussed in Section 5.2. The method to account for the non-conformal interfaces will then be discussed in Section 5.3. In Section 5.4, three-dimensional tests representative of more realistic engineering problems will then be introduced. These test cases will include; a wing during pitching motion, an isolated rotor in hover, and a tilt-rotor configuration in aeroplane mode. In this work the flow field will be computed using the SU2 solver [133]. The particle tracking will then be performed using an in-house particle tracking code [199].

5.2 Arbitrary Mesh Motion

In rotorcraft applications, it is frequently a requirement that grids are able to independently move and deform to account for the movement of the rotating blades and flexible structures. The main rotor of a conventional helicopter, for instance, moves in relative motion to the fuselage, whilst in forward flight, the blades are also flapping and pitching to eliminate rolling moments and generate lift. The SU2 solver allows for rigid grid rotations as well as surface and volumetric mesh deformation which makes simulating challenging geometries possible.

In our in-house Lagrangian particle tracking software for an unsteady flow field in a stationary mesh, the particles equations of motion are integrated between two flow solution time-steps and tracked using the known-vicinity algorithm described in Bellosta [199]. The solution remains constant until the particle time reaches the next flow time-step. Within this work, we extend this procedure to moving mesh problems, which require the mesh to be updated with the solution. After the update, the particles must be reassigned to new mesh elements. Moreover, during the mesh displacement, some particles may end up outside the computational domain or intersect a boundary multiple times meaning it may renter the computational domain. Each of these issues does not allow for the accurate computation of the particle impingement on the boundary, which is crucial for accurately modelling ice accretion.

In order to avoid the aforementioned issues, we account for the mesh displacement as we track the particles. The particle displacement and the grid displacement are combined to give the displacement of the particle relative to the grid as shown in Fig. 5.1. This particles relative motion, $\mathbf{x}_{\text{relative}}$ can be expressed as,

$$\mathbf{x}_{\text{relative}} = \mathbf{x}_p - \mathbf{x}_{\text{grid}} \tag{5.3}$$

The new relative particle position can then be obtained using a forward Euler integration scheme which can be iteratively solved and expressed as,

$$\begin{cases} \mathbf{u}_p^{n+1} = \mathbf{u}_p^n + f(\mathbf{u}_p^n, \mathbf{x}_p^n)\Delta t \\ \mathbf{x}_p^{n+1} = \mathbf{x}_p^n + \mathbf{u}_p^{n+1}\Delta t \; \underbrace{- \mathbf{u}_{\text{grid}}\Delta t}_{\text{grid motion}} \end{cases} \tag{5.4}$$

where the function f is the right hand side of the velocity equation reported in equation 5.1 and $\mathbf{u}_{\text{grid}}$ is the grid velocity at the particle position. Using this approach arbitrary mesh motion can be accounted, while the only information needed is the grid velocity in equation (5.4).

When the next flow time step is reached the new mesh and solution can be loaded and the new grid velocity obtained. Since the particles were tracked within a relative frame of reference they already occupy the correct relative position in the new mesh. To then recover the absolute position in the new mesh, the position is updated using shape functions. This is done through inverting the shape functions of the elements of the old mesh to evaluate the positions in the new mesh as described below,

$$\boldsymbol{\xi} = \mathbb{I}_o^{-1}(\mathbf{x}_o) \quad \rightarrow \quad \mathbf{x}_n = \mathbb{I}_n(\boldsymbol{\xi}) \tag{5.5}$$

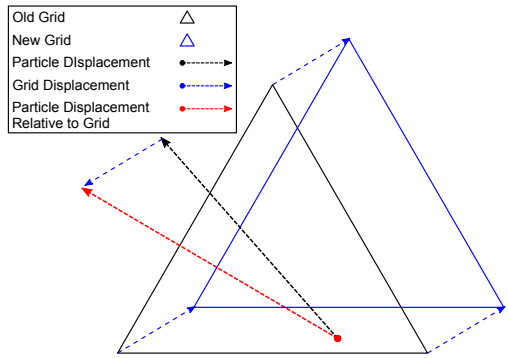

Figure 5.1: *Schematic showing the particles relative displacement within a 2-dimensional triangle.*

where the subscripts o and n refer to the old and new mesh respectively and $\mathbb{I}$ is the function that maps the local element coordinate $\boldsymbol{\xi}$ to the global position $\mathbf{x}$. The overall process described can be summarized in Fig. 5.2.

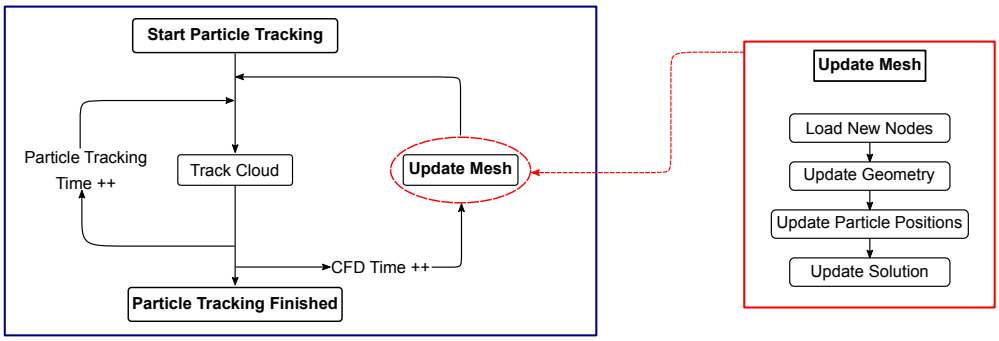

Figure 5.2: *Flowchart displaying the process for particle tracking simulations in moving mesh.*

An attempt to verify the process of tracking particles in mesh with arbitrary motion is hereinafter outlined. If one considers two identical mesh in which an airfoil is undergoing pitching motion. The first mesh achieves the pitching motion by deforming the mesh, while the second mesh achieves the pitching motion by rigidly deforming the entire domain. A schematic illustrating this is shown in Fig. 5.3. Furthermore, it highlights that if one were to overlay the two mesh there would be significant differences in the shape and position of the mesh elements. The particle trajectories within these two domains are then computed and shown overlapping one on top of the other in Fig. 5.4. It indicates that the two results are similar enough so that only the top layer of particles are visible which are contained by the deforming mesh.

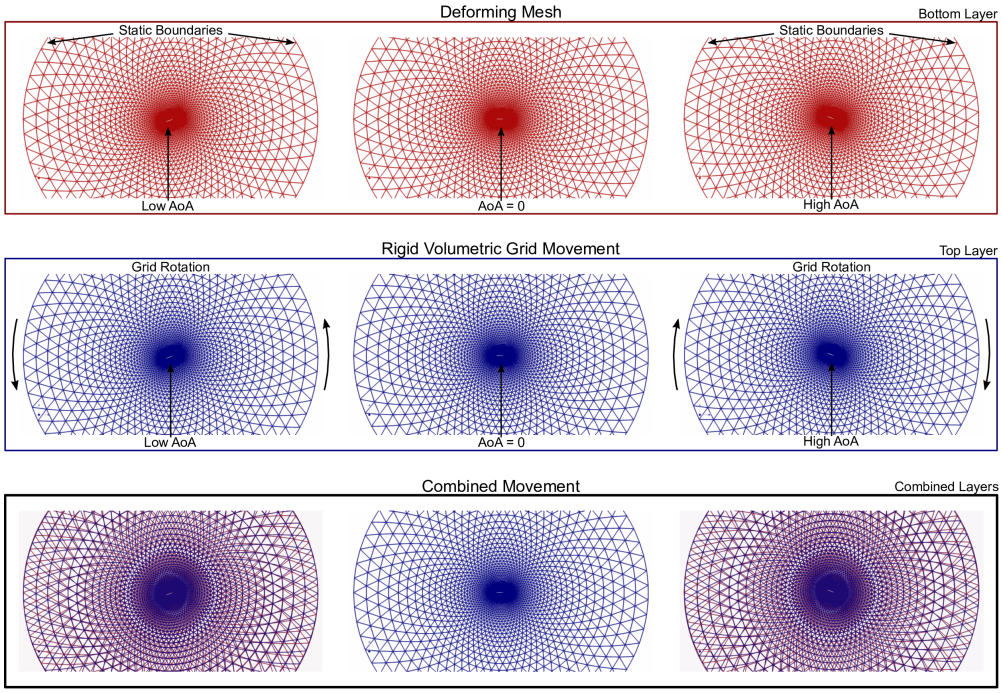

Figure 5.3: *Different kinds of grid movement used to apply motion to an arbitrary object.*

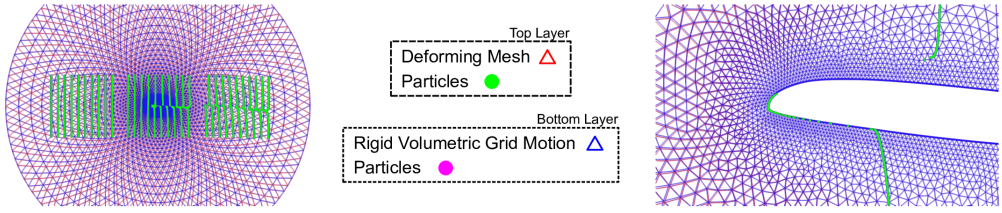

Figure 5.4: *Particle tracking simulation comparing the kind of grid movement. On the left, the particle front is shown at different time steps. On the right, a single time snapshot is shown close to the airfoil.*

5.3 Non-Conformal Interfaces

The support of the supermesh feature within SU2 allows multiple independently moving grids to slide within one another whilst maintaining connectivity between them. Each zone is considered as a separate entity within SU2 where the flow field is subsequently solved and associated with the corresponding zones solution. Different techniques can be used for the interpolation between zone interfaces such as the nearest-neighbour and weight-average approaches. One requirement of the supermesh implementation within SU2 is that there must not be any continuous voids between grids and the interfaces must be complementary.

Once the solution of the flow field is computed the multi-zone particle tracking can start. The process used to implement the multi-zone particle tracking based on the sliding mesh scheme is outlined in Fig. 5.5 and will now be discussed. First, each zone's mesh and its corresponding solution is loaded. A cloud is then defined for each of the zones. Within each zone's domain, a cloud of supercooled water droplets is initialized and the fluid data from the zone's solution are applied to the particles. The cloud is then updated as the particles are tracked using a forward Euler time integration algorithm until the final simulation time is reached. To ensure a particle travelling along a trajectory crossing a boundary interface can communicate from one zone to another and does not simply stop at the intersection, the following method is proposed.

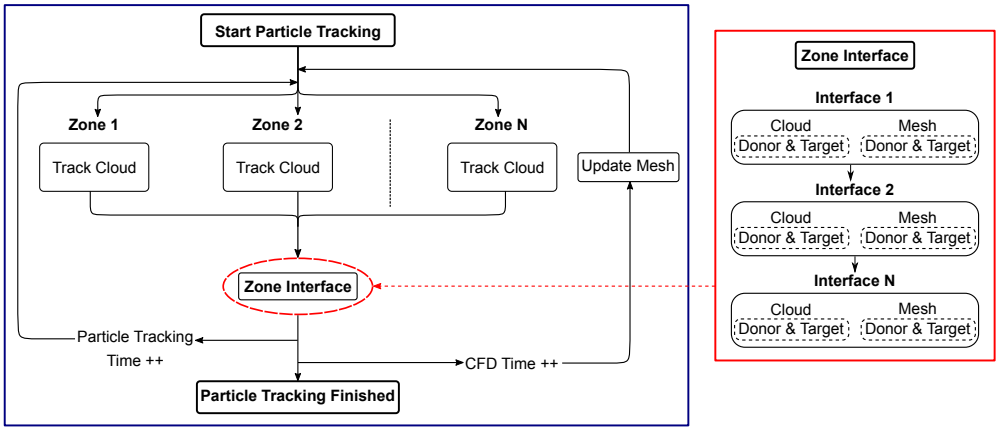

Figure 5.5: *Flowchart displaying the process for a multi-zone particle tracking simulation. Including the implementation of the boundary interface cloud transfer from donor to target meshes.*

With the known-vicinity algorithm mentioned above the boundaries can easily be identified during intersections. The final position, $\mathbf{x}_p$ of a particle can then be described dependent upon its trajectory and intersections,

$$\mathbf{x}_p = \begin{cases} \mathbf{x}_{\text{intersection}} & \text{boundary intersection} \\ \mathbf{x}_{\text{destination}} & \text{interface intersection} \\ \mathbf{x}_{\text{destination}} & \text{no intersection} \end{cases} \tag{5.6}$$

When a particle impinges on an interface boundary a transfer routine is called to pass the particle onto the neighbouring zone. Inside the interface routine, the particle being transferred over the interface from the donor cloud to the target cloud is assigned within the new target mesh. The donor cloud then consequently loses a particle and the target cloud gains a particle.

The particle is then located in the target mesh where either a brute force or nearest neighbour algorithm is used to find the cell with the closest centroid to speed up the search. Once the cell containing the particle is found, the fluid properties are then assigned to the particle using an inverse distance weighted interpolation. The particle then continues to be tracked in the target mesh for the following time-steps until the simulation time either finishes or another boundary interface intersection occurs in which case the particle is transferred across the next interface into the next target zone.

If however, during the particle transfer from the donor to the target mesh, the particle end position is in a void as it has left the donor mesh but not entered the target mesh due to the non-conformal boundary interfaces that are not overlapping, an additional check is required. In this case, the particle maintains the previous time-steps fluid properties and a semi-adaptive integration time-step is used to ensure that during the following time-step it enters the target mesh. The particle can then inherit the fluid properties of the target mesh cell and again continue to be tracked in the target mesh. The donor or target host, of any particle, $\mathcal{P}$, can thus be described by the following conditions,

$$\mathcal{P} = \begin{cases} \mathcal{P}_{\text{donor}} & \text{boundary intersection} \\ \mathcal{P}_{\text{target}} & \text{interface intersection} \\ \mathcal{P}_{\text{donor}} & \text{in a void} \end{cases} \tag{5.7}$$

This process is shown in the schematic in Fig. 5.6 where it shows the effect of tracking a particle across multiple zones. For clarity, the stationary donor outer mesh is shown in blue whilst the moving target inner mesh is shown in red. Particles contained within the outer zone are shown in pink whilst the particles contained within the inner zone are shown in green. The schematic shows that when accounting for the zone interface a particle can arrive at its final destination whereas when a particle is tracked without accounting for the zone interface remains bound to the edge of the zone interface as if the zone interface represents a boundary wall.

An attempt to verify the process of tracking particles across sliding mesh interfaces is hereinafter outlined. If one considers an airfoil undergoing pitching motion again. However, now the computational domain is decomposed into two separate domains. The internal domain rotates to account for the pitching motion of the airfoil, while the external zone remains stationary. Accordingly, the particle positions are updated in time and tracked as they intersect with the sliding mesh interface as shown in Fig. 5.7. It shows the particles being successfully transferred between donor and target zones and highlights the partition of the cloud at the interface where the two mesh are non-conformal. It features particles in voids which maintain the donor cloud properties without being lost.

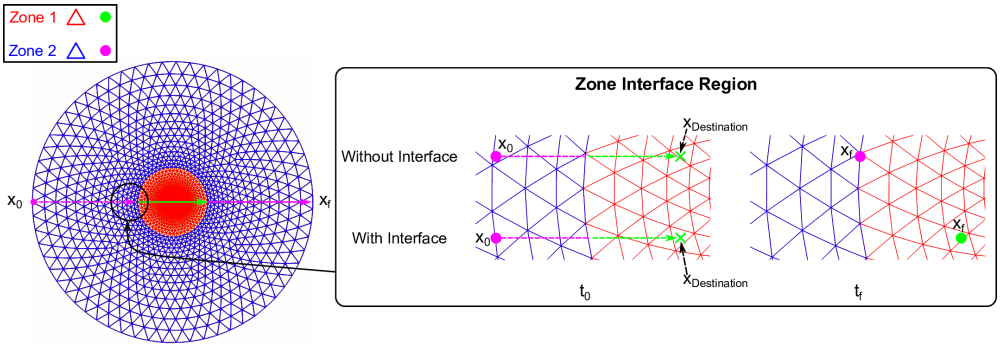

Figure 5.6: *Schematic showing particle tracking across a boundary interface with and without zone interface treatment.*

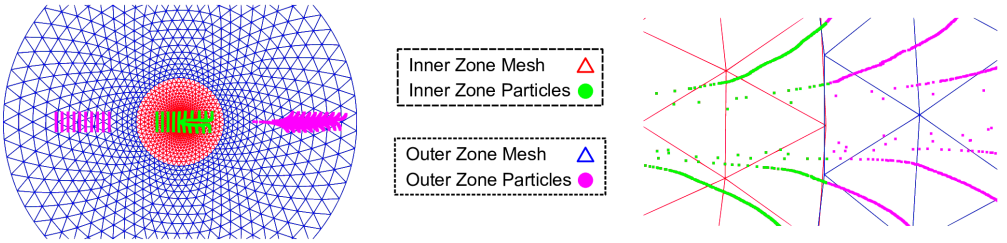

Figure 5.7: *Results of a 2-dimensional pitching airfoil particle tracking simulation showing the multi-zone implementation and passing of particles between donor and target zones. On the left, the particle front is shown at different time steps. On the right, a single snapshot is shown close to the interface.*

5.4 Results

The compressible Euler equations within SU2 are used to represent the flow for the verification of the proposed particle tracking methods in arbitrary mesh motion and across non-conformal interfaces. In distinction from the CFD model which does not account for flow viscosity, the particle equation of motion accounts for viscous effects. In this work, the viscosity is computed locally based on the temperature field available from the CFD solution using Sutherland's law [166]. Three exemplary test cases provide numerical verification. A single-zone grid undergoing mesh deformation is consider in Section 5.4.1, while, two- and three-zone grids of varying complexity experiencing rotation are considered in Section 5.4.2 and 5.4.3. All tests are conducted under unsteady conditions in subsonic flow regimes. In each of the test cases, particulates are initialized upstream in the far-field and traced while entrained in the flow.

5.4.1 Pitching Wing

The first set of computations are performed on a straight untwisted NACA 0012 wing configuration. The wing has a nominal aspect ratio of, $AR = 4$ and has sharp rectangular edges at the wing tips. A low free-stream Mach number of $M_\infty = 0.3$ is specified. The wing is pitching about its quarter-chord axis where the following conditions describe its motion; the mean angle of attack is $\alpha_0 = 8°$, and it experiences $5°$ of oscillation so that the minimum angle of incidence is $\alpha_{min} = 3°$ and its maximum angle of incidence is $\alpha = 13°$. The simulation lasts for six full periods of oscillations.

A fully unstructured mesh is used containing a total of $1\,506\,549$ elements and $269\,383$ nodes. Along each section of the wing surface in the chord-wise direction 300 nodes congregate towards the leading and trailing edge. There are a total of $43\,090$ quad elements on the wing and far-field surface meaning there are $43\,090$ associated pyramid elements in the volume mesh. These pyramid elements are then connected to the remaining tetrahedral volume elements. The far-field is placed 8 chord lengths from the tips of the wing and 10 chord lengths from the leading and trailing edges. The coordinate system is defined so that the free-stream velocity is in the positive x-direction and the pitching motion is along the y-axis whilst z is positive in the upward direction. The single-zone mesh described is shown in Fig. 5.8.

The SU2 software suite [133] is able to solve implicitly unsteady problems using a dual-time stepping strategy, leading to second-order accuracy in time. While a Monotonic Upwind Scheme for Conservation Laws coupled with the Venkatakrishnan limiter is used in the flow equations for second order accuracy. The computation prescribes a non-dimensional time-step $\Delta t U_\infty / c = 0.12$ to provide sufficient temporal resolution. Here U_∞ is the freestream flow velocity and c is the wing chord. This value of Δt corresponds to 100 time-steps per pitching cycle which means 600 instantaneous flow fields are saved for the unsteady particle tracking computations. To account for the motion of the pitching wing the volume mesh is deforming at each time-step. The technique for the volume mesh deformation is based on the linear elasticity analogy. The element stiffness imposed for the mesh deformation is based on the inverse volume so that the mesh deformation mainly occurs in the far-field away from the wing surface. During each deformation, there are 500 internal smoothing iterations and 3 non-linear defor-

mation iterations to maintain the deformed grid quality. The resultant flow field of the pitching wing is shown in Fig. 5.9 where it clearly shows the three-dimensional effects caused by the wing tips as strong vortical structures are present. It also shows that at the center of the wing the flow can also be classified almost entirely as two-dimensional.

Using the method described in Section 5.2 to account for arbitrary mesh motion, the unsteady particle tracking is shown in Fig. 5.10. The particle tracking simulation uses $50\,000$ uniformly distributed supercooled water droplets which are positioned as two cloud fronts upstream in the farfield. The particles have a mean volume diameter of $20\,\mu\mathrm{m}$ and a constant liquid water density of $1\,\mathrm{g/m^3}$. The particles are tracked with an integration time-step of 10^{-5} s for a simulation time of $0.2\,\mathrm{s}$ whilst the mesh is updated 100 times per oscillation. It shows that during the pitching cycle at different time instances the quantity of particles impacted is highly influenced by the angle of attack. At instances of higher angles of attack, the aerodynamic forces are not great enough to exceed the inertial forces of the particles and so more particles impact on the wing. At high angles of attack, there is also slight flow separation causing a small omega-type vortex, which was first described experimentally by Lorber et al. [200] and can be visualized in the trajectories of the particles. The tip vortices are also clearly visible in the particle trajectories as the particles roll up and disperse from the core of the vortex.

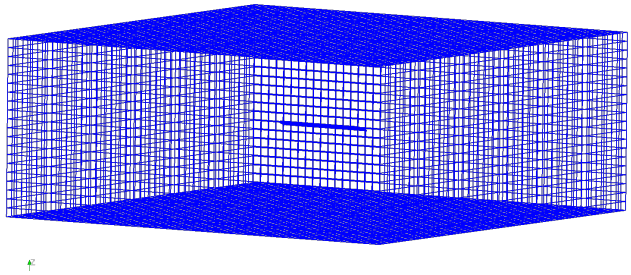

Figure 5.8: *Single-zone mesh containing a wing undergoing pitching motion via mesh deformation.*

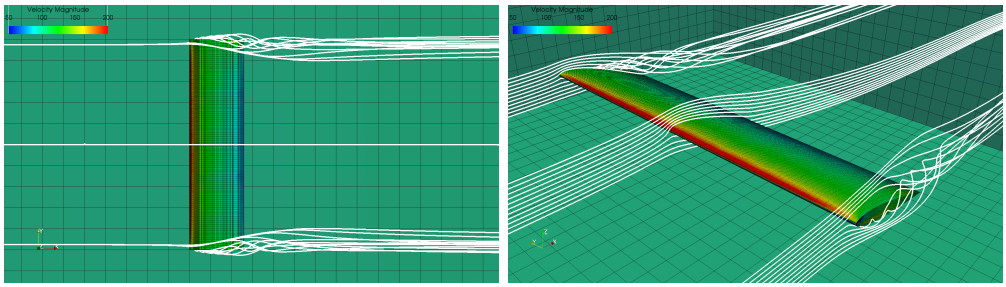

(a) *View from above.* **(b)** *Isometric view.*

Figure 5.9: *Flow field of a wing during pitching motion displaying streamlines at the wing tips and center of the wing. Exhibiting how complex tip vortices roll up in opposite directions.*

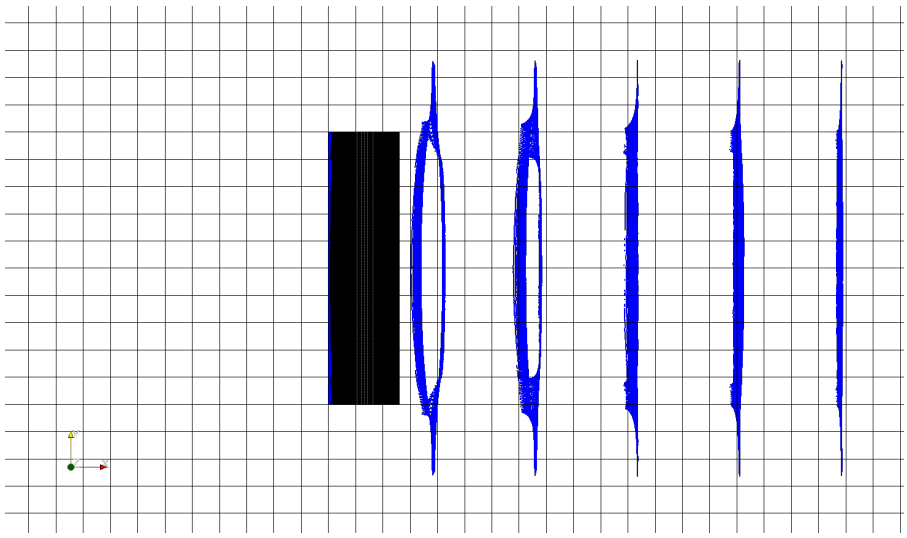

(a) *View from above.*

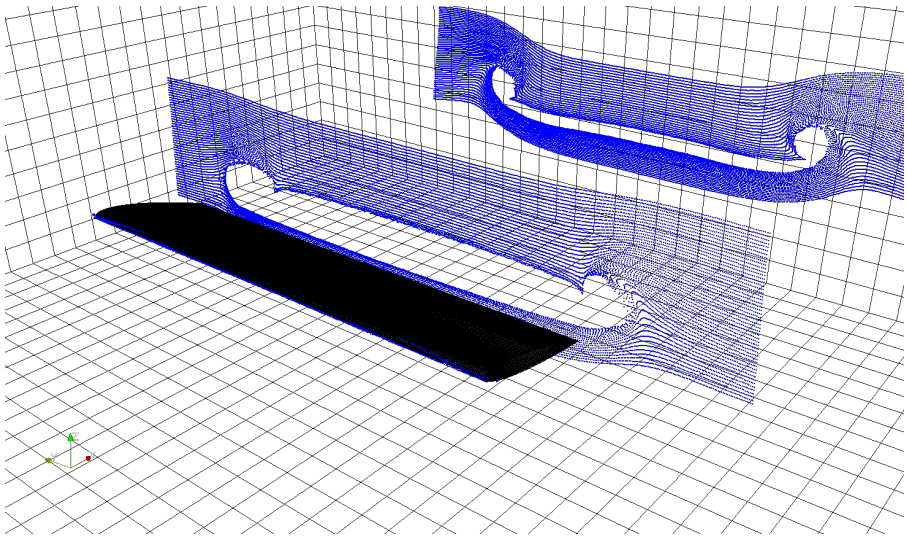

(b) *Isometric view.*

Figure 5.10: *Visualization of particle trajectories over a pitching wing in a deforming mesh. Displaying different time instances at which the particles pass over the wing. The initial front is a planar rectangle.*

5.4.2 Rotor in Hover

The Caradonna and Tung rotor [183] is used for the assessment of the non-conformal interface particle treatment. It is a two-bladed untwisted rotor with a NACA 0012 profile. The experimental rotor has a $1.143\,\mathrm{m}$ radius an aspect ratio of, $AR = 6$. The test conditions used are based on Table 18 from the experiment which consists of a rotor with a collective pitch of $\Theta_c = 8^\circ$, a rotational velocity of $\Omega = 1\,500$ rpm, and consequently a tip Mach number of $M_{tip} = 0.526$. These test conditions were chosen so that the rotor induced velocity would visibly affect the particle trajectories.

A fully unstructured multi-zone mesh is used containing two-zones. The first zone is the stationary background mesh comprising of $237\,015$ elements and $41\,850$ nodes. The external interface – the location at which properties of flow are exchanged between zones – is positioned 0.43 radii from the tips of the rotor blades and has $8\,668$ elements. The far-field is positioned just over 6 radii from the rotor blade tips. The second zone is the moving inner mesh with the embedded rotor blades and comprises of $1\,598\,613$ elements and $283\,434$ nodes. The internal interface is positioned complementary to the external interface and likewise has $8\,668$ elements on the surface. Each of the rotor blades has $23\,024$ elements on the surface. The fluid region contains mainly tetrahedral volume elements. The total number of elements and nodes in the multi-zone grid is $1\,835\,628$ and $325\,284$, respectively. The multi-zone mesh is shown in Fig. 5.11.

The supermesh method described by Rinaldi [176] is used to account for the conservation of fluid properties between the non-conformal boundary interfaces which are present in multi-zone problems. A weight average interpolation between the concentric mesh is used. The resultant flow field of the rotor blades is shown in Fig. 5.12. Here the z-component of the velocity represents the rotor induced velocity and the continuity between the zone solutions is apparent. Fig. 5.12a displays the velocity field in a vertical plane and shows that fluid velocity increases as the fluid passes through the rotor disk plane. The strength of the downward velocity is greatest towards the rotor blade tip. Since no rotor hub has been modelled, there is an upward velocity present at the root cutout. Fig. 5.12b shows the z-component of the velocity in the disk plane of the rotor; the flow field is azimuthally axisymmetric.

Using the method outlined in Section 5.3 for the treatment of non-conformal interfaces, the results of particle tracking through the flow field of a rotor in hover are shown in Fig. 5.13. The particle tracking simulation initializes a singular uniformly distributed cloud of $40\,000$ supercooled water droplets just above the rotor disk interface. The duration of the particle tracking simulation is long enough for 10 full revolutions of the main rotor. The simulation shows that the induced velocity produced by the rotor is significant enough to entrain the particles into and through the rotor disk plane. The particles trail behind and below each blade and are convected through the wake. The particles remain within the wake boundary which separates the quiescent flow from the rotor wake. As the trajectories of the particles progress there is a contraction which represents an increase in the particle velocity. As the particles move further into the free-stream the contrary occurs as the flow begins to dissipate where the grid coarsens. Also as the downwash through the rotor ages, the particles begin to suppress as the induced velocity decreases. Finally, it is possible to visualize the blade passing frequency in the perturbations of the particles as they convect downwards.

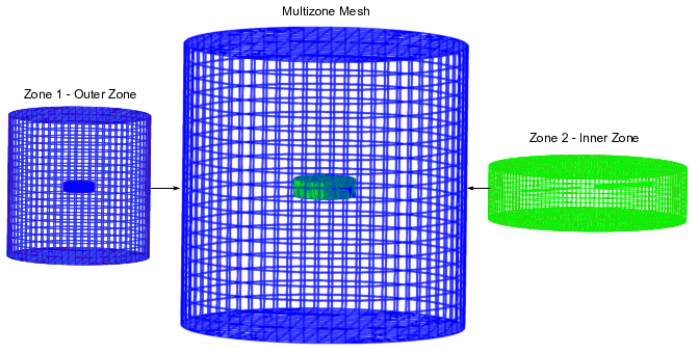

Figure 5.11: *Multi-zone mesh containing a rotor in hover via sliding mesh.*

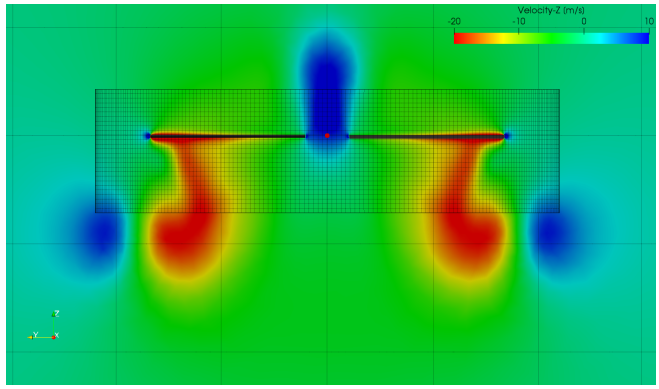

(a) *Diametric plane.*

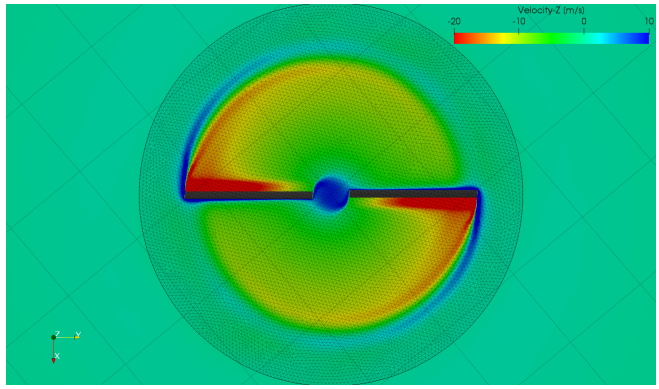

(b) *Disk plane.*

Figure 5.12: *Results of the flow field of a rotor in hover. Displaying the connectivity present between the multi-zone solutions.*

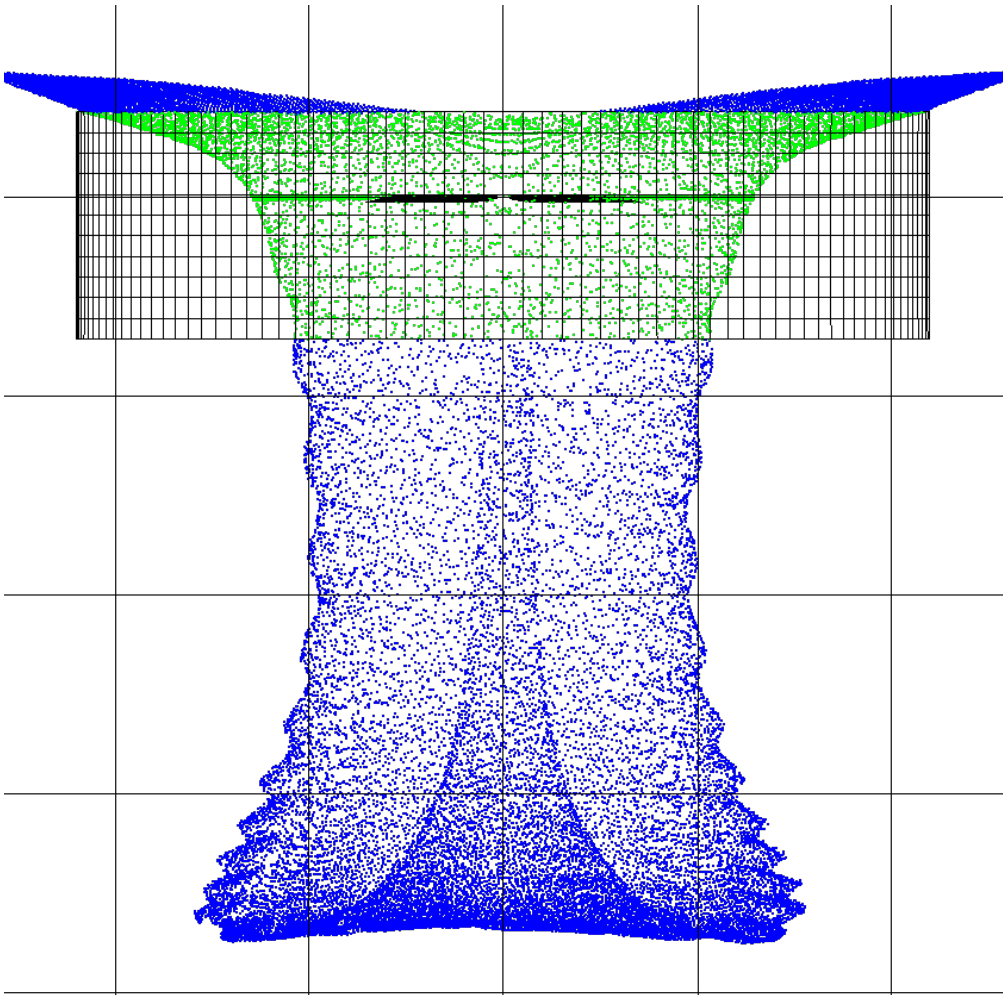

Figure 5.13: *Results of the particle tracking of a rotor in hover. Displaying the connectivity between zones where the particles in the outer zone and inner zone are represented by blue and green respectively.*

5.4.3 Full Tilt-Rotor Configuration

The purpose of this test case is to show the effectiveness of the particle tracking in sliding mesh on a problem of engineering interest and so the tilt-rotor by Leonardo Helicopters in forward flight was chosen due to it being designed for flight in known icing conditions. Since little data for this aircraft can be found in the public domain, the geometry has been approximated. The tilt-rotors main characteristics taken from Malpica [201] are be summarized as follows. Each rotor has 3 blades which have a nominal rotor speed of 569 RPM. The rotor radius is $3.96\,\mathrm{m}$ resulting in a tip speed of Mach 0.695. The blades are non-linearly taped and twisted. The blade twist from root to tip is 47.5° and the rotor solidity is 0.09. The rotor airfoil geometry is based on the Narramore airfoil design [202]. The fuselage geometry is taken from GrabCAD [203] and simplified to allow for unstructured mesh generation. The period of time for this simulation is 6 full blade rotations, where one set of blades rotates in the clockwise direction and the other the counter-clockwise direction to eliminate the moments produced from each of the rotors. The goal here is the demonstration of particle tracking methods for highly complex applications and not for the validation of in-flight icing trails.

A fully unstructured multi-zone mesh is used containing three-zones. The first zone is the stationary background mesh comprising of $6\,410\,004$ elements and $1\,110\,729$ nodes. The fuselage contains $427\,329$ elements. The clockwise and counter-clockwise external interface cutouts contains $32\,012$ elements and the far-field contains $14\,340$ elements. The second zone is the clockwise set of rotor blades comprising of $5\,504\,883$ elements and $980\,020$ nodes. The rotor blades, nacelle and internal interface contain $104\,782$, $13\,586$, and $14\,054$ elements respectively. The third zone is the counter-clockwise set of rotor blades and is identical to the clockwise mesh except for the direction of which the blades rotate. The total size of the three-zone mesh is $17\,419\,770$ elements and $3\,070\,769$ nodes. The multi-zone mesh described is shown in Fig. 5.14.

Once again the supermesh technique is used to account for the non-conformal interfaces due to the multiple zones in the flow field. The resultant flow field computations of the tilt-rotor configuration in aeroplane mode are shown in Fig. 5.15. The velocity magnitude is shown here to display the combined contributions of the two rotors and the fuselage on the flow field. It portrays how the rotor wake directly influences and disturbs the flow over the wing and nacelle. The rotor blades highly twisted geometric nature allows them to efficiently operate in both hover and forward flight, however, the associated flow physics is very complex. It appears that due to the highly twisted root and negatively twisted tip, the largest forward propelling force is produced around 70% along the radius of the blades.

Using the method discussed in Section 5.3 for the treatment of non-conformal interfaces, the particle tracking results of the tilt-rotor while in aeroplane mode are shown in Fig. 5.16. The particle tracking simulation initializes $40\,000$ uniformly distributed supercooled water droplet particles upstream of the aircraft. The particle tracking simulation lasts for 6 full revolutions of the rotor blades to ensure the particles are entrained past the aircraft. The deformation of the particle trajectories is quite large. As the particles transfer from the outer stationary zone into the moving internal zones, they interact with the rotor blades and significantly increase their relative motion. These particles

then enter the wake of the rotor ahead of the main front of particles. The particles which are slowed by the fuselage, wing, nacelle, and tail of the aircraft appear aft of the main front of particles. The location with the highest collection efficiency, by a large margin, is the rotor blades which for flight in icing conditions is concerning.

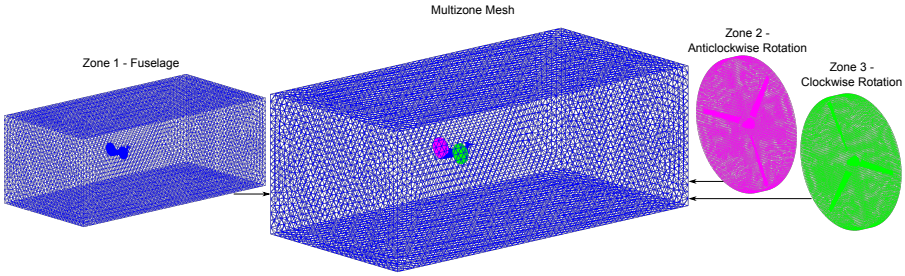

Figure 5.14: *Multi-zone mesh containing a tilt-rotor configuration in forward flight via sliding mesh.*

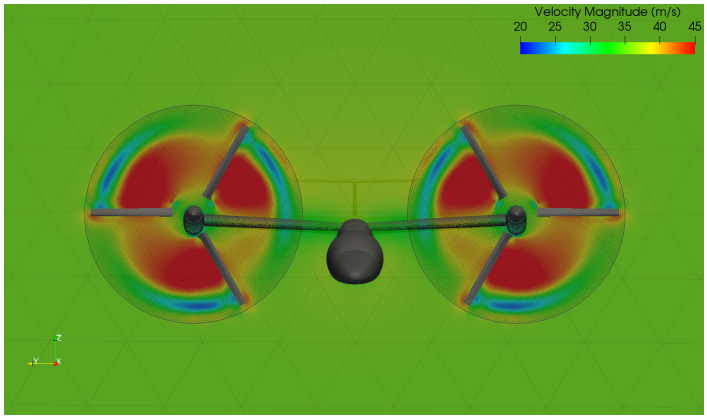

(a) *Cross section through the disk plane.*

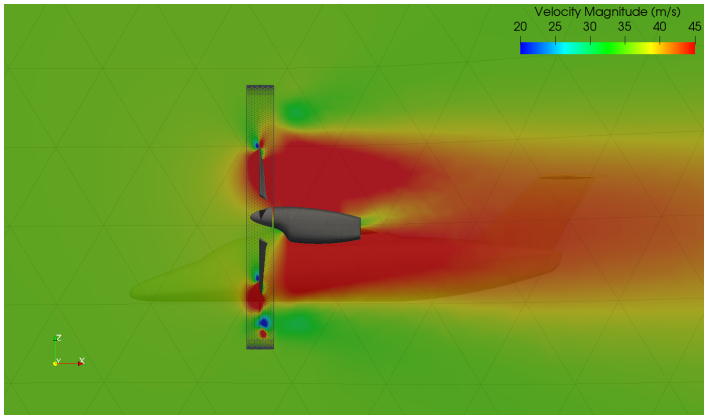

(b) *Cross section through the rotor, wing and nacelle.*

Figure 5.15: *Results of the flow field of a tilt-rotor configuration in aeroplane mode. Displaying the solution continuity between the rotating zones and the stationary zone.*

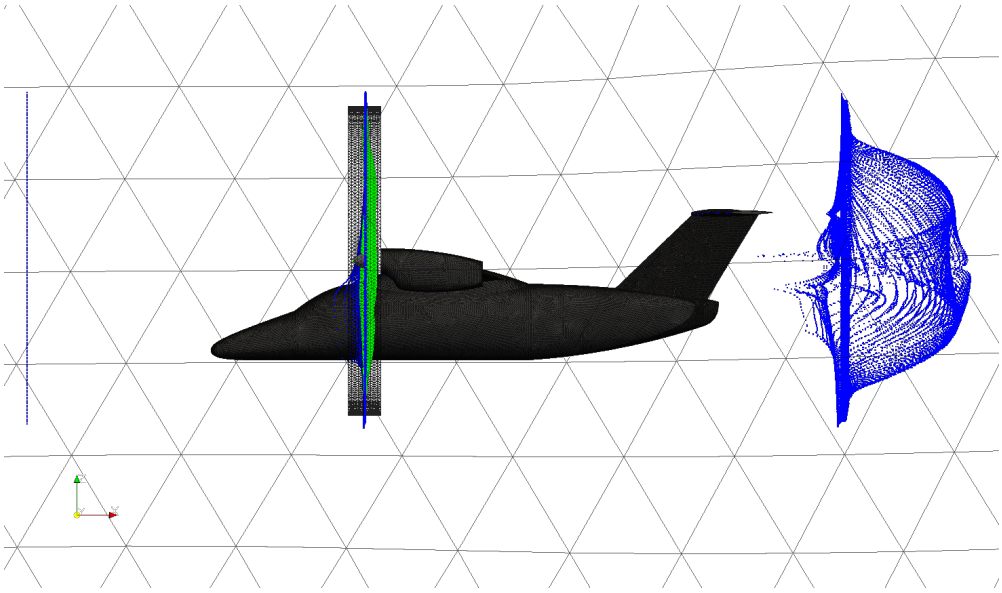

(a) *View from above.*

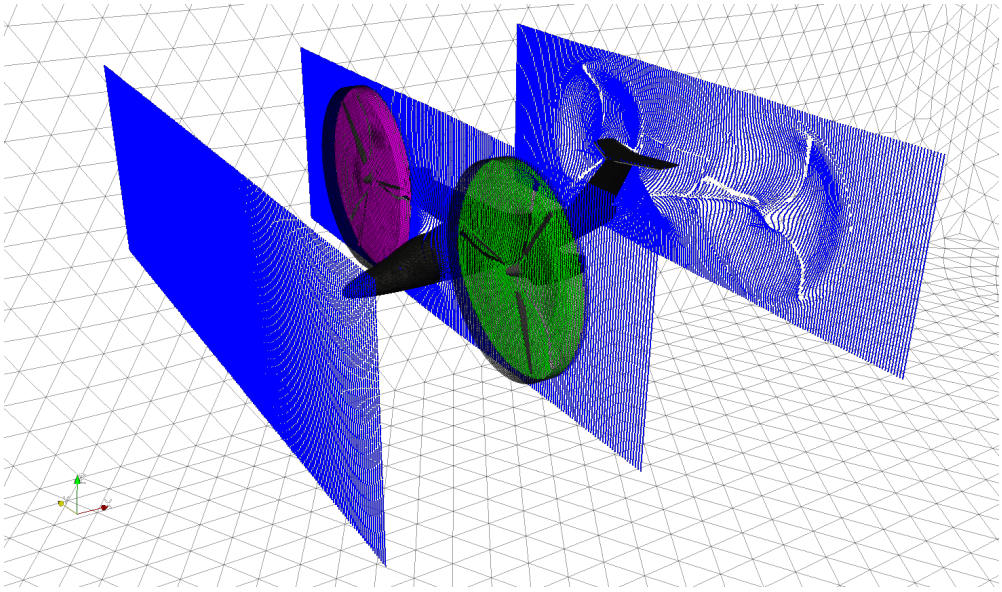

(b) *Isometric view.*

Figure 5.16: *Results of the particle tracking over a tilt-rotor in aeroplane mode. Displaying the connectivity between zones where the particles in the 1st, 2nd and 3rd zones are respectively represented in blue, green and pink.*

5.5 Conclusion

Most computational rotorcraft icing codes use the Eulerian frame of reference for particle tracking, whereas, the most obvious description of the dynamics of individual particles is in a Lagrangian frame of reference. An important feature of the Lagrangian framework is that it allows for a better description of the underlying physics of supercooled large water droplets. In this work, two new techniques are introduced to address two of the main limitations of Lagrangian particle tracking techniques for computational rotorcraft icing codes. The first technique introduced allows for particles to be tracked in mesh with arbitrary motion. The second technique introduced deals with the issues intrinsic to non-conformal boundary interfaces such as those present with sliding mesh. The simulation of clouds containing supercooled water droplets on complex problems of engineering interest are shown. The first test case presented exhibits particles moving throughout continuously deforming mesh without being lost or misplaced. The second and third test cases feature particles moving across non-conformal interfaces in sliding mesh. Overall, the efficacy of the Lagrangian particle tracking techniques for computational rotorcraft icing codes is demonstrated.

Part III

High-Fidelity Ice Prediction and Detection

CHAPTER 6

A Three-Dimensional High-Fidelity Simulation Approach for Rotorcraft Icing

Abstract

This chapter presents an original framework to simulate the rotorcraft icing problem by utilizing state-of-the-art high-fidelity, three-dimensional numerical techniques. The inter-dependency between numerical techniques is one of the main complicating reasons explaining why rotorcraft icing codes are so underdeveloped. To that end, techniques to address issues including mesh deformation,particle tracking, and phase change modelling are introduced. In particular, radial basis function mesh deformation techniques are used to update the three-dimensional moving ice boundary. Meanwhile, Lagrangian particle tracking techniques specific to rotorcraft flows are used to compute the collection efficiency of the rotor. Additionally, phase change models are applied to compute the ice thickness and a model to predict ice shedding events is introduced. Icing wind tunnel tests conducted on the Spinning Rotor Blade (SRB-II) model rotor are used for an assessment of the numerical predictions. Quantities used for comparisons between the numerical predictions and experimental measurements on the SRB-II model rotor include the ice thickness and shedding location. Numerical predictions are in good agreement with the measured data at all temperatures. The outcome of influential parameters which directly impact computational rotor ice shapes are assessed. Furthermore, numerical results characterizing the noise signals of rime and glaze iced rotors are presented to further establish computational aeroacoustic ice detection technologies.

6.1 Introduction

NUMERICAL rotorcraft icing predictions are only as credible as the models are reliable. Consequently, it is of interest to limit model assumptions to ensure the highest possible fidelity of model predictions. As highlighted within the literature review of this thesis in Chapter 1, Section 1.3.3, hybrid two/three-dimensional reduced-order methods have predominantly been used for the prediction of rotorcraft ice accretion over the past decade [65–72], which is concerning given that rotorcraft are dominated by three-dimensional behaviour. To the authors knowledge, presently only one other research group are reportedly capable of modelling rotor blade icing using fully three-dimensional techniques [73–75]. The reported approach adopts an Eulerian particle tracking technique to track clouds of supercooled water droplets and model the collection efficiency. The phase change behaviour within the ice layer is based on the classical Messinger model. The rotor aerodynamics is simulated based on a structured grid approach and a Chimera overset grid system is used to account for the blade motion. However, even this three-dimensional approach has limitations for simulating rotorcraft icing as discussed in Chapter 1, Section 1.3.3.

Concerns over the fidelity of current rotorcraft icing simulations are shared by the regulatory authorities as emphasized in Chapter 1, Section 1.2. Neither the European Aviation Safety Agency [204, 205] nor the Federal Aviation Administration [206, 207] currently recognize simulation techniques as adequate for certification of rotorcraft ice detection and protection systems. The progression of numerical rotorcraft icing tools is therefore a requirement before certification by simulation can be considered. This progression includes extensive verification and validation of numerical models with wind tunnel measurements and artificial in-flight icing trails. However as is now the case with fixed-wing aircraft, numerical tools may become pivotal to aid the design of rotorcraft ice detection and protection systems at the most challenging test points within the icing envelope.

To overcome the limitations of contemporary rotorcraft icing codes, a new framework for the simulation of rotorcraft icing is proposed. Modelling the behaviour of individual supercooled water droplet particles is critical to capture important physical effects including droplet splashing [78]. Subsequently, a Lagrangian particle tracking approach is adopted within this framework to model individual droplets [199]. This framework utilizes an unstructured grid approach and deforming sliding mesh to account for the blade motion [208]. An unstructured grid approach proves advantageous for Lagrangian particle tracking as the exact positions and velocities of individual droplets can be tracked across non-conformal sliding mesh boundaries [209]. Unstructured grids also provide greater flexibility for the mesh deformation and icing process. Finally, the exact solution of the Stefan problem for temperature profiles within the glaze ice layer is adopted to improve the representation of glaze ice structures [113]. Radial Basis Function mesh deformation is utilized to efficiently update the unstructured mesh while also providing a robust solution with high mesh quality [182].

This new framework for simulating rotorcraft icing is demonstrated on a model rotor in forward flight. The operation of the SRB-II model rotor, when exposed to a range of icing conditions, has been identified for validation of the numerical predic-

tions. The experimental measurements allow for metrics such as the ice thickness and shape to be compared with numerical solutions at various radial locations. Ice shedding measurements are used to assess ice shedding prediction capabilities. In the past, numerical ice shedding analyses have been based on hybrid two/three-dimensional approaches [210–212]. Given that ice shedding is a quintessentially three-dimensional phenomena, this work seeks to demonstrate an entirely three-dimensional numerical ice shedding approach.

The new high-fidelity approach for the three-dimensional modelling of rotorcraft icing can aid in the development of new ice detection and protection technologies. The limitations of the conceptual design of computational aeroacoustic ice detection technologies discussed in Chapter 2 are therefore addressed in this work. Consequently, computational aeroacoustic analyses of the SRB-II model is used to further understand the characteristics of glaze and rime iced rotors and may help develop new ice detection technologies.

The organisation of this work follows the subsequent structure; the SRB-II model is introduced in Section 6.2, the numerical methods for the ice prediction, shedding, and detection are discussed in Section 6.3, the numerical ice predictions are presented in Section 6.4, the numerical ice detection results are presented in Section 6.5, finally the concluding remarks from this work are outlined in Section 6.6.

6.2 SRB-II Model

In 2006, the Spinning Rotor Blade (SRB) experimental apparatus was developed at the Anti-icing Material International Laboratory (AMIL) in the Université du Québec à Chicoutimi (UQAC), Canada, in collaboration with Bell Helicopter, Textron [53]. The set up provided a cost-effective and repeatable source of icing wind tunnel data for the development of de-icing systems. Between April, 2006 and June, 2008, the SRB-II configuration performed a standardized test based on typical in-flight icing conditions representative of a continuous icing cloud for helicopters. The influence of the outside air temperature was also critically assessed under these conditions. In total, 155 tests were performed. The primary objective of these tests was to investigate ice physics and the use of hydrophobic coatings for de-icing systems on small helicopters. An extensive number of tests were also used to evaluate the test reproducibility and wind tunnel behaviour.

The AMIL Icing Wind Tunnel (IWT) is a closed-loop, low-speed wind tunnel which operates at subzero temperatures. Throughout the set of standardized tests, the free-stream airspeed, outside air temperature (OAT), liquid water content (LWC), and, mean volume diameter (MVD) of the supercooled water droplets is controlled in the IWT. The hub is connected to a motor to control the rotors rotational speed and the power required to drive the rotor was recorded. The rotor was exposed to the icing cloud until the presence of a shedding event and the length of shed ice was recorded. Finally, the differential between the clean and iced rotor power was recorded. The values of these parameters with their known uncertainty are outlined in Table 6.1.

The influence of the IWT temperature on the ice structure was assessed. The adhesive shear stress, τ_{shear}, between the ice and surface substrate was recorded at different

Table 6.1: *SRB-II Standardized Test.*

OAT	LWC	MVD	Mach $[-]$		Shedding	
[K]	$[\mathrm{g/m^3}]$	[µm]	Freestream	Blade-Tip	Time [s]	Length [mm]
258	0.842	26.7	0.046	0.41	130 ± 50	70 ± 15

⋆ Experimental conditions and results taken from Ref. [53].

temperatures due to its significant impact on the shedding events. Four temperatures were evaluated ranging from a predominantly rime ice regime at $-20°C$, to a predominantly glaze ice regime at $-5°C$. At each temperature, the period of exposure to the icing cloud and iced rotor power was recorded. The experimental results are shown in Table 6.2

Table 6.2: *SRB-II Temperature Tests.*

Tag	OAT	τ_{shear}	Shedding	
	[K]	[MPa]	Time [s]	Length [mm]
T268	268	0.07 ± 0.02	82 ± 26	123 ± 49
T263	263	0.12 ± 0.03	105 ± 34	111 ± 44
T258	258	0.21 ± 0.06	130 ± 42	70 ± 28
T253	253	0.26 ± 0.08	163 ± 52	36 ± 14

⋆ Experimental conditions and results taken from Ref. [53].

The SRB-II configuration uses a $1/18$ sub-scale model helicopter rotor. The blades are constructed from extruded 6066-T6 aluminium. The adhesive shear stress between the ice and the 6066-T6 aluminium substrate decreases with increasing temperature and the relationship is shown in Ref. [213]. The blades are $315\,\mathrm{mm}$ in length and are offset from the hub by $75\,\mathrm{mm}$. The blades have a chord of $69.75\,\mathrm{mm}$. The rotor diameter is thus $780\,\mathrm{mm}$. The blades are untwisted and have a NACA0012 profile. Throughout all the standardized and temperature-dependent tests the rotor collective is set at $+6°$, while no cyclic motion was introduced. The rotor geometry and characteristics are summarized by a schematic in Fig. 6.1.

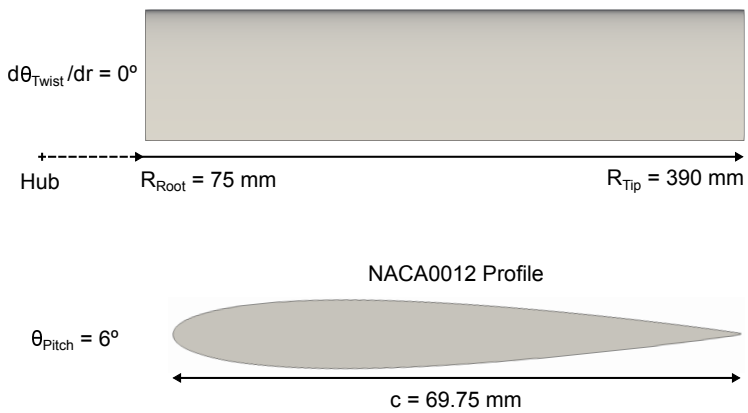

Figure 6.1: *SRB-II model geometry and characteristics.*

6.3 Numerical Methods

6.3.1 Ice Prediction Methodology

The rotor ice predictions heavily rely on the numerical tool development and validation discussed throughout Part II. The open-source SU2 solver [133] was used for simulating the turbulent flow-field around the rotor. This work utilized the methodologies introduced in Chapter 4 & Appendix A to ensure a high resolution of the flow. Consequently, the flow domain was split into two septate regions and the multi-zone problem was solved. The near-field domain used an unstructured mesh approach and the far-field domain used a structured mesh approach. Particle tracking of clouds containing supercooled water droplets within the multi-zone domain was achieved using the numerical methods introduced during Chapter 5. With the particle trajectories determined, the collection efficiency of the impacted particles on the blades was computed based on the unsteady approach introduced in Chapter 2. The PoliMIce software library provides state-of-the-art ice formation models [57]. The model used in this work to capture the complex ice shapes is the local exact solution of the unsteady Stefan problem for the temperature profiles within the ice layer in glaze conditions [113]. Radial Basis Function mesh deformation techniques introduced in Chapter 3 were used to account for the evolving ice boundary and data-reduction schemes were used to reduce the computational cost associated with the large data sets.

6.3.2 Ice Shedding Methodology

A three-dimensional ice shedding module was introduced into the PoliMIce software for the computation of ice shedding events. The approach radially discretizes the iced rotor into several ice blocks. The summation of the forces acting on each block of ice determines if a shedding event occurs. Shedding is present when the centrifugal forces, $F_{\text{centrifugal}}$, acting on the ice exceeds a combination of both the cohesive force, $F_{\text{conhesive}}$, and adhesive force, F_{adhesive}, of the ice,

$$F_{\text{centrifugal}} > F_{\text{conhesive}} + F_{\text{adhesive}} \tag{6.1}$$

where the centrifugal, cohesive, and adhesive forces acting on the ice are respectively computed by the following formulae,

$$F_{\text{centrifugal}} = m_{\text{ice}} r\omega, \quad F_{\text{conhesive}} = \sigma_{\text{cohesion}} A_{\text{ice}}, \quad F_{\text{adhesive}} = \tau_{\text{adhesion}} A_{\text{surface}} \tag{6.2}$$

and where the mass of ice is represented by m_{ice}, the cohesion shear stress of ice is represented by σ, the adhesion shear stress of ice is represented by τ_{shear}. The mass of ice is determined by,

$$m_{\text{ice}} = h\rho_{\text{ice}} A_{\text{surface}} \tag{6.3}$$

where h is the ice thickness, ρ_{ice} is the density of ice, and A_{surface} is the surface area in contact with the blade substrate. Where the density of ice is dependent on the type of ice, be it rime or glaze.

Ice adhesion models to predict shear stress at shedding were developed by Fortin and Perron [213]. Their work measured the adhesion shear stress between the 6066-T6 aluminium substrate of the SRB-II rotor and the accreted ice. The adhesion shear stress measurements are shown in Fig. 6.2. An empirical relationship between the adhesion shear stress and temperature on the SRB-II rotor can subsequently be determined,

$$\tau_{\text{adhesion}} = -0.0132806\,T + 3.62295 \tag{6.4}$$

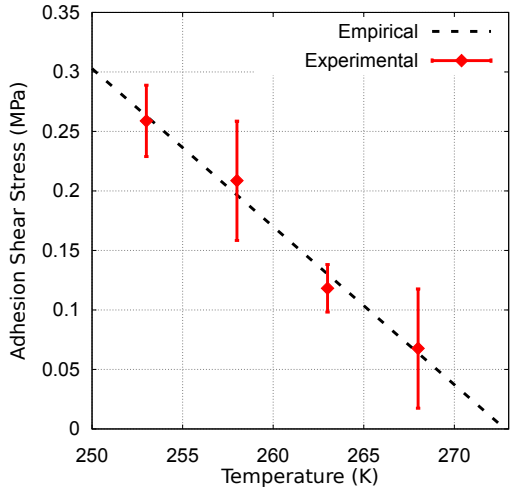

Figure 6.2: *Experimental adhesion shear stress vs temperature results on the SRB-II Aluminium substrate taken from Ref. [213]. Where the empirical relationship of the adhesive shear stress vs temperature is based on* $\tau_{shear} = -0.0132806\,T + 3.62295$.

Additionally, a cohesive ice model was developed by Fortin and Perron as part of the SRB-II experimental rotor icing tests [53,213]. Their model is summarised. It indicates that under increasing tensile load, crack nucleation begins when the normal stress is approximately $0.5\,\text{MPa}$. Cracks then increase in size and when the strain reaches the critical grain boundary value proportionate to a critical wedge displacement of $x_c = 0.47\ \mu\text{m}$, crack propagation takes place. Subsequently, cohesive failure occurs and the ice breaks. While considering that viscoplastic strain is negligible during rotor ice accretion, the cohesive failure stress can be expressed as,

$$\sigma_{\text{cohesion}} = \left(\frac{x_c}{9 \times 10^{-3} + d}\right) E(T) \tag{6.5}$$

where the Young's modulus of ice and grain size are respectively denoted by $E(T)$ and d. Each of which are temperature dependent. Subsequently, the cohesive force between the blocks of ice is computed, requiring the cross sectional area, A_{ice}, at each block interface. The steps for computing the cross sectional area at each block interface is subsequently described and a schematic of the routine is illustrated in Fig. 6.3:

1. Compute the normalized radial distance to the centroid of E_A.
2. Identify the shared nodes of E_A to find E_B.

3. Compute the distance between N_1 and N_2.
4. Calculate the ice thickness h, at the intersection.
5. Calculate the cross sectional area A_{ice}, of the block interface.

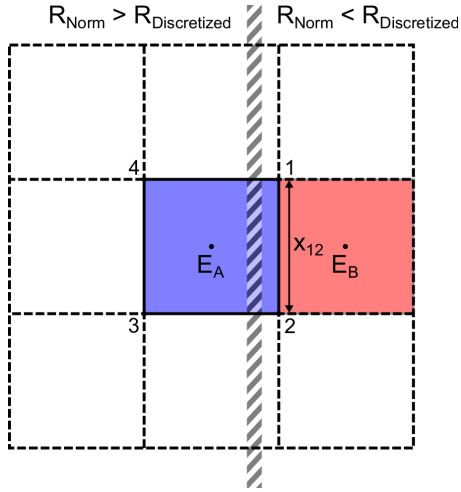

Figure 6.3: *Schematic illustrating the method for computing the cross sectional area at each block interface to determine the cohesive force.*

6.3.3 Ice Detection Methodology

A computational aeroacoustic analysis was conducted on the clean and iced rotors using the Ffowcs Williams-Hawkings (FW-H) method [214]. In particular, the Farassat-1A formulation [215, 216] of the FW-H equation was solved for a solid-surface. The approach computes the far-field noise level using the surface pressure data obtained from Computational Fluid Dynamic simulations. The instantaneous pressure fluctuations on the rotor blade surface are therefore of interest and can be evaluated as $p' = p - p_{\text{mean}}$. The instantaneous pressure fluctuations of the iced rotor blades are therefore used to give an early insight into the potential of computational aeroacoustic rotorcraft ice detection techniques. For a more comprehensive analysis, the far-field noise signals are later assessed at several observer locations beneath the rotor. In total four observer locations were chosen to evaluate the position of the microphone for potential ice detection. The selected observer locations are depicted in Fig. 6.4.

6.4 Ice Prediction Results

The following section introduces the most important numerical results of the three-dimensional ice prediction on the SRB-II model rotor. Key aspects discussed include an approach for the rotor mesh generation, an analysis of the particle tracking simulations, and an analysis of the ice prediction capabilities.

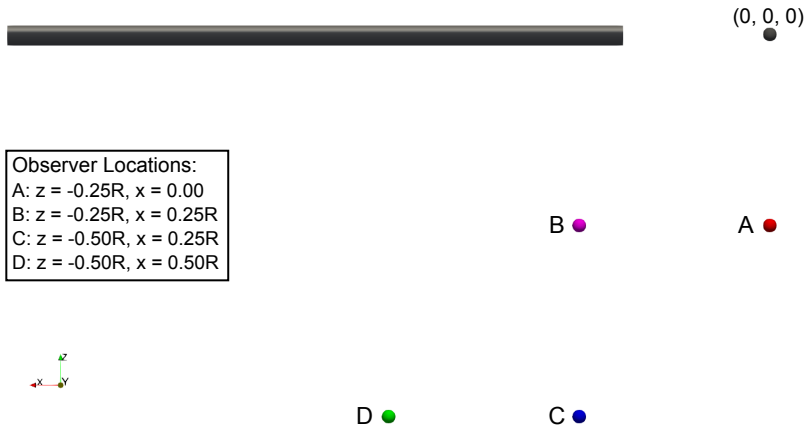

Figure 6.4: *Observer locations chosen for the computational aeroacoustic analysis. With the respective vertical and radial placement:* $z = 0.25R$, & $0.50R$, *and* $x = 0.0$, $0.25R$, & $0.50R$.

6.4.1 Mesh Generation

The computational domain was decomposed into two separate sub-regions to capture and model both large and small-scale vortical structures present in the iced rotor flow-field. The internal domain contains the SBR-II rotor blades and was generated using an unstructured meshing approach. The internal domain contains a total of 9 660 383 elements, and 2 604 650 nodes. The external domain was generated using a structured multi-block grid approach. The boundary layer of the rotor uses quadrilateral elements and is sufficiently resolved to ensure $y^+ < 1$. The external domain contains a total of 11 512 476 elements, and 11 707 937 nodes. The mesh has a cylindrical cut-out where the rotor is positioned. The mesh was hereafter considered as a multi-zone problem and communication between the two non-conformal boundary interfaces was achieved using the supermesh approach implemented by Gori et al. [164] in the SU2 solver [133]. A constant rotational velocity was applied to the internal domain to achieve the rotational motion of the blades.

Suitable treatment of the non-conformal artificial boundary interface becomes crucial for multi-zone problems. The supermesh approach allows for flux-conserving treatment of non-conformal interfaces. Similarity between the sizes of the structured and unstructured elements at the sliding interface was ensured so to have a continuous discretization of the solution as shown in Fig. 6.5 at various cut-planes of the mesh. The maximum element size of both the hexahedra elements at the background mesh interface and tetrahedra elements at the internal mesh interface was $x = 0.07c$.

6.4.2 Particle Tracking Analysis

The SRB-II rotor flow-field was computed for the different test conditions presented in Table 6.2. Clouds containing 6×10^6 supercooled water droplets were then tracked within the different flow solutions. The particle tracking simulation for the standardized test is shown in Fig. 6.6. The results are shown in both the $x-y$ plane and the $x-z$ plane.

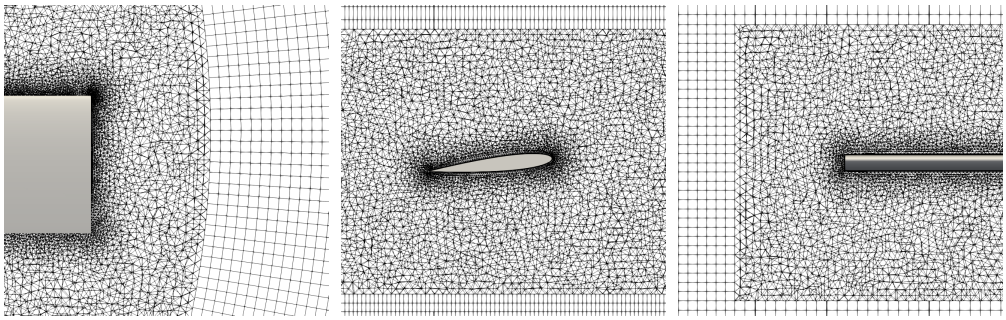

(a) $x - y$ *plane at* $z = 0$. **(b)** $x - z$ *plane at* $y = R$. **(c)** $y - z$ *plane at* $x = 1/4c$.

Figure 6.5: *Non-conformal boundary interfaces between the stationary structured mesh and moving unstructured mesh. Displayed in the* $x - y$*,* $x - z$*, and* $y - z$ *plane of the mesh coordinate system.*

An isometric view of the simulation is also provided to give an alternative perspective of the three-dimensional behaviour of the particles. In an attempt to illustrate the dynamic motion of the particles, three different stages of the simulation are shown at the 2^{nd}, 4^{th}, and 6^{th} rotor revolutions. The results give an insight to the complexities of the rotor flow-field and how it resultantly impacts the particle trajectories. Particles in the near vicinity of the rotor wake are convected downstream and away from the rotor, with this effect being most prevalent towards the blade tip.

A qualitative assessment of the location of the impacted particles on the rotor for the standardized test is displayed in Fig. 6.7a. A greater number of particles are shown to impact towards the blade-tip due to the increased rotational velocity of the blade. The region around the leading edge indicates that there are a sufficient quantity of particles impacted to ensure a smooth distribution for the collection efficiency. A quantitative assessment of the collection efficiency of the rotor for the standardized test is shown in Fig. 6.7b at radial locations $r/R = 0.6,\ 0.7,\ 0.8,\ 0.9,\ 0.95$. At the radial locations up to approximately $r/R = 0.8$ there is a relatively low collection efficiency. Beyond this, while moving radially outwards, the collection efficiency increases significantly. It indicates that the collection efficiency of the rotor does not increase linearly as a function of the rotor radius. This highlights that the three-dimensional effects of the flow-field have a significant influence on the particle trajectories, and importantly, in turn, the collection efficiency.

6.4.3 Ice Accretion and Shedding Analysis

The kinetic heating of the blades increases along the blade radius due to the increased rotational velocity of the blade. Subsequently, the ice regime can potentially transition from rime ice near the blade-root to glaze ice near the blade-tip. The ice structures themselves are therefore not only dependent on the outside-air-temperature but also their location radially along the blade. The ice accretion and shedding results for the temperature tests outlined in Table 6.2 are shown in Fig. 6.8. The results shown in Fig. 6.8 allow for a qualitative analysis of the three-dimensional ice structures pre and post-shedding events. In general, it can be observed that the lower temperatures tests

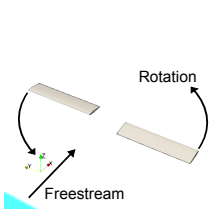

(a) *Initial solution: isometric view.*

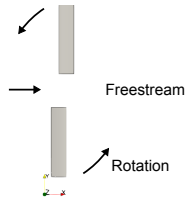

(b) *Initial solution:* $x - y$ *plane.*

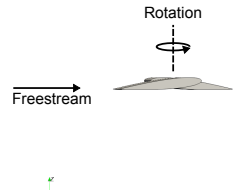

(c) *Initial solution:* $x - z$ *plane.*

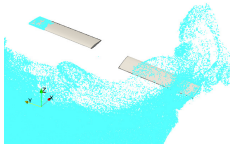

(d) 2^{nd} *revolution: isometric view.*

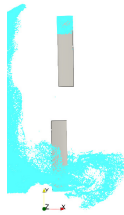

(e) 2^{nd} *revolution:* $x - y$ *plane.*

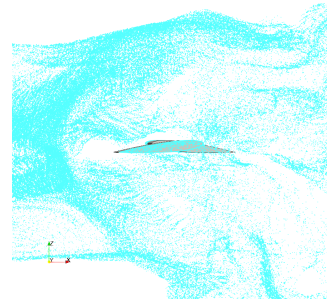

(f) 2^{nd} *revolution:* $x - z$ *plane.*

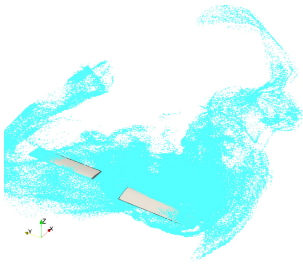

(g) 4^{th} *revolution: isometric view.*

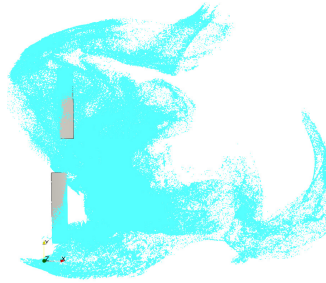

(h) 4^{th} *revolution:* $x - y$ *plane.*

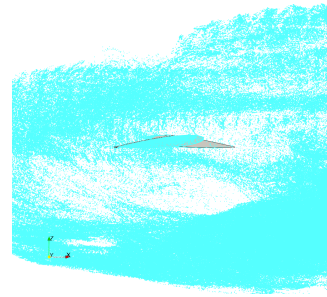

(i) 4^{th} *revolution:* $x - z$ *plane.*

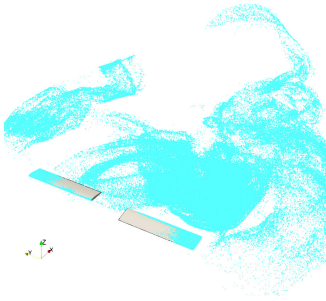

(j) 6^{th} *revolution: isometric view.*

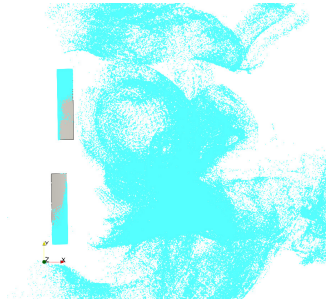

(k) 6^{th} *revolution:* $x - y$ *plane.*

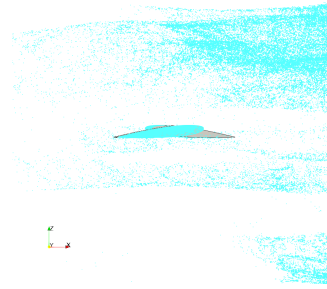

(l) 6^{th} *revolution:* $x - z$ *plane.*

Figure 6.6: *Particle tracking on the SRB-II model rotor during the standardized test condition. The cloud of particles is shown in blue at its initial position as well as at time instances corresponding to the* 2^{nd}*,* 4^{th}*, and* 6^{th} *rotor revolution. Three visualisations include an isometric view, a view in the* $x - y$ *plane, and a view in the* $x - z$ *plane. Displaying every* 10^{th} *particle contained within the cloud.*

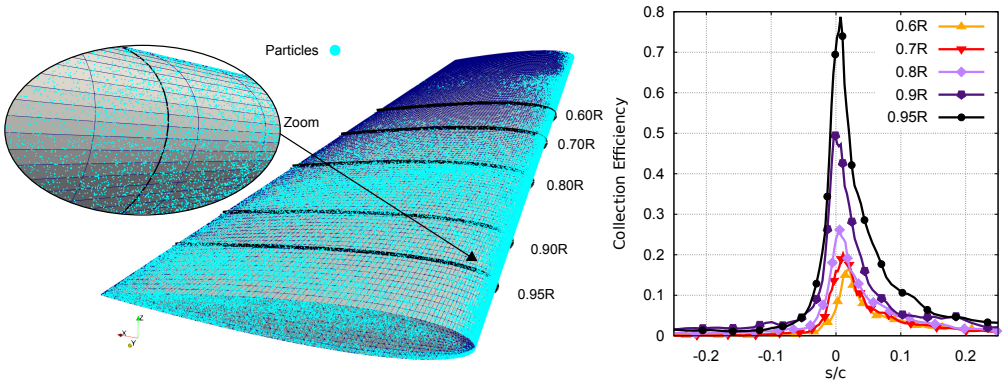

(a) *Individual particles impacted after six rotor revolutions.*

(b) *Computation of the collection efficiency at select radial positions.*

Figure 6.7: *Analysis of the impacted particles after six full rotor revolutions. First, displaying the distribution of the individual particles along the blade and leading edge. Where the blue particles indicate the supercooled water droplets. Second, depicting the computation of the collection efficiency at radial positions:* $r/R = 0.6,\ 0.7,\ 0.8,\ 0.9,\ 0.95$.

exhibit ice structures containing a greater mass of ice prior to shedding events. This is particularly noticeable towards the blade-tip where the ice thickness is greatest. Closer towards the blade-root the quantity of accreted ice is lower and resultantly differences are less clear.

The ice shedding module based on the adhesive shear stress expressed in Equation 6.4 allows for the analysis of shedding events in Fig. 6.8. In particular, it allows for the comparison of the shedding location at various outside-air-temperatures. Although the mass of ice at the lower temperature tests is greater, the value of the adhesion shear stress between the ice and blade surface is higher, and resultantly, the quantity of ice shed is less. Conversely, at the higher temperature tests, the mass of ice is less, however, since the value of the adhesion shear stress is significantly lower, the quantity of ice shed is greater.

A quantitative analysis of the rotor ice shape numerical predictions based on the environmental conditions from Table 6.2 is provided in Fig. 6.9. The results displayed in Fig. 6.9 help to assess the ice regime at different radial locations during each of the test conditions. Unfortunately, the literature lacks experimental sectional ice shape measurements of the SRB-II model rotor for numerical comparison. During the two test cases at the lowest temperatures namely, $T253$ and $T258$, it can be concluded that rime ice dominates up until around $r/R = 0.8$ due to the ice shapes forming *spearhead* like structures. Radial beyond this, glaze ice dominates due to the ice shapes possessing *double-horn* like structures. During the two highest temperature test cases namely, *T263* and *T268*, it can be concluded that glaze ice dominates at all radial locations. The only portion of ice which appears to remain within the rime ice regime is up until approximately $r/R = 0.6$ during test case *T263*.

An assessment of the ice modelling techniques on the SRB-II model during the standardised test conditions from Table 6.1 at radial positions $r/R = 0.7$ & 0.9 is

provided in Fig. 6.10. Firstly, a comparison of the standard Myers model [79] with the local, exact solution of the unsteady Stefan problem for temperature profiles within the glaze ice layer as published by Gori et al. [113] is shown in Fig. 6.10a. The results depict the importance of the local, exact solution of the unsteady Stefan problem for the glaze ice regime towards the blade-tip. The model from Gori et al. [113] is able to capture the ice *horns* whereas, the Myers model [79] is not.

Secondly, the influence of the inclusion of the inertial terms within the liquid film layer is shown in Fig. 6.10b. The influence of the inertial terms appears significant for this test case under these conditions. As observed in Fig. 6.9b, rime ice extends to approximately 80% radius. Consequently, the introduction of the inertial terms to the liquid film is only significant beyond this radial location and resultantly, differences are negligible for the rime ice shape at $r/R = 0.7$. However, at the radial location of $r/R = 0.9$,where glaze ice prevails, the influence of the inertial terms on the liquid film is considerable. Subsequently, the angle of the ice horn is more acute, leading to poorer aerodynamic properties and performance. This finding is contrary to the outcome of the published work from Nanjing University of Aeronautics and Astronautics while using the same test conditions and SRB-II model rotor [74]. Their work suggests negligible differences in glaze ice shapes while comparing the influence of the inertial terms in the liquid film. This highlights the urgent need for advancements in fully three-dimensional rotorcraft icing codes and in particular code-to-code comparison. Furthermore, this is an effect which cannot be captured whilst using hybrid two/three dimensional approaches.

Additionally, it is beneficial to assess the current predictions with the rotor icing code from Nanjing University of Aeronautics and Astronautics [73–75]. Consequently, a preliminary code-to-code comparison during the standardised test conditions from Table 6.1 at radial positions $r/R = 0.58$ & 0.84 is provided in Fig. 6.11. The radial position at $r/R = 0.58$ is shown in Fig. 6.11a with each code predicting a rime ice shape. The code from Nanjing University of Aeronautics and Astronautics predicts greater asymmetry in the ice shape. The radial position at $r/R = 0.84$ is shown in Fig. 6.11b with each code predicting significantly different ice shapes. The code from Nanjing University of Aeronautics and Astronautics predicts a similar shape to Fig. 6.11a however with increased ice thickness. Conversely, the predictions from this work indicate that at this radial position the ice accretion is predominately glaze as depicted by the *horn*-like ice structures. In general, both codes predict ice shapes with a tip thickness within the variations present during the experimental measurements in Ref. [53].

Useful experimental data recorded during the SRB-II icing tests includes information regarding the ice thickness at the blade-tip leading edge. Furthermore, the ice shed location was also recorded. Both sets of data help to partially provide a means of numerical validation. An assessment of the numerical ice thickness predictions at the blade-tip leading edge prior to shedding is shown in Figs. 6.12a & 6.12b. The radial variation of the ice thickness at the different temperatures is shown in Fig. 6.12a. Overall, there is a slight under prediction of the ice thickness at the blade-tip. However, the non-linearity of the radial ice accretion is importantly highlighted. The experimental variation in ice thickness is displayed in Fig. 6.12b. The numerical predictions are well within the experimental uncertainties and also align with the empirical relationship outlined in Ref. [53]. The ice shed location at different temperatures is displayed in Fig. 6.12c.

The ice shed location is expressed in terms of the radial position. The adhesion shear stress model is based on a linear relationship with the temperature. Consequently, this is reflected in the numerical prediction of the shed location. The numerical shedding predictions are within the large uncertainty errors recorded during the experimental tests. However, there is quite a significant difference when comparing with the empirical relationship from Ref. [53].

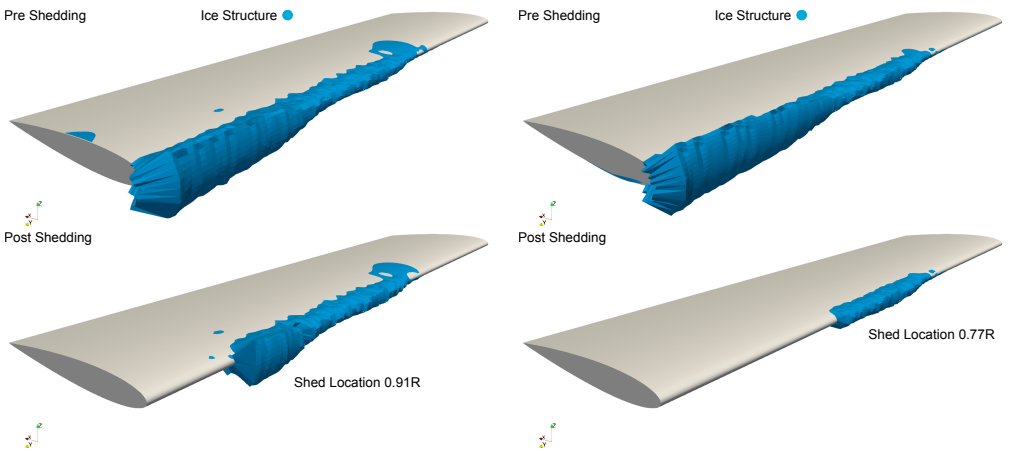

(a) *T253.* **(b)** *T258.*

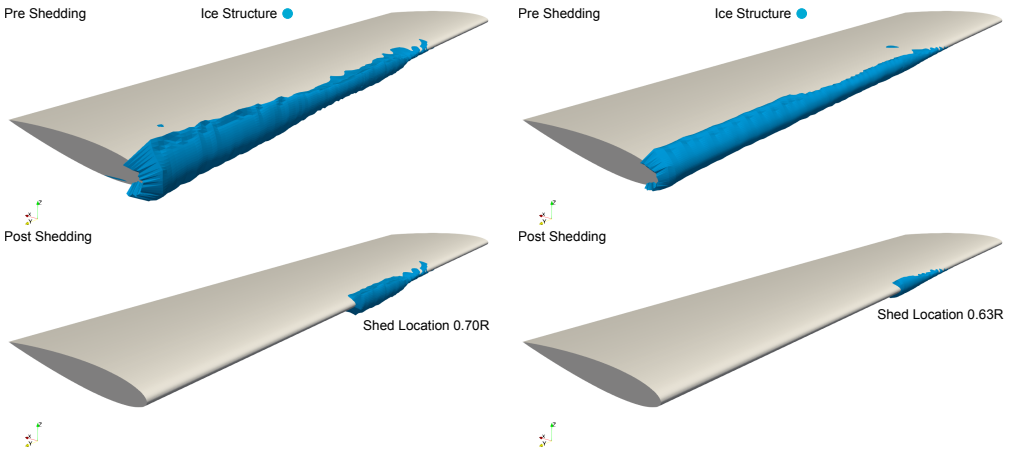

(c) *T263.* **(d)** *T268.*

Figure 6.8: *SRB-II numerical ice shape predictions displayed throughout the temperature dependent conditions outlined in Table 6.2. Where the ice accretion is represented in blue. Displaying both the instance prior to and post ice shedding events. For each test case, the ice shed location is shown in terms of the radial position.*

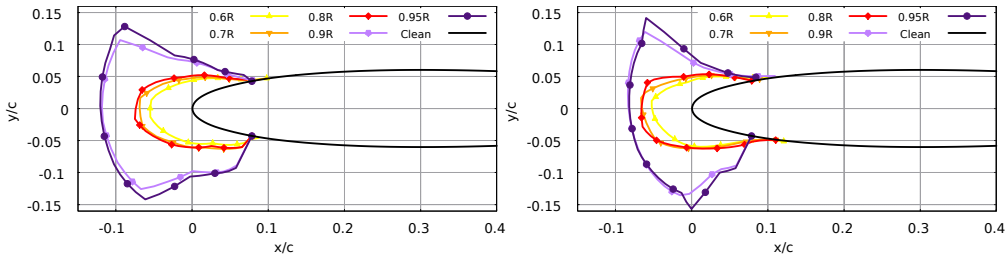

(a) *T253.*

(b) *T258.*

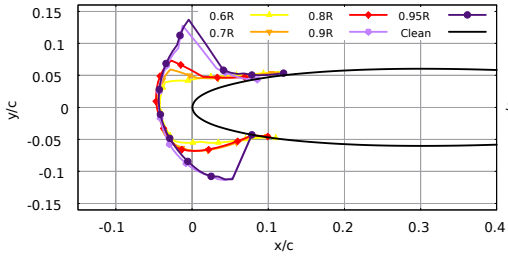

(c) *T263.*

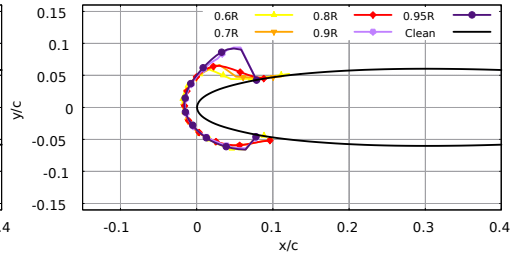

(d) *T268.*

Figure 6.9: *SRB-II numerical ice shape predictions displayed at selected radial sections for the test conditions outlined in Table 6.2. Displayed at radial locations* $r/R = 0.6,\ 0.7,\ 0.8,\ 0.9,\ 0.95$*. The ice shapes are normalized by the rotor chord length and are shown in the* $x - y$ *plane.*

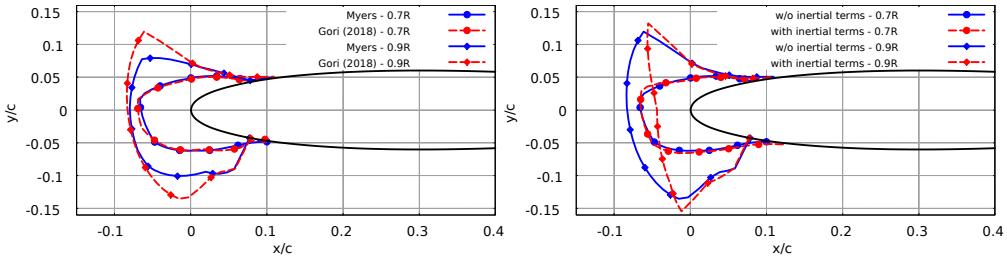

(a) *Comparison of icing models.* **(b)** *Inclusion of the interial terms in the liquid.*

Figure 6.10: *Assessment of ice modelling techniques on the SRB-II model during the standardized test conditions from Table 6.1 at radial positions $r/R = 0.7$ & 0.9. Firstly, comparing the standard Myers model [79] with the local, exact solution of the unsteady Stefan problem for temperature profiles within the glaze ice layer as published by Gori et al. [113]. Secondly, comparing the influence of the inclusion of the inertial terms within the liquid film layer.*

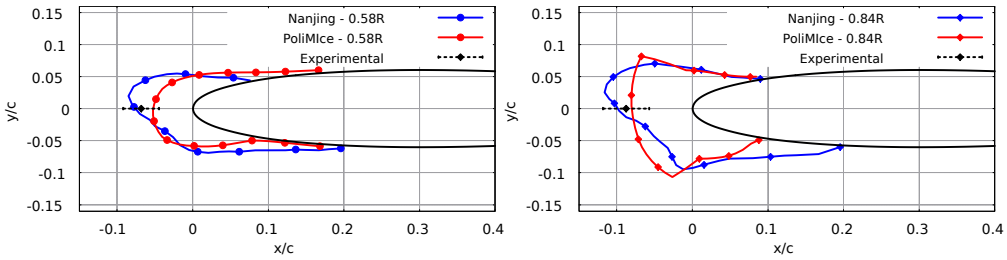

(a) *Comparison of codes at $r/R = 58\%$.* **(b)** *Comparison of codes at $r/R = 84\%$.*

Figure 6.11: *Comparison of numerical predictions with the rotor icing code from authors the at Nanjing University of Aeronautics and Astronautics [73–75]. Experimental ice thickness measurements taken from Ref. [53]. The selected radial locations were based on the available data.*

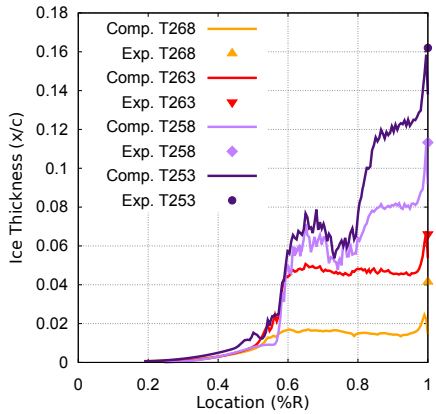

(a) *Ice thickness along the blade radius.*

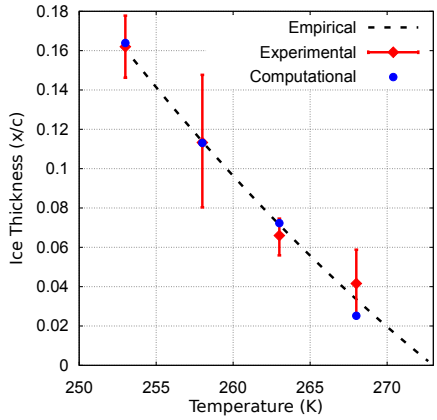

(b) *Ice thickness at* $r/R = 1$.

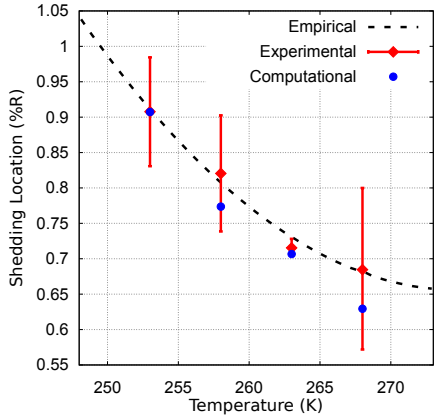

(c) *Ice shedding location.*

Figure 6.12: *Direct comparison of the computational ice predictions with the experimental and empirical results from Ref. [53]. Compared for each of the temperature dependent test conditions outlined in Table 6.2. Firstly, displaying the ice thickness at the leading edge as a function of the radial position. Secondly, showing the ice thickness at the blade-tip alongside the experimental uncertainties. Thirdly, presenting the ice shedding predictions at the blade-tip.*

6.5 Ice Detection Results

The subsequent section of the work introduces the ice detection results. Significant contributions include an aerodynamic and aeroacoustic analysis of both clean and iced rotors.

6.5.1 Test Conditions

The cardinal role of ice detection systems is to alert the pilot of hazardous icing conditions at the earliest stage possible. Consequently, performing ice detection tests based on the original test conditions from Table 6.2 would be naive since the ice structures are already well established and would be detectable due to their severe performance degradation. It is therefore desirable to detect ice prior to the stage at which performance degradation becomes hazardous to flight safety. Accordingly, a set of ice detection test conditions is deduced based on much shorter icing exposure times and is outlined in Table 6.3.

Table 6.3: *SRB-II Ice Detection Test Conditions.*

Tag	OAT	LWC	MVD	Time	Mach [−]	
	[K]	[g/m^3]	[μm]	[s]	Freestream	Blade-Tip
ID-Glaze	268	0.842	26.7	15	0.046	0.41
ID-Rime	253	0.842	26.7	15	0.046	0.41

Two sets of conditions are selected, the first being at a low temperature where the rime ice regime is likely to dominate, and the second at a high temperature where the glaze ice regime is likely to be most prevalent. The results of the numerical ice shape predictions are shown in Fig. 6.13. At these early stages of ice accretion, there are no ice shedding events present due to the ice mass not being sufficient to produce significant centrifugal forces as outlined in Equation 6.2. Resultantly, ice accretes up until the blade-tip. The high-temperature test case namely, *ID-Glaze*, exhibits a small *horn* on the upper surface of the blade beyond $r/R = 0.80$. While the low-temperature test case namely, *ID-Rime*, displays a much smoother *spearhead*-like ice structure at all radial positions, indicating the rime ice limit has not been reached. In conjunction, a quantitative analysis of the ice shapes is shown in Fig. 6.14. Test case *ID-Rime* illustrates a higher ice thickness at the leading-edge in the chord-wise direction, while test case *ID-Glaze* displays greater ice thickness aft of the leading edge.

6.5.2 Aerodynamic Analysis

The influence of the ice accretion on the aerodynamics of the rotor is assessed in Fig. 6.15. The results display the pressure distribution over the normalised chord length. Additionally, results are shown at radial positions $r/R = 60,\ 70,\ 80,\ \& 90\%$, on both the advancing and retreating side of the rotor at $\psi = 90°$ and $\psi = 180°$. The aerodynamic predictions reveal that even lightly iced rotors can have a significant impact on pressure profile distribution. Both test cases drastically alter the suction peak on the upper surface at the leading edge. The high-temperature test case, *ID-Glaze*, exhibits

greater influence on the rotor performance than the low-temperature test case, *ID-Rime*. The abrupt pressure peaks observed during the *ID-Glaze* test case are likely to be caused by the early formation of ice *horns*. Aft of approximately $1/4$ c, the influence of the ice shapes is negligible and the pressure distribution remains comparable to the clean rotor predictions.

6.5.3 Aeroacoustic Analysis

To provide an early insight into the acoustics, the influence of the ice accretion on the instantaneous pressure fluctuation on the blade surface is revealed in Fig. 6.16. The results are shown at azimuth angles $\psi = 90°$ and $\psi = 180°$. While considering the contrasting pressure profiles displayed in Fig. 6.15, it is not surprising to likewise observe differences in the instantaneous pressure fluctuations of the iced rotors with the clean rotor. On the advancing side of the rotor, the main differences lie towards the blade-tip, while on the retreating side of the rotor the main discrepancies are located along the blade leading edge. The instantaneous pressure of test case *ID-Rime* shows a similar trend to the clean rotor with the magnitude and distribution of p' being comparable. Contrarily, the *ID-Glaze* test case exhibits markedly different behaviour. A peak in the instantaneous pressure fluctuation is observed at the location of the ice *horn* during the *ID-Glaze* test case. The ice *horns* subsequently represent a strong and potentially distinguishable noise source.

Subsequently, a computational aeroacoustic analysis using the set of FW-H equations is conducted to further comprehend the noise signals of the iced rotors. The noise signals are evaluated at the four observer locations highlighted during Section 6.3.3. It can be seen that at each observer location there is a slight increase in the strength of the noise signal of the iced rotors when compared to the clean rotor. In particular of the test case *ID-Glaze*. This is thought to be an effect of the more significant change in leading edge profile caused by the slight ice *horns* towards the rotor tip. The noise signals from observer locations *B*, *C*, and *D* exhibit peaks corresponding to the blade passing frequency. The peak of the noise signal is when the difference between the clean and iced rotors is greatest. With there being no flow separation, there is no high frequency noise content as observed in Chapter 2. In general, it is observed that the position of the ice detection system would be best placed where the noise signal of the main rotor is greatest. Ideally, this means as far towards rotor blade tip and as close beneath the rotor as possible.

Although this work now considers the three-dimensional flow physics of the rotor, capturing the smaller scale vortical structures produced by the ice shapes remains important. To that end, a limitation of this work is that the RANS equations are used to solve the flow field. While the larger scale vortices such those produced at the blade-tip can be captured, the smaller scale vortices such as those produced by the ice cannot be captured. To address this issue, work presented in Ref. [217] used a hybrid RANS/LES approach to assess the acoustic noise signal of an iced oscillating wing. The study showed considerable improvement with respect to modelling the smaller scale vortical structures and consequentially the higher frequency ice induced noise content.

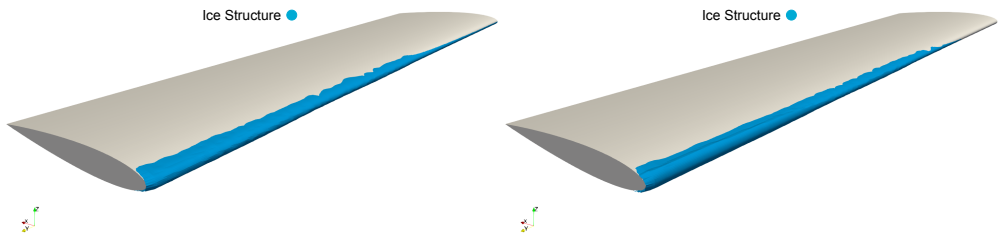

(a) *ID-Rime.* **(b)** *ID-Glaze.*

Figure 6.13: *SRB-II numerical ice shape predictions displayed throughout the ice detection conditions outlined in Table 6.3. Where the ice accretion is represented in blue. Selected test conditions do not induce ice shed events due to there being a limited icing exposure time of* 15 *seconds.*

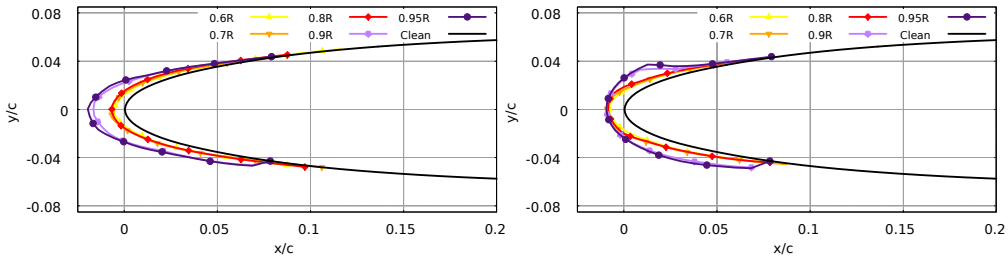

(a) *ID-Rime.* **(b)** *ID-Glaze.*

Figure 6.14: *SRB-II numerical ice shape predictions displayed at selected radial sections for the test conditions outlined in Table 6.3. Displayed at radial locations* $r/R = 0.6, 0.7, 0.8, 0.9, 0.95$. *The ice shapes are normalized by the rotor chord length and are shown in the* $x - y$ *plane.*

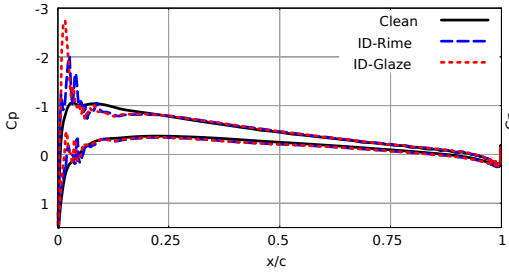

(a) $r/R = 60\%$, $\psi = 90°$.

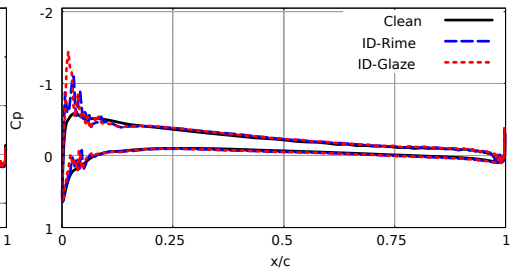

(b) $r/R = 60\%$, $\psi = 180°$.

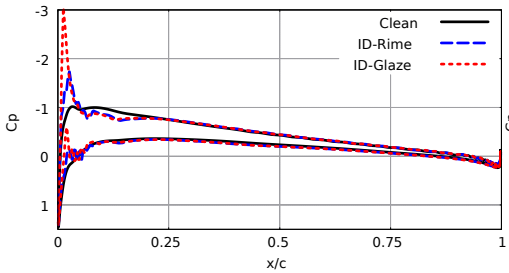

(c) $r/R = 70\%$, $\psi = 90°$.

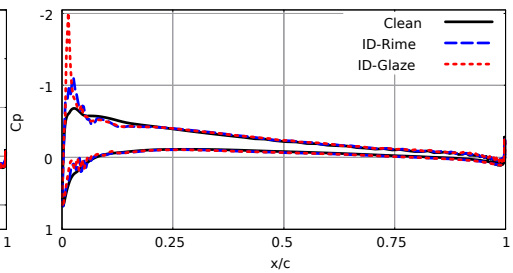

(d) $r/R = 70\%$, $\psi = 180°$.

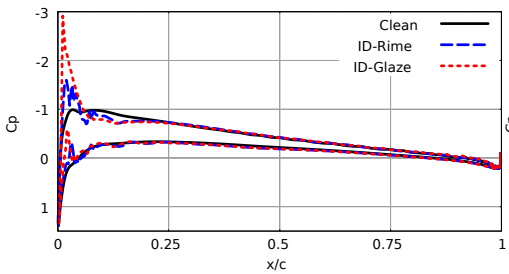

(e) $r/R = 80\%$, $\psi = 90°$.

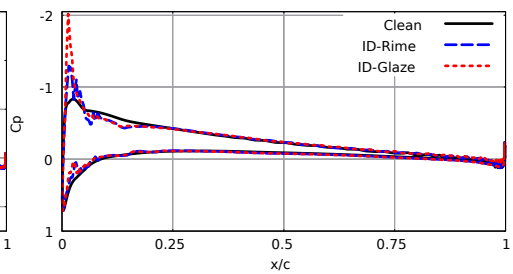

(f) $r/R = 80\%$, $\psi = 180°$.

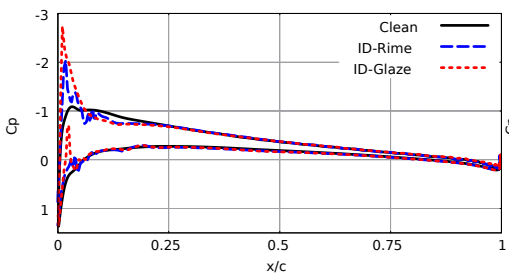

(g) $r/R = 90\%$, $\psi = 90°$.

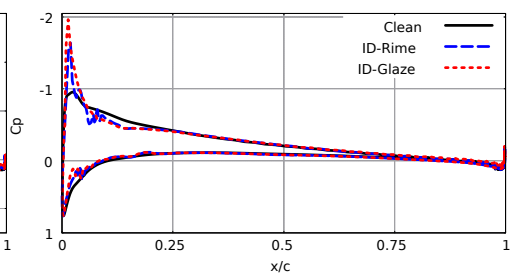

(h) $r/R = 90\%$, $\psi = 180°$.

Figure 6.15: *Pressure distributions of the clean and iced rotors from Table 6.3. Displayed at radial locations* $r/R = 60, 70, 80, 90\%$ *and at advancing and retreating azimuth positions* $\psi = 90°$ *&* $180°$. *The spatial distribution is normalized by the rotor chord length plus the ice thickness at the leading edge.*

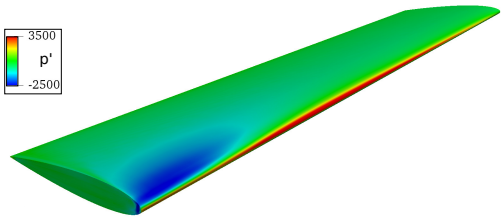

(a) *Clean rotor at* $\psi = 90°$.

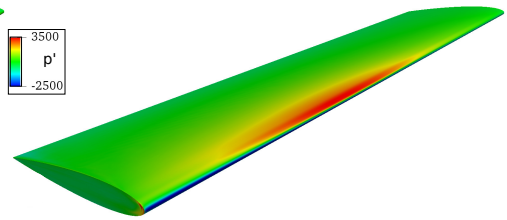

(b) *Clean rotor at* $\psi = 180°$.

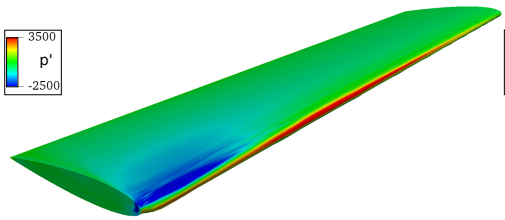

(c) *ID-Rime rotor at* $\psi = 90°$.

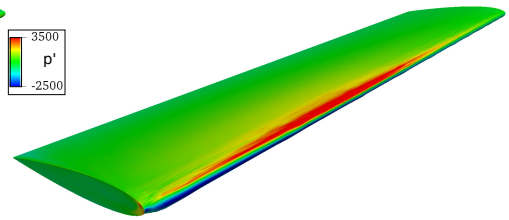

(d) *ID-Rime rotor at* $\psi = 180°$.

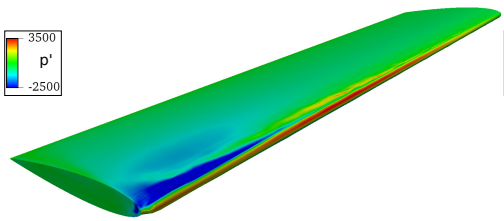

(e) *ID-Glaze rotor at* $\psi = 90°$.

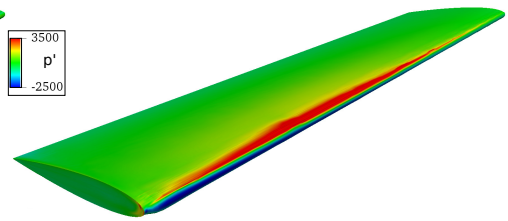

(f) *ID-Glaze rotor at* $\psi = 180°$.

Figure 6.16: *Instantaneous pressure fluctuations,* p'*, over the clean and iced rotors during the test conditions from Table 6.3. Displayed at azimuth angles,* $\psi = 90°$ *and* $\psi = 180°$*. Where the instantaneous pressure fluctuations can be described by* $p' = p - p_{mean}$ *and are used to highlight the iced rotor noise sources.*

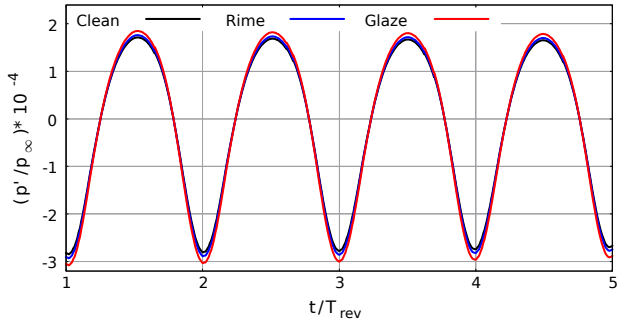

(a) *Observer location A.*

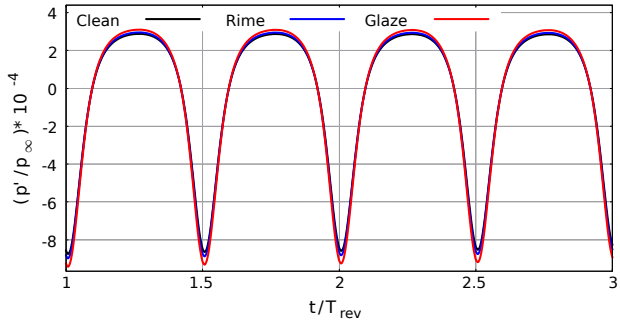

(b) *Observer location B.*

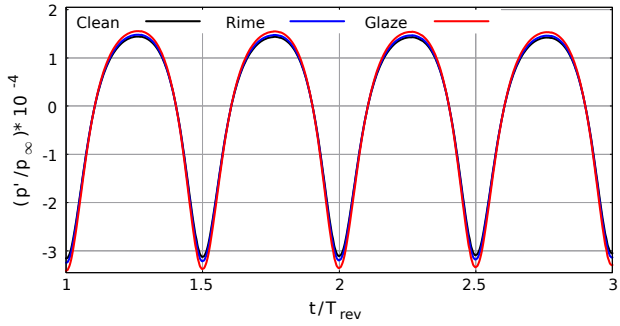

(c) *Observer location C.*

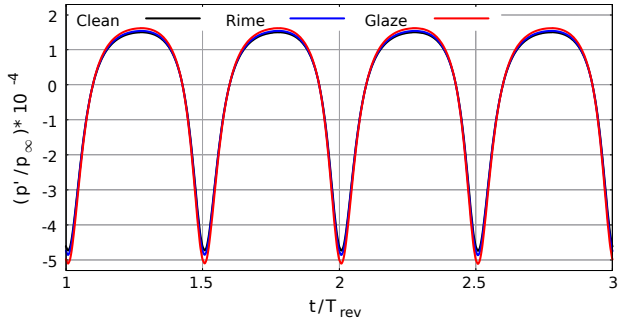

(d) *Observer location D*

Figure 6.17: *Far-field noise signal of the clean and iced blades at selected observer locations. Where the acoustic pressure is normalized by freestream pressure and the time is non-dimensionalized by the period of revolution.*

6.6 Conclusion

In this work, a new approach towards simulating and detecting fully three-dimensional ice accretion on rotors is introduced. The approach utilizes a collective suite of numerical tools to successfully simulate ice accretion on rotorcraft. A key aspect of the work is the inter-relationship between the numerical tools, in that, each tool is highly dependent on the others. Accordingly, each tool has been developed primarily with rotorcraft ice accretion in mind. The environmental conditions replicate those of the SRB-II test campaign from the Anti-icing Material International Laboratory in the Université du Québec à Chicoutimi, Canada. Experimental measurements obtained during the icing tests are compared to the numerical predictions from this work, which include properties such as the ice thickness at the blade-tip and the ice shedding location. Overall, the numerical predictions are in good agreement with the experimental data. Significantly, the numerical predictions underline the non-linearity of the ice accretion radially. Suggesting greater quantities of ice accrete towards the blade-tip, leading to the presence of ice *horns* which are particularly detrimental to rotor performance. Subtleties in the modelling techniques, which subsequently have a significant impact on the final ice shapes, are highlighted. These include the influence of the model for the temperature profile within the ice layer, and appropriate modelling of the liquid film on the blade surface. Finally, a set of ice detection test cases were setup to establish the performance degradation of iced rotors with limited exposure times. The results demonstrate the increased safety concerns associated to the glaze ice regime due to the severe performance penalities of even small ice *horns*. Additionally, the instantaneous pressure fluctuations and noise signals of the iced rotors are analysed to provide an early insight into the potential use of acoustic ice detection technologies.

CHAPTER 7

Conclusions and Perspectives

7.1 Summary

ROTORCRAFT icing remains a relatively rudimentary research field despite having been studied since as early as the 1970's by means of artificial in-flight icing trails and icing research wind tunnels. Lately, numerical techniques have been identified for simulating rotorcraft icing. However, current limitations have restricted their ability to accurately capture many of the physical attributes present in three-dimensional ice formation on rotors. This doctoral thesis presents original research by developing and evaluating numerical techniques to enable a high-fidelity computational analysis of the rotorcraft icing problem. A comprehensive understanding of rotorcraft icing is pivotal for improving rotorcraft safety and encouraging innovation to mitigate the risks and costs associated with the icing problem.

This thesis was divided into three main parts containing six technical chapters, each address a specific issue directly related to rotorcraft icing. The first part of this thesis contained one chapter and was dedicated to identifying possible technologies for the in-flight ice warning systems. The conceptual design phase of an acoustic ice detection system was subsequently introduced. The second part of the thesis was devoted to the development and validation of three-dimensional rotorcraft icing tools. This part contained four chapters which discussed advancements in mesh deformation techniques, rotorcraft computational fluid dynamics, and particle in cell methods. The third part and final technical chapter of this thesis established a novel high-fidelity ice prediction and detection approach, utilizing previously presented numerical advancements.

7.2 Conclusions

The research questions established at the beginning of this work conveyed the known unknowns within the field of rotorcraft icing. Over the course of this work, these underlying questions, which may be considered as fundamental to the progression of rotorcraft icing, have been investigated and carefully studied. Resultantly, this thesis closes with the final remarks of the now known knowns present in the research questions:

Research Question 1: Are the acoustic signals generated by glaze and rime ice types distinguishable on rotor blades?

Conclusion 1: The work reported in this thesis has established the first acoustic characterisation of glaze and rime ice structures. Through analysing the signals of iced oscillating airfoils and rotors, a clear distinction between the high-frequency noise of glaze and rime ice structures has been observed. In general, rime ice structures exhibit a tonal peak corresponding to the oscillating frequency of the airfoil or the rotational frequency of the rotor. While glaze ice structures display similar noise levels at this low frequency, they also contribute to significant levels of noise at the higher frequency range of the sound spectra where there is minimal contribution from rime ice structures. It has been shown that glaze and rime ice structures produce recognizably different noise signatures and therefore the acoustic signature of the iced rotor can be used to determine the ice characteristics

Research Question 2: What are the most effective mesh deformation strategies to account for moving ice boundaries?

Conclusion 2: Standard mesh deformation strategies for icing are either computational expensive for large three-dimensional problems or suffer from poor mesh quality properties. Radial Basis Function mesh deformation techniques and data reduction schemes have been introduced in this thesis to address the issues intrinsic to the moving ice boundary. Radial Basis Functions provide a suitable approach to ensure high-quality mesh deformation for challenging iced geometries and multi-step ice accretion. The data reduction schemes presented facilitate the use of Radial Basis Functions even on large datasets. The Radial Basis Function mesh deformation technique is highly recommended and provides a significant advantages over more conventional techniques including the spring and linear elasticity analogy.

Research Question 3: What is the status of open-source Computational Fluid Dynamics software for rotorcraft flows?

Conclusion 3: This thesis provides a preliminary evaluation of the first open-source rotorcraft Computational Fluid Dynamics code by developing rotorcraft simulation capabilities in the well established SU2 solver. A new core feature to enabling simulations of the blade kinematics of rotorcraft has been introduced. Simulations have been demonstrated for hover and forward flight test conditions. The contemporary open-source nature of the code means that it provides benefits of new and effective numerical techniques such as radial basis function mesh deformation and the supermesh technique for non-conformal boundary interfaces. This work now establishes a platform to further explore issues at the forefront of the rotorcraft community, including research topics such as blade design optimisation and coupled fluid-structure interactional problems.

Research Question 4: Are particle tracking techniques able to capture the fundamental physics of clouds containing supercooled water droplets entrained in rotor flows?

Conclusion 4: Tracking particles in complex rotorcraft configurations requires the design of efficient point-locating algorithms. The simulation of rotorcraft flows frequently make use of multi-zone unstructured deforming mesh. However, numerical techniques to perform particle tracking on such mesh were not available in the literature. New techniques have been introduced for Lagrangian particle tracking in a mesh with arbitrary motion as well as across non-conformal boundary interfaces to enable the simulation of clouds containing individual supercooled water droplets in complex rotorcraft flow fields. These new techniques have been demonstrated on practical test cases including a hovering rotor and a tilt-rotor configuration.

Research Question 5: Are numerical tools at a stage where they can be used to aid the certification process for rotorcraft flight in icing conditions?

Conclusion 5: It is widely recognised that natural in-flight icing trails cannot be substituted by a singular alternative form of testing and that artificial in-flight icing trails and icing wind tunnel research should be used harmoniously alongside natural in-flight icing trails throughout the certification process. Accordingly, the role of alternative icing approaches is to aid and not replace natural in-flight icing test during

the certification process while ensuring the full icing envelope is covered. Even with the aid of conventional alternative icing approaches, certain areas within the icing envelope are more challenging to assess than others. Certification through means of simulation may therefore provide a reasonable solution to some of the most challenging test conditions within the icing envelope. The development of high-fidelity numerical tools within this thesis has helped advance such simulation capabilities. Numerical techniques may now safely simulate some of the most environmentally challenging and dangerous points within the icing envelope. Moreover, numerical techniques help to address the limitations of artificial in-flight tests and experimental wind tunnels by simulating full-scale rotors without restricting cloud size and droplet diameter. The progression from standard hybrid two/three-dimensional tools towards more advanced fully three-dimensional tools has long been a requirement to improve the authenticity of rotorcraft icing code predictions. Looking ahead, with these recent advancements there is certainly scope for the use of numerical tools throughout the certification process of rotorcraft as is now common practice in the fixed-wing aircraft industry.

7.3 Wider Impact

The original research presented in this thesis contributes to better knowledge and understanding of rotorcraft icing. The scientific contributions of this thesis are twofold and consist of (i) the development and validation of numerical tools to improve three-dimensional rotorcraft icing predictions, and of (ii) the innovation of computational aeroacoustic ice detection technologies capable of distinguishing different types of ice in real-time. The research has led to improved predictions in rotorcraft icing and will hopefully have a long-lasting impact on future research.

In acknowledgement of the European Union for its funding of the NITROS project, it was paramount that this work was able to give something back to the wider scientific community. For this reason, the dissemination of this work was taken seriously as shown by the list of publications. Additionally, the focus on developing open-source numerical tools ensures the majority of the software developed in this thesis is available to the general public. This will provide the foundation to motivate further development and promote innovation. An example of this is the open-source SU2 code which is freely available on GitHub where all the latest code developments can be found alongside up-to-date code documentation and tutorials.

7.4 Perspectives

The conclusions to the major research questions from this work indicate how far the numerical modelling of rotorcraft icing and acoustic ice detection technologies have progressed. However, despite this, there remain key areas of research that require additional investigation beyond the scope of this project due to its restricted time-window. The outlook for rotorcraft icing will now be discussed along with the remaining open questions:

- Numerical predictions of in-flight ice accretion on rotorcraft help us to understand the dangers associated to icing without the inherent risks which accompany natural in-flight icing trails. However, a major critique of numerical predictions is that they lack sufficient validation due to the absence of reliable data from artificial in-flight icing trails and icing research wind tunnels. To that end, it is imperative that rotorcraft icing codes use code-to-code comparisons as a method of cross-code validation. Needless to say, numerous codes are needed to make code-code validation possible. However, the work from Nanjing University [73–75] is currently the only potential candidate for code-to-code comparison of fully three-dimensional icing predictions. Despite this, further comparisons between the work from this thesis and the referenced work would provide a more comprehensive insight into three-dimensional rotorcraft icing prediction capabilities.

- Rotor blades exhibit strong aeroelastic behaviour as an occurrence of the interactions between the aerodynamic and inertial forces on the blade. To address this, comprehensive numerical tools are required which can appropriately model both the complex rotor flow field and the aeroelastic response of the rotor blades within a single process. To allow the coupling of flow solvers with structural solvers, the airloads computed within the flow solver have to be provided to the structural solver and blade deflections computed within the structural solver have to be provided to the flow solver. Within the wide spectrum of literature, multiple approaches have been used. The most commonly used method is the loosely coupled approach [146, 218–222] where the blade position is updated usually after each full revolution. This approach is well suited for the identification of trim conditions. The alternative approach is a tightly coupled one where the loads and the blade deflections are updated at every time-instance [144, 222–226]. However, what remains lacking within the literature is a coupled fluid and structural model which is open-source. The open-source flow solver SU2 [133] and structural solver MBDyn [227] are already well established within their own disciplines. The emergence of the open-source preCICE coupling library [228] could now provide an entirely open-source framework for the aeroelastic modelling of rotor blades.

- Collaborative work together with the Technical University of Kaiserslautern and the University of Michigan has helped address the impracticalities of using high-fidelity numerical simulations for real-time ice detection systems. The work proposes a novel approach towards developing a real-time in-flight ice detection system using computational aeroacoustics and Bayesian neural networks [217, 229, 230]. A dataset of the computational aeroacoustics of iced components such as a wing is first generated in an offline phase. The dataset generated is then used to construct a Bayesian neural network that provides (i) mapping from observed far-field broadband noise level to predictions of aerodynamic performance indicators, and (ii) uncertainty information indicating the quality and credibility of these predictions. While the icing simulation, aeroacoustic prediction as well as the construction of Bayesian neural network model all require potentially extensive computational resources in the offline phase, the prediction of aerodynamic

performance indicators based on measured far-field noise level as well as their associated uncertainty information can both be obtained rapidly in the time-critical online phase in-flight. While this collaborative project is showing promising early signs, it requires larger datasets to improve the predictions of the neural networks. Moreover, current simulations are based on iced airfoils and wings and the extension towards rotors would also provide valuable additional information.

Part IV

Appendix

APPENDIX $\mathcal{A}$

Simulation of a Wing-Tip Mounted Propeller Configuration from the Workshop for Integrated Propeller Prediction (WIPP)

The contents of this chapter appeared in:

Zhou, B.Y., Gauger, N.R., Morelli, M., & Guardone, A., *Special Session: Aerodynamics and Performance of Integrated Propellers II, AIAA Aviation Forum*, Reno, Nevada, June 15–19, 2020. DOI: https://doi.org/10.2514/6.2020-2683.

Abstract

In this work, the turbulent flow field around a wing-tip mounted propeller configuration is simulated using the model and test conditions released by the Workshop for Integrated Propeller Prediction (WIPP). In particular, the unsteady Reynolds-averaged Navier-Stokes and enhanced delayed detached eddy simulations with Spalart-Allmaras turbulence model are performed in a time-accurate manner with the multi-zone sliding mesh technique in which the propeller is allowed to rotate while the wing and the nacelle remain stationary. Time-averaged pressure coefficients at six spanwise locations along the wing surface are shown to be in good agreement with the experimental data, including the two locations directly in the propeller slipstream. Numerical predictions on finer grids are found to capture the general shapes of the wake profiles well compared with experimental data from the wake survey, but the peak values are under-predicted on all wake profiles except for the swirl velocity. Moreover, there appears to be a shift radially inward indicating that the wake quantities, and the thrust in particular, do not extend beyond the propeller tip, as suggested by the experiment. The simulations on finer grids reveal two major noise sources of this wing-tip mounted propeller configuration, namely the turbulent wake and tip vortex generated by the propeller blades, both impinging upon the wing and nacelle surfaces as they convect downstream. Visualization of the surface pressure fluctuations reveals the noise footprints on this integrated propeller-wing system. In particular, the impingement of propeller blade tip vortices on the leading edge of the wing immediately below the nacelle is identified to be the dominant noise source. Making inroads into sensitivity analysis of the full propeller-wing assembly, an unsteady discrete adjoint approach based on algorithmic differentiation is applied to evaluate the surface sensitivity of an isolated WIPP propeller with respect to the mean thrust coefficient design objective.

A.1 Research Question and Hypothesis

Research Question A1: What impact do propeller-wing interactional effects have on aircraft performance and noise predictions with reference to future full-electric configurations?

Hypothesis A1: The simulation of isolated components such as rotor blades, propellers, or wings provides helpful insight into the design and performance of critical components. However, when rotors or propellers operate in the vicinity of external bodies such as the fuselage or wing, the performance can become compromised and subsequently quite different. The simulation of complete configurations is, therefore, necessary to fully understand the interactional behaviour of complex multi-body systems. Currently, only a limited number of experimental test campaigns have taken place with the primary objective to understand the interactional behaviour between wing-tip mounted propeller configurations, subsequently hindering the progression of numerical predictive capabilities.

A.2 Introduction

PROPELLER driven aircraft have garnered renewed interest in the aircraft industry due to the emergence of electric and distributed propulsion systems. These systems, typically installed on lighter and slower vehicles, demand less engine power and attain lower blade tip speed, allowing them to achieve 10-20% higher fuel efficiency over typical turbofan engines in static and flight test conditions [231]. This inclination has led NASA to reinstate its X-Plane series, and with this, the latest aircraft under development is the experimental X-57 plane. Throughout the research and development of this aircraft, one of the key features is the use of wing-tip mounted propellers to increase the efficiency of the aircraft. A clean wing-tip produces strong three-dimensional vortical structures, so intuitively, the placement of propellers mounted on the wing-tips can help reduce the wings induced drag by attenuating the wing-tip vortex by the propeller slipstream. In the past, a major drawback of wing-tip mounted propellers has been the integration of the propeller with the airframe and the issue of having a high mass at the wing tip causing aeroelastic problems. The emergence of electric and distributed propulsion systems however increases the design flexibility by eliminating potential penalties of down-scaling the motors [232].

Wing-tip mounted propellers have a long and rich history due to their performance enhancements which have been well known for years on end. As early as 1969 Snyder [233] showed that wing-tip mounted tractor propellers could decrease wing drag and increase the wing's maximum lift if the propeller rotated in the opposite direction to that of the wing-tip vortex. Later the work of J. C. Patterson et al. in 1985 used wind tunnel experiments to study the effects of a wing-tip mounted pusher turboprop on the aerodynamic characteristics of a semi-span wing [234]. Their work suggested that large propulsive efficiency benefits and significant induced drag reductions could be achieved through the use of wing-tip mounted propellers. A year later in 1986, L. R. Miranda and J. E. Brennan began numerically investigating the benefits which could be achieved by properly mounting propellers at the wing-tips [235]. Their results confirmed the

experimental wind tunnel test findings found the previous year and concluded that indeed significant aerodynamic performance improvements could be found from wing-tip mounted propellers. More recently in 2019, Sinnige et al. [236] noted that the present literature lacks comprehensive analyses of the aerodynamic interaction effects relevant of the wing-tip mounted propeller which are of crucial importance to fully exploit the configuration and harness the potential aerodynamic benefits. Their work used experimental PIV measurements downstream of the propeller and surface oil flows to to understand the interaction effects of the wing-tip mounted propeller. Moreover, it showed significant performance improvements when compared to a conventional configuration.

An undesirable factor associated with propeller-driven engines is their noise level. While the dominant noise source in such engines is due to the unsteady aerodynamic loading on the rotating propeller blades, various installation/integration noise sources have also been shown to be significant. These are typically known as the propeller-wing or propeller-fuselage interaction noise whereby the turbulent wake and tip vortices from the propeller blades impinge on the wing and the pylon transmitting unsteady aerodynamic loads leading to structure-borne cabin noise [237]. It is widely recognized that for certification of propeller-driven vehicles, aeroacoustic considerations must be the central focus of the design and no longer be treated a side constraint. Therefore accurate and robust numerical tools are urgently needed by the aircraft industry to characterize, predict and more importantly optimize novel propeller-powered configurations.

It is only until recently, however, that wing-tip mounted propellers are beginning to be seriously considered as viable configurations. To further understand wing-tip mounted propellers an open Workshop for Integrated Propeller Prediction (WIPP) has been established. The WIPP configuration provides experimental results of an isolated wing-tip mounted propeller for numerical cross-code validation. The database allows for the assessment of important parameters to predict complex propeller-wing interactional effects and to understand the impact of the propeller on the wing's aerodynamic efficiency.

In this work, we seek to utilize the extensive and open experimental WIPP database to simulate and validate the flow field of the full WIPP configuration. The open-source multi-physics SU2 solver [112] will be used for the validation exercise. To accurately capture the rich propeller-wing interactional flow physics the blades will be fully resolved and to allow the propeller to move in relative motion to the wing a sliding mesh technique will be used. In so doing, we aim to elucidate the key noise generation mechanisms and visualize the noise footprint both on the propeller and wing surfaces.

The remainder of this extended abstract is organized as follows. In Section A.3, the WIPP model, as well as the test conditions are described. In Section A.4, the multi-physics SU2 solver is presented. Section A.5 presents the SU2 simulation results and their comparison against experimental data while the conclusion and outlook for furture work are discussed in Section A.6.

A.3 WIPP Model Description

The computational test case replicates the WIPP experiment of a wing-tip mounted propeller, as shown on Figure A.1. The test took place in the Lockheed Martin Low-Speed Wind Tunnel (LSWT) in Marietta, Georgia, USA as part of the NASA/Armstrong X-57 research program. The WIPP model was designed by Mark Skeehan at Lockheed Martin Aeronautical Systems and was fabricated by Empirical Systems Aerospace (ESAero). The WIPP model is a $40.5\,\%$-scale semi-span model of the X-57, specifically designed to allow it to be mounted onto the LSWT external balance. The model is positioned vertically and incorporates a non-metric boundary layer splitter plate which is mounted to the LSWT external balance. The span of the wing relative to the wind tunnel floor is $67.065\,\mathrm{in}$. The wing has a taper ratio of 0.7 and an aspect ratio of 6.7. The chord of the wing at its root is $11.6\,\mathrm{in}$ and the chord of the wing at its tip is $8.6\,\mathrm{in}$. The mean aerodynamic chord of the wing can then be considered as $10.15\,\mathrm{in}$. The wing also contains a slight leading-edge sweep of $1.9°$. The model uses a four-bladed propeller system based on an already available $10\,\%$-scale C-130 model. The propeller diameter is $16.2\,\mathrm{in}$. The propeller blades are calibrated for a $38°$ pitch at the root and have a significant negative twist from the root to the tips of the blades. The propeller is mounted onto a nacelle at the wing tip. The nacelle is $24.15\,\mathrm{in}$ long and has a maximum diameter of $4.75\,\mathrm{in}$ at its center before being tapered and rounded at the leading and trailing edges.

To measure the interactional effect of the propeller on the wing, the model was instrumented with a total of 96 static pressure taps which were located at six different wing spanwise locations. These spanwise locations were $34\,\mathrm{in}$, $44\,\mathrm{in}$, $54\,\mathrm{in}$, $57\,\mathrm{in}$, $60.75\,\mathrm{in}$ and $63\,\mathrm{in}$ from the wind tunnel floor. Each of these spanwise sections then contained 10 static pressure taps on the upper surface and 6 static pressure taps on the lower surface. Wake data also captured the flow-field behind the propeller, nacelle and wing during the experiment using a wake survey system. This system used a wake rake which contained a total of twelve 7-hole pressure probes mounted on a strut $3.0\,\mathrm{in}$ apart.

The tests were then conducted at a variety of Mach numbers, thrust coefficients, and angles-of-attack. The flight speeds investigated were Mach 0.04, 0.08 and 0.11. To achieve variations in the thrust coefficient, the rotational speed of the model propeller was altered. The thrust coefficients investigated ranged from $C_T = 0 \rightarrow 0.40$. There were then three different angle-of-attack schedules planned termed A1, A2, and A3 which ranged from $-10° \rightarrow 20°$.

Various experimental configurations were also tested for the calibration of the instrumentation, for the assessment of the effectiveness of the ailerons during flow separation, and for determining the influence of the propeller on the performance of the wing. The configurations tested hence included an empty wind tunnel with the model removed, an isolated wing, and an integrated wing and propeller. In total 198 test runs were completed.

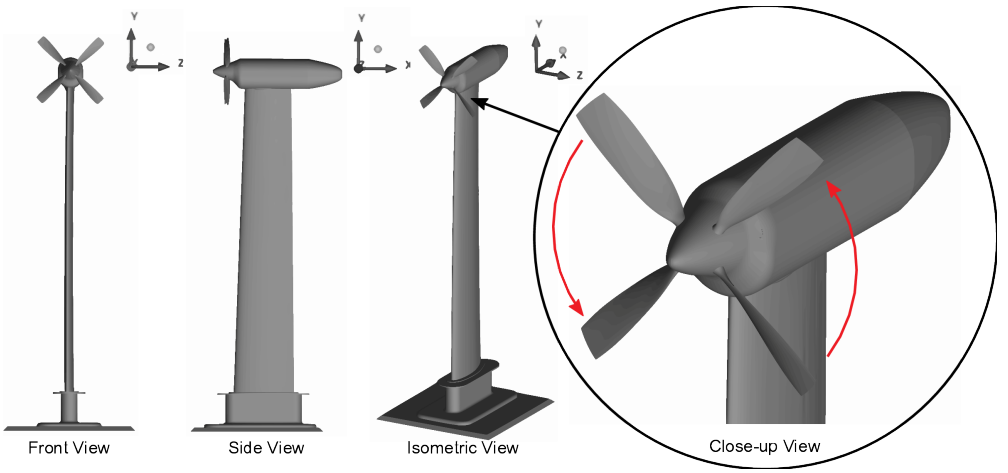

Figure A.1: *The wing-tip mounted propeller configuration*

A.4 Prediction Analysis Methodologies

The SU2 open-source software suite was specifically developed for solving problems governed by partial differential equations (PDEs) and PDE-constrained optimization problems. It was developed with the aerodynamic shape optimization problems in mind. Therefore the suite is centered around a Reynolds-averaged Navier-Stokes (RANS) solver capable of simulating compressible, turbulent flows commonly found in problems in aerospace engineering. The governing equations are spatially discretized using the finite volume method, on unstructured meshes. A number of convective fluxes discretization schemes have been implemented, such as the Jameson-Schimdt-Turkel (JST) scheme and the upwind Roe scheme. The turbulence can be either modelled by the Spalart-Allmaras(S-A) model or the Menter Shear Stress Transport (SST) Model. For unsteady flows, a second-order dual time-stepping method can be used to obtain time-accurate solutions.

For scale-resolving capabilities, the enhance delayed detached eddy simulation (EDDES) based on the S-A model was implemented in SU2 by Molina [238] and has been demonstrated to successfully predict separated flows [118, 239]. To mitigate the “grey area" problem characterized by slow transition from RANS to LES mode in the shear-layer, a shear-layer adapted (SLA) sub-grid scale model [240] was implemented. In addition, to limit the numerical dissipation in LES part of the EDDES model, the inviscid flux is computed using the so-called simple low dissipation advection upstream (SLAU2) [241].

A.5 Results

A.5.1 Test Conditions

The preliminary simulation results of the WIPP wind tunnel test are based on the fully integrated wing and propeller configuration. Run numbers 33 and 80 of the experimental database were used for the validation of the flow field. The test conditions from run

number 33 and 80 are shown in Table A.1. The experimental results from run number 33 contain the surface pressure data along the spanwise direction of the wing and the experimental results from run number 80 contain the wake survey data. The α schedule used in this run was A3 where the angle-of-attack ranged from $-10^\circ \rightarrow 20^\circ$, however, only $\alpha = 0.0$ was considered during the early stages of this work. The flight speed of this run was the highest tested in the LSWT at Mach $= 0.11$. The wind tunnel freestream pressure, at this flight speed was recorded and measured as Q $= 18.31$ lbf/ft^2. The mean aerodynamic chord of the wing was used as the reference length for computing the Reynolds number of flow field and was computed to be Re $= 0.660 \times 10^6$. The propellers were approximately rotating at 8000 RPM to achieve a thrust coefficient of $C_T = 0.4$.

Table A.1: *WIPP Configuration and Parameters.*

Configuration	α Schedule	Mach [-]	Q [lbf/ft^2]	Re [-]	C_T [-]	Run No
Integrated Wing/Propeller	A3	0.11	18.31	0.660×10^6	0.4	33, 80

A.5.2 Mesh Generation

The simulation of propeller-wing interactions are rich in flow physics and so require a high fidelity of computational modelling. Thus, to allow the propeller to move in relative motion to the wing the numerical discretization of the mesh is required. In this work, the sliding mesh technique is used to allow the propeller to rotate while the wing remains stationary. The sliding mesh implementation used in SU2 is based on the super-mesh approach described by Rinaldi et al. [176] and allows for flux-conserving treatment of non-conformal interfaces. The numerical discretization of the mesh used in this work is shown in Fig. A.2 and shows the cylindrical cut-out where the propeller is positioned. The mesh is hereafter considered as a multi-zone problem where the external stationary zone and the internal rotating internal zone are considered as separate entities and a nearest-neighbour interpolation technique is used for data exchange between the zone interfaces.

To simplify the generation of the mesh, the clamp at the base of the wing was not considered since there was no pressure tap measurements and wake data collected this close to the root of the wing. An artificial wall was then introduced into the simulation where the root of the wing meets the external balance at $y = 7.115$ in using euler boundary conditions to avoid the need of modelling the boundary layer of the artificial wind tunnel floor. The leading edge of the nacelle was also reconstructed in order to insert the sliding mesh surface interfaces. With the reduction in the length of the nacelle being only slight and with there being no wake data recorded in this region due to it being too close to the propeller this assumption was justified. Artificial wind tunnel inflow and outflow walls were placed at 25 propeller radii upstream and downstream of the model propeller and wing at $x = \pm 25$R. Wind tunnel walls were also placed above the model at $y = 15$R and either side of the model at $z = \pm 10$R.

The stationary zone containing the wing and nacelle consists of mixed quadrilateral and triangular surface elements elements. The rotating propeller surface mesh uses tri-

angular elements. The boundary layer of the wing, nacelle and propeller is sufficiently resolved to ensure $y^+ < 1$. Tetrahedral volume elements are used outside of the boundary layer. The rotating internal boundary interface and stationary external boundary interface both use entirely triangular surface elements.

A prerequisite for accurate wake modelling of the WIPP configuration is a high-quality and high resolution mesh in the region behind the propeller to preserve the main blade-tip vortices and smaller scale vortex structures. Suitable refinement is important to reduce numerical dissipation of the wake so that blade-tip vortex/wing interaction effects are correctly modelled. The importance of the mesh refinement region in the near-field propeller wake around the nacelle is thus studies in this work. Three levels of refinement are evaluate with different node distributions. The details of the individual grids is outlined in Table A.2.

Table A.2: *Details of the three levels of grid refinement.*

Name	No. Volume Elements			Wake Element Size*	Density Region
	Propeller	Wing	Total	(l/c_{tip})	
Grid-01 (G1)	5.14M	5.8M	10.9M	0.4195	No
Grid-02 (G2)	12.3M	23.0M	35.3M	0.167	No
Grid-03 (G3)	12.3M	52.6M	64.9M	0.0682	Yes

* cell edge length l non-dimensionalized by blade tip chord c_{tip}, measured at a distance $0.5R_{\text{prop}}$ behind the tip of the propeller.

Grid G1 has the lowest refinement in this study and is shown in Fig. A.2a. In G1 there are 5.14M elements in the internal propeller zone and 5.8M elements in the external wing zone. In total, the combined number of elements across both zones is 10.9M. It has a maximum surface element size of $0.004\,\text{m}$ which expand at a ratio of 1.2 away from the surface. The distribution of elements in the near-field wake region is shown more closely in Fig. A.2d. This leads to a computational efficient solution at the expense of the wake accuracy. Grid G2 has a higher refinement than grid G1 and is shown in Fig. A.2b. There are 12.3M elements in the internal propeller zone and 23.0M elements in the external wing zone. In total, the combined number of elements across both zones is 35.3M. It has a maximum surface element size of $0.004\,\text{m}$ which expand at a ratio of 1.05 away from the surface. The distribution of elements in the near-field wake region is shown more closely in Fig. A.2e. This improves wake refinement globally over the entire span of the wing as well as the propeller wake. In the positive y-direction away from the nacelle and towards the blade tip the wake however naturally begins to coarsen. Grid G3 has the highest refinement of all the grids and is shown in Fig. A.2c. In G3 there are 12.3M elements in the internal propeller zone and 52.6M elements in the external wing zone. In total, the combined number of elements across both zones is 64.9M. It has a maximum surface element size of $0.002\,\text{m}$ which expand at a ratio of 1.1 away from the surface. Increasing the expansion ratio allowed for points with minimal influence, such as close to the wing root where there is no measured wake data, to be redistributed elsewhere. A local density region was then placed around the nacelle and propeller wake with a maximum element size of $0.003\,\text{m}$ in this region. The distribution of elements in the near-field wake region is shown more closely in Fig. A.2f. This further improved the wake refinement however only locally and in the critical area

to minimize the computational cost where possible.

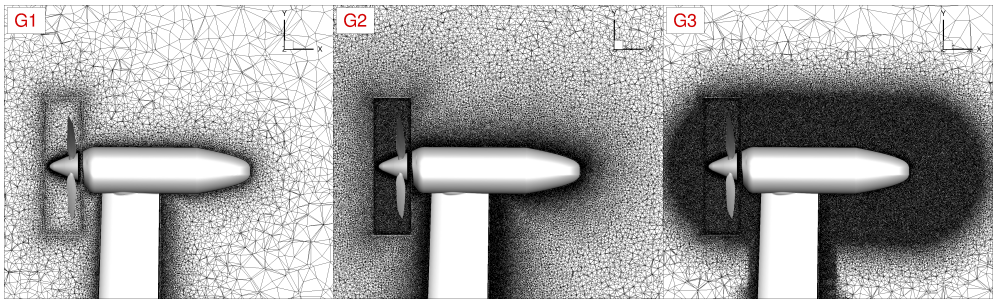

(a) *Grid-01 at $z = 0$ in.* **(b)** *Grid-02 at $z = 0$ in.* **(c)** *Grid-03 at $z = 0$ in.*

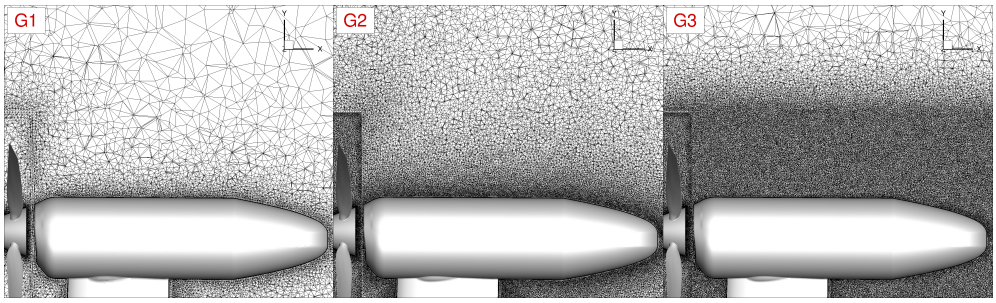

(d) *Grid-01 near-field wake refinement* **(e)** *Grid-02 near-field wake refinement* **(f)** *Grid-03 near-field wake refinement*

Figure A.2: *Spatial resolution of the grids G1, G2, and G3 used for the sensitivity analysis. Displaying the distribution of nodes surrounding the nacelle and near-field wake region.*

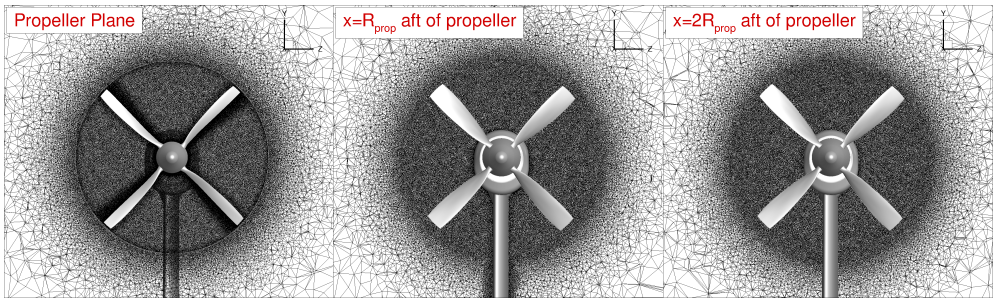

(a) *Propeller plane.* **(b)** $x = R_{prop}$. **(c)** $x = 2R_{prop}$.

Figure A.3: *Spatial resolution of grid G3 in the $y - z$ plane at the propeller and stations aft of the propeller at $x = R_{prop}$ and $x = 2R_{prop}$. Displaying the continuous refinement in the propeller wake region.*

A.5.3 Aerodynamic Prediction

The simulation are performed on all three grids using unsteady RANS with Spalart-Allmaras turbulence model (URANS-SA). In addition, EDDES-SA simulations are also performed on grids G2 and G3 in attempt to better resolve the turbulent wake behind the propeller. A total of 15 propeller revolutions are simulated. The flow statistics are computed over the last 10 revolutions. The physical time step is 2.1×10^{-5} s which is equivalent to 1° of revolution per time step at approximately 8000 RPM.

The static pressure tap measurements recorded during run number 33 are used for validation of the chordwise pressure coefficient distribution along spanwise sections of the wing. The conditions simulating $M_{\infty} = 0.11$ corresponds to the highest dynamic pressure obtained throughout the experimental test campaign. The numerical results of the mean pressure coefficient at six different spanwise locations along the wing are shown in Fig. A.4. Pressure tap locations $y = 34.386$ in, $y = 44.386$ in, and $y = 54.386$ in are outwith the propeller slipstream. Pressure tap location $y = 57.386$ in is aligned approximately 1.5 in outward of the propeller tip. Pressure tap locations at $y = 60.955$ in and $y = 63.469$ in are directly in the propeller slipstream. The results shown begin close to the root of the wing and progressively get closer towards the tip of the wing. Time-averaged URANS-SA predictions on grid G1 are used for comparison with experimental data. The predicted pressure coefficient distributions at the spanwise locations outwith the propeller wake are in close agreement with the measured data and are shown in Fig. A.4a-A.4c. The predicted pressure coefficient distribution at the spanwise location which corresponds to being marginally outward of the blade tip is shown in Fig. A.4d. It illustrates that the pressure tap is beyond the wake of the propeller which the prediction captures. The predicted pressure coefficient distributions at the spanwise locations inside the propeller slipstream are shown in Fig. A.4e & A.4f. The interaction effects of the propeller slipstream at these spanwise locations are shown to have a significant influence on the pressure coefficient distributions, leading to a clear suction peak near the wing leading edge on the blade retreating side. This dynamic effect is more challenging to simulate and accurately model however the blade-tip vortex disturbances on the surface of the wing appear to well represented. Overall, the computed pressure coefficient is in good agreement with the measured data from run number 33. This close agreement is particularly true for the results outwith the influence of the propeller. As the influence of the propeller becomes apparent slight discrepancies arise, however despite this, the suction peak is well captured.

The wake rake measurements recorded during run number 80 are used for validation of the downstream propeller velocity profile and performance characteristics. The velocity profile is decomposed into the separate velocity components to obtain the normal velocity, swirl velocity and radial velocity. The propeller performance is separated into the propeller thrust distribution and torque distribution. The thrust and torque distributions are computed respectively as,

$$\text{Thrust} = \int_0^{2\pi} \int_0^{R_{\text{prop}}} \rho U \left(U - U_\infty\right) r dr d\Theta \,,$$
$$\frac{\text{Thrust}}{Q_\infty R_{\text{prop}}^2} = 2\pi \int_0^1 \frac{\rho U \left(U - U_\infty\right)}{Q_\infty} \frac{r}{R_{\text{prop}}} d\frac{r}{R_{\text{prop}}} \,. \tag{A.1}$$

$$\text{Torque} = \int_0^{2\pi} \int_0^{R_{\text{prop}}} \rho U W_{\text{swirl}} r dr d\Theta \,,$$
$$\frac{\text{Torque}}{Q_\infty R_{\text{prop}}^3} = 2\pi \int_0^1 \frac{\rho U W_{\text{swirl}}}{Q_\infty} \left(\frac{r}{R_{\text{prop}}}\right)^2 d\frac{r}{R_{\text{prop}}} \,. \tag{A.2}$$

where the area to the left of the thrust and torque distributions integrates to the total thrust and total torque. The predictions use the thrust and torque distributions to compare against the measured data. The strong relationship between the normal velocity and thrust, and, the swirl velocity and torque is the rationale behind also comparing the normal and swirl components of the velocity profiles with the measured data.

The experimental wake data was measured at five locations downstream of the propeller in the positive x-direction. The measurements were record at 2.65 in, 6.15 in, 14.15 in, 22.15 in, and 42.15 in downstream from the propeller plane. These measurement locations correspond to positions $x = 1.5$ in, $x = 5.0$ in, $x = 13.0$ in, $x = 21.0$ in, and $x = 41.0$ in in the mesh coordinate system. As a safety precaution, measurements were not recorded any closer to the propeller. This work focuses on the four critical locations closest to the propeller due to these being in the near-field wake of the propeller. The fifth position is significantly further from the nacelle's trailing edge and given the computational and time constraints it is currently not feasible to include in the current simulations. Future work will however seek to consider the fifth wake location.

The predicted normal and swirl velocity at the four wake stations are respectively shown in Fig. A.5 and Fig. A.6. The velocity profiles closest to the propeller at position $x = 1.5$ in are predicted well in Fig. A.5a and Fig. A.6a. Notably, the swirl velocity, given that it is particularly challenging to capture. The difference between the coarse and fine grid results are minimal. The same can be said for the URANS and EDDES comparison this close to the propeller. Slight differences only arise just beyond $R/R_{\text{prop}} = 1$. Progressing downstream, to the wake stations at positions $x = 5.0$ in, $x = 13.0$ in, and $x = 21.0$ in as shown in Figs. A.5b-A.5d and Figs. A.6b-A.6d, a trend emerges and the simulations performed on the finest grid (G3) prevail. Discrepancies between simulations on the three grid levels increase further downstream. The finest grid (G3) results show limited influence of grid dissipation evidenced by the peaks of the velocity profiles maintaining their strength to the furthest position from the propeller at $x = 21.0$ in as depicted by Fig. A.5d and Fig. A.6d. At this location there are significantly different results between the grids at $R/R_{\text{prop}} = 1$. A general trend of the predictions at each location is that the velocity profiles appear to be shifted radially inwards. The predictions suggest that the velocity profiles produced by the propeller do not extend beyond $R/R_{\text{prop}} = 1$ as suggest by the wake survey.

The predicted thrust and torque distribution at the four wake stations are respectively shown in Fig. A.7 and Fig. A.8. The thrust and torque distributions shown in Eq. A.1

and Eq. A.2 are used for comparison with wake survey. From these relationships, it is apparent that the influence of the normal velocity on the thrust distribution, and, the swirl velocity on the torque distribution, is significant and thus, similar trends are expect to the results illustrated in Fig. A.5 and Fig. A.6. The thrust and torque distributions closest to the propeller at position $x = 1.5$ in are predicted closely to the measured data in Fig. A.7a and Fig. A.8a. Similarly to the velocity profiles, it is observed that the differences between the thrust and torque predictions increase at the downstream locations as shown in Figs. A.7b-A.7d and Figs. A.8b-A.8d. The finest grid (G3) results show limited influence of grid dissipation evidenced by the thrust and torque distribution peaks maintaining their strength to the furthest position from the propeller at $x = 21.0$ in as depicted by Fig. A.7d and Fig. A.8d. Overall, the performance characteristics tend to be predicted radially inwards and the distribution peaks are slightly under predicted when compared against the measurements. The simulations suggest that the propeller produces its peak performance between $R/R_{\text{prop}} = 0.8 - 0.95$ whereas the wake survey suggests the propeller produces its peak performance at the propeller tip $R/R_{\text{prop}} = 1$ and even slightly beyond.

A summary of the normal and swirl velocity profiles and thrust and torque distributions is deduced. The general observation on all four quantities of interest predicted in the wake are:

- Grid G1 is too coarse and therefore too dissipative to accurately capture the wake profiles at the downstream locations $x = 5.0$ in, $x = 13.0$ in, and $x = 21.0$ in.
- While better agreement with experiment is obtained using grids G2 and G3, they still significantly under-predict the peak values of the normal velocity and thrust distribution. The observation of the swirl velocity and torque distribution is markedly improved however they remain below the measured peaks.
- While the general shapes of all wake profiles are well captured for grids G2 and G3, the predicted profiles all show a downward offset when compared with the wake measurement data. The same observation has also been made in numerical results of many participants in the last WIPP workshop. This may indicate a systematic measurement error.
- No discernible improvement in the wake profile prediction is achieved when switching from URANS to EDDES. This indicates that even grid G3 may still be too coarse for the wake to develop in a physically plausible manner when EDDES is supposedly operating in the LES mode in that region. As shown on Table A.2, the ratio between the edge length of a cell in the wake and the tip chord of the propeller is 0.0682 for G3 – much larger than the typical value of 0.01 or less often used for scale-resolving simulations.

To help visualize the highly three-dimensional nature of the problem the Q-criterion colored by dimensionless streamwise velocity is shown in Fig. A.9 for the URANS-SA simulations performed on all 3 grids and in Fig. A.10 for the EDDES-SA simulations performed on G2 and G3. The vortical structures are preserved and persist further downstream as the grid is refined. In addition, the EDDES simulations further resolve smaller turbulence structures in the wake region compared to their URANS counterparts. The

EDDES-SA simulation on G3 clearly reveals two major interactional noise sources: the turbulent wake and tip vortex generated by the propeller blades, both impinging upon the wing and nacelle surfaces as they convect downstream. In addition, the secondary vortex emanating from the trailing edge of the blade tip is also captured. It is this interactional behaviour close to the propeller which influences the pressure coefficient on the wing displayed in Fig. A.4e & A.4f.

In light of the promising aerodynamic results, progression towards the prediction of the aeroacoustics was the subsequent area of interest. As a first step in assessing the noise sources in this integrated wing-propeller configuration, the instantaneous pressure fluctuations over the full configuration captured by URANS and EDDES simulations on G3 are shown in Fig. A.11. The locations at which the blade-tip vortices impact on the wing and nacelle correlate into strong noise sources, as evidenced by the alternating pressure fluctuation patterns near the wing-tip below the nacelle. In addition, the turbulent wake shed by the propeller blades leaves spiralling patterns around the nacelle surface. EDDES appears to capture the finer features of the surface pressure fluctuation patterns much more clearly, especially around the nacelle.

The surface 'noise footprint' is visualized by the root-mean-square of the pressure fluctuation and shown in Fig. A.12. The dominant noise source is located at the leading edge of the wing immediately below the nacelle where the tip vortex in the propeller slipstream makes first contact with the wing surface. This is consistent with the findings of Avallone et al. in their computational aeroacoustic study of a similar configuration [237]. From a noise reduction perspective, this indicate that in addition to optimizing the shape of the blades, it may also be highly effective to consider also optimally morphing the leading edge of the wing in the slipstream.

A.6 Conclusion

In this work, we simulate the turbulent flow field around a wing-tip mounted propeller configuration using the model and test conditions released by the Workshop for Integrated Propeller Prediction (WIPP). In particular, the unsteady RANS equations with Spalart-Allmaras turbulence model (URANS-SA) are solved in a time-accurate manner with the multi-zone sliding mesh technique in which the propeller is allowed to rotate while the wing and the nacelle remain stationary. In addition, enhanced delayed detached eddy simulations based on the Spalart-Allmaras model (EDDES-SA) are performed on the finer grids in an attempt to better resolve the turbulent wake behind the propeller. Current results are based on the test conditions from run number 33 and 80, namely $M_\infty = 0.11$, $C_T = 0.40$ and $AoA = 0°$.

Time-averaged pressure coefficients at six spanwise locations along the wing surface are shown to be in good agreement with the experimental data. The two locations in the propeller slipstream in particular closely resemble the measurements and capture the blade-wing interaction effects. Time-averaged wake profiles of normal velocity, swirl velocity, thrust distribution and torque distribution at four stations downstream of the propeller are compared with experimental data from the wake survey. In general, while the overall shapes of all profiles are captured correctly on finer grids, the peak values are under-predicted on all wake profiles except for the swirl velocity. Moreover, there

appears to be a shift radially inward indicating that the wake quantities, and the thrust in particular, do not extend beyond the propeller tip, as suggested by the experiment. Supplementary to the wake quantity predictions, the Q-criterion iso-surface helps visualize the vortical structures produced by the propeller blades and assess how they interact with wing and nacelle surfaces as they are convected downstream. This highlights the importance of the high level of mesh refinement required for such a complex configuration like a wing-tip mounted propeller. Furthermore, going beyond the original WIPP requirements, aeroacoustic aspects of this configuration are also studied in the current work. Visualization of the surface pressure fluctuations reveals the noise footprints on this integrated propeller-wing system. In particular, the impingement of propeller blade tip vortices on the leading edge of the wing immediately below the nacelle is identified to be the main noise source.

Looking ahead, we intend to improve the mesh resolution in the propeller wake region around the nacelle to approximately $150\mathrm{M}$ elements and reduce the physical time-step to 0.25° of revolution per time step to ensure an even higher resolution of the fine-grained vortical structures for the EDDES simulation. We would also like to assess addition conditions at other Mach numbers, propeller thrust settings and angle of attacks specified by the WIPP workshop and compare our predictions with available experimental data. In addition to build on the current noise footprints, a solid-surface Ffowcs Williams-Hawkings (FWH) method [242] will be used to evaluate the far-field noise level of the configuration using surface pressure data obtained from CFD simulations.

Research Question A1: What impact do propeller-wing interactional effects have on aircraft performance and noise predictions with reference to future full-electric configurations?

Conclusion A1: The flow physics associated to complex interactional behaviour of rotors and wings can be unlike that of isolated components and thus required additional assessment of the SU2 solver. In particular, the sliding mesh routine which permits bodies to move in relative motion required attention. The turbulent flow field around a wing-tip mounted propeller configuration was therefore simulated and validated using the model and test conditions released by the Workshop for Integrated Propeller Prediction. This allowed for the assessment of the super-mesh approach used to account for the non-conformal boundaries of the sliding interface. The simulation results successfully demonstrated conservation of the solution across the artificial boundary interface. Subsequently, numerical performance predictions could be compared to those from the Workshop for Integrated Propeller Prediction. Resultantly, the influence of the vortices generated by the propeller-tip on the wing was shown to be significant, having a large impact on the noise footprint of the wing-tip mounted propeller configuration.

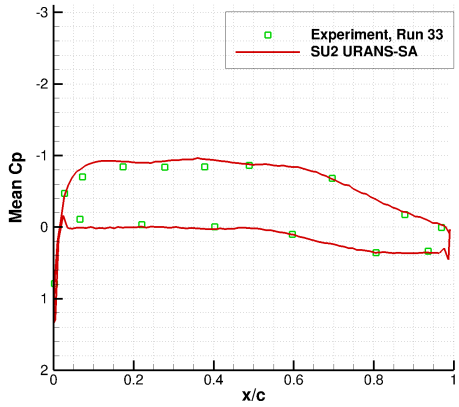

(a) $y = 34.386$ *in.*

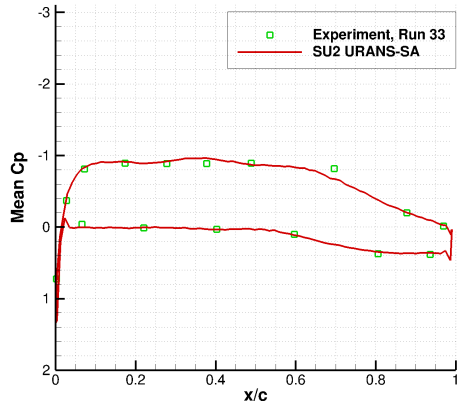

(b) $y = 44.386$ *in.*

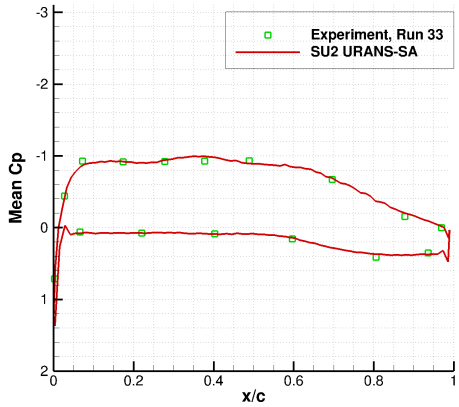

(c) $y = 54.386$ *in.*

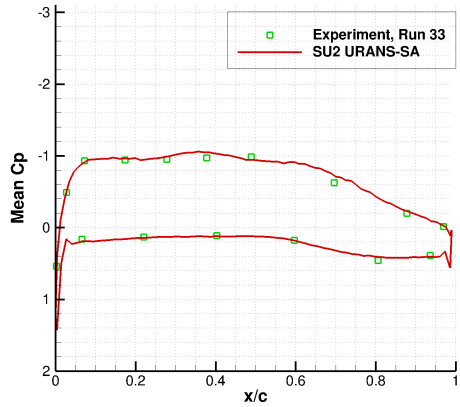

(d) $y = 57.386$ *in.*

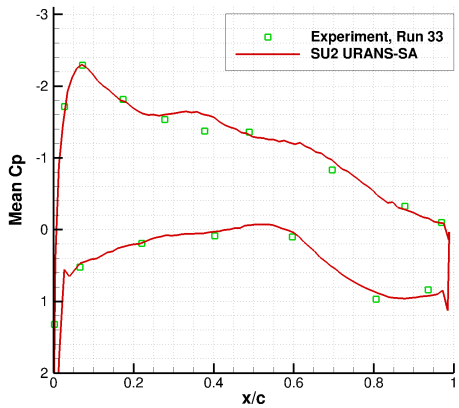

(e) $y = 60.955$ *in.*

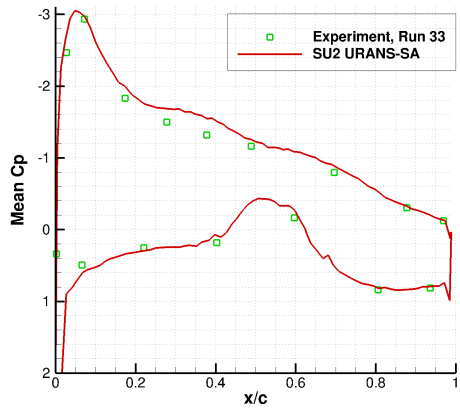

(f) $y = 63.469$ *in.*

Figure A.4: *Mean pressure coefficient at six spanwise stations along the wing,* $M_\infty = 0.11$, $C_T = 0.40$, $AoA = 0°$

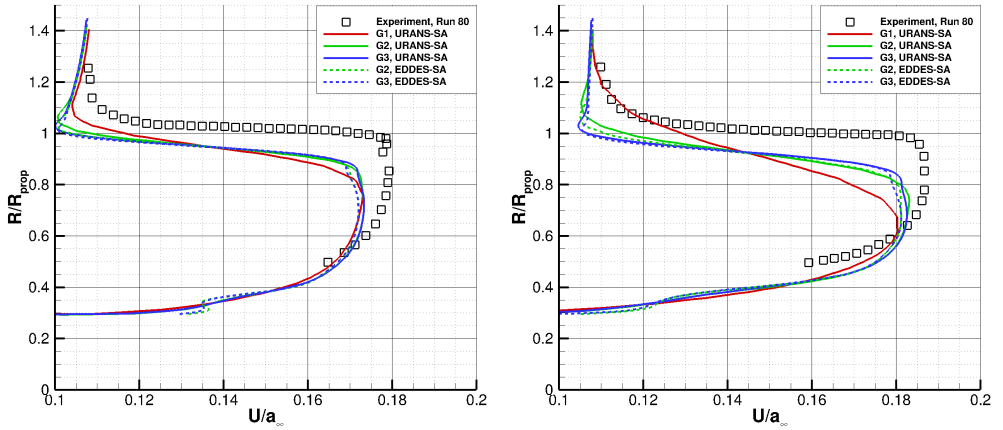

(a) $x = 1.5$ *in.* **(b)** $x = 5.0$ *in.*

(c) $x = 13.0$ *in.* **(d)** $x = 21.0$ *in.*

Figure A.5: *Normal velocity distribution at four stations in the wake of the propeller,* $M_\infty = 0.11$, $C_T = 0.40$, $AoA = 0°$

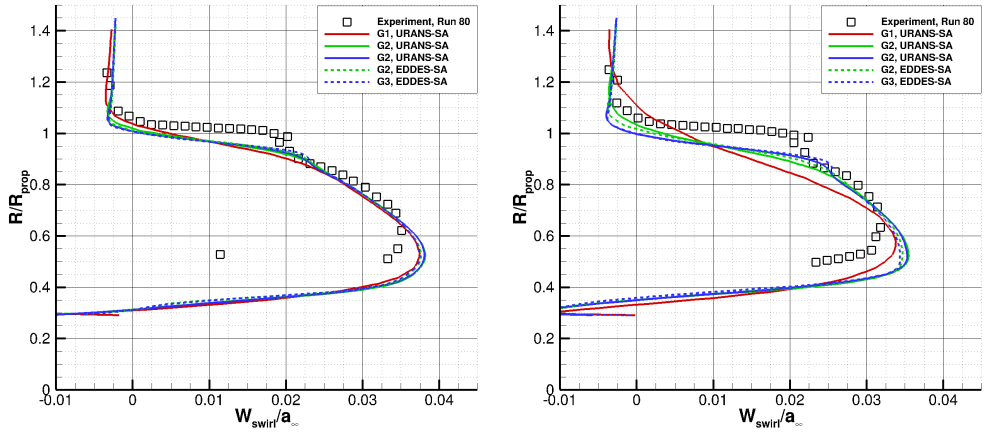

(a) $x = 1.5$ *in.*

(b) $x = 5.0$ *in.*

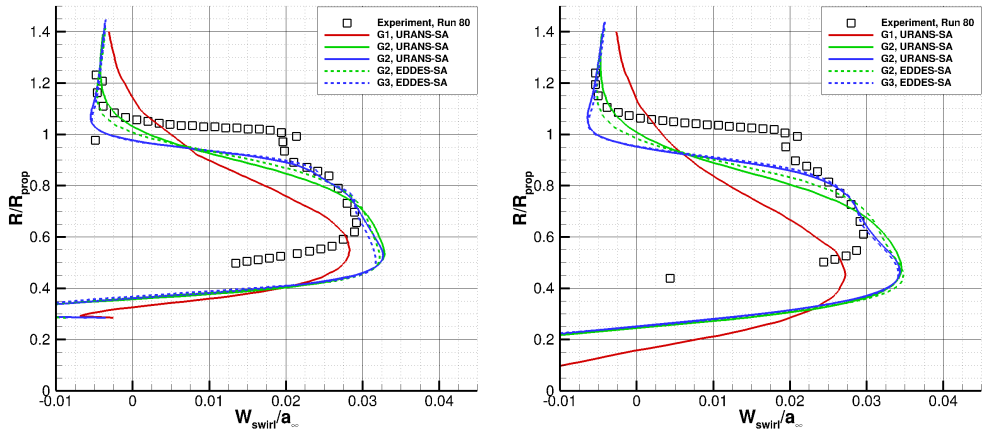

(c) $x = 13.0$ *in.*

(d) $x = 21.0$ *in.*

Figure A.6: *Swirl velocity distribution at four stations in the wake of the propeller,* $M_\infty = 0.11$, $C_T = 0.40$, $AoA = 0°$

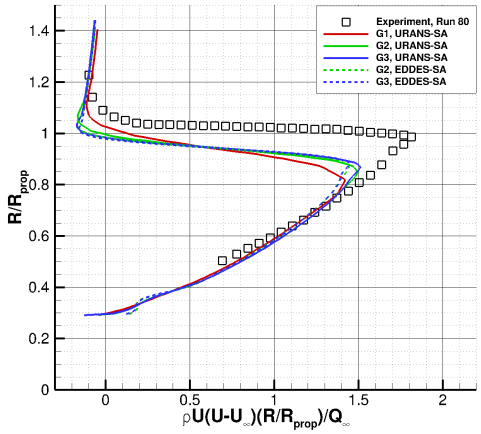

(a) $x = 1.5$ *in.*

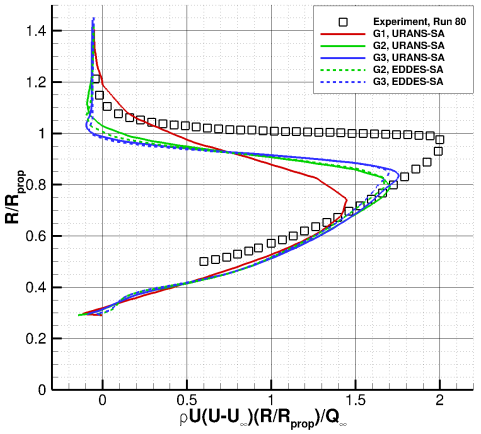

(b) $x = 5.0$ *in.*

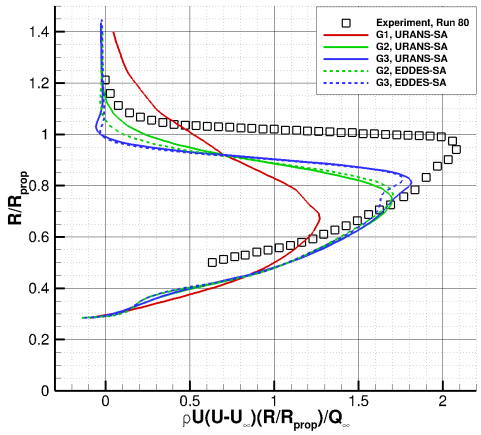

(c) $x = 13.0$ *in.*

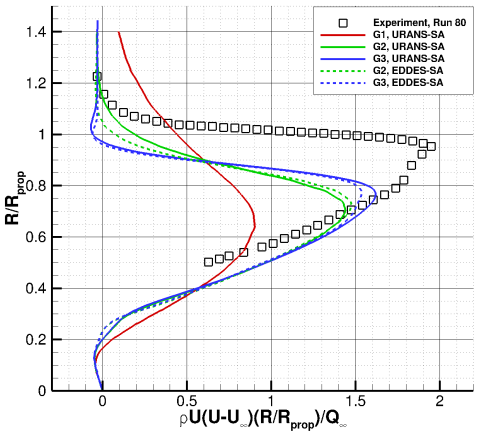

(d) $x = 21.0$ *in.*

Figure A.7: *Thrust distribution at four stations in the wake of the propeller,* $M_\infty = 0.11$, $C_T = 0.40$, $AoA = 0^\circ$

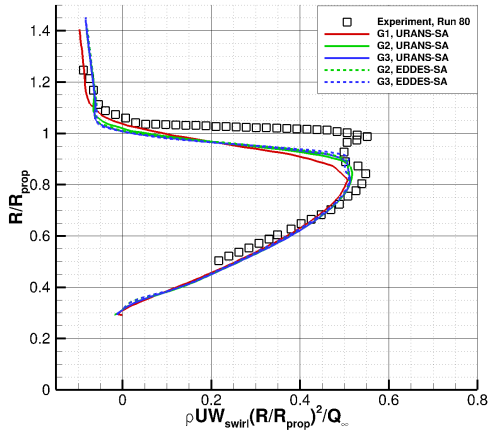

(a) $x = 1.5$ *in.*

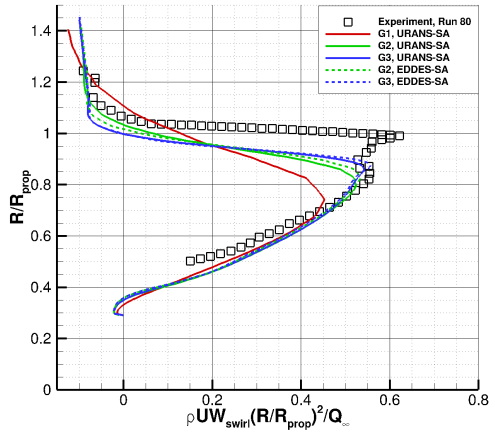

(b) $x = 5.0$ *in.*

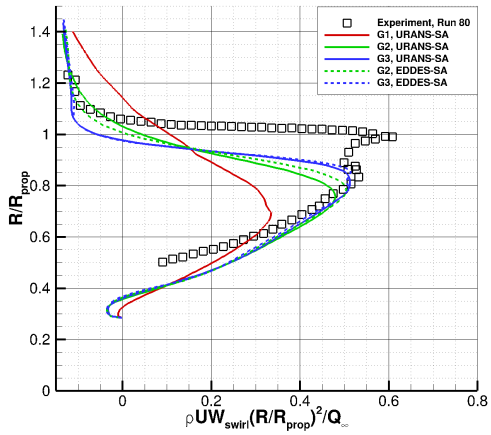

(c) $x = 13.0$ *in.*

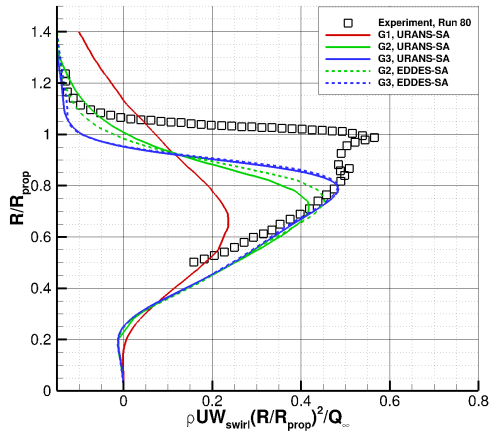

(d) $x = 21.0$ *in.*

Figure A.8: *Torque distribution at four stations in the wake of the propeller,* $M_\infty = 0.11$, $C_T = 0.40$, $AoA = 0^\circ$

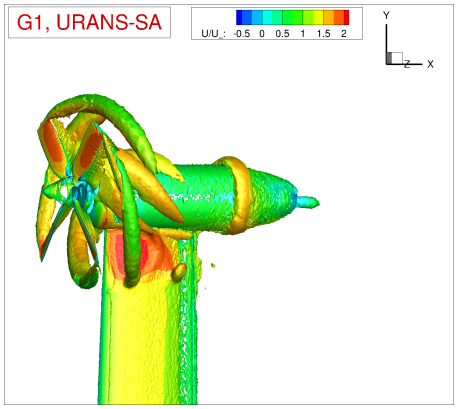

(a) *Grid-01 R.*

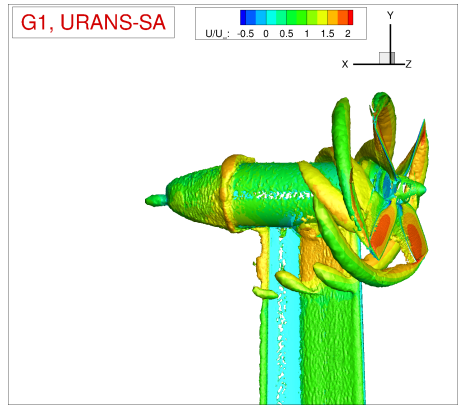

(b) *Grid-01 A.*

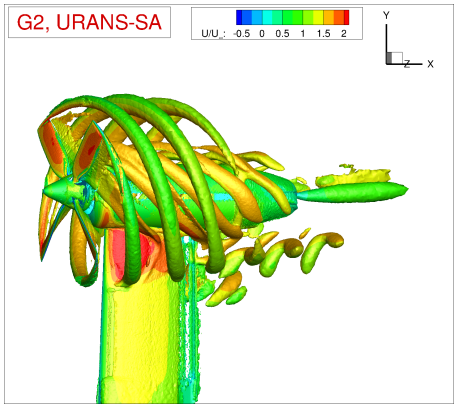

(c) *Grid-02 R.*

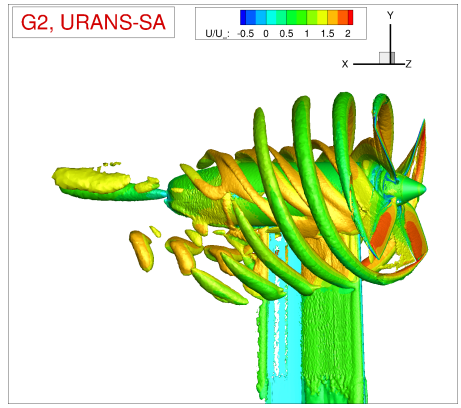

(d) *Grid-02 A.*

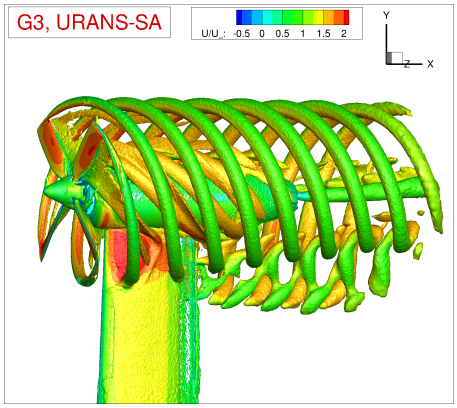

(e) *Grid-03 R.*

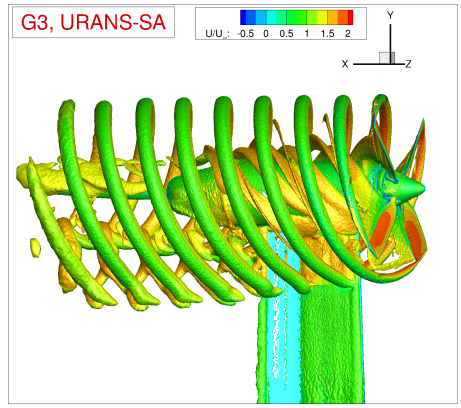

(f) *Grid-03 A.*

Figure A.9: *Q-criterion iso-surface colored by the dimensionless streamwise velocity computed by URANS-SA on Grid-01, Grid-02 and Grid-03,* $M_\infty = 0.11$, $C_T = 0.40$, $AoA = 0^\circ$

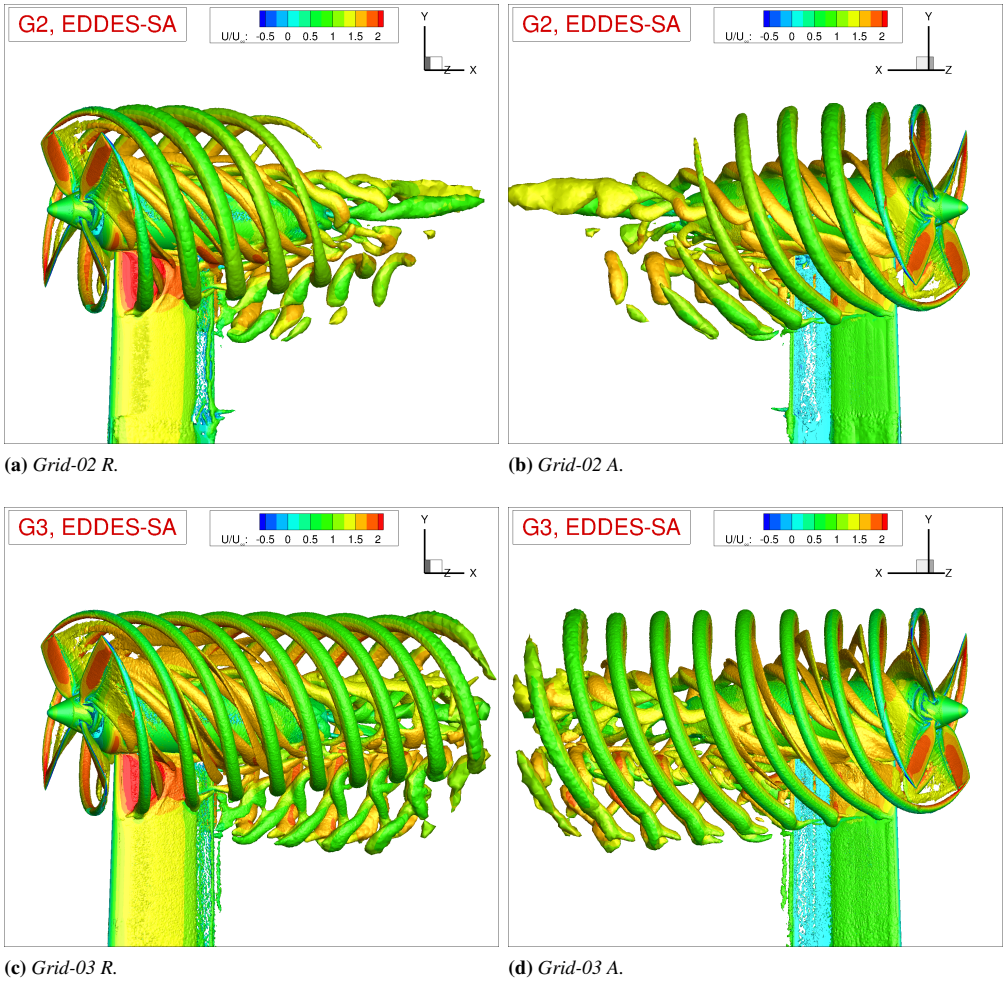

(a) *Grid-02 R.*

(b) *Grid-02 A.*

(c) *Grid-03 R.*

(d) *Grid-03 A.*

Figure A.10: *Q-criterion iso-surface colored by the dimensionless streamwise velocity computed by EDDES-SA on Grid-02 and Grid-03,* $M_\infty = 0.11$, $C_T = 0.40$, $AoA = 0°$

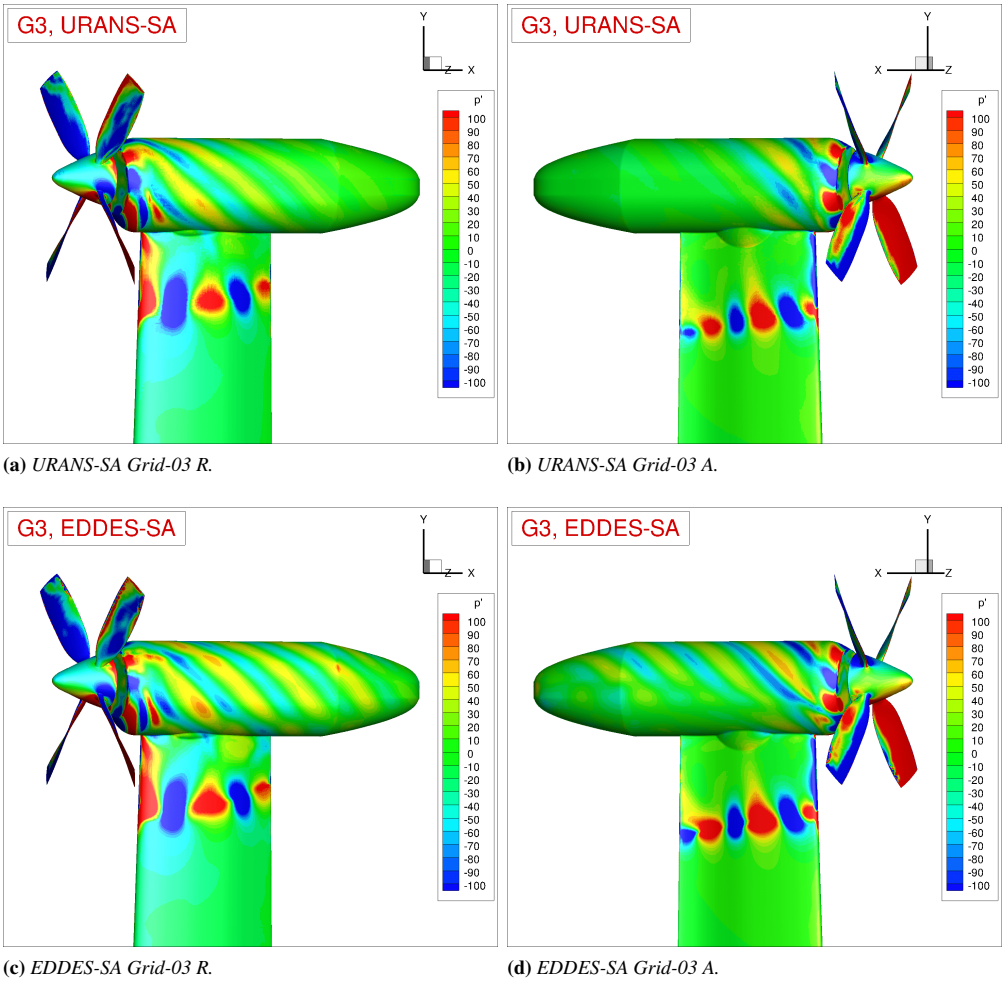

(a) *URANS-SA Grid-03 R.*

(b) *URANS-SA Grid-03 A.*

(c) *EDDES-SA Grid-03 R.*

(d) *EDDES-SA Grid-03 A.*

Figure A.11: *Instantaneous pressure fluctuation computed by URANS-SA and EDDES-SA on Grid-03,* $M_\infty = 0.11$, $C_T = 0.40$, $AoA = 0°$

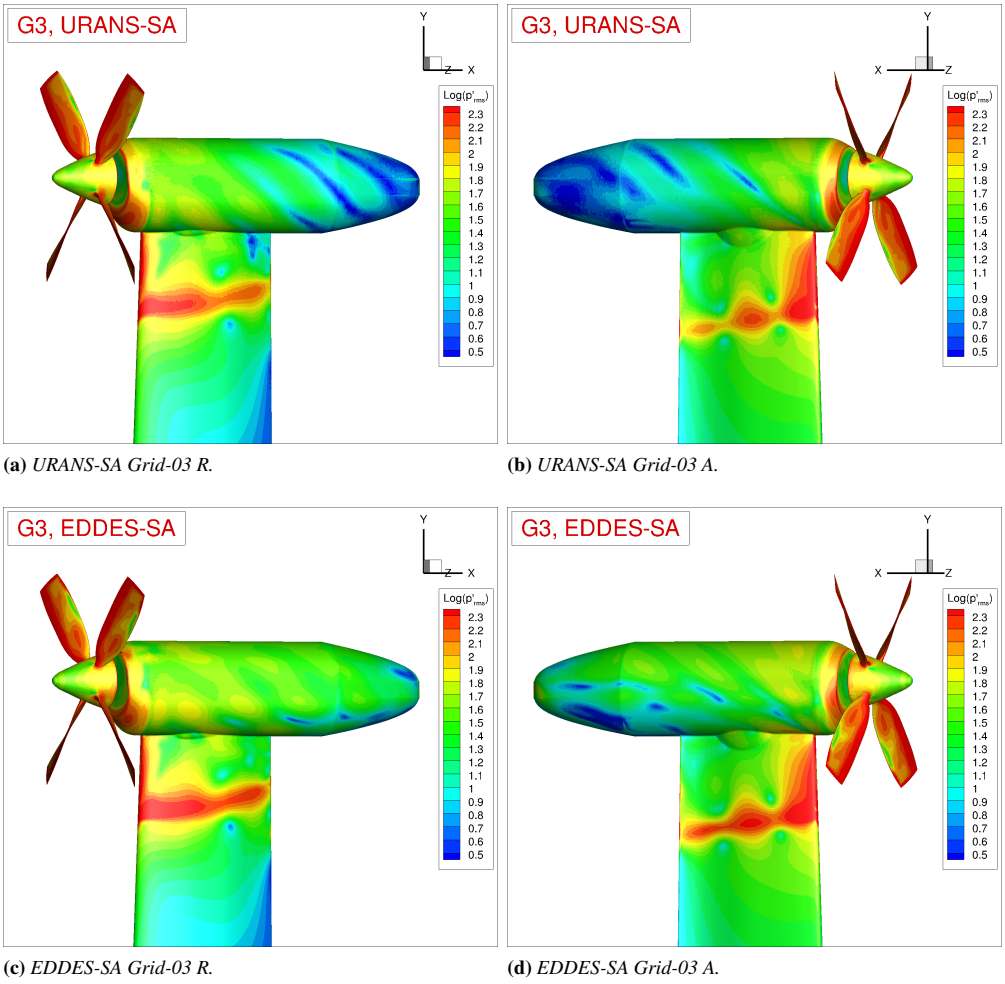

(a) *URANS-SA Grid-03 R.*

(b) *URANS-SA Grid-03 A.*

(c) *EDDES-SA Grid-03 R.*

(d) *EDDES-SA Grid-03 A.*

Figure A.12: *The log of root-mean-square of pressure fluctuation computed by URANS-SA and EDDES-SA on Grid-03,* $M_\infty = 0.11$, $C_T = 0.40$, $AoA = 0^\circ$

List of Publications

Journal Papers

- Morelli, M., Zhou, B.Y. & Guardone, A., "Acoustic Characterization of Glaze and Rime Ice Structures on an Oscillating Airfoil via Fully Unsteady Simulations", *Journal of the American Helicopter Society*, vol. 65, 2020. Available online at, DOI: 10.4050/JAHS.65.032000.
- Morelli, M., Bellosta, T. & Guardone, A., "Development and Preliminary Assessment of the Open-Source Toolkit SU2 for Rotorcraft Flows", *Journal of Computational Applied Mathematics*, Volume 389, No. 113340, June 2021. https://doi.org/10.1016/j.cam.2020.113340
- Morelli, M., Bellosta, T. & Guardone, A., "Efficient Radial Basis Function Mesh Deformation Methods for Aircraft Icing", *Journal of Computational and Applied Mathematics*, Status: Accepted for Publication.

Book Chapters

- Arizmendi, B., Morelli, M., Parma, G., Zocca, M., Quaranta, G., Guardone, A., "In-Flight Icing: Modeling, Prediction and Uncertainty", In Vasile, M. (Ed.) *Optimization Under Uncertainty with Applications to Aerospace Engineering*, Springer Nature, Publish Date: November, 2020.

Conference Proceedings

- Morelli, M., Zhou, B.Y. & Guardone, A., "Simulation and Analysis of Oscillating Airfoil Ice Shapes via a Fully Unsteady Collection Efficiency Approach", Presented at the Vertical Flight Society 75th Annual Forum Technology Display, Philadelphia, Pennsylvania, U.S.A, May 13-16, 2019.
- Morelli, M., Bellosta, T. & Guardone, A., "Lagrangian Particle Tracking in Deforming Sliding Mesh For Rotorcraft Icing Applications", *Presented at* 45^{th} *European Rotorcraft Forum*, paper 146, Warsaw, Poland, September 17–20, 2019.
- Zhou, B.Y., Gauger, N.R., Morelli, M., & Guardone, A., "Simulation and Sensitivity Analysis of a Wing-Tip Mounted Propeller Configuration from the Workshop for Integrated Propeller Prediction (WIPP)", *Special Session: Aerodynamics and Performance of Integrated Propellers II, AIAA Aviation Forum*, Reno, Nevada, June 15–19, 2020. DOI: https://doi.org/10.2514/6.2020-2683.
- Zhou, B.Y., Gauger, N.R., Morelli, M., Guardone, A., Hauth, J. & Huan X., "Towards a Real-Time In-Flight Ice Detection System via Computational Aeroacoustics and Bayesian Neural Networks", *Multidisciplinary Analysis and Optimization, AIAA Aviation Forum*, Dallas, Texas, June 17–21, 2019. DOI: https://doi.org/10.2514/6.2019-3103.
- Zhou, B.Y., Gauger, N.R., Morelli, M., Guardone, A., Hauth, J. & Huan X. "Development of a Real-Time In-Flight Ice Detection System via Computational Aeroacoustics and Bayesian Neural Networks", *Multidisciplinary Analysis and*

Optimization, AIAA SciTech Forum, Orlando, Florida, January 6–10, 2020. DOI: https://doi.org/10.2514/6.2020-1638.

- Hauth, J., Huan X., Zhou, B.Y., Gauger, N.R., Morelli, M. & Guardone, A., "Correlation Effects in Bayesian Neural Networks for Computational Aeroacoustics Ice Detection", *Multidisciplinary Analysis and Optimization, AIAA SciTech Forum*, Orlando, Florida, January 6–10, 2020. DOI: https://doi.org/10.2514/6.2020-1414.

- Morelli, M., Ghiasvand, S., Nabi, H.N, Taymourtash, N., Masarati, P., Quaranta, G., Barakos, G., Fasiello, S., Huercas, S., White, M., Akel, E., Yu, Y., Friesen, D., Scaramuzzino, P.F. & Pavel, M., "Assessment of the Feasibility of an Extended Range Helicopter Operational Standard for Offshore Flights", *Presented at* 44^{th} *European Rotorcraft Forum*, paper 171, Delft, The Netherlands, September 19–20, 2018.

Bibliography

[1] G. D. Padfield, *Helicopter Flight Dynamics: The Theory and Application of Flying Qualities and Simulation Modelling*. John Wiley & Sons, Second Edition, 2008.

[2] M. Bragg, G. Gregorek, and J. Lee, "Airfoil Aerodynamics in Icing Conditions," *Journal of Aircraft*, vol. 23, no. 1, pp. 76–81, 1986.

[3] R. Gent, N. Dart, and J. Cansdale, "Aircraft Icing," *Philosophical Transactions of the Royal Society of London. Series A: Mathematical, Physical and Engineering Sciences*, vol. 358, no. 1776, pp. 2873–2911, 2000. https://doi.org/10.1098/rsta.2000.0689.

[4] H. Gao and J. L. Rose, "Ice Detection and Classification on an Aircraft Wing With Ultrasonic Shear Horizontal Guided Waves," *IEEE transactions on ultrasonics, ferroelectrics, and frequency control*, vol. 56, no. 2, pp. 334–344, 2009.

[5] C. A. Martin and J. C. Putt, "Advanced Pneumatic Impulse Ice Protection System (PIIP) for Aircraft," *Journal of Aircraft*, vol. 29, no. 4, pp. 714–716, 1992.

[6] The European Parliament and the Council of the European Union, *Regulation (EU) No 376/2014*. Official Journal of the European Union, April 2014.

[7] European Union Aviation Safety Agency (EASA), *Annual Safety Review 2019*. Report Number TO-AA-19-001-EN-N, DOI:10.2822/098259, July 2019.

[8] European Union Aviation Safety Agency (EASA), *The European Plan for Aviation Safety 2020 - 2024*. Volume I., November 2019.

[9] European Union Aviation Safety Agency (EASA), *The European Plan for Aviation Safety 2020 - 2024: 9. Design and Production, RES.017*. Volume I, p. 196, November 2019.

[10] European Union Aviation Safety Agency (EASA), *The European Plan for Aviation Safety 2020 - 2024: 9. Design and Production, RES.010*. Volume I, p. 195, November 2019.

[11] European Union Aviation Safety Agency (EASA), *Certification Specifications and Acceptable Means of Compliance for Small Rotorcraft*. CS-27 Amendment 7, June 2020.

[12] European Union Aviation Safety Agency (EASA), *Certification Specifications and Acceptable Means of Compliance for Large Rotorcraft*. CS-29 Amendment 8, June 2020.

[13] European Aviation Safety Agency, *AW139 Type Certificate Data Sheet*. EASA Report No. 006, Issue 22, January 2019.

[14] European Aviation Safety Agency, *AW189 Type Certificate Data Sheet*. EASA Report No. 510, Issue 10, June 2020.

[15] European Union Aviation Safety Agency (EASA), *Certification Specifications and Acceptable Means of Compliance for Small Rotorcraft: CS 27.1419 Ice Protection, b.* CS-27 Amendment 7, p. 1-F-11, June 2020.

[16] European Union Aviation Safety Agency (EASA), *Certification Specifications and Acceptable Means of Compliance for Large Rotorcraft: CS 29.1419 Ice Protection, b.* CS-29 Amendment 8, p. 1-F-14, June 2020.

[17] European Union Aviation Safety Agency (EASA), *Certification Specifications and Acceptable Means of Compliance for Small Rotorcraft: CS 27.1419 Ice Protection, e.* CS-27 Amendment 7, p. 1-F-11, June 2020.

[18] European Union Aviation Safety Agency (EASA), *Certification Specifications and Acceptable Means of Compliance for Large Rotorcraft: CS 29.1419 Ice Protection, e.* CS-29 Amendment 8, p. 1-F-15, June 2020.

[19] Federal Aviation Administration, *Certification of Normal Category Rotorcraft*. Adivisory Circular No. 27-1B, Issue 7, June 2018.

[20] Federal Aviation Administration, *Certification of Transport Category Rotorcraft*. Adivisory Circular No. 29-2C, Issue 8, July 2018.

[21] Federal Aviation Administration, *Certification of Normal Category Rotorcraft: Section 27.1419. Ice Protection, a. Background*. Adivisory Circular No. 27-1B, Issue 7, p. F75, June 2018.

[22] Federal Aviation Administration, *Certification of Transport Category Rotorcraft: Section 29.1419. Ice Protection, a. Background*. Adivisory Circular No. 29-2C, Issue 8, p. F93, July 2018.

[23] Federal Aviation Administration, *Certification of Normal Category Rotorcraft: Section 27.1419. Ice Protection, b. Explanation, (3) Objective*. Adivisory Circular No. 27-1B, Issue 7, p. F77, June 2018.

[24] Federal Aviation Administration, *Certification of Transport Category Rotorcraft: Section 29.1419. Ice Protection, b. Explanation, (3) Objective*. Adivisory Circular No. 29-2C, Issue 8, p. F94, July 2018.

[25] Federal Aviation Administration, *Certification of Normal Category Rotorcraft: Section 27.1419. Ice Protection, b. Explanation, (1) General, (iii)*. Adivisory Circular No. 27-1B, Issue 7, p. F77, June 2018.

[26] Federal Aviation Administration, *Certification of Transport Category Rotorcraft: Section 29.1419. Ice Protection, b. Explanation, (1) General, (iii)*. Adivisory Circular No. 29-2C, Issue 8, p. F94, July 2018.

[27] Federal Aviation Administration, *Certification of Normal Category Rotorcraft: Section 27.1419. Ice Protection, c. Procedures, (1) Compliance, (vi)*. Adivisory Circular No. 27-1B, Issue 7, p. F83, June 2018.

[28] Federal Aviation Administration, *Certification of Transport Category Rotorcraft: Section 29.1419. Ice Protection, c. Procedures, (1) Compliance, (vi)*. Adivisory Circular No. 29-2C, Issue 8, p. F100, July 2018.

[29] D. Bell, "Icing at the McKinley Climatic Laboratory," in *41st Aerospace Sciences Meeting and Exhibit*, (Reno, Nevada, USA), p. 902, January 2004.

[30] R. Ward, W. Horton, G. Bender, L. Free, and J. O'Connor, "Climatic Laboratory Evaluation-Iranian Model 214A Helicopter," *Final Report for US Army USAAEFA Project*, no. 74-32, 1974.

[31] R. Flemming, P. Alldridge, and R. Doeppner, "Artificial Icing Tests of the S-92A Helicopter in the McKinley Climatic Laboratory," in *42nd AIAA Aerospace Sciences Meeting and Exhibit*, p. 737, 2004.

[32] D. L. Bailey, *Description of the Spray Rig Used to Study Icing on Helicopters in Flight*. National Research Council Canada, September 1960.

[33] J. D. Lee, R. Harding, and R. L. Palko, *Documentation of Ice Shapes on the Main Rotor of a UH-1H Helicopter in Hover*. National Aeronautics and Space Administration, Contractor Report No. 168332, January 1984.

[34] W. Y. Abbott, D. Belte, R. Williams, and F. Stellar, *Evaluation of UH-1H Hover Performance Degradation Caused by Rotor Icing*. US Army Aviation Engineering Flight Activity, Edwards Air Force Base, California, USA, May 1983.

[35] R. Shaw and G. Richter, "The UH-1H Helicopter Icing Flight Test Program-An Overview," in *23rd Aerospace Sciences Meeting*, (Reno, Nevada, USA), p. 338, January 1985.

[36] D. Belte and K. R. Ferrell, "Helicopter Icing Spray System," (Washington, D.C, USA), 36th American Helicopter Society Annual Forum, May 1980.

[37] D. Belte, *Helicopter Icing Spray System (HISS) Nozzle Improvement Evaluation*. US Army Aviation Engineering Flight Activity, Edwards Air Force Base, California, USA, September 1981.

[38] D. Belte and R. Woratschek, "Helicopter icing spray system (hiss) evaluation and improvement," U.S. Army Aviation Engineering Flight Activity, Project No.82-05-3, Edwards Air Force Base, California, April 1986.

[39] A. I. Ramage, "Artificial Icing Flight Trials on the EH101," (Marseilles, France), 30th European Rotorcraft Forum, September 2004.

[40] E. Bellussi, *Use of HISS Test Results for Rotorcraft Civil Certification*. SAE Technical Paper, June 2015. DOI:10.4271/2015-01-2128.

[41] J. Reinmann, R. Shaw, and W. Olsen, "NASA Lewis Research Center's Program on Icing Research," in *21st Aerospace Sciences Conference*, (Reno, Nevada, USA), January 1985.

[42] T. L. Miller and T. H. Bond, "Icing research tunnel test of a model helicopter rotor," Proceedings of the 45th Annual Forum of the American Helicopter Society, Boston, Massachusetts, May 1989.

[43] R. Flemming, T. Bond, and R. Britton, "Results of a sub scale model rotor icing test," (Reno, Nevada, USA) Proceedings of the 49th Aerospace Sciences Meeting, January 1991.

[44] R. Flemming and A. Saccullo, "Tests of a Model Main Rotor in the NASA Lewis Research Center Icing Research Tunnel," *NASA Contractor Report No. 189071*, January 1991.

[45] R. Britton, T. Bond, and R. Flemming, "An Overview of a Model Rotor Icing Test in the NASA Lewis Icing Research Tunnel," in *32nd Aerospace Sciences Meeting and Exhibit*, (Reno, Nevada, USA), p. 716, January 1994.

[46] T. Reinert, R. J. Flemming, R. Narducci, and R. J. Aubert, "Oscillating Airfoil Icing Tests in the NASA Glenn Research Center Icing Research Tunnel," SAE Technical Paper No. 2011-38-0016, June 2011.

[47] J. Wright and R. Aubert, "Icing Wind Tunnel Test of a Full Scale Heated Tail Rotor Model," in *AHS 70th Annual Forum*, (Montreal, Canada), pp. 20–22, 2014.

[48] R. J. Flemming, R. K. Britton, and T. H. Bond, "Role of Wind Tunnels and Computer Codes in the Certification and Qualification of Rotorcraft for Flight in Forecast Icing," in *20th European Rotorcraft Forum*, (Amsterdam, Netherlands), October 1994.

[49] J.-C. Tsao and R. E. Kreeger, "Evaluation of Scaling Methods for Rotorcraft Icing," NASA Technical Memorandum No. 215801, March 2010.

[50] J. L. Palacios, Y. Han, E. W. Brouwers, and E. C. Smith, "Icing Environment Rotor Test Stand Liquid Water Content Measurement Procedures and Ice Shape Correlation," *Journal of the American Helicopter Society*, vol. 57, no. 2, pp. 29–40, 2012.

[51] Y. Han, J. L. Palacios, and E. C. Smith, "An Experimental Correlation Between Rotor Test and Wind Tunnel Ice Shapes on NACA 0012 Airfoils," in *SAE Technical Paper*, June, 2011.

[52] E. W. Brouwers, J. L. Palacios, E. C. Smith, and A. A. Peterson, "The Experimental Investigation of a Rotor Hover Icing Model With Shedding," in *American Helicopter Society 66th Annual Forum*, (Phoeniz, Arizona, USA), pp. 1863–1875, May, 2010.

[53] G. Fortin and J. Perron, "Spinning Rotor Blade Tests in Icing Wind Tunnel," in *1st AIAA Atmospheric and Space Environments Conference, Session: ASE-11: Icing Aerodynamics*, (San Antonio, Texas), p. 4260, 22-25 June, 2009. DOI: 10.2514/6.2009-4260.

[54] European Aviation Safety Agency (EASA), *Certification Specifications for Aeroplane Flight Simulation Training Devices*. CS-FSTD(A), May 2018.

[55] C. S. Bidwell and M. G. Potapczuk, "Users manual for the NASA Lewis three-dimensional ice accretion code (LEWICE 3D)," (Cleveland, Ohio, USA), NASA Technical Memorandum No. 105974, December 1993.

[56] F. Morency, H. Beaugendre, G. Baruzzi, and W. Habashi, "FENSAP-ICE-A Comprehensive 3D Simulation System for In-Flight Icing," in *15th AIAA Computational Fluid Dynamics Conference*, (Anaheim, California, USA), p. 2566, June 2001.

[57] Gori, G., and Zocca, M., and Garabelli, M., and Guardone, A., and Quaranta, G., "PoliMIce: A Simulation Framework for Three-Dimensional Ice Accretion," *Applied Mathematics and Computation*, vol. 267, pp. 96–107, September 2015. DOI: 10.1016/j.amc.2015.05.081.

[58] ICE GENESIS Coordinator – Airbus Operations SAS, *Definition of Numerical Capability Requirements for Liquid Icing Conditions*. EU H2020 – Research and Innovation Action, May 2019.

[59] R. Britton and T. Bond, "A Review of Ice Accretion Data From a Model Rotor Icing Test and Comparison With Theory," in *29th Aerospace Sciences Meeting*, (Reno, Nevada, USA), p. 661, January 1991.

[60] R. Britton, "Development of an Analytical Method to Predict Helicopter Main Rotor Performance in Icing Conditions," in *30th Aerospace Sciences Meeting and Exhibit*, (Reno, Nevada, USA), p. 418, January 1992.

[61] W. B. Wright, "Users manual for the improved NASA Lewis ice accretion code LEWICE 1.6," NASA Contractor Report No.198355, June 1995.

[62] J. L. Hess and A. O. Smith, "Calculation of Potential Flow About Arbitrary Bodies," *Progress in Aerospace Sciences*, vol. 8, pp. 1–138, 1967.

[63] B. L. Messinger, "Equilibrium Temperature of an Unheated Icing Surface as a Function of Air Speed," *Journal of the aeronautical sciences*, vol. 20, no. 1, pp. 29–42, 1953.

[64] J, Hall and J, Hammerschmidt and J, Goglia and G, Black, *National Transportation Safety Board Aviation Accident Final Report*. NTSB/AAR-96/01, July 1996.

[65] J. Bain, L. Sankar, T. Egolf, R. Flemming, and R. Kreeger, "Progress Towards Modeling the Effects of Ice Accretion on Rotorcraft Performance in Hover and Forward Flight," in *35th European Rotorcraft Forum*, (Hamburg, Germany), September 2009.

[66] N. Rajmohan, J. Bain, M. Nucci, L. Sankar, R. Flemming, T. A. Egolf, and R. Kreeger, "Icing Studies for the UH-60A Rotor in Forward Flight," in *American Helicopter Socitety Aeromechanics Specialists Conference*, (San Francisco, California, USA), January 2010.

[67] M. Nucci, J. Bain, L. Sankar, T. A. Egolf, R. Flemming, and E. Kreeger, "A Methodology for Modeling the Effects of Icing on Rotary Wing Aerodynamics," in *48th AIAA Aerospace Sciences Meeting*, (Orlando, Florida, USA), January 2010.

[68] J. Bain, R. Deresz, L. Sankar, T. A. Egolf, R. Flemming, and E. Kreeger, "Effects of Icing on Rotary Wing Loads and Surface Heat Transfer," in *49th AIAA Aerospace Sciences Meeting including the New Horizons Forum and Aerospace Exposition*, (Orlando, Florida, USA), p. 1100, January 2011.

[69] R. Narducci and R. E. Kreeger, "Analysis of a Hovering Rotor in Icing Conditions," in *American Helicopter Society 66th Annual Forum*, (Phoenix, Arizona, USA), 2010.

[70] R. Narducci, S. Orr, and R. E. Kreeger, "Application of a High-Fidelity Icing Analysis Method to a Model-Scale Rotor in Forward Flight," in *American Helicopter Society 67th Annual Forum*, (Virginia Beach, Virginia, USA), May 2011.

[71] D. Kelly, H. Fouladi, M. Fossati, W. G. Habashi, R. Alicino, G. Quaranta, and P. Masarati, "Assessment of Ice Accretion Effects on Rotor Dynamics via Multi-Body and CFD Approaches," in *70th American Helicopter Society International Annual Forum 2014*, pp. 1840–1851, American Helicopter Society, 2014.

[72] D. Kelly, W. G. Habashi, G. Quaranta, P. Masarati, and M. Fossati, "Ice Accretion Effects on Helicopter Rotor Performance, via Multibody and CFD Approaches," *Journal of Aircraft*, vol. 55, no. 3, pp. 1165–1176, 2018.

[73] G.-q. Zhao, Q.-j. Zhao, and X. Chen, "New 3-D Ice Accretion Method of Hovering Rotor Including Effects of Centrifugal Force," *Aerospace Science and Technology*, vol. 48, pp. 122–130, 2016.

[74] C. Xi and Z. Qi-Jun, "Numerical Simulations for Ice Accretion on Rotors Using New Three-Dimensional Icing Model," *Journal of Aircraft*, vol. 54, no. 4, pp. 1428–1442, 2017.

[75] X. Chen, Q. Zhao, and G. Barakos, "Numerical Analysis of Aerodynamic Characteristics of Iced Rotor in Forward Flight," *AIAA Journal*, vol. 57, no. 4, pp. 1523–1537, 2019.

[76] Z. Qijun, Z. Guoqing, W. Bo, W. Qing, S. Yongjie, and X. Guohua, "Robust Navier-Stokes Method for Predicting Unsteady Flowfield and Aerodynamic Characteristics of Helicopter Rotor," *Chinese Journal of Aeronautics*, vol. 31, no. 2, pp. 214–224, 2018.

[77] X. Chen and Q.-J. Zhao, "Computational Investigations of Water Collection Efficiency on Blades in Unsteady Vortex Flowfield of Rotor," *Aerospace Science and Technology*, vol. 79, pp. 482–491, 2018.

[78] W. Wright and M. Potapczuk, "Semi-Empirical Modelling of SLD Physics," in *42nd AIAA aerospace sciences meeting and exhibit*, (Reno, Nevada, USA), p. 412, January 2004.

[79] T. G. Myers, "Extension to the Messinger Model for Aircraft Icing," *AIAA journal*, vol. 39, no. 2, pp. 211–218, 2001.

[80] M. Bragg, T. Basar, W. Perkins, M. Selig, P. Voulgaris, J. Melody, and N. Sarter, "Smart Icing Systems for Aircraft Icing Safety," in *40th AIAA Aerospace Sciences Meeting & Exhibit*, p. 813, 2002.

[81] V. K. Varadan, V. V. Varadan, and X.-Q. Bao, "IDT, SAW, and MEMS Sensors for Measuring Deflection, Acceleration, and Ice Detection of Aircraft," in *Smart Structures and Materials 1997: Smart Electronics and MEMS*, vol. 3046, pp. 209–219, International Society for Optics and Photonics, 1997.

[82] S. Roy, A. Izad, R. G. DeAnna, and M. Mehregany, "Smart Ice Detection Systems Based on Resonant Piezoelectric Transducers," *Sensors and actuators a: physical*, vol. 69, no. 3, pp. 243–250, 1998.

[83] J. W. Melody, T. Başar, W. R. Perkins, and P. G. Voulgaris, "Parameter Identification for Inflight Detection and Characterization of Aircraft Icing," *Control Engineering Practice*, vol. 8, no. 9, pp. 985–1001, 2000.

[84] D. D. Hongerholt, G. Willms, and J. L. Rose, "Summary of Results From an Ultrasonic In-Flight Wing Ice Detection System," in *AIP Conference Proceedings*, vol. 615, pp. 1023–1028, American Institute of Physics, 2002.

[85] P. Jarvinen, "Aircraft Ice Detection Method," in *45th AIAA Aerospace Sciences Meeting and Exhibit*, (Reno, Nevada), p. 696, 2007. https://doi.org/10.2514/6.2007-696.

[86] C. E. Bassey and G. R. Simpson, "Aircraft Ice Detection Using Time Domain Reflectometry With Coplanar Sensors," in *2007 IEEE Aerospace Conference*, pp. 1–6, IEEE, 2007. DOI:10.1109/AERO.2007.352857.

[87] F. Caliskan, R. Aykan, and C. Hajiyev, "Aircraft Icing Detection, Identification, and Reconfigurable Control Based on Kalman Filtering and Neural Networks," *Journal of Aerospace Engineering*, vol. 21, no. 2, pp. 51–60, 2008.

[88] J. C. Zhuge, Z. J. Yu, and J. S. Gao, "Ice Detection Based on Near Infrared Image Analysis," in *Applied Mechanics and Materials*, vol. 121, pp. 3960–3964, Trans Tech Publ, 2012.

[89] J. Zou, L. Ye, and J. Ge, "Ice Type Detection Using an Oblique End-Face Fibre-Optic Technique," *Measurement Science and Technology*, vol. 24, no. 3, p. 035201, 2013.

[90] A. A. Ikiades, D. Spasopoulos, K. Amoiropoulos, T. Richards, G. Howard, and M. Pfeil, "Detection and Rate of Growth of Ice on Aerodynamic Surfaces Using its Optical Characteristics," *Aircraft Engineering and Aerospace Technology*, 2013.

[91] Y. Liu, W. Chen, L. J. Bond, and H. Hu, "A Feasibility Study to Identify Ice Types by Measuring Attenuation of Ultrasonic Waves for Aircraft Icing Detection," in *Fluids Engineering Division Summer Meeting*, vol. 46223, p. V01BT22A003, American Society of Mechanical Engineers, 2014.

[92] T. Schlegl, M. Moser, and H. Zangl, "Wireless and Flexible Ice Detection on Aircraft," tech. rep., SAE Technical Paper, 2015.

[93] X. Zhao and J. L. Rose, "Ultrasonic Guided Wave Tomography for Ice Detection," *Ultrasonics*, vol. 67, pp. 212–219, 2016.

[94] S. A. Bagherzadeh and D. Asadi, "Detection of the Ice Assertion on Aircraft Using Empirical Mode Decomposition Enhanced by Multi-Objective Optimization," *Mechanical Systems and Signal Processing*, vol. 88, pp. 9–24, 2017.

[95] Y. Liu, L. J. Bond, and H. Hu, "Ultrasonic-Attenuation-Based Technique for Ice Characterization Pertinent to Aircraft Icing Phenomena," *AIAA Journal*, vol. 55, no. 5, pp. 1602–1609, 2017.

[96] B. Cheng, Y. Han, K. S. Brentner, J. Palacios, P. J. Morris, D. Hanson, and M. Kinzel, "Surface Roughness Effect on Rotor Broadband Noise," *International Journal of Aeroacoustics*, vol. 17, no. 4-5, pp. 438–466, 2018.

[97] X. Chen, Q. Zhao, G. N. Barakos, and A. Kusyumov, "Numerical Analysis of Rotor Aero-Acoustic Characteristics for Ice Detection," *International Journal of Aeroacoustics*, vol. 18, no. 6-7, pp. 596–620, 2019.

[98] C. Deiler and N. Fezans, "Performance-Based Ice Detection Methodology," *Journal of Aircraft*, vol. 57, no. 2, pp. 209–223, 2020.

[99] A. P. Broeren and M. B. Bragg, "Effect of Airfoil Geometry on Performance With Simulated Intercycle Ice Accretions," *Journal of Aircraft*, vol. 42, no. 1, pp. 121–130, 2005.

[100] C. Schwarz, P. Ohme, and C. Deiler, "The SENS4ICE EU project-SENSors and certifiable hybrid architectures for safer aviation in ICing Environment," (Minneapolis, Minnesota, USA), SAE International Conference on Icing of Aircraft, Engines, and Structures, 2019.

[101] European Union Aviation Safety Agency (EASA), *Certification Specifications and Acceptable Means of Compliance for Large Aeroplanes: CS-25 Appendix O: Supercooled Large Drop icing conditions*. CS-25 Amendment 26, p. 1-App O: 1-11, December 2020.

[102] R. Flemming, "The Past Twenty Years of Icing Research and Development at Sikorsky Aircraft," Proceedings of the 40th AIAA Aerospace Sciences Meeting & Exhibit, Reno, Nevada, January 2002.

[103] R. Narducci and R. Kreeger, "Analysis of a Hover Rotor in Icing Conditions," Proceedings of the 66th Annual Forum of the American Helicopter Society, Phoenix, Arizona, May 2010.

[104] J. Bain, L. N. Sankar, R. J. Aubert, and R. J. Flemming, "A Methodology for the Prediction of Rotor Blade Ice Formation and Shedding," SAE Technical Paper No. 2011-38-0090, June 2011.

[105] R. Narduucci and T. Reinert, "Calculations of Ice Shapes on Oscillating Airfoils," SAE Technical Paper No. 2011-38-0015, June 2011.

[106] Sears, W. R., "Some aspects of non-stationary airfoil theory and its practical application," *Journal of the Aeronautical Sciences*, vol. 8, pp. 104–108, January 1941. DOI:10.2514/8.10655.

[107] L. W. Carr and W. J. McCroskey, "Analysis of the development of dynamic stall based on oscillating airfoil experiments," NASA Technical Note D-8382, January 1977.

[108] R. E. Kreeger, L. Sankar, R. Narducci, and R. Kunz, "Progress in Rotorcraft Icing Computational Tool Development," SAE Technical Paper No. 2015-01-2088, June 2015.

[109] B. Cheng, Y. Han, K. S. Brentner, J. L. Palacios, and P. J. Morris, "Quantification of Rotor Surface Roughness Due to Ice Accretion via Broadband Noise Measurement," Proceedings of the 70th Annual Forum of the American Helicopter Society, Montreal, Quebec, May 2014.

[110] X. Chen, Q. Zhao, and G. Barakos, "Numerical Analysis of Rotor Aero-acoustic Characteristics for Ice Detection based on HMB Solver," Proceedings of the 73rd Annual Forum of the American Helicopter Society, Fort Worth, Texas, May 2018.

[111] Zocca, M., and Gori, G., and Guardone, A., "Blockage and Three-Dimensional Effects in Wind-Tunnel Testing of Ice Accretion over Wings," *Journal of Aircraft*, vol. 54, pp. 759–767, April 2016. DOI: https://doi.org/10.2514/1.C033750.

[112] Economon, T. D., and Palacios, F., and Copeland, S. R., and Lukaczyk, T. W., and Alonso, J. J., "SU2: An Open-Source Suite for Multiphysics Simulation and Design," *AIAA Journal*, vol. 54, pp. 828–846, December 2015. DOI: https://doi.org/10.2514/1.J053813.

[113] Gori, G., and Parma, G., and Zocca, M., and Guardone, A., "Local Solution to the Unsteady Stefan Problem for In-Flight Ice Accretion Modeling," *Journal of Aircraft*, vol. 55, pp. 251–262, September 2017. DOI: https://doi.org/10.2514/1.C034412.

[114] L. W. Carr, K. W. McAlister, and W. J. McCroskey, "Analysis of the Development of Dynamic Stall Based on Oscillating Airfoil Experiments," NASA Technical Note D-8382, January 1977.

[115] B. Y. Zhou, T. Albring, N. R. Gauger, C. R. Ilario, T. D. Economon, and J. J. Alonso, "Reduction of Airframe Noise Components Using a Discrete Adjoint Approach," Proceedings of the 18th AIAA/ISSMO Multidisciplinary Analysis and Optimization Conference, Denver, Colorado, June 2017.

[116] Richardson, L. F. and Gaunt, J. A., "VIII. The Deferred Approach to the Limit," *Philosophical Transactions of the Royal Society of London. Series A, Containing Papers of a Mathematical or Physical Character*, vol. 226, pp. 299–361, January 1927. DOI: https://doi.org/10.1098/rsta.1927.0008.

[117] Roache, P. J., "Perspective: A Method for Uniform Reporting of Grid Refinement Studies," *Journal of Fluids Engineering*, vol. 116, pp. 405–413, September 1994. DOI: https://doi.org/10.1115/1.2910291.

[118] E. Molina, C. Spode, R. Annes da Silva, D. Manosalvas-Kjono, S. Nimmagadda, T. Economon, J. Alonso, and M. Righi, "Hybrid RANS/LES calculations in SU2," Proceedings of the 23rd AIAA Computational Fluid Dynamics Conference, Denver, Colorado, June 2017.

[119] Molina E.S., and Silva D.M., and Broeren A.P., and Righi M., and Alonso J.J., "Application of DDES to Iced Airfoil in Stanford University Unstructured (SU2)," *Progress in Hybrid RANS-LES Modelling*, vol. 143, pp. 283–293, November 2019. DOI: https://doi.org/10.1007/978-3-030-27607-2_23.

[120] J. T. Batina, "Unsteady Euler Airfoil Solutions Using Unstructured Dynamic Meshes," *AIAA journal*, vol. 28, no. 8, pp. 1381–1388, 1990. https://doi.org/10.2514/3.25229.

[121] C. Farhat, C. Degand, B. Koobus, and M. Lesoinne, "Torsional Springs for Two-Dimensional Dynamic Unstructured Fluid Meshes," *Computer methods in applied mechanics and engineering*, vol. 163, no. 1-4, pp. 231–245, 1998. https://doi.org/10.1016/S0045-7825(98)00016-4.

[122] T. Baker and P. Cavallo, "Dynamic Adaptation for Deforming Tetrahedral Meshes," in *14th Computational Fluid Dynamics Conference*, (Norfolk, Virginia, U.S.A), p. 3253, 01-05 November, 1999. https://doi.org/10.2514/6.1999-3253.

[123] E. J. Nielsen and W. K. Anderson, "Recent Improvements in Aerodynamic Design Optimization on Unstructured Meshes," *AIAA journal*, vol. 40, no. 6, pp. 1155–1163, 2002. https://doi.org/10.2514/2.1765.

[124] A. De Boer, M. Van der Schoot, and H. Bijl, "Mesh Deformation Based on Radial Basis Function Interpolation," *Computers & structures*, vol. 85, no. 11-14, pp. 784–795, 2007. https://doi.org/10.1016/j.compstruc.2007.01.013.

[125] T. C. Rendall and C. B. Allen, "Efficient Mesh Motion Using Radial Basis Functions With Data Reduction Algorithms," *Journal of Computational Physics*, vol. 228, no. 17, pp. 6231–6249, 2009. https://doi.org/10.1016/j.jcp.2009.05.013.

[126] T. C. Rendall and C. B. Allen, "Unified Fluid–Structure Interpolation and Mesh Motion Using Radial Basis Functions," *International journal for numerical methods in engineering*, vol. 74, no. 10, pp. 1519–1559, 2008. https://doi.org/10.1002/nme.2219.

[127] A. Beckert and H. Wendland, "Multivariate Interpolation for Fluid-Structure-Interaction Problems Using Radial Basis Functions," *Aerospace Science and Technology*, vol. 5, no. 2, pp. 125–134, 2001. https://doi.org/10.1016/S1270-9638(00)01087-7.

[128] T. C. Rendall and C. B. Allen, "Reduced Surface Point Selection Options for Efficient Mesh Deformation Using Radial Basis Functions," *Journal of Computational Physics*, vol. 229, no. 8, pp. 2810–2820, 2010. https://doi.org/10.1016/j.jcp.2009.12.006.

[129] G. Wang, H. H. Mian, Z.-Y. Ye, and J.-D. Lee, "Improved Point Selection Method for Hybrid-Unstructured Mesh Deformation Using Radial Basis Functions," *AIAA Journal*, vol. 53, no. 4, pp. 1016–1025, 2015. https://doi.org/10.2514/1.J053304.

[130] L. Xie and H. Liu, "Efficient Mesh Motion Using Radial Basis Functions With Volume Grid Points Reduction Algorithm," *Journal of Computational Physics*, vol. 348, pp. 401–415, 2017. https://doi.org/10.1016/j.jcp.2017.07.042.

[131] X. Tong, D. Thompson, Q. Arnoldus, E. Collins, and E. Luke, "Three-Dimensional Surface Evolution and Mesh Deformation for Aircraft Icing Applications," *Journal of Aircraft*, vol. 54, no. 3, pp. 1047–1063, 2017. https://doi.org/10.2514/1.C033949.

[132] C. Groth, E. Costa, and M. E. Biancolini, "RBF-Based Mesh Morphing Approach to Perform Icing Simulations in the Aviation Sector," *Aircraft Engineering and Aerospace Technology*, 2019. https://doi.org/10.1108/AEAT-07-2018-0178.

[133] T. D. Economon, F. Palacios, S. R. Copeland, T. W. Lukaczyk, and J. J. Alonso, "SU2: An Open-Source Suite for Multiphysics Simulation and Design," *Aiaa Journal*, vol. 54, no. 3, pp. 828–846, 2016. https://doi.org/10.2514/1.J053813.

[134] H. Wendland, "Piecewise Polynomial, Positive Definite and Compactly Supported Radial Functions of Minimal Degree," *Advances in computational Mathematics*, vol. 4, no. 1, pp. 389–396, 1995. https://doi.org/10.1007/BF02123482.

[135] G. Ruff and B. Berkowitz, "Users Manual for the Nasa Lewis Ice Accretion Prediction Code (LEWICE)," 1990.

[136] G. Gori, G. Parma, M. Zocca, and A. Guardone, "Local Solution to the Unsteady Stefan Problem for In-Flight Ice Accretion Modeling," *Journal of Aircraft*, vol. 55, no. 1, pp. 251–262, 2018. https://doi.org/10.2514/1.C034412.

[137] J.-C. Tsao and S. Lee, *Evaluation of Icing Scaling on Swept NACA 0012 Airfoil Models*. Glenn Research Center, Cleveland, Ohio: National Aeronautics and Space Administration, Contractor Report No. 217419, May, 2012. https://doi.org/10.4271/2011-38-0081.

[138] "Aviation Accident Reports - National Transportation Safety Board." `https://www.ntsb.gov/investigations/AccidentReports/Pages/aviation.aspx`, Accessed: May, 2020.

[139] R. C. Strawn, F. X. Caradonna, and E. P. Duque, "30 Years of Rotorcraft Computational Fluid Dynamics Research and Development," *Journal of the American Helicopter Society*, vol. 51, no. 1, pp. 5–21, 2006. https://doi.org/10.4050/1.3092875.

[140] D. Jespersen, T. Pulliam, and P. Buning, "Recent Enhancements to OVERFLOW," in *35th Aerospace Sciences Meeting and Exhibit*, (Reno, Navada, U.S.A), p. 644, 06-09 January, 1997. https://doi.org/10.2514/6.1997-644.

[141] W. K. Anderson and D. L. Bonhaus, "An Implicit Upwind Algorithm for Computing Turbulent Flows on Unstructured Grids," *Computers & Fluids*, vol. 23, no. 1, pp. 1–21, 1994. https://doi.org/10.1016/0045-7930(94)90023-X.

[142] G. R. Whitehouse, "Investigation of hybrid grid–based computational fluid dynamics methods for rotorcraft flow analysis," *Journal of the American Helicopter Society*, vol. 56, no. 3, pp. 1–10, July 2011.

[143] R. C. Strawn, E. P. Duque, and J. Ahmad, "Rotorcraft aeroacoustics computations with overset-grid cfd methods," *Journal of the American Helicopter Society*, vol. 44, no. 2, pp. 132–140, 1999.

[144] A. Datta, M. Nixon, and I. Chopra, "Review of Rotor Loads Prediction With the Emergence of Rotorcraft CFD," *Journal of the American Helicopter Society*, vol. 52, no. 4, pp. 287–317, 2007.

[145] A. Datta, J. Sitaraman, J. D. Baeder, and I. Chopra, "Analysis refinements for prediction of rotor vibratory loads in high-speed forward flight," in *American Helicopter Society 60th Annual Forum*, (Baltimore, Maryland, USA).

[146] M. Potsdam, H. Yeo, and W. Johnson, "Rotor Airloads Prediction Using Loose Aerodynamic/structural Coupling," *Journal of Aircraft*, vol. 43, no. 3, pp. 732–742, 2006.

[147] M. J. Smith, M. Potsdam, T.-C. Wong, J. D. Baeder, and S. Phanse, "Evaluation of computational fluid dynamics to determine two-dimensional airfoil characteristics for rotorcraft applications," *Journal of the American Helicopter Society*, vol. 51, no. 1, pp. 70–79, 2006.

[148] J. W. Lim, T. A. Nygaard, R. Strawn, and M. Potsdam, "Blade-vortex interaction airloads prediction using coupled computational fluid and structural dynamics," *Journal of the American Helicopter Society*, vol. 52, no. 4, pp. 318–328, 2007.

[149] D. D. Boyd, "HART-II acoustic predictions using a coupled CFD/CSD method," in *American Helicopter Society 65th Annual Forum*, (Grapevine, Texas, USA), May 27, 2009.

[150] E. M. Lee-Rausch and R. T. Biedron, "FUN3D airloads predictions for the full-scale UH-60A airloads rotor in a wind tunnel," *Journal of the American Helicopter Society*, vol. 59, no. 3, pp. 1–19, July, 2014.

[151] L. Wang, B. Diskin, R. T. Biedron, E. J. Nielsen, and O. A. Bauchau, "High-fidelity multidisciplinary sensitivity analysis and design optimization for rotorcraft applications," *AIAA Journal*, vol. 57, no. 8, pp. 3117–3131, 2019.

[152] L. Wang, B. Diskin, R. T. Biedron, E. J. Nielsen, and O. A. Bauchau, "Evaluation of high-fidelity multidisciplinary sensitivity-analysis framework for multipoint rotorcraft optimization," *Journal of Aircraft*, vol. 57, no. 5, pp. 830–842, 2020.

[153] R. Steijl, G. Barakos, and K. Badcock, "A Framework for CFD Analysis of Helicopter Rotors in Hover and Forward Flight," *International journal for numerical methods in fluids*, vol. 51, no. 8, pp. 819–847, 2006. https://doi.org/10.1002/fld.1086.

[154] M. Biava and L. Vigevano, "Simulation of a Complete Helicopter: A CFD Approach to the Study of Interference Effects," *Aerospace Science and Technology*, vol. 19, no. 1, pp. 37–49, 2012. https://doi.org/10.1016/j.ast.2011.08.006.

[155] A. Antoniadis, D. Drikakis, B. Zhong, G. Barakos, R. Steijl, M. Biava, L. Vigevano, A. Brocklehurst, O. Boelens, M. Dietz, *et al.*, "Assessment of CFD Methods Against Experimental Flow Measurements for Helicopter Flows," *Aerospace Science and Technology*, vol. 19, no. 1, pp. 86–100, 2012. https://doi.org/10.1016/j.ast.2011.09.003.

[156] G. R. Srinivasan, J. Baeder, S. Obayashi, and W. McCroskey, "Flowfield of a Lifting Rotor in Hover-a Navier-Stokes Simulation," *AIAA journal*, vol. 30, no. 10, pp. 2371–2378, 1992. https://doi.org/10.2514/3.11236.

[157] G. Srinivasan and J. Baeder, "TURNS: A Free-Wake Eule/navier-Stokes Numerical Method for Helicopter Rotors," *AIAA journal*, vol. 31, no. 5, pp. 959–962, 1993. https://doi.org/10.2514/3.49036.

[158] M. Gazaix, A. Jolles, and M. Lazareff, "The elsA Object-Oriented Computational Tool for Industrial Applications," in *23rd Congress of ICAS*, (Toronto, Canada), p. 220, 08-13 September, 2002. Corpus ID: 56582723.

[159] J. Raddatz and J. K. Fassbender, *Block Structured Navier-Stokes Solver FLOWer*, vol. 89. Berlin, Heidelberg: Springer, MEGAFLOW - Numerical Flow Simulation for Aircraft Design. Notes on Numerical Fluid Mechanics and Multidisciplinary Design (NNFM) ed., 2005. https://doi.org/10.1007/3-540-32382-1.

[160] W. L. Oberkampf and F. G. Blottner, "Issues in Computational Fluid Dynamics Code Verification and Validation," *AIAA journal*, vol. 36, no. 5, pp. 687–695, 1998. https://doi.org/10.2514/2.456.

[161] F. Palacios, T. D. Economon, A. Aranake, S. R. Copeland, A. K. Lonkar, T. W. Lukaczyk, D. E. Manosalvas, K. R. Naik, S. Padron, B. Tracey, *et al.*, "Stanford University Unstructured (SU2): Analysis and Design Technology for Turbulent Flows," in *In 52nd Aerospace Sciences Meeting*, (National Harbor, Maryland), p. 0243, January 13-17, 2014. https://doi.org/10.2514/6.2014-0243.

[162] T. D. Economon, F. Palacios, and J. J. Alonso, "A Viscous Continuous Adjoint Approach for the Design of Rotating Engineering Applications," in *21st AIAA computational fluid dynamics conference*, (San Diego, California, U.S.A), p. 2580, 24-27 June, 2013. https://doi.org/10.2514/6.2013-2580.

[163] R. Ö. Içke, O. Baysal, L. V. Lopes, B. Y. Zhou, B. Diskin, and A. Moy, "Toward adjoint-based aeroacoustic optimization for propeller and rotorcraft applications," in *AIAA Aviation 2020 Forum*, (Virtual Event), p. 3140, June 15-19, 2020. https://doi.org/10.2514/6.2020-3140.

[164] G. Gori, E. van der Weide, and A. Guardone, "On Conservation in Compressible Flow Simulations Using Sliding Mesh Coupling," in *VII International Conference on Computational Methods for Coupled Problems in Science and Engineering conference*, (Rhodes Island, Greece), June 12-14, 2020.

[165] D. C. Wilcox *et al.*, *Turbulence Modeling for CFD*. DCW industries La Canada, CA, 2 ed., 1998. ISBN 13: 9780963605153.

[166] W. Sutherland, "The Viscosity of Gases and Molecular Force," *The London, Edinburgh, and Dublin Philosophical Magazine and Journal of Science*, vol. 36, no. 223, pp. 507–531, 1893. https://doi.org/10.1080/14786449308620508.

[167] P. Spalart and S. Allmaras, "A One-Equation Turbulence Model for Aerodynamic Flows," in *30th aerospace sciences meeting and exhibit*, (Reno, Nevada, U.S.A), p. 439, 06-09 January, 1992. https://doi.org/10.2514/6.1992-439.

[168] H. K. Versteeg and W. Malalasekera, *An Introduction to Computational Fluid Dynamics: The Finite Volume Method*. Pearson education, 2 ed., 2007. ISBN: 978-0-13-127498-3.

[169] A. Jameson, W. Schmidt, and E. Turkel, "Numerical Solution of the Euler Equations by Finite Volume Methods Using Runge Kutta Time Stepping Schemes," in *14th fluid and plasma dynamics conference*, (Palo Alto, California, U.S.A), p. 1259, 23-25 June, 1981. https://doi.org/10.2514/6.1981-1259.

[170] P. L. Roe, "Approximate Riemann Solvers, Parameter Vectors, and Difference Schemes," *Journal of computational physics*, vol. 43, no. 2, pp. 357–372, 1981. https://doi.org/10.1016/0021-9991(81)90128-5.

[171] B. Van Leer, "Towards the Ultimate Conservative Difference Scheme. V. A Second-Order Sequel to Godunov's Method," *Journal of computational Physics*, vol. 32, no. 1, pp. 101–136, 1979. https://doi.org/10.1016/0021-9991(79)90145-1.

[172] A. Jameson, "Time Dependent Calculations Using Multigrid, With Applications to Unsteady Flows Past Airfoils and Wings," in *10th Computational Fluid Dynamics conference*, (Honolulu, Hawaii, U.S.A.), p. 1596, 24-26 June, 1991. https://doi.org/10.2514/6.1991-1596.

[173] D. Mavriplis, Z. Yang, and N. Mundis, "Extensions of time spectral methods for practical rotorcraft problems," in *50th AIAA Aerospace Sciences Meeting including the New Horizons Forum and Aerospace Exposition*, (Nashville, Tennessee, USA), p. 423, 9-12 January, 2012. https://doi.org/10.2514/6.2012-423.

[174] K. C. Hall, J. P. Thomas, and W. S. Clark, "Computation of Unsteady Nonlinear Flows in Cascades Using a Harmonic Balance Technique," *AIAA journal*, vol. 40, no. 5, pp. 879–886, 2002. https://doi.org/10.2514/2.1754.

[175] A. Rubino, M. Pini, P. Colonna, T. Albring, S. Nimmagadda, T. Economon, and J. Alonso, "Adjoint-Based Fluid Dynamic Design Optimization in Quasi-Periodic Unsteady Flow Problems Using a Harmonic Balance Method," *Journal of Computational Physics*, vol. 372, pp. 220–235, 2018. https://doi.org/10.1016/j.jcp.2018.06.023.

[176] E. Rinaldi, P. Colonna, and R. Pecnik, "Flux-Conserving Treatment of Non-Conformal Interfaces for Finite-Volume Discretization of Conservation Laws," *Computers & Fluids*, vol. 120, pp. 126–139, 2015. https://doi.org/10.1016/j.compfluid.2015.07.017.

[177] P. Thomas and C. Lombard, "Geometric conservation law and its application to flow computations on moving grids," *AIAA journal*, vol. 17, no. 10, pp. 1030–1037, 1979. https://doi.org/10.2514/3.61273.

[178] S. A. Morton, R. B. Melville, and M. R. Visbal, "Accuracy and coupling issues of aeroelastic navier-stokes solutions on deforming meshes," *Journal of Aircraft*, vol. 35, no. 5, pp. 798–805, September, 1998. https://doi.org/10.2514/2.2372.

[179] R. Biedron and J. Thomas, "Recent enhancements to the fun3d flow solver for moving-mesh applications," in *47th AIAA Aerospace Sciences Meeting including The New Horizons Forum and Aerospace Exposition*, (Orlando, Florida, USA), p. 1360, 5-8 January, 2009. https://doi.org/10.2514/6.2009-1360.

[180] T. Rendall and C. Allen, "Parallel Efficient Mesh Motion Using Radial Basis Functions With Application to Multi-Bladed Rotors," *International journal for numerical methods in engineering*, vol. 81, no. 1, pp. 89–105, 2010. https://doi.org/10.1002/nme.2678.

[181] M. Schuff, P. Kranzinger, M. Keßler, and E. Krämer, "Advanced CFD-CSD coupling: Generalized, high performant, radial basis function based volume mesh deformation algorithm for structured, unstructured and overlapping meshes," in *40th European Rotorcraft Forum*, (Southampton, UK), September 2-5, 2014.

[182] M. Morelli, T. Bellosta, and A. Guardone, "Efficient Radial Basis Function Mesh Deformation Methods for Aircraft Icing," in *In the 7th European Seminar on Computing*, (Pilsen, Czech Republic), June 8-12, 2020.

[183] F. X. Caradonna and C. Tung, "Experimental and Analytical Studies of a Model Helicopter Rotor in Hover," in *Presented at the 6th European Rotorcraft and Powered Lift Aircraft Forum*, (Bristol, England), September 16-19, 1980.

[184] J. L. Cross and M. E. Watts, *Tip Aerodynamics and Acoustics Test: A Report and Data Survey*. Ames Research Center, Moffett Field, California: National Aeronautics and Space Administration, Scientific and Technical Information Division, Reference Publication No. 1179, December, 1988.

[185] Y. M. Park and O. J. Kwon, "Simulation of unsteady rotor flow field using unstructured adaptive sliding meshes," *Journal of the American Helicopter Society*, vol. 49, no. 4, pp. 391–400, 2004.

[186] F. Tejero E, P. Doerffer, O. Szulc, *et al.*, "Application of a passive flow control device on helicopter rotor blades," *Journal of the American Helicopter Society*, vol. 61, no. 1, pp. 1–13, 2016.

[187] J. Benek, J. Steger, F. Dougherty, and P. Buning, "Chimera. A Grid-Embedding Technique," tech. rep., Arnold Engineering Development Center Arnold AFB TN, 1986.

[188] Z. Wang, "A Fully Conservative Interface Algorithm for Overlapped Grids," *Journal of Computational Physics*, vol. 122, no. 1, pp. 96–106, 1995.

[189] Z. Wang, N. Hariharan, and R. Chen, "Recent Development on the Conservation Property of Chimera," *International Journal of Computational Fluid Dynamics*, vol. 15, no. 4, pp. 265–278, 2001.

[190] P. Farrell, M. Piggott, C. Pain, G. Gorman, and C. Wilson, "Conservative Interpolation Between Unstructured Meshes via Supermesh Construction," *Computer Methods in Applied Mechanics and Engineering*, vol. 198, no. 33-36, pp. 2632–2642, 2009.

[191] R. Steijl and G. Barakos, "Sliding Mesh Algorithm for CFD Analysis of Helicopter Rotor–Fuselage Aerodynamics," *International Journal for Numerical Methods in Fluids*, vol. 58, no. 5, pp. 527–549, 2008.

[192] H. Nam, Y. Park, and O. Kwon, "Simulation of Unsteady Rotor-Fuselage Aerodynamic Interaction Using Unstructured Adaptive Meshes," *Journal of the American Helicopter Society*, vol. 51, no. 2, pp. 141–149, 2006.

[193] F. A. Morrison, *An introduction to fluid mechanics*. Cambridge University Press, May, 2013. ISBN: 9781107003538.

[194] R. Clift, J. R. Grace, and M. E. Weber, *Bubbles, drops, and particles*. Courier Corporation, January, 2005. ISBN: 0486317749.

[195] R. Löhner and J. Ambrosiano, "A Vectorized Particle Tracer for Unstructured Grids," *Journal of Computational Physics*, vol. 91, no. 1, pp. 22–31, 1990.

[196] A. Haselbacher, F. Najjar, and J. Ferry, "An Efficient and Robust Particle-Localization Algorithm for Unstructured Grids," *Journal of Computational Physics*, vol. 225, no. 2, pp. 2198–2213, 2007.

[197] R. Chorda, J. Blasco, and N. Fueyo, "An Efficient Particle-Locating Algorithm for Application in Arbitrary 2D and 3D Grids," *International Journal of Multiphase Flow*, vol. 28, no. 9, pp. 1565–1580, 2002.

[198] Q. Zhou and M. Leschziner, "An Improved Particle-Locating Algorithm for Eulerian-Lagrangian Computations of Two-Phase Flows in General Coordinates," *International Journal of Multiphase Flow*, vol. 25, no. 5, pp. 813–825, 1999.

[199] T. Bellosta, G. Parma, and A. Guardone, "A Robust 3D Particle Tracking Solver for In-Fight Ice Accretion Using Arbitrary Precision Arithmetic," in *VIII International Conference on Computational Methods for Coupled Problems in Science and Engineering*, 2019.

[200] P. Lorber, A. Covino, and F. Carta, "Dynamic Stall Experiments on a Swept Three-Dimensional Wing in Compressible Flow," in *22nd Fluid Dynamics, Plasma Dynamics and Lasers Conference*, p. 1795, 1991.

[201] C. Malpica, "Parametric Investigation on the Use of Lateral and Logitudinal Rotor Trim Flapping for Tiltrotor Noise Reduction," in *AHS International 73rd Annual Forum and Technology Display, Fort Worth, Texas, USA*, 2017.

[202] J. Narramore, "Airfoil Design, Test, and Evaluation for the V-22 Tilt Rotor Vehicle," in *43rd Annual Forum of the American Helicopter Society, St. Louis, Missouri*, 1987.

[203] GrabCAD Inc., "GrabCAD: Design community, cad library, 3d printing software." `https://grabcad.com`, 2009.

[204] European Union Aviation Safety Agency (EASA), *Certification Specifications and Acceptable Means of Compliance for Small Rotorcraft: CS 27.1419 Ice Protection, c.* CS-27 Amendment 7, p. 1-F-11, June 2020.

[205] European Union Aviation Safety Agency (EASA), *Certification Specifications and Acceptable Means of Compliance for Large Rotorcraft: CS 29.1419 Ice Protection, c.* CS-29 Amendment 8, p. 1-F-14, June 2020.

[206] Federal Aviation Administration, *Certification of Normal Category Rotorcraft: Section 27.1419. Ice Protection, c. Procedures, (1) Compliance, (iii).* Adivisory Circular No. 27-1B, Issue 7, p. F81, June 2018.

[207] Federal Aviation Administration, *Certification of Transport Category Rotorcraft: Section 29.1419. Ice Protection, c. Procedures, (1) Compliance, (iii).* Adivisory Circular No. 29-2C, Issue 8, p. F98, July 2018.

[208] M. Morelli, T. Bellosta, and A. Guardone, "Development and Preliminary Assessment of the Open-Source CFD toolkit SU2 for Rotorcraft Flows," in *In the 7th European Seminar on Computing*, (Pilsen, Czech Republic), June 8-12, 2020.

[209] M. Morelli, T. Bellosta, and A. Guardone, "Lagrangian particle tracking in sliding mesh for rotorcraft icing applications," in *45th European Rotorcraft Forum*, (Warsaw, Poland), pp. 1–13, September, 2019.

[210] J. Bain, J. Cajigas, L. Sankar, R. Flemming, and R. Aubert, "Prediction of rotor blade ice shedding using empirical methods," in *AIAA Atmospheric and Space Environments Conference*, (Toronto, Ontario, Canada), p. 7985, August 2-4, 2010. https://doi.org/10.2514/6.2010-7985.

[211] A. Gupta, E. Halloran, L. N. Sankar, J. Palacios, and R. E. Kreeger, "Development and validation of physics based models for ice shedding," in *44th European Rotorcraft Forum*, (Delft, The Netherlands), September 19-20, 2018.

[212] M. J. Anthony, M. Nathoo, Z. Zhan, W. G. Habashi, and M. Fossati, "Rotor ice shedding and trajectory analyses in forward flight," in *2018 Atmospheric and Space Environments Conference*, (Atlanta, Georgia, USA), p. 3659, June 25-29, 2018. https://doi.org/10.2514/6.2018-3659.

[213] G. Fortin and J. Perron, "Ice Adhesion Models to Predict Shear Stress at Shedding," *Journal of adhesion science and technology*, vol. 26, no. 4-5, pp. 523–553, 2012. DOI: 10.1163/016942411X574835.

[214] J. F. Williams and D. L. Hawkings, "Sound generation by turbulence and surfaces in arbitrary motion," *Philosophical Transactions for the Royal Society of London. Series A, Mathematical and Physical Sciences*, pp. 321–342, 1969.

[215] F. Farassat, "Linear acoustic formulas for calculation of rotating blade noise," *AIAA journal*, vol. 19, no. 9, pp. 1122–1130, 1981.

[216] P. Di Francescantonio, "A new boundary integral formulation for the prediction of sound radiation," *Journal of Sound and Vibration*, vol. 202, no. 4, pp. 491–509, 1997.

[217] B. Y. Zhou, N. R. Gauger, M. Morelli, A. Guardone, J. Hauth, and X. Huan, "Development of a Real-Time In-Flight Ice Detection System via Computational Aeroacoustics and Bayesian Neural Networks," in *AIAA Scitech 2020 Forum*, p. 1638, 2020.

[218] R. Biedron and E. Lee-Rausch, "Rotor Airloads Prediction Using Unstructured Meshes and Loose CFD/CSD Coupling," in *26th AIAA Applied Aerodynamics Conference*, p. 7341, 2008.

[219] P. Beaumier, G. Arnaud, and C. Castellin, "Performance Prediction and Flowfield Analysis of Rotors in Hover, Using a Coupled Euler/boundary Layer Method," *Aerospace science and technology*, vol. 3, no. 8, pp. 473–484, 1999.

[220] B. Ortun, M. Potsdam, H. Yeo, and K. Van Truong, "Rotor Loads Prediction on the ONERA 7A Rotor Using Loose Fluid/Structure Coupling," *Journal of the American Helicopter Society*, vol. 62, no. 3, pp. 1–13, 2017.

[221] H. Yeo and M. Potsdam, "Rotor Structural Loads Analysis Using Coupled Computational Fluid Dynamics/Computational Structural Dynamics," *Journal of Aircraft*, vol. 53, no. 1, pp. 87–105, 2015.

[222] A. Altmikus, S. Wagner, P. Beaumier, and G. Servera, "A comparison- weak versus strong modular coupling for trimmed aeroelastic rotor simulations," in *AHS International, 58th Annual Forum Proceedings*, vol. 1, (Montreal, Canada), pp. 697–710, June 11-13, 2002.

[223] H. Pomin and S. Wagner, "Navier-stokes analysis of helicopter rotor aerodynamics in hover and forward flight," *Journal of Aircraft*, vol. 39, no. 5, pp. 813–821, 2002. https://doi.org/10.2514/2.3001.

[224] H. Pomin and S. Wagner, "Aeroelastic analysis of helicopter rotor blades on deformable chimera grids," *Journal of aircraft*, vol. 41, no. 3, pp. 577–584, 2004. https://doi.org/10.2514/1.11484.

[225] V. Sankaran, M. Potsdam, A. Wissink, A. Datta, B. Jayaraman, and J. Sitaraman, "Rotor Loads Prediction in Level and Maneuvering Flight Using Unstructured-Adaptive Cartesian CFD," in *American Helicopter Society 67th Annual Forum*, 2011.

[226] J. Sitaraman and B. Roget, "Prediction of Helicopter Maneuver Loads Using a Fluid-Structure Analysis," *Journal of Aircraft*, vol. 46, no. 5, pp. 1770–1784, 2009.

[227] P. Masarati, M. Morandini, G. Quaranta, and P. Mantegazza, "Computational Aspects and Recent Improvements in the Open-Source Multibody Analysis Software MBDyn," *Multibody dynamics*, pp. 21–24, 2005.

[228] H.-J. Bungartz, F. Lindner, B. Gatzhammer, M. Mehl, K. Scheufele, A. Shukaev, and B. Uekermann, "PreCICE–A Fully Parallel Library for Multi-Physics Surface Coupling," *Computers & Fluids*, vol. 141, pp. 250–258, 2016.

[229] B. Y. Zhou, N. R. Gauger, M. Morelli, A. Guardone, J. Hauth, and X. Huan, "Towards a Real-Time In-Flight Ice Detection System via Computational Aeroacoustics and Bayesian Neural Networks," in *AIAA/ISSMO Multidisciplinary Analysis and Optimization at the AVIATION Forum*, 2019.

[230] J. Hauth, X. Huan, B. Y. Zhou, N. R. Gauger, M. Morelli, and A. Guardone, "Correlation Effects in Bayesian Neural Networks for Computational Aeroacoustics Ice Detection," in *AIAA Scitech 2020 Forum*, p. 1414, 2020.

[231] S. Mann and C. Stuart, "Advanced Propulsion Through the 1990s - an Airframers View," in *21st Joint Propulsion Conference, AIAA 1985-1192*, 1985.

[232] M. D. Moore, "Misconceptions of Electric Aircraft and Their Emerging Aviation Markets," in *52nd Aerospace Sciences Meeting*, p. 0535, 2014.

[233] M. H. SNYDER JR and G. W. ZUMWALT, "Effects of Wingtip-Mounted Propellers on Wing Lift and Induced Drag," *Journal of Aircraft*, vol. 6, no. 5, pp. 392–397, 1969.

[234] J. Patterson, Jr and G. Bartlett, "Effect of a Wing-Tip Mounted Pusher Turboprop on the Aerodynamic Characteristics of a Semi-Span Wing," in *21st Joint Propulsion Conference, AIAA 1985-1286*, 1985.

[235] L. Miranda and J. Brennan, "Aerodynamic Effects of Wingtip-Mounted Propellers and Turbines," in *4th Applied Aerodynamics Conference, AIAA 1986-1802*, 1986.

[236] T. Sinnige, N. van Arnhem, T. C. Stokkermans, G. Eitelberg, and L. L. Veldhuis, "Wingtip-Mounted Propellers: Aerodynamic Analysis of Interaction Effects and Comparison with Conventional Layout," *Journal of Aircraft*, vol. 56, no. 1, pp. 295–312, 2019.

[237] F. Avallone, D. Casalino, and D. Ragni, "Impingement of a Propeller-Slipstream on a Leading Edge With a Flow-Permeable Insert: A Computational Aeroacoustic Study," *International Journal of Aeroacoustics*, vol. 17, no. 6-8, pp. 1–25, 2018.

[238] E. Molina, *Detached Eddy Simulation in SU2*. Ph.d. thesis, Aeronautical Institute of Technology, 2015.

[239] E. S. Molina, D. M. Silva, A. P. Broeren, M. Righi, e. Y. Alonso, Juan J.", S.-H. Peng, D. Schwamborn, A. Revell, and C. Mockett, "Application of DDES to Iced Airfoil in Stanford University Unstructured (SU2)," in *Progress in Hybrid RANS-LES Modelling*, (Cham), pp. 283–293, Springer International Publishing, 2020.

[240] M. L. Shur, P. R. Spalart, M. K. Strelets, and A. K. Travin, "An Enhanced Version of DES with Rapid Transition from RANS to LES in Separated Flows," *Flow, Turbulence and Combustion*, vol. 95, no. 4, pp. 709–737, 2015.

[241] K. Kitamura and A. Hashimoto, "Reduced Dissipation AUSM-family Fluxes: HR-SLAU2 and HR-AUSM+-up for High Resolution Unsteady Flow Simulations," *Computers & Fluids*, vol. 126, pp. 41–57, 2016.

[242] R. O. Icke, O. Baysal, A. Moy, L. Lopes, B. Y. Zhou, and B. Diskin, "Toward Adjoint-Based Aeroacoustic Optimization for Propeller and Rotorcraft Applications," in *AVIATION 2020 Forum, AIAA-2020-3140*, 2020.